# NOTE TO USERS

DISSERTATION

# ATMOSPHERIC PRESSURE MICROPLASMA CHARACTERIZATION

Submitted by

Abdur Rahman

Electrical and Computer Engineering Department

In partial fulfillment of the requirements

For the Degree of Doctor of Philosophy

Colorado State University

Fort Collins, Colorado

Summer 2005

COLORADO STATE UNIVERSITY

April 28, 2005

WE HEREBY RECOMMEND THAT THE DISSERTATION PREPARED UNDER OUR SUPERVISION BY ABDUR RAHMAN ENTITLED ATMOSPHERIC PRESSURE MICROPLASMA CHARACTERIZATION BE ACCEPTED AS FULFILLING IN PART REQUIREMENTS FOR THE DEGREE OF DOCTOR OF PHILOSOPHY.

Committee on Graduate Work

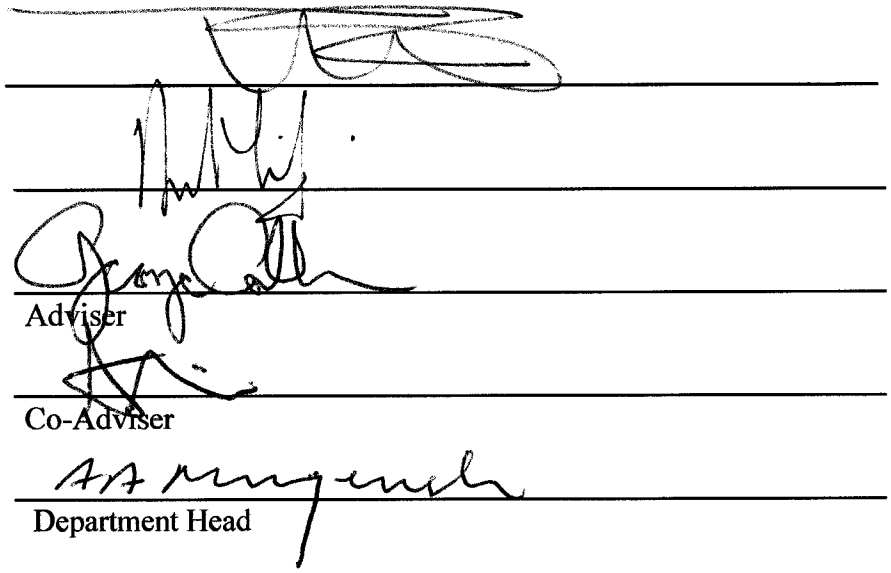

Adviser

Co-Adviser

Department Head

ABSTRACT OF DISSERTATION

ATMOSPHERIC PRESSURE MICROPLASMA CHARACTERIZATION

We present electrical measurements and absolute optical emission spectra in the VUV, UV, and visible regions in order to characterize radio frequency (RF) driven hollow slot microplasmas operating in open air at atmospheric pressure. The term microplasma in our research refers to interelectrode separation (100 to 600 microns) only, as electrode lengths are scalable from 1-30 cm. The electrode geometry creates a stable extended slot plasma and associated afterglow plume. Electrical measurements and emission spectra are presented for argon and helium plasmas with small admixtures of hydrogen and nitrogen into open air. Electrical measurements characterize sheath oscillations, sheath thickness, electron density, and effects of discharge asymmetry and external circuitry. Optical emission measurements provide a qualitative understanding of plasma chemistry and kinetics, and enable quantitative determinations of key plasma parameters including gas temperature, vibrational temperature, electron temperature (plasma nonequilibirum), and electron density. We also use the optical emission spectra to compare the efficiency and magnitude of light emission from the open-air microplasmas with corresponding values from commercial sealed mercury lamps in the UVB and UVC regions.

Abdur Rahman
Electrical and Computer Engineering Department
Colorado State University
Fort Collins, CO 80523
Summer 2005

ACKNOWLEDGEMENT

After more than two years of pain and suffering, I would like to recognize certain persons for their help. I appreciate the support of my advisor, Dr. George Collins for his guidance and generosity. I would like to express my gratitude to my co-advisor, Dr. Azer Yalin, who provided direction for this work and survived innumerable hours of discussion and multiple revisions. Dr. Jorge Rocca gave me confidence to become an experimentalist.

Katsumi Hoshimiya, Vijay Surla, and Rahul Ravi assisted with the experiments. Dr. Dinesh Patel and Ann Fitzgerald provided experimental expertise and encouragement.

This work is partially funded by a grant from the National Science Foundation.

TABLE OF CONTENTS

TABLE OF CONTENTS

TABLE OF CONTENTS

LIST OF FIGURES

LIST OF FIGURES

LIST OF FIGURES

LIST OF FIGURES

## LIST OF TABLES

LIST OF TABLES

# Chapter 1

# Introduction to Atmospheric Pressure Plasma Discharge (APGD)

## 1.1 Introduction

Atmospheric pressure glow discharge (APGD) plasmas have the potential to become a versatile technological tool [1] as alternative photon, radical and ion sources for various applications including: biochemical decontamination and remediation of toxic gases and pollution/exhaust emission reduction [2], material deposition [3] and etching [4], and deactivation of bacteria, spores and viruses [5-7]. In the past decade a variety of atmospheric pressure glow discharges have been reported, including microhollow cathode discharges [8, 9] RF driven plasma jets [6, 10], DC and pulsed pin discharges [11] as well as various resistive and dielectric barrier discharges [7, 12]. These atmospheric plasmas have potential to be low cost compared to vacuum plasmas; however, they suffer significant challenges in terms of generating uniform and stable large volume plasmas [1, 13]. Better understanding of the origin of spatial instabilities is required to develop new APGD plasma sources. This thesis is directed towards characterization, and understanding of a novel atmospheric pressure glow discharge (APGD) microplasma that operates uniformly over lengths up to 30 cm. External measurements (electrical and optical) are performed on an RF (radio frequency) driven hollow slot microplasma device in order

to better characterize the APGD plasma properties and elucidate its excitation and stabilization mechanisms. In this chapter we provide an introduction to plasmas themselves, with a focus of the recently developing field of APGDs.

Section 1.2 defines basic plasma and plasma parameters that distinguish them from gases. Section 1.3 emphasizes on glow discharge plasmas. Section 1.4 discusses instability issues of glow discharge plasmas, Section 1.5 discusses unique features of the APGD plasmas. Section 1.6 focuses on gas breakdown mechanisms and finally Section 1.7 briefly describes different types of APGD plasma sources.

## 1.2 Introduction to Plasma and Plasma Parameters

The majority of matter in the universe is in plasma state [14, 15], for example, stars, interstellar space, and even the upper layers of our atmosphere. In early gas discharge studies, Langmuir characterized the electron and ion oscillations using the term plasma oscillations [16]. Although the term "plasma" was originated by Irving Langmuir in 1928 [17], concerted efforts to study plasma physics did not come until the second half of the last century. This research included gas discharge physics, energy related applications such as controlled thermonuclear fusion, and astrophysics [18, 19]. Gas discharge physics usually deals with low temperature plasmas (<1000 K) whereas thermonuclear fusion and solar plasma studies deal with very high temperature plasmas (>1000 K). Currently there are extensive ongoing research efforts in a variety of fields associated with plasmas and their applications.

***Plasma,*** the fourth state of matter, can be defined as a completely or partially ionized gas that maintains quasineutrality and exhibits collective behavior. Although plasma most commonly form in gases, plasma behavior is also observed in liquid and solid phase

[13]. Here the discussion focuses on gas phase plasmas only. Quasineutrality implies that the net charge density is zero but at any instant of time at any particular position in the plasma, the charge balance may deviate by a small amount. The term collective behavior indicates that the charged particles suffer long range coulomb interactions that do not fall off as $1/r^2$ ($r$ is average distance between an electron and an ion). Instead, the interaction potential, $\Phi$, falls of as [20]:

$$\Phi \sim \Phi_0 \exp(-|r|/\lambda_d) \tag{1.1}$$

where $\lambda_d$ is the Debye length given by

$$\lambda_d = \left( \frac{KT_e}{4\pi n_e e^2} \right)^{1/2} \tag{1.2}$$

where, $K$ is Boltzmann's constant, $e$ is the charge of an electron, $n_e$ is the electron density (also known as plasma density), and $T_e$ is the electron temperature. Ions are moving in the plasma, and the plasma ion temperature, $T_i$, is typically much less than the electron temperature, $T_e$. Figure 1.1 shows the potential distribution next to an isolated metal strip immersed in a plasma. Electrons have higher kinetic energy compared to ions (owing to their smaller mass) and strike the metal strip more often than the ions. Since the strip is isolated, these electrons eventually charge up the strip negatively. This process continues until the strip is sufficiently negatively charged to repel the plasma electrons, that is, a potential barrier is built. Only highly energetic electrons with kinetic energy more than the potential energy of the barrier can reach the metal strip. The negatively charged strip attracts positive ions and space charges accumulate next to the strip. Each layer of space charges screens the negative potential of the strip and eventually the potential approaches the plasma potential. The length from the strip at which its effect is completely screened

(i.e. the value of the local potential returns to the plasma potential) is called as the Debye screening length or Debye length ($\lambda_d$) and the space charge region is called the plasma sheath.

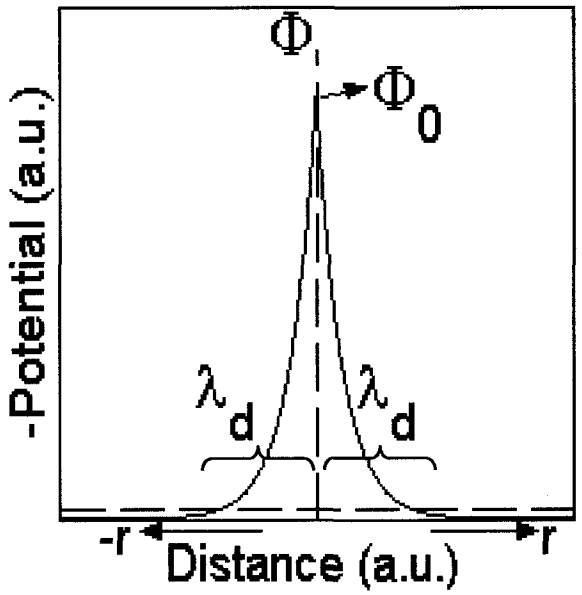


**Figure 1.1: Potential distribution due to ion accumulation next to a metal strip (at *r=0*) immersed in a plasma. The distances from the metalic strip are represented *by r* and the spatial decay of (negative) potential is plotted on the vertical axis and distance on the horizontal axis. The base of the vertical axis is the plasma potential and the dashed horizontal line represents zero potential. $\lambda_d$ is the Debye screening length, defining the spatial decay constant at which the potential approaches the plasma potential [20].**

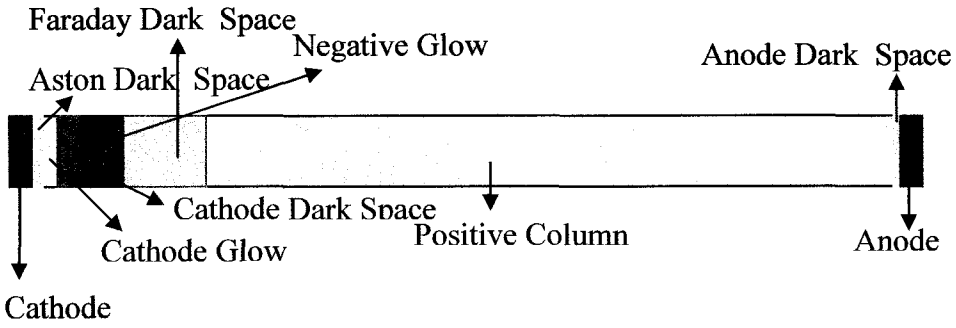


**Figure 1.2: Different spatial regions of a normal glow discharge plasma in between the two electrodes [21].**

Figure 1.2 shows the typical spatial regions of a (low pressure) glow discharge formed in a discharge tube. In this case the region between the cathode and the negative glow in Figure 1.2 is a plasma sheath and surprisingly most of the discharge voltage

drops across the sheath region[1] and the voltage drop is termed the cathode fall voltage or sheath voltage. The voltage that drops across the positive column of Figure 1.2 is called the bulk voltage. Any ion that enters the sheath must maintain a minimum kinetic energy or velocity ($v_b$) and can be expressed as [22]:

$$v_b > (KT_e/m_i)^{1/2} \tag{1.3}$$

where $m_i$ is the mass of the ion and $v_b$ is the Bohm *velocity*.

Due to separation of ions and electrons at walls and electrodes, disturbances in the neutral plasma result in an electric field originating from the net charged density $\rho_{net}=N_+ - N_-$ ($N_+$ and $N_-$ are the positive and negative charges). Restoring electrostatic force causes the electrons and ions to oscillate. The frequency of oscillation defines the electron and ion plasma oscillation frequencies. The electron plasma frequency, $\omega_{pe}$ can be written as [16]:

$$\omega_{pe} = \sqrt{\frac{n_e e^2}{\varepsilon_0 m_e}} \tag{1.4}$$

where, $\varepsilon_0$ is the free space permittivity. The ion plasma frequency can be obtained by replacing the electron mass ($m_e$) by the ion mass ($m_i$). The electron plasma frequency is also called the plasma frequency, and is much greater than the ion plasma frequency ($m_i >> m_e$).

For weakly ionized low temperature plasmas, the electron plasma frequency (i.e. electron density) determines the coupling efficiency of power from external power to the plasma sources. When the applied frequency exceeds the electron plasma frequency, electromagnetic (e.m.) waves penetrate the plasma. If the applied frequency is less than

[1] This is true for non-LTE glow discharge plasmas only.

plasma frequency, plasma electrons follow the applied field and quickly absorb energy from the incident electromagnetic (e.m.) field so that the applied fields do not penetrate far into the plasma. The electron density at which the electron plasma frequency equals the frequency of the applied e.m. field is termed the critical electron density ($n_c$). Typically, for low temperature weakly ionized RF driven plasmas, the electron density is below $n_c$ whereas in microwave plasmas, the electron density can be either below or above $n_c$. Because of their larger mass, ions can follow the applied e.m. field variation only at lower applied frequencies.

### 1.3 Glow Discharge Plasma

Depending on the gas temperature, $T_g$, compared to the electron temperature, $T_e$, plasmas can be divided into two classes: low temperature plasmas and high temperature plasmas. In a low temperature plasma, the electron temperature is much higher than the ion temperature and the gas temperature, in other words, the temperature of the plasma constituents are not at equilibrium and the plasma is referred to as a cold or nonequilibrium (non-LTE) plasma. In the other class, temperatures of all constituents are in local thermal equilibrium (LTE) and the plasma is referred to as thermal or LTE plasma. Welding, plasma cutting, metal melting and remelting etc. require high temperature and thus LTE plasmas are employed [23].

The applications of non-LTE plasmas are more versatile. Plasma ion energies and densities can be controlled externally (by tuning current and voltage, changing or altering gas species and gas pressure etc.) over a wide range. This controlling capability allows precision work using non-LTE plasmas. Notable applications of non-LTE plasmas are in semiconductor industries for material deposition [3] and etching [4]. Non-LTE plasmas

are also used in space science as thrusters and plasma contactors [24], for thin film coating on architectural glasses, and as spectral light sources [24, 25], and in other applications. Note that the non-LTE plasma applications mentioned above usually require low pressure, typically in the range of $10^{-3}$ Torr or below. As will be further discussed, atmospheric pressure non-LTE plasma could extend the aforementioned applications and ensure new ones.

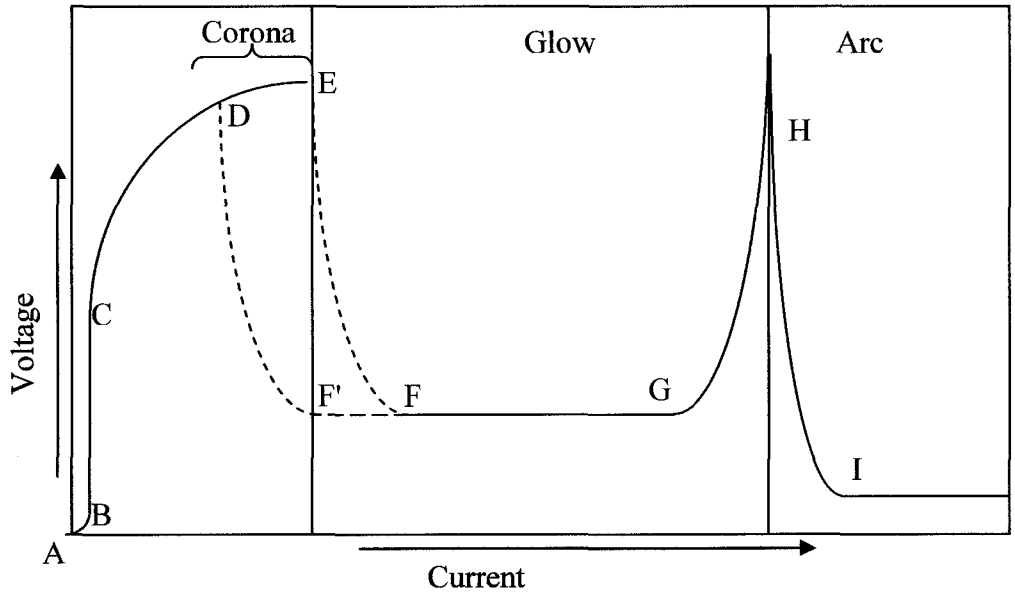


**Figure 1.3: *I-V* curve showing three major regions of DC plasma operation [21].**

1.3.1 Non-LTE Plasma

Non-LTE plasma are those in the which electrical energy applied flows primarily into energetic electrons and $T_e >> T_g$. Thermal plasmas in contrast heat the gas so that $T_e \cong T_g$. Figure 1.3 shows the *I-V* characteristics of the three main operating regions for typical low pressure DC plasmas [21]. The region at left corresponds to Townsend's dark discharge region, also referred to as the corona discharge region. A corona discharge appears when a very high voltage is applied to a tip or a very sharp edge. The corona discharge is a unipolar discharge in which the presence of the charged particles does not

distort the (applied) electric field. Corona discharges are extensively used for ozone generation [26]. The right most side of the Figure 1.3 shows the arc region. The arc is an LTE plasma is characterized by thermionic emission and low cathode fall voltage.

The middle section in Figure 1.3 is the non-LTE glow plasma region. The normal glow region is the operating region for many industrial applications because of its high plasma uniformity and low gas temperature. The plasma glow appears after the gas breakdown at point E and the voltage drops sharply to F. As the current increases beyond the point F, the voltage remains constant up to a certain current (point G) and the discharge is termed as normal glow. In the normal glow discharge region (at constant pressure), the current density remains constant as the current varies [13, 27], i.e., the area of the glow discharge increases with increasing current (F to G). Beyond the point G, the positive slope in the *I-V* curve indicates that the current density is no longer constant, corresponding to the discharge occupying the entire electrode area. The positive slope in the *I-V* curve is termed the abnormal glow region. As the current further increases (beyond H), a thermal plasma replaces the glow plasma. A hysteresis is observed in the glow discharge if the current is reduced below the initiation point after the ignition of glow discharge plasmas (F'F).

In a normal glow discharge plasma, a high cathode fall voltage appears at the cathode where a net positive charge density, $\rho_{net}=N_+-N_-$, density builds up due to higher electron mobility compared to ion mobility in the cathode electric field (see next chapter). The region over which this high voltage gradient builds up is also called the sheath. Figure 1.2 shows different regions of a low pressure glow discharge plasma [21]. The high cathode fall voltage (cathode dark space) is an important feature of the normal glow

discharge (in contrast to the small cathode fall voltage in the arc discharge). The most optically intense region is next to the cathode fall region, known as the negative glow region, and is created by the highly energetic electrons that are accelerated through the high voltage gradient of the sheath potential. Electrons are created at the cathode by ion bombardment or other means including thermal emission, field emission, photoelectric effect. The number of electrons ($n_w$) emitted from the discharge wall per photon and bombarding ion is defined as the secondary electron emission coefficient ($\gamma$). The area between the electrodes is predominantly covered by continuous luminous glow, known as the positive column. Bulk electrons maintain ionization and excitation in the positive column. The number of ionization collision per unit length made by an electron in traversing the plasma column is given by Townsend's first ionization coefficient ($\alpha$). The potential in the positive column is nearly constant, thus the electric field is nearly zero.

## 1.4 Instabilities

Glow discharge plasmas may suffer numerous instabilities due to thermal instability, electronic instability, streamers, striations etc. Different types of plasma instabilities can cause glow plasma to transition to arcs (so called glow-to-arc transition) or can reduce plasma uniformity or even terminate the plasma. Understanding and mitigating the effects of these instabilities is important to developing (useful) glow discharge plasmas. Primary instability mechanisms are described below:

### 1.4.1 Thermal Instability

The physical basis of this type of instability is the ohmic (Joule heating) dissipation in the discharge [28]. Transverse inhomogeneity in the $\boldsymbol{E}$ field causes electron temperature, $T_e$, to increase with increasing electron density [29]. This in turn decreases the

gas density, $N$, which increases reduced electric field ($E/N$) values. Therefore increase in the electron density (discharge current) follows a positive feedback as shown below and ultimately results in glow to arc transition [29].

$$\delta n_e \uparrow \rightarrow \delta(jE) \uparrow \rightarrow \delta T \uparrow \rightarrow \delta N \downarrow \rightarrow \delta(E/N) \uparrow \rightarrow \delta(T_e) \uparrow \rightarrow \delta n_e \uparrow$$

The mechanism can be explained as follows, electrons generated at the cathode surface accelerate through the entire cathode fall voltage, and thus acquire very high energy so they can ionize neutrals in bulk plasma effectively [30]. This process can cause a fluctuation (increase) in the electron density in the bulk plasma. The sudden increase in the electron density changes the plasma resistivity such that it is much lower than that of the driving circuit. Increase in current density increases joule heating and thus gas temperature. The increase in gas temperature reduces neutral density and increases the reduced electric field ($E/N$) and thus the electron temperature. The increased electron temperature result in more ionization in the bulk hence electron density gets a positive feedback. In some cases, this process can lead to glow to arc transition [31].

Electron emission at the cathode by ion/neutral bombardment, thermionic emission (from a hot cathode), and field emission are the most common sources of thermal instability [32, 33]. Cooling of the cathode reduces the probability of the thermal instability from thermionic emission [33]. In the case of field emission the sudden increase in the electron density results from field emitted electrons, which are very highly energetic, and thus more effective in ionizing as compared to electrons emitted by other means. The addition of a ballast resistor is an effective method to reduce the sudden increase in discharge current, but reduces system efficiency.

1.4.2 Electronic Instability

Attachment Induced Instability

Multistage ionization and attachment induced instabilities are examples of electronic instability. The fundamental source of this type of instability is temporal imbalance in the rate of charge production and loss processes which together result in runway ionization [13, 34]. As opposed to thermal instability, the electronic instability results from longitudinal inhomogeneity in the electric field which causes $n_e$ to decrease with increasing electron temperature [34, 35] along the axis of the electric field. The flow chart indicates how the positive feedback takes place in the attachment induced instability [29].

$$\delta n_e \uparrow \rightarrow \delta(T_e) \downarrow \rightarrow \nu_a \downarrow \rightarrow (Z_+ - Z_-) \uparrow \rightarrow \delta n_e \uparrow$$

Here the $Z_+$ and $Z_-$ denote densities of positive and negative ions in the plasma and $\nu_a$ represents the attachment frequency. Increase in the electron density causes the electron temperature to decrease that results in fewer attachments and thus increases free electrons in the plasma[2]. Since detachment does not depend on the electron temperature [29], the net electron density in the plasma increases. The process continues and the instability is formed in very short time compared to the thermal instability. Discharges containing electronegative gases (e.g. Oxygen, $SF_6$) are prone to this type of instability. For example [35], in an oxygen containing discharge ($CO_2$ laser) where detachment is compensated considerably by the attachment process (e.g. $O^-$ or $O_2^-$) the steady state is obtained at low electron temperature because ionization compensates only the small difference between attachment and detachment. Change in the electron density at any instant of time therefore develops electronic instability in such a discharge system. The attachment

induced instabilities are not observed for rare gas discharges and $N_2$ discharges due to their low electron affinity [36].

Inverse ionization instability

In high pressure discharges, external electron beam sources introduced via foils which act as electron windows are often used to balance the electron production and loss rates. Inverse ionization instability may occur in this type of discharge [36, 37]. Electron-neutral attachment depends on the dissociative attachment threshold energy, i.e. for a certain range of reduced electric field (***E/N***), dissociative attachment rate is an increasing function of electric filed (***E***). If the reduced electric field (***E/N***) is such that the dissociative attachment grows sharply causing $n_e$ to decrease, the discharge increases the electric field (i.e. ***E/N***) to sustain the plasma. Since the attachment is an increasing function in this ***E/N*** range, this process keeps building up attachment rate. The local field will be enhanced due to the increased attachment rate and cause glow to arc transition.

1.4.3 Striations

This type of instability is common in contaminated rare gas, e.g. contaminated with molecular gases or in pure molecular discharges [38]. The term striations originated from the observation of alternate bright and dark bands in the gas discharge plasma. The striation can be stationary or moving. Moving striations can sometimes be made stationary with appropriate choice of gas velocity [38]. There is a correlation among discharge current, discharge radius and gas pressure for which striations are observed in He discharge [39]. Ionization waves or oscillations usually generate alternating luminous bands in the axial direction, i.e., they form longitudinal inhomogeneity. For certain operating

[2] Here it is assumed that the attachment rate of the species considered has strong $T_e$ dependence. Note that, attachment rate for some species do not have such strong dependence on $T_e$ [36].

conditions, we have observed striations in the atmospheric pressure RF slot discharge studied in this work (Figure 1.4). Kiselev-skii and Suzdalov [40] first observed striations in the radial direction in atmospheric pressure plasmas.

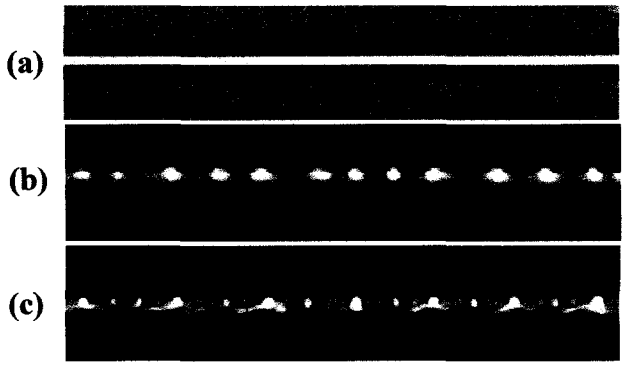


**Figure 1.4: RF (60 MHz) driven hollow slot microplasmas: (a) normal glow operation without presence of striations, (b)&(C) radial striations (plasma conditions are: ~0.20 slpm of argon with admixtures of ~0.70 sccm of nitrogen per cm of slot length ) are observed at delivered powers as low as ~3.3 W/cm ($I_{RMS}$~ 0.06 amp/cm ).**

## 1.5 Atmospheric Pressure Glow Discharge Plasma

Non-thermal low pressure plasmas are extensively used in current plasma processing technologies. These plasmas operate under very low pressure and the electrical energies are deposited to the plasma constituents (charged particles and neutrals) efficiently. Technological application of atmospheric pressure or high pressure LTE plasmas has been very limited and has mostly been for metallurgy [1, 23]. However atmospheric pressure nonequilibrium plasmas have the potential to revolutionize industrial plasma applications. They have the potential to reduce cost by removing the expensive vacuum equipment and increase the production (or treatment) rates due to higher densities and fluxes of radicals, ions, electrons and photons. APGD plasmas not only have the potential to process materials that currently use low pressure nonequilibrium plasmas, but may allow processing of high vapor pressure materials that can not be treated at low pressure.

These include, foods, water, certain chemical and biological materials [7, 10], dry cleaning fuel and certain (contaminated) gases [41].

**1.6 Gas Breakdown Voltage & Paschen Curve and Similarity Law**

There are two primary gas breakdown mechanisms: the Townsend mechanism and the spark mechanism (also known as streamer breakdown) [42]. In the Townsend mechanism, the $\gamma$ electrons created at the cathode collide with atoms or molecules in the discharge gap and liberate electrons. Some of the newly generated ($\alpha$) electrons regenerate more electrons in the discharge gap leading to formation of electron avalanches. The electron avalanches therefore move from the cathode toward the anode. When the criterion ($\gamma[exp(\alpha d)-1]=1$) for a discharge gap, $d$, is satisfied, a self sustained current is established [29, 42, 43]. A relation between gas breakdown voltage, pressure and discharge gap for low pressure nonequilibrium DC plasma is established below.

The gas breakdown voltage, $V_b$, can be expressed by the Paschen law [43];

$$V_b = \frac{Cpd}{\ln(Apd/\ln[1+(1/\gamma)])} \qquad 1.5$$

where, $C$ and $A$ are constants (that vary with the gas), $p$ and $d$ are the pressure and distance of the discharge gap respectively, and $\gamma$ is the secondary electron emission coefficient (which depends on the cathode material).

To determine the minimum breakdown voltage $(V_b)_{min}$ with respect to pd product (gas pressure multiplied by distance between electrodes), we differentiate equation 1.5 with respect to $pd$ and equate to zero, thus we obtain,

$$(pd)_{\min} = \frac{2.718}{A}\ln\left(1+\frac{1}{\gamma}\right) \qquad 1.6$$

where, $(pd)_{min}$ is the pd product corresponding to $(V_b)_{min}$. The universal Paschen curve that relates the breakdown voltage and discharge gap, can be obtained by considering the dimensionless variables [43]:

$$X=pd/(pd)_{min} \quad 1.7$$

$$Y=V_b/(V_b)_{min} \quad 1.8$$

Equation 1.5 must be satisfied for any arbitrary value *pd*, hence using equation 1.5 we find [43],

$$Y=\frac{X}{1+\ln X} \quad 1.9$$

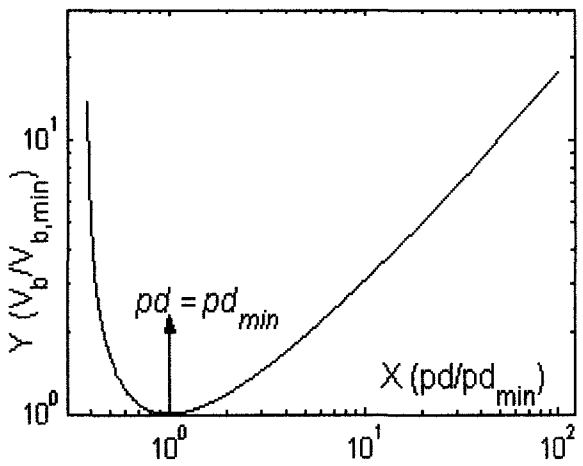


**Figure 1.5: Theoretical Paschen curve of normalized breakdown voltage versus normalized *pd* products[43].**

Figure 1.5 shows the $Y$ vs $X$ plot. At $X$ values below 1, the increase in the breakdown potential is due to an insufficient number of neutrals that can be ionized to obtain gas breakdown. As $X$ values above 1, the gas breakdown voltage increases because electrons lose energy due to increased number of collisions. This curve is known as Paschen curve and the point where $pd = pd_{min}$ is called as the Stoletow's point (where the ion-electron pair generation is most efficient in terms of power expenditure) [43].

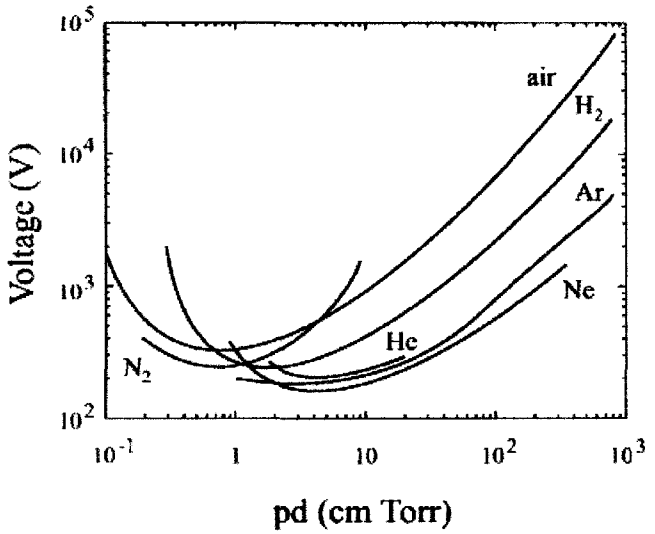


**Figure 1.6: Breakdown voltages for different operating gases as a function of *pd* product ([1] and references therein).**

Figure 1.6 (from [1] and references therein) shows the experimental breakdown voltages for several gases as a function of the *pd* product. The graph shows that the minima of the breakdown voltages for rare gases are less than for molecular gases although the minima occur for larger $pd_{min}$ values. The theoretical curve (Figure 1.5) and the experimental data (Figure 1.6) apply to DC excitation and are $\gamma$ dependant. Since $\gamma$ is the measure of the electron yield from the electrode surface due to ion bombardment and photoelectric effect, the breakdown voltage is also dependent on electrode material.

Generation of uniform APGD plasmas tends to be difficult due to the limitation imposed by the *pd* product. Specifically large volume plasma generation is limited by the *pd* product; so that breakdown of atmospheric pressure plasmas requires high voltage. Note that the *pd* product of the RF driven hollow slot (Ar/He) microplasma investigated in this thesis is approximately 10 Torr-cm, i.e., to the right of the Paschen minima (Figure 1.6). RF frequencies, $\omega_{RF}$, herein varies from 1 - 60 MHz.

In the case of low pressure RF discharges, ions are immobile (i.e., they can not follow the electric field due to their large inertia.) Because the ion plasma frequency, $\omega_i << \omega_{RF}$ the breakdown of the gas is not due to ion bombardment of electrodes, and thus does not depend on the electrode material. On the other hand the electron plasma frequency $\omega_{pe} >> \omega_{RF}$ so that electrons can follow the applied field, and oscillate back and forth between the electrodes. The electrons ionize the volume of the gas and when the mean free path of ionization is approximately equal to the discharge gap, the Paschen minima occurs [44]. It has been observed that the gas breakdown voltage in low pressure RF discharge is smaller than the DC breakdown voltage for the same gas species [44]. At high pressure, RF discharge breakdown is similar to DC breakdown because the increased collisional frequency decreases the mean free path of ionization compared to the discharge gap [44]. As a result, the discharge breakdown depends on the secondary emission from the electrode surface (as in the case for DC discharges).

Hence, the glow discharge operation requires larger voltage across the discharge gap at higher *pd* values. Since most of the applied voltage drops across the sheath the probability of the arc formation is enhanced beyond a certain *pd* product, the non-thermal glow discharge often turns into thermal (equilibrium) plasma. For glow operation of rare gases, the *pd* product is usually restricted between ~ 1 Torr-cm to 10 Torr-cm [24, 45]. These values correspond to a discharge gap (*d*), ~10 μm<d<100 μm at atmospheric pressure. If the *pd* product lies in this range, the gas breakdown is due to primary avalanche in the bulk region and can be explained by the Paschen gas breakdown law [46].

We now briefly discuss the second breakdown mechanism (spark or streamer breakdown). At higher *pd* values, the gas breakdown can also occur due to space charge

accumulation anywhere between the electrodes (as opposed to the cathode in the Townsend's breakdown mechanism). As the space charge field becomes comparable to the applied field, highly conducting filamentary channels causes gas breakdown (known as Raether's breakdown) [45, 46] or streamer breakdown. Non-uniformity arises in the APGD plasma from streamer induced spark channel formation. The streamer induced breakdown is therefore not helpful for material processing.

Note that the high end limit of the *pd* product (i.e. 10 Torr-cm) may not allow glow operation at atmospheric pressure [9]. Different approaches have been made by researchers to overcome this shortcoming and are discussed in the next section.

### 1.7 Approaches to APGD Plasma Generation

Different techniques have been employed by researchers to generate APGD plasmas using DC sources, capacitively coupled RF driven sources, inductively coupled RF plasma and pulsed plasma sources. The DC sources require comparatively cheap circuitry compared to capacitively coupled or inductively coupled sources but are more prone to thermal and electronic instabilities as they require higher gas breakdown and plasma sustaining voltages. On the other hand capacitively coupled RF sources are more robust against instabilities since the electrons are sufficiently energized (to ionize the gas) only for a fraction of the oscillating cycle. Inductively coupled plasmas (ICPs) have an advantage over both because most of the instabilities originate next to the electrodes and ICPs are not in contact with the electrodes. ICPs may require very high voltage (or employ very large inductance) to generate the required magnetic field to sustain the plasmas. Large inductance essentially reduces the efficiency of the system. Different types of APGD plasmas using DC, pulsed DC, capacitively coupled, and inductively coupled plasmasa are described briefly.

1.7.1 DC Glow Discharge

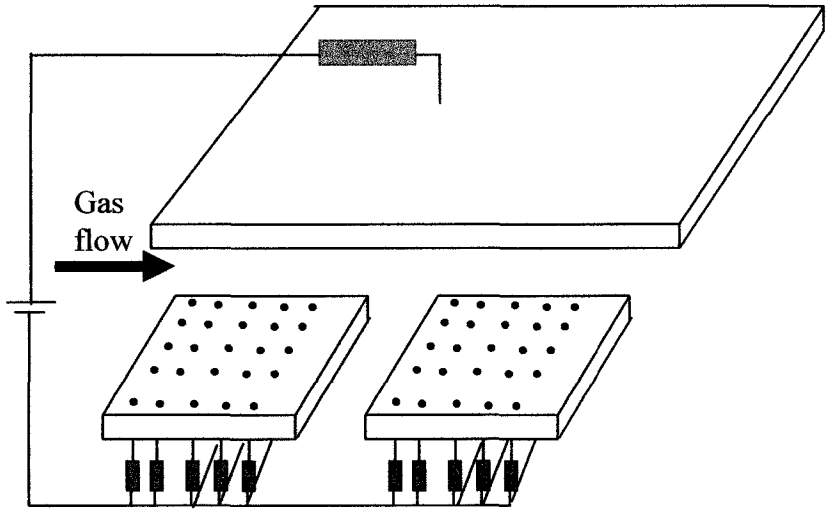


**Figure 1.7: Atmospheric pressure normal glow plasma, generated using high gas flow rate and high voltage (~30 kV). Direction of the *E* field is transverse to the gas flow rate. Each dots in the lower plates (cathodes) represents a pin, ballasted with a resistor [2].**

As discussed earlier, an atmospheric pressure DC glow discharge requires high voltage both for gas breakdown and for sustaining the plasma. Akishev and his group [2, 41, 47] applied a multi-pin method to generate large volume APGD plasmas (Figure 1.7) in order to decontaminate industrially generated SOx and NOx. The distance between the pins and the anode was up to 1 cm. The multipin approach is similar to a corona configuration, but the current density in this case was much higher as compared to a corona discharge and a diffuse glow could be observed. The applied DC voltage (~30 kV) across the pins and the anode was large and each pin was individually ballasted with resistors to prevent arcing. The gas flow was transverse to the electric field and the flow rate was high. Because of the high voltage requirement and large ballast resistors, the application of this type of APGD plasma has poor efficiency.

Kruger et al [48, 49] generated non-thermal atmospheric pressure air and nitrogen plasmas using pulsed DC source between ballasted stainless steel tubes (with platinum

pins). Figure 1.8 shows a 1 atm. nitrogen plasma generated between two pins separated by 1.8 cm. Diameter of the discharge is ~ 1.7 mm . Electron number density and the gas temperature are $10^{12}$ $cm^{-3}$ and 2000 K respectively.

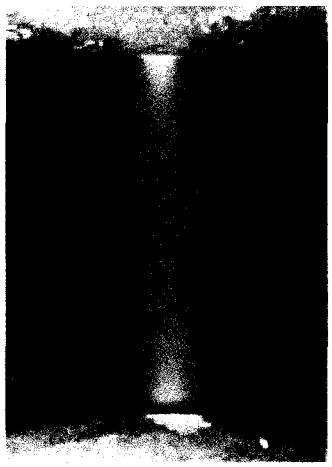

**Figure 1.8: A pulsed DC source is applied between two platinum ball pins to generate, $N_2$ glow discharge at atmospheric pressure [48].**

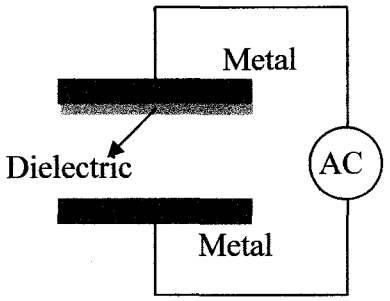


**Figure 1.9: Dielectric barrier discharge configuration. One or more conducting planes are Insulated with dielectric material to force pulsed current operation as shown in Figure 1.10.**

1.7.2 Dielectric Barrier Discharge (DBD)

If one or both electrodes are insulated with dielectric material, the discharge is termed as a dielectric barrier discharge (DBD). Figure 1.9 shows a schematic of DBD. The DBD requires an AC source (or a pulsed current source) and is an example of a capacitively coupled discharge. The advantage of the DBD at atmospheric pressure is that it can operate at a very high *pd* value (~500 Torr-cm) [45]. The initiation of the plasma in the DBD is usually due to streamer formation instead of primary electron avalanche.

DBDs are typically non-uniform as they are comprised of a large number of small rapidly moving filamentary channels. The filamentary channels are short lived (~nanosecond) and diameters of these channels are of the order of 100 μm; (parameter values are dependant on the type of the gas and dielectric material used [50]). Since these are essentially spark channels, the electron energies are very high and the electrons can ionize the gas very efficiently. As a result, large (average) current densities can exist in DBD plasmas. Transition from glow to arc is likely in DBD discharges due to their very high current density. It has been shown that the DBDs can operate in the glow mode with a suitable choice of gas, pressure, discharge gap length and voltage. In this way the filamentary channel disappears prior to arc having time to form [51, 52].

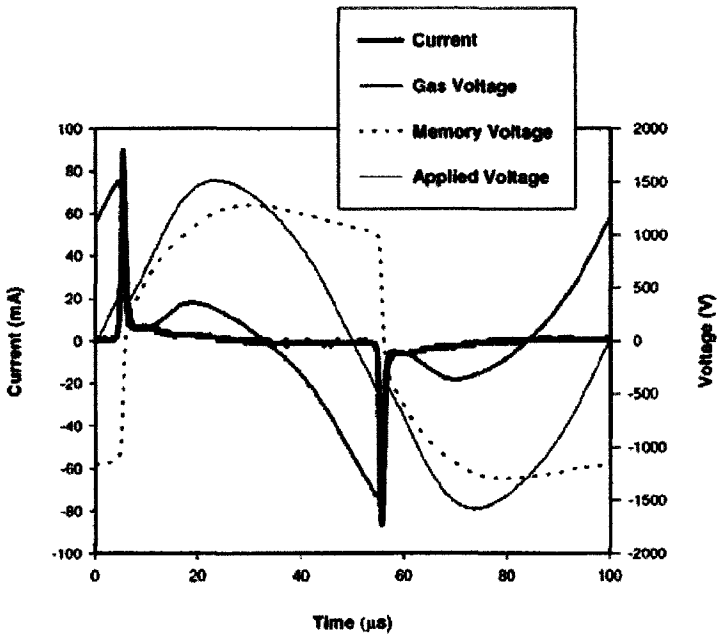


**Figure 1.10: Time variation of measured current and voltages over one cycle [45].**

Kanazawa et al [53, 54] and Okazaki and Kogoma [52-56] used a similar pin method as well as a parallel plate method to generate large volume APGD plasmas. Their work differs significantly from the previously mentioned work in the sense that they have employed AC sources with frequencies higher than 1 kHz. Further; the whole process

was in an enclosed chamber and at least one electrode was insulated with a dielectric, i.e., the discharge was dielectric barrier discharge (DBD).

DBDs that cause spatially filamentary channels throughout the electrode area are not constant with time and do not allow processing of materials that require high spatial uniformity (e.g. semiconductor and flat panel processing). However, they are effective in processes such as ozone generation [50]. It had been claimed [45, 57] that stable glow mode plasmas were obtained using DBDs with no streamers observed. However the *I-V* curve show large current spikes (~of nanosecond duration) [45] considering with plasma initiation at the start of each AC cycle (Figure 1.10). These spikes indicate non-niformity of current density during these short periods of time. As mentioned, any non-uniformity is damaging to the plasma processing of materials, so that these DBDs are likely inappropriate for such applications. On the other hand the DBDs may be appropriate for applications including decontamination, food-processing etc.

1.6.3 Capacitively Coupled RF Plasma Jet

Koinuma et al [58] generated an atmospheric pressure glow discharge plasma jet for the purpose of micromachining and etching. A cylindrical quartz tube surrounded the RF powered cathode rod and separated the stainless cylindrical anode. Helium gas flowed through the quartz tube to generate and sustain plasma. The diameter of the plasma was dictated by the quartz tube diameter (1.7 mm ID). In other work Koinuma et al [59], instead of using the rod electrode, used alumina coated cylindrical shaped hollow metal with a disc like opening for larger area treatment. Following this idea, Babayan et al [3, 60] also demonstrated capacitively couple RF plasma jets. They employed similar approach except that the dielectric insulation between the RF powered electrode and the

grounded electrode was absent. Littelefield and Collins [61] have very recently developed RF generated needle(s) plasma for the purpose of circuit testing. The RF powered hollow needle(s) through which He gas flows has a diameter of ~0.5 - 1 mm. The ground electrode is a plane metal strip that lies a few millimeters away from the gas exit port of the needle. The ground plane has hole(s) aligned with the gas exit port of the needle(s) such that the RF generated glow plasma protrudes (up to ~1 cm) beyond the ground plane.

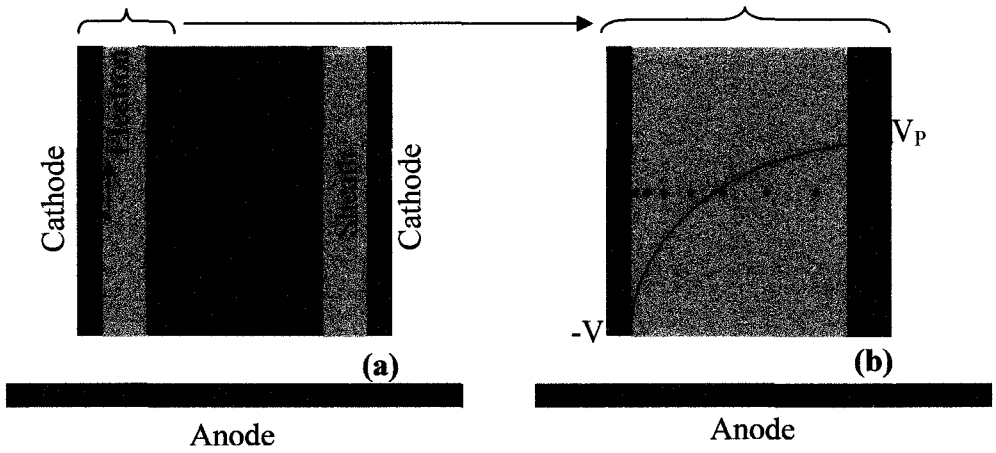


**Figure 1.11: (a) Cross section of a cylindrical hollow cathode discharge located within the inner cylinder. Gray regions are the sheath. Red region is the overlapped negative glow region. An electron reaches the left cathode wall. (b) Enlarged view of the sheath region next to the cathode (left). The electron is accelerating through the negative potential. The distance between the successive electrons (dots) indicates the increased velocity of the electron as it traverse the sheath region. This highly energetic electron will traverse through the negative glow region and reach the cathode (right) then turn back and again reach the left cathode. The electron will oscillate between the cathode walls.**

### 1.7.4 Hollow Cathode Discharge

Low pressure hollow cathode discharges find their application in spectral lamps [24, 25] due to their low voltage operation and high optical emission capacity. They are also used as plasma switches[24], lasers [25], plasma contactors [24], propulsion systems in space science [43], and plasma jets [24].

The operating principal of the hollow cathode discharges that allow low voltage excitation can be explained as follows. When the electrodes of a plane parallel discharge are brought close to each other so that the negative glow regions overlap, enhanced

electron density is achieved [62]. In the conventional hollow cathode (CHC), discovered by Paschen [25], the cathode may have a cylindrical shape or a parallel plate shape as shown in Figure 1.11. In the CHC anode lies outside the hollow cathode region. The pressure of the discharge and the distance between the opposite walls of the hollow cathode(s) are such that the negative glow regions are overlapped. The electrons have the highest possible energy in the negative glow-cathode dark space boundary region, therefore these high energy electrons can penetrate far into the sheath of the opposite wall. An energetic electron moving towards a cathode decelerates from the opposing electric field and then turns around and accelerates toward the negative glow region again. The further it penetrates the higher the velocity it acquires in its return path to the plasma. The same electron thus swings back and forth many times (Pendel effect) and can excite/ionize atoms/molecules before it finally is depleted. Thus, one has increased electron density and brightness in the hollow cathode geometry.

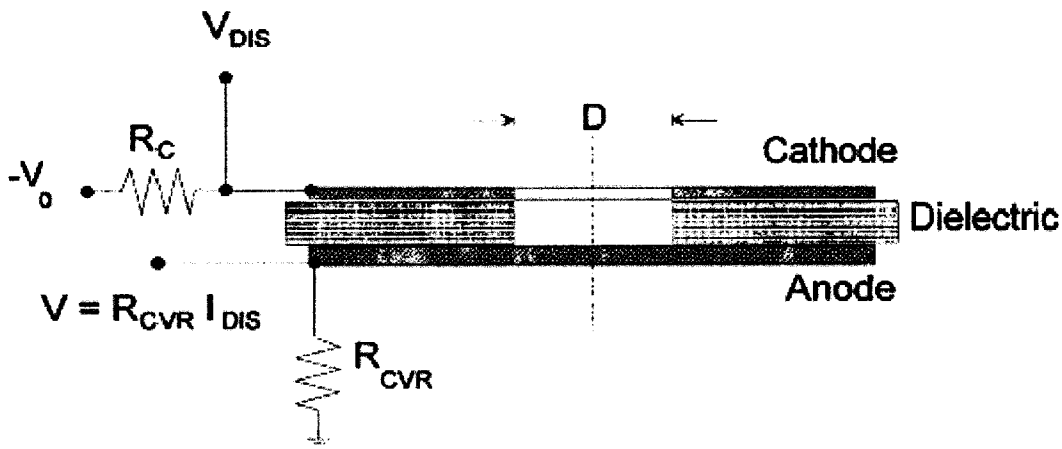


**Figure 1.12: Schematic of DC microhollow discharge between two plates the cathode of which has an open hole [9].**

High pressure (up to 1 atm.) hollow cathode glow discharge operation has been demonstrated by many researchers in both DC and RF modes [9, 64-68]. Schoenbach et

al demonstrated normal glow operation at high pressure using DC power hollow cathode discharges [8, 9, 69, 70]. Figure 1.12 shows one of the early design employed by Schoenbach [9] where the anode and cathode are separated by a mica spacer (250 μm). The cylindrical hole diameter, *D*, was varied between 200 μm to 750 μm. A normal glow discharge was observed for a pressure as high as 896 Torr for a *pD* product of ~18 Torr-cm. Since the pressure times the distance product limits the dimension of the hole size(*D*) in microns at atmospheric pressure, Schoenbach et al [63] modified their design and used arrays of two dimensional microhollow cathode discharges. Figure 1.13 shows a photo-graph of the two dimensional array of microhollow discharges operating in the normal glow mode [63]. This type of array can be used as a lamp, specifically in VUV (vacuum ultra-violet) region because of strong emission from excimer bands of rare gases ([71] and references therein). In addition, the strong VUV emissions generate secondary elec-trons [72] and may help sustain the plasma in the normal glow mode with high electron density even when the negative glow regions do not overlap. In fact, Schoenbach et al [63] observed normal glow mode operation of for a discharge gap (here, diameter (*D*)) greater than the overlap of the negative glow region; which suggests that the VUV pho-tons play a role and couple the sheaths (of opposite sides of the hollow electrode). Stark and Schoenbach [73] used a third electrode along with their hollow cathode discharge to generate larger volume nonequilibrium plasmas, though the plasma volume was limited to a few cubic millimeters. Similar approaches have been employed by Eden et al [74] to generate displays with two dimensional array of microplasmas. Instead of using only a cylindrical hole, they introduced other shapes, such as inverted pyramids and rectangular holes with different depths.

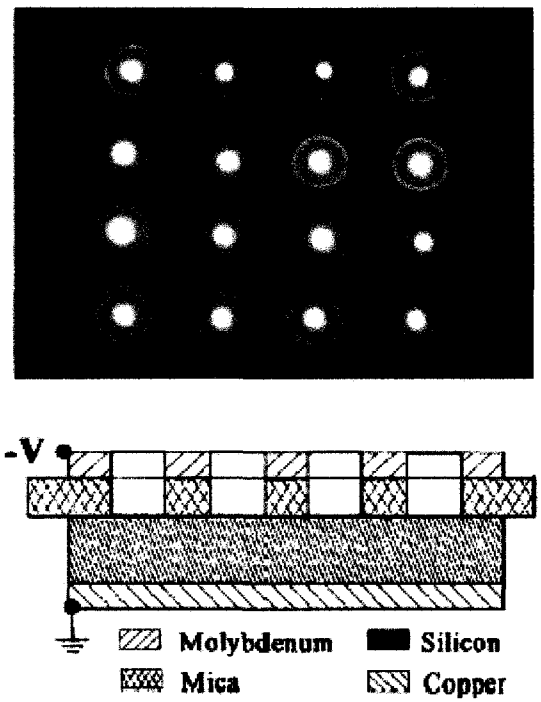


**Figure 1.13: Two dimensional array of DC sustained microhollow plasma discharges [63].**

Yu et al [71, 75, 76] designed a one dimensional slot microplasma device of 1-30 cm length to generate normal glow plasmas. This device also have been used as the source of energetic species and helps rare gas breakdown and generation of large volume ($\sim 6\ cm^3$) plasma at high pressure (1 atm). The following chapters will focus on the plasma characterization generated from this microhollow discharge.

1.7.5 Inductively Coupled Plasma (ICP)

Nonequilibrium plasmas are also generated using inductively coupled RF or microwave power. An inductively coupled plasma is also referred to as an electrodeless plasma, since the plasma is not in contact with the electrodes. Figure 1.14 shows the schematic of an inductively coupled plasma source. The oscillating electric field in the coil creates a time varying magnetic field hence an induced electric field, thus the plasma is sustained once the gas breakdown is achieved. Figure 1.15 shows a schematic of an in-

ductively coupled LTE plasma generator [77]. Usually, inductively coupled plasma generators for processing applications require lower pressure (<1 Torr, typically 1-100 milli-Torr) [78, 79] as compared to capacitively coupled plasma generators, but they can provide higher electron and ion densities, and better directionality [80]. ICPs have a small sheath voltage drop and thus are more convenient to use in processing applications since less damage is caused to the wafer from ion bombardment [80]. In addition, ICPs have excellent spatial uniformity, independent control over ion flux and ion energy [78-80].

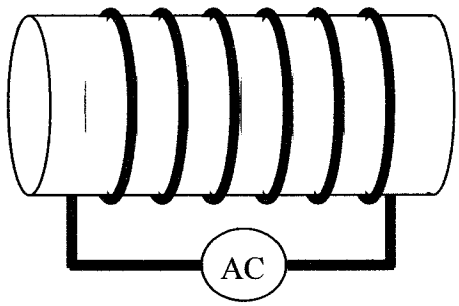


**1.14: Simple inductive circuit for ICP generation. Alternating current induces an electric field inside the quartz tube. The induced electric field generates the plasma.**

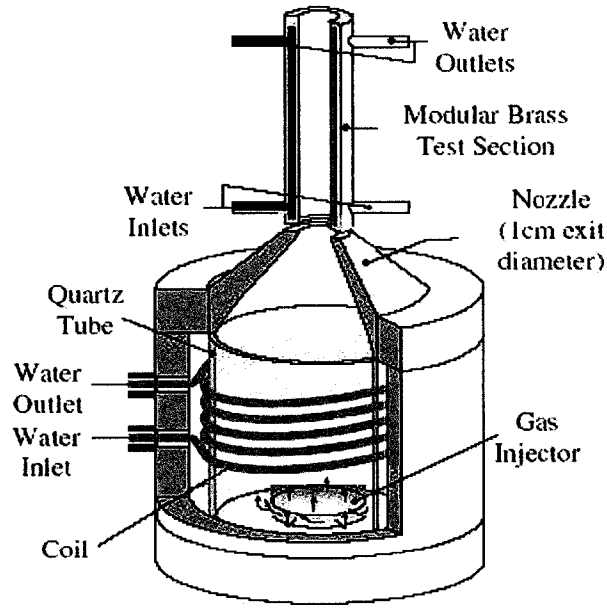


**1.15: LTE plasma generator [77].**

An inductively coupled nonequilibrium atmospheric pressure Ar and He plasma was first generated by Beenakkar [81]. The ICP was in a cavity resonator, allowing only

the $TM_{010}$ mode. The intended application of this type of plasma is trace elemental analysis (gas chromatography) using atomic emission detection [82-84]. Since their first discovery, ICPs have been generated from other species (such as $O_2$, $N_2$, air etc.) at various pressures [82-84]. The volume of the ICP plasmas generated in the cavity resonator is limited by the $TM_{010}$ mode.

Recently, microplasma sources using microstrip technology have been reported [85, 86]. The microstrip split-ring resonator device operates at a very low power (3 W) and over wide variable pressure range (less than 1 Torr to 1 atm.). Possible applications include optical emission spectrometry, bio-MEMS sterilization, miniature material processing, and lab-on-chip detectors etc.

**Reference:**


1. Schutze, A., et al., *The atmospheric-pressure plasma jet: A review and comparison to other plasma sources.*, IEEE Trans. Plasma Sci., 1998. **26**(6): p. 1685-1694.
2. Akishev, Y.S., A.A. Deryugin, I.V. Kochetov, A.P. Napartovich, and N.I. Trushkin, *DC glow discharge in air flow at atmospheric pressure in connection with waste gases treatment.*, J. Phys. D: Appl. Phys., 1993. **26**: p. 1630-1637.
3. Babayan, S.E., et al., *Deposition of silicon dioxide films with an atmospheric-pressure plasma jet.*, Plasma Sources Sci. Technol., 1998. **7**: p. 286-288.
4. Young, J.Y., et al., *Etching materials with an atmospheric-pressure plasma jet.*, Plasma Sources Sci. Technol., 1998. **7**(3): p. 282-285.
5. Kelly-Wintenberg, K., et al., *Room temperature sterilization of surfaces and fabrics with a one atmosphere uniform glow discharge plasma.*, J. Indust. Microbiol Biotechnol., 1998. **20**(1): p. 69-74.
6. Herrmann, H.W., I. Henins, J. Park, and G.S. Selwyn, *Decontamination of chemical and biological warfare (CBW) agents using an atmospheric pressure plasma jet (APPJ).*, Physics of Plasmas, 1999. **6**(5): p. 2284-2289.
7. Laroussi, M., *Sterilization of contaminated matter with an atmospheric pressure plasma.*, IEEE Trans. Plasma Sci., 1996. **24**(3): p. 1188-1991.

8. Schoenbach, K.H., R. Verhappen, T. Tessnow, F.E. Peterkin, and W.W. Byszewski, *Microhollow Cathode Discharges.*, Applied Physics Letters, 1996. **68**(1): p. 13-15.

9. Schoenbach, K.H., A. El-Habachi, W. Shi, and M. Ciocca, *High-pressure hollow cathode discharge.*, Plasma Sources Science and Technology, 1997. **6**: p. 468-477.

10. Selwyn, G.S., H.W. Herrmann, J. Park, and I. Henins, *Materials processing using an atmospheric pressure, RF-generated plasma source.*, Contributions to Plasma Physics, 2001. **41**(6): p. 610-619.

11. Kruger, C.H., C.O. Laux, L. Yu, D.M. Packan, and L. Pierrot, *Nonequilibrium Discharges in Air and Nitrogen Plasmas at Atmospheric Pressure,.*, Pure and Applied Chemistry, 2002. **74**(3): p. 337-347.

12. Laroussi, M., I. Alexeff, J. Richardson, and F. Dyer, *The resistive barrier discharge.*, IEEE Transactions on Plasma Science, 2002. **30**(1): p. 158-159.

13. Kunhardt, E.E., *Generation of Large-Volume, Atmospheric-Pressure, Nonequilibrium Plasmas.*, IEEE Trans Plasma Sci., 2000. **28**(1): p. 189-200.

14. Frank-Kamenetskii, D.A., *Plasma the fourth state of matter*. 1972, New York: Plenum Press.

15. Chen, F.F., *Introduction to plasma physics*. 1974, New York: Plenum Press.

16. Tonks, L. and I. Langmuir, *Oscillations in ionized gas.*, Phys. Rev., 1929. **33**: p. 195-210.

17. Brown, S.C., *A short history of gaseous electronics*, in *Gaseous electronics*, M.N. Hirsh and H.J. Oskam, Editors. 1978, Academy press: New York.

18. Rosenbluth, M.N., R.Z. Sagdeev, A.A. Galeev, and R.N. Sudan, in *Basic Plasma Physics (1st ed.)*. 1983, North-Holland Publishing Company: New York.

19. Boyd, T.J.M. and J.J. Sanderson, *The physics of plasmas*. 2003, Cambridge: Cambridge University Press (1st ed.).

20. Chen, F.F., in *Introduction to plasma physics (Chapter 1)*. 1974, Plenum Press: New York.

21. Raizer, Y.P., *Gas Discharge Physics (Chapter 8)*. 1991, New York: Springer.

22. Chen, F.F., in *Introduction to plasma physics*. 1974, Plenum Press: New York:. p. 244-246.

23. Heberlein, J., *New approaches in thermal plasma technology.*, Pure and Appl. Chem., 2002. **74**: p. 327-335.

24. Kirkici, H. and D. Bruno, *Operating characteristics of a segmented hollow cathode over a wide pressure range.*, IEEE Trans. Plasma Sci., 1995. **23**(3): p. 229-234.

25. Arslanbekov, R.R., A.A. Kudryavtsev, and R.C. Tobin, *On the hollow-cathode effect: conventional and modified geometry.*, Plasma Sources Sci. Tech., 1998. **7**: p. 310-322.

26. Roth, J.R., *Industrial plasma engineering (1st ed)*. Vol. 1. 2000:: Institute of physics publications. p.255.

27. Gambling, W.A., *Cathodic glow to arc transition.*, Can. J. Phys., 1956. **34**: p. 1466-1470.

28. Kuo, S.P., S.C. Kuo, and E.E. Kunhardt, *The effect of axial temperature profile on the thermal instability in high current-carrying plasmas.*, J. App. Phys., 1988. **63**(5): p. 1889-1893.

29. Raizer, Y.P., *Gas Discharge Physics*. 1st ed. 1991, New York: Springer.

30. Westberg, R.G., *Nature and role of ionizing potential space waves in glow-to-arc transitions.*, Phys. Rev., 1959. **114**: p. 1-17.

31. Levatter, J.I. and S. Lin, *Necessary condition for the homogenous formation of pulsed avalanche discharges at high gas pressures.*, J. Appl. Physics, 1980. **51**(1): p. 210-222.

32. Boyle, W.S. and F.E. Haworth, *Glow-to-arc transitions.*, Phys. Rev., 1956. **101**(3): p. 935-945.

33. Fan, H.Y., *The transition from glow discharge to arc.*, Phys. Rev., 1939. **55**: p. 769-775.

34. Nighan, W.L., W.J. Wiegand, and R.A. Hass, *Ionization instability in $CO_2$ laser discharges.*, Appl. Phys. Lett., 1973. **22**(11): p. 579-582.

35. Raizer, Y.P., *Gas Discharge Physics (Chapter 9)*. 1st ed. 1991, New York: Springer.

36. Nighan, W.L. and W.J. Wiegand, *Influence of negative-ion processes on steady-state properties and striations in molecular gas discharges.*, Phys. Rev. A, 1974. **10**(3): p. 922-945.

37. Dougas-Hamilton, D.H. and S.A. Mani, *Attachment instability in an externally ionized discharge.*, J. Appl. Phys., 1974. **45**(10): p. 4506-4415.

38. Dougas-Hamilton, D.H. and S.A. Mani, *An electron attachment plasma instability.*, Appl. Phys. Lett., 1973. **23**(9): p. 508-510.

39. Hirsh, M.N. and H.J. Oskam, *Gaseous electronics (Chapter 2)*. 1978, New York: Academic Press.

40. Wellenstein, H.F. and W.W. Robertson, *Positive column of a helium discharge in transition from the homogeneous to the striated state.*, J. Appl. Phys., 1972. **43**: p. 4823-4824.

41. Kiselevskii, L.I. and I.I. Suzdalov, Sov. Phys. -Tech.Phys., 1974. **18**: p. 1318.

42. Akishev, Y.S., et al., *Numerical simulation and experimental study of an atmospheric-pressure direct-current glow discharge.*, Plasma Physics Reports, 1994. **20**(6): p. 511-524.

43. Fridman, A., A. Chirokov, and A. Gutsol, *Non-thermal atmospheric pressure discharges.*, J. Phys. D: Appl. Phys., 2005. **38**.

44. Roth, J.R., *Industrial plasma engineering*. 1st ed. Vol. 1. 2000: Institute of physics publications.

45. Smith, H.B., C. Charles, and R.W. Boswell, *Breakdown behavior in radio-frequency argon discharges.*, Physics of Plasmas, 2003. **10**(3): p. 875-881.

46. Massines, F., et al., *Experimental and theoretical study of a glow discharge at atmospheric pressure controlled by dielectric barrier.*, J. of Applied Physics, 1998. **83**(6): p. 2950-2957.

47. Palmer, A.J., *A physical model on the initiation of atmospheric-pressure glow discharges.*, Appl. Phys. Lett., 1974. **25**(3): p. 138-140.

48. Akishev, Y.S., et al., *Calculation of air glow discharge spatial structure.*, Plasma Physics Reports, 1994. **20**(5): p. 437-441.

49. Duten, X., D. Packan, L. Yu, C.O. Laux, and C.H. Kruger, *DC and Pulsed Glow Discharges in Atmospheric Pressure Air and Nitrogen.*, IEEE Trans Plasma Sci., 2002. **30**(1): p. 178-179.

50. Yu, L., C.O. Laux, D. Packan, and C.H. Kruger, *Direct-current glow discharges in atmospheric pressure air plasmas.*, J. Appl. Phys., 2002. **91**(5): p. 2678-2686.

51. Eliasson, B. and U. Kogelschatz, *Modeling and applications of silent discharge plasmas.*, IEEE Trans. Plasma Sci., 1991. **19**: p. 309-323.

52. Kekez, M.M., M.R. Barrault, and J.D. Craggs, *Spark channel formation.*, J. Phys. D: Appl. Phys., 1970. **3**: p. 1886-1896.

53. Yokoyma, T., M. Kogoma, T. Moriwaki, and S.J. Okazaki, *The mechanism of the stabilisation of glow plasma at atmospheric pressure.*, J. Phys. D: Appl. Phys., 1990. **23**: p. 1125-1128.

54. Yokoyma, T., M. Kogoma, S. Kanazawa, T. Moriwaki, and S.J. Okazaki, *The improvement of the atmospheric-pressure glow plasma method and the deposition of organic films.*, J. Phys. D: Appl. Phys., 1990. **23**: p. 374-377.

55. Kanazawa, S., M. Kogoma, T. Moriwaki, and S.J. Okazaki, *Stable glow plasma at atmospheric pressure.*, J. Phys. D: Appl. Phys., 1988. **21**: p. 836.

56. Kanazawa, S., M. Kogoma, T. Moriwaki, and S.J. Okazaki, *Stable glow plasma at atmospheric pressure.*, J. Phys. D: Appl. Phys., 1988. **21**: p. 838-840.

57. Kogoma, M. and S.J. Okazaki, *Raising of ozone formation efficiency in a homogenous glow discharge plasma at atmospheric pressure.*, J. Phys. D: Appl. Phys., 1994. **27**: p. 1985-1987.

58. Yang, Y., *Alternating-current glow and pseudowglow discharges in atmospheric pressure.*, IEEE Trans. on Plasma Science, 2003. **31**(1): p. 174-176.

59. Koinuma, H., et al., *Development and application of a microbeam plasma generator.*, Appl. Phys. Lett., 1992. **60**(7): p. 816-817.

60. Koide, M., et al., *A novel low temperature plasma generator with alumina coated electrode for open air material processing.*, Thin solid films, 1998. **316**: p. 65-67.

61. Jeong, J.Y., et al., *Etching materials with an atmospheric-pressure plasma jet.*, Plasma Sources Sci. Technol., 1998. **7**(3): p. 282-285.

62. Littlefield, E. and G.J. Collins, *(Personal communication).*

63. Engel, A.V. and P.F. Little, *The hollow-cathode effect and the theory of glow discharge.*, Proc. Roy. Soc. A, 1954. **224**(1157): p. 209-227.

64. Schoenbach, K.H., A. El-Habachi, M. Moselhy, W. Shi, and R.H. Stark, *Micro-hollow cathode discharge excimer lamps.*, Physics of Plasmas, 2000. **7**(5): p. 2186-2191.

65. Frame, J.W., D.J. Wheeler, T.A. DeTemple, and J.G. Eden, *Microdischarge devices fabricated in silicon.*, Appl. Phys. Lett., 1997. **71**(9): p. 1165-1167.

66. Barankova, H. and L. Bardos, *Hollow Cathode plasma Sources for Large Area Surface Treatment.*, Surfaces and Coating Technology, 2001. **146-147**: p. 486-490.

67. Barankova, H. and L. Bardos, *Fused hollow cathode cold atmospheric plasma.*, Catalysis Today, 2002. **72**: p. 237-241.

68. Guo, Y.B. and F.C. Hong, *Radio-frequency microdischarge arrays for large-area cold atmospheric plasma generation.*, Appl. Phys. Lett., 2003. **82**(3): p. 337-39.

69. Moon, S. and W. Choe, *A uniform glow discharge plasma source at atmospheric pressure.*, Appl. Phys. Lett., 2004. **84**(2): p. 188-190.

70. Moselhy, M., R.H. Stark, K.H. Schoenbach, and U. Kogelschatz, *Resonant energy transfer from argon dimers to atomic oxygen in microhollow cathode discharges.*, Appl. Phys. Lett., 2001. **78**(7): p. 880-882.

71. El-Habachi, A. and K.H. Schoenbach, *Emission of excimer radiation from direct current, high-pressure hollow cathode discharges.*, Appl. Phys. Lett., 1998. **72**(1).

72. Rahman, A., et al., *Absolute UV and VUV Emission in the 110-400 nm Region from 13.56 MHz Driven Hollow Slot Microplasmas Operating in Open Air.*, Plasma Sources Sci. Tech., 2004. **13**(3): p. 537-547.

73. Phelps, V.A. and Z.L. Petrovic, *Cold-cathode discharges and breakdown in argon: surface and gas phase production of secondary electrons.*, Plasma Sources Sci. Technol., 1999. **8**: p. R21-R44.

74. Stark, R.H. and K.H. Schoenbach, *Direct current glow discharges in atmospheric pressure air.*, Appl. Phys. Lett., 1999. **74**(25): p. 3770-3772.

75. Chen, J., S. Park, Z. Fan, J.G. Eden, and C. Liu, *Development and characterization of micromachined hollow cathode plasma display devices.*, J. of Microelectromechanical Systems, 2002. **11**(5): p. 536-543.

76. Yu, Z., K. Hoshimiya, and G.J. Collins. *Rf Hollow Cathode Discharge with micro-Slot at High Gas Pressures*. in *GEC*. 2002. Minneapolis, MN.

77. Yalin, A.P., et al., *Electrical and optical emission characteristics of radio-frequency-driven hollow slot microplasmas operating in open air.*, Applied Physics Letters, 2003. **83**(14): p. 2766-2768.

78. Laux, C.O., T.G. Spence, C.H. Kruger, and R.N. Zare, *Optical Diagnostics of Atmospheric Pressure Air Plasmas.*, Plasma Sources Science and Technology, 2003. **12**: p. 125-138.

79. Hopwood, J., *Review of inductively coupled plasma for plasma processing.*, Plasma Sources Sci. Tech., 1992. **1**: p. 109-116.

80. Lee, D.S., Y.K. Lee, and C.H. Chang, *Characteristics of an inductively coupled plasma source using a parallel resonance antenna.*, Plasma Sources Sci. Technol., 2004. **13**: p. 701-706.

81. DiPeso, G., V. Vahedi, D.W. Hewett, and T.D. Rognlien, *Two-dimensional self-consistent fluid simulation of radio frequency sources.*, J. Vac. Sci. Technol. A, 1994. **12**(4): p. 1387-1396.

82. Beenakker, C.I.M., *A cavity for microwave-induced plasmas operated in helium and argon at atmospheric pressure.*, Spectrochimica Acta, 1976. **31B**: p. 483-486.

83. Deutsch, R.D. and G.M. Hieftje, *Development of a microwave-induced nitrogen discharge at atmospheric pressure (MINDAP).*, Applied Spectroscopy, 1985. **39**(2): p. 214-222.

84. Michlewicz, K.G., J. Urh, and J.W. Carnahan, *A microwave induced system for the maintenance of moderate power plasma of helium, argon, nitrogen and air.*, Spectrochimica Acta, 1985. **40B**(3): p. 493-499.

85. Quimby, B.D. and J.J. Sullivan, *Evaluation of a microwave cavity, discharge tube, and gas flow system for combined gas chromatography-atomic emission detection.*, Anal. Chem., 1990. **62**: p. 1027-1034.

86. Bilgic, A.M., U. Engel, E. Voges, M. Kuckelheim, and J.A.C. Broekaert, *A new low-power microwave plasma source using microstrip technology for atomic emission spectrometry.*, Plasma Sources Sci. Tech., 2000. **9**: p. 1-4.

87. Iza, F. and J.A. Hopwood, *Low-power microwave plasma source based on a microstrip split-ring resonator.*, IEEE Trans. Plasma Sci., 2003. **31**(4): p. 782-787.

# Chapter 2

# RF Measurements

## 2.1 Introduction

Atmospheric pressure glow discharge (APGD) plasmas are a rapidly emerging technology. APGD sources do not require complex and expensive vacuum systems, unlike their low pressure counterparts. Therefore low cost and simple operation may enable wider industrial application of APGD sources. However generation of APGD plasmas possess challenges, associated with temporal stability and spatial uniformity, e.g. onset of glow to arc transition, uncontrolled filamentary channels, striations etc. To overcome these shortcomings one needs to both theoretically model and experimentally characterize (electrically and optically) features of the APGD plasma. Plasma characterization becomes very difficult for high pressure operation, primarily because probe measurements are not valid as the case of Langmuir probes in determining electron/ion temperatures and densities for low pressure, low density, cold plasmas [1]. Note that Debye screening restricts Langmuir probes application only to low density plasmas [1].

Figure 2.1 shows a photograph and Figure 2.2 shows a schematic of the microhollow plasma discharge device. The microdischarge operates with a flow of rare gas directly into atmospheric pressure ambient air and is driven by RF (4 to 60 MHz) sources.

The configuration has similarities with low pressure hollow anode/cathode discharges, but does not provide very high electron density as is the case in low pressure hollow

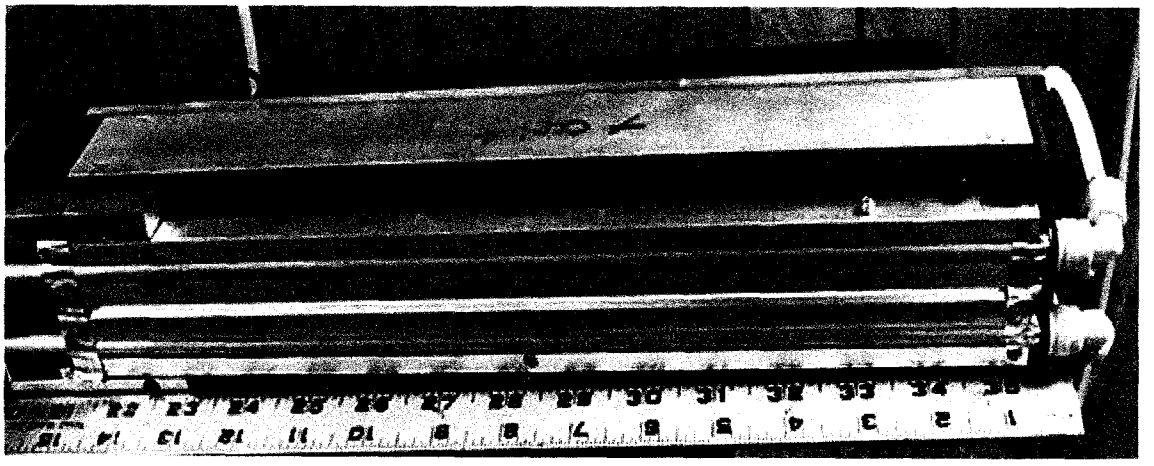

**Figure 2.1: Photograph of microhollow discharge operation under atmospheric pressure with argon gas flowing through the slot. Operating plasma has linear dimension of ~35 cm.**

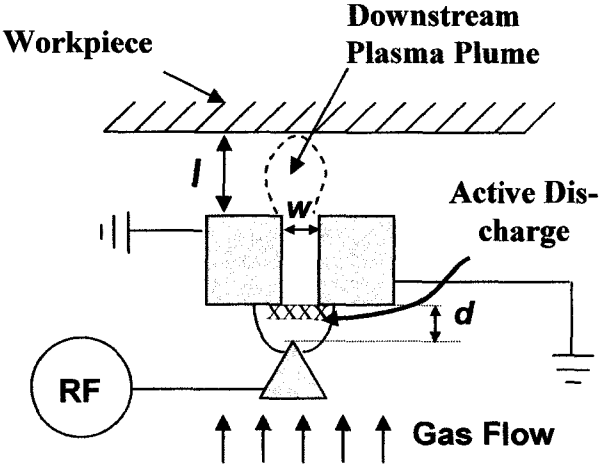


**Figure 2.2: Schematic of the microhollow plasma device (end on view). The wedge shaped electrode is powered with RF, and rare gas flows into the slot from beneath the powered electrode. Typical dimensions are $d$ = 400 μm, $w$ =200 μm, $S$ = 5 cm and $l$ = 1~3mm.**

cathode/anode geometry [2][3]. At low pressure, the hollow cathode geometry allows fast electrons to oscillate (Pendel effect [3]) between the opposite walls of the hollow cathode so that energetic electrons are reused and can sustain the plasma [4]. These energetic electrons generate numerous secondary electrons in the bulk of the plasma, thus

[3] Hollow cathode discharge is described in Chapter 1.

providing a very high electron density. The reuse of energetic electrons allows hollow cathode plasmas to be sustained at relatively low voltages.

On the other hand, at high pressure, electrons lose energy due to high collision rates and do not have sufficient energy to penetrate the sheath. Hence reuse of energetic electrons is hindered. The microhollow plasma discharge device described here operates at atmospheric pressure and does not allow the Pendel effect. However, the discharge geometry does provide high current density in comparison to other APGD microplasma devices [5]. Its 1 to 30 cm length is also advantageous over other similar microplasma devices and allows use in wide area processing application in push-broom approach.

Figure 2.1 shows the open air operation of the microhollow discharge device. In this case, plasma created in the hollow slot geometry is extended linearly up to ~35 cm. The width, $w$, is restricted to facilitate the breakdown and to minimize the mixing effect of the ambient air. The device operates in the normal glow mode at relatively high current density and generates energetic species that can be used in a variety applications [6, 7]. Generation of microplasma using this device requires RF excitation field and inert gas(es) as the plasma medium. Operation in the open air allows ambient air species to mix into the plasma.

In this chapter we discuss the results of RF electrical measurements of plasma input impedance which were performed in order to determine APGD microplasma properties such as: current-voltage characteristics, sheath and bulk voltage, sheath non-linearity, electron density etc. Electrical parameters ($R$, $X$, $V$, $I$, $\Phi$, $P$ etc.) of the hollow slot micro discharge device are measured in order to explain voltage-current characteristics, sheath dynamics, bulk properties, electron density, sheath non-linearity etc. In general time

averaged measurements alone do not capture sheath dynamics and can not take account of sheath non-linearity [8]. However, it will be shown that at high pressure, the sheath non-linearity is small and the time varying electric field can be considered as an effective DC field. Thus the APGD microplasmas considered here can be treated with the time averaged measurements.

## 2.2 Microdischarge Geometry, Experimental Setup and Operating Conditions

### 2.2.1 Microdischarge Geometry

Figure 2.2 shows the microhollow discharge geometry. The device consists of a wedge shaped electrode and a of pair electrodes with a slotted opening. The wedge shaped electrode is powered with RF and insulated (from the outside) which makes handling of the device easy and safe. The wedge is made of copper and the top of the wedge is separated from the bottom surface of the slotted electrodes. The slotted aluminum electrodes are grounded. The distance, $d$, between the grounded electrodes and the powered electrode is varied (400, 500 and 600 μm). The device used for electrical measurements is similar to that shown in Figure 2.1 but shorter. Slot width, $w$, is ~200 μm and length ($L$) is ~ 7.5 cm (direction perpendicular to the plane of the paper). Both the powered electrode and the slotted electrodes are water cooled to reduce thermal emission (i.e. secondary emission) from the cathode surface that may cause glow to arc instability, and to prevent material (melting) failure. There is a recess beneath the powered electrode through which rare gas (typically industrial grade helium (He) or argon (Ar)) flows into the gap between the electrodes prior to exiting through the opening of the grounded slots. Once gas breakdown is achieved, RF power sustains the plasma inside the slot. An extended plasma beyond the slots, referred to as the plume plasma, is sustained by energetic

species (metastables, superelastic electrons, vibrationally excited molecules etc.) that exit the active discharge region. We note that all plasma operation is under open air conditions and ambient gas may enter the slot due to diffusion and entrainment. (These effects are expected to minimal due to positive pressure of rare gas inside the slot). As will be seen, optical data shows that there are contributions from the ambient to the slot plasma [6, 7].

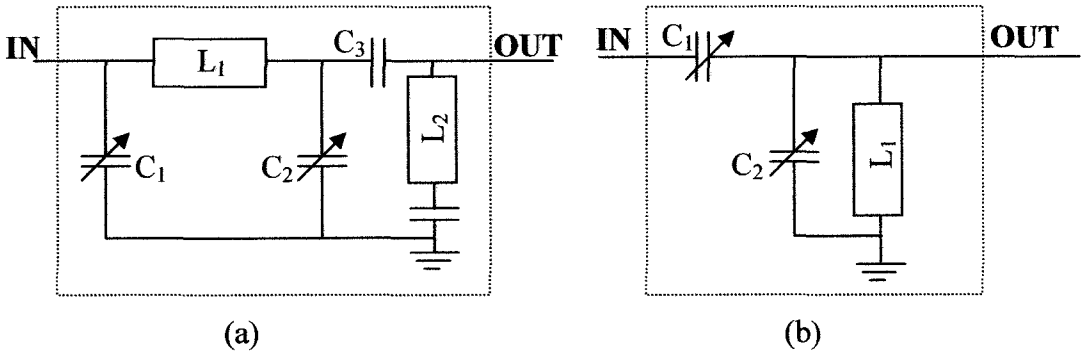


**Figure 2.3: Schematics of the matching network used to deliver maximum power to the microhollow discharge, (a) matching network used for plasma generation at 13.56 MHz and 27.12 MHz and (b) for 60 MHz.**

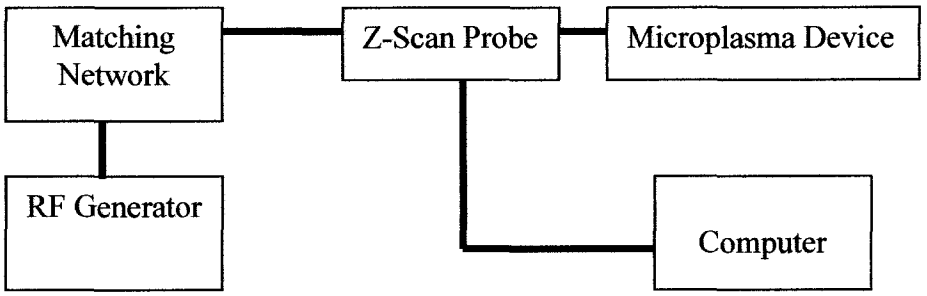


**Figure 2.4: Schematics of the experimental setup for microplasma generation from microhollow plasma device.**

2.2.2 Setup for Electrical Measurements

Figures 2.3 and 2.4 show the impedance matching networks and experimental setup for electrical measurements respectively. Advanced Energy (AE) RF generators are used to deliver RF power to the slotted microdischarge device via the matching network. An AE Z-scan probe is inserted between the matching network and the microplasma device. The AE Z-scan probe measures root-mean-square (RMS) values of current ($I$(t)),

voltage ($V$(t)) and phase ($\Phi$(t)) which are collected to computer via a Labview program. The real part of the RF generator exit impedance is 50 Ω. The purpose of the matching network is to match the source impedance to the load (plasma) impedance in order to deliver maximum power. Since the plasma condition may vary with the operating parameters (discharge gap, rare gas, impurity etc.), variable capacitors are introduced in the matching networks to match impedance and phase of the load (plasma) such that standing wave ratio (SWR) is minimum, i.e. the effect of the reflected wave is minimized [9]. Other plasma parameters, such as resistance ($R$) and reactance ($X$), capacitance ($C$), power ($P$) etc. are calculated from RMS values of $I$ (t), $V$ (t) and $\Phi$ (t).

2.2.3 Operating Conditions

A rare gas (helium or argon) is flowed (10~15 slpm) into the open space between the powered electrode and the slotted electrodes as shown in Figure 2.2. After initial gas breakdown, the plasma in this region is sustained by the RF power. A bright luminous plasma is observed inside and outside the slot due to outward gas flow. The spatial extent of the plume plasma (plasma outside the top-surface) depends on the gas flow rate and composition, delivered power. The electrode separation is varied from 400 to 600 μm in steps of 100 μm. As will be seen, after the breakdown of rare gas the voltage across the discharge remains nearly constant.

The discharge operates in open-air conditions with $pd$ of ~10 Torr-cm where $p$ stands for pressure and $d$ for discharge gap. At different frequencies and gas flow combinations typical values of electric field $\boldsymbol{E}$ =1~10 kV/cm and $\boldsymbol{E/N}$ values of 10~70 Td (1 Td = $10^{-21}$ V-m$^2$). Diffuse non-filamentary discharges are created at currents below ~1.5 A per cm of slot length, corresponding to a current density of, $j$~1.5 A/cm$^2$. For $j$>1.5

$A/cm^2$, glow-to-arc *I-V* discharge instabilities are observed, and above 3.0 $A/cm^2$ spatially confined filamentary discharges occur.

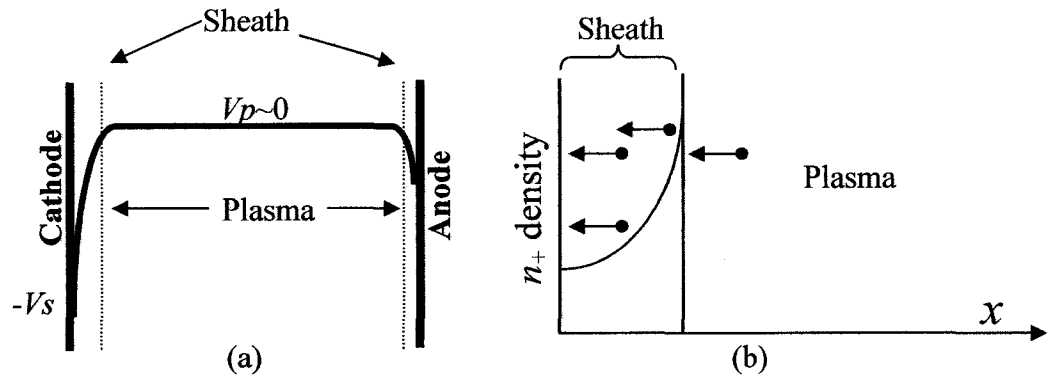


**Figure 2.5: (a) DC sheaths are formed next to the cathode and the anode (the regions between the dotted lines and the electrodes (cathode and anode)) [10]. b) Curve shows the ion density distribution in the sheath. The density of ions decreases toward the electrode but the velocities of ions increase.**

## 2.3 Theory

The experimental setup for the electrical characterization of the RF driven hollow electrode microdischarge plasma was described above. Electrical measurements are made primarily in the normal glow discharge mode.

In general, DC normal glow plasmas have well defined sheath and bulk regions [11, 12]. The bulk has quasi neutrality of charge. Sheaths form next to electrodes due to space charge (ions) accumulation. In DC discharges sheaths are well defined and stationary, whereas in RF discharges the sheaths are not stationary and tend to vary with the applied excitation frequency. The varying sheath makes interpretation of the discharge mechanism more difficult than in DC discharges. It will be shown that in high pressure plasmas the varying sheath dimension does not contribute significantly to sheath non-linearity (Section 2.4.1), and sheath non-linearity arising from inhomogeneous ion

velocity distribution is small[4]. Thus RF driven APGD microplasmas can be treated with DC approximations (i.e. time averaged measurements).

For better understanding of the sheath and bulk region characteristics of microhollow discharge plasmas, a brief discussion of DC plasmas [11, 12, 14] is presented below.

2.3.1 DC Sheath

We expand on the discussion of Section 1.2. In a DC plasma, generation of each electron in the bulk is accompanied by creation of an ion. These electrons have higher kinetic energy than the ions, and are lost at a faster rate as they hit the electrodes. Thus a net positive charge builds up in the plasma. However, this behavior is not observed experimentally and charge neutrality holds. Therefore, the plasma must have a positive potential with respect to the electrodes (and the electrodes acquire a net negative potential). The function of the negative potential at the electrodes is to attract ions and repel electrons. The accumulation of ions near the electrode forms a sheath through which electron conduction current is very small (only sufficiently energetic electrons can overcome the potential barrier and balance the ion losses). For any negative potential at the electrode, the thickness of the sheath is determined the by the characteristic Debye length [15, 16], $\lambda_d$, at which the negative potential is screened and prohibits further accumulation of positive ions. The sheath formation ensures the charge neutrality. Voltage drops across the cathode sheath and anode sheath are different in a DC discharge (Figure 2.5a).

[4] In the atmospheric pressure cold plasmas, ion collision frequencies with neutrals are very high (Table 2.1). It is known that the accelerating ions moving through the same gas species suffer charge exchange collisions [13], the process is fast and the new ion which was moving under the thermal velocity will have to start anew to follow the applied RF frequency. Since the collision frequency (Table 2.1) and cross sections are high, the new ion will again suffer collisions, possibly charge exchange collisions. Hence it is suggested that the ionic sheath oscillation will have very small effect in the sheath dynamic behavior compared to sheath oscillations due to electrons.

Since the potential falls off sharply from the sheath boundary towards the electrode, a potential gradient causes the ions to accelerate. Following particle conservation, acceleration of the positive ions results in a nonlinear distribution of ions in the sheath (Figures 2.5b shows the ion distribution in a DC sheath). At the boundary of the plasma and sheath, the electron density and ion density are approximately the same but the electron density tails off faster in the sheath compared to the ion. The nonlinear distribution of ions can generate harmonic contributions and its effect will be discussed in a later section.

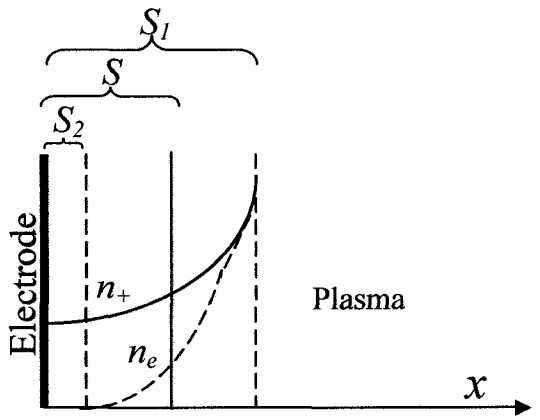


**Figure 2.6: Oscillating sheath [8]. $S$ represents the ionic sheath. $S_1$ and $S_2$ are the maximum and minimum sheath widths due to electrons motion in the RF field. Solid and dashed curves represent ion and electron densities in the sheath.**

2.3.2 AC Sheath

In general when an AC field sustains a plasma, the sheath widths and voltages are no longer constant in time but vary with the applied frequency. We assume an oscillating (RF) electrical field of the form,

$$E(t) = E_0 \cos \omega_{RF} t \qquad 2.1$$

where, $E_0$ and $\omega_{RF}$. are the amplitude and the frequency of the applied RF electric field respectively.

If the applied RF frequency is such that equation 2.2 below is a good approximation, then the discharge current is carried by the electrons, which follow the instantaneous electric field [17].

$$\omega_{pe}^2 >> \omega_{RF}^2 \left(1 + \frac{\nu_m^2}{\omega_{RF}^2}\right)^{1/2} \qquad 2.2$$

where, $\nu_m$ = electron collision frequency (with neutrals in APGD plasmas).

When $\omega_i << \omega_{RF} << \omega_{pe}$, then ions follow the time averaged electric field and the electrons follow the instantaneous electric field [18]. In this situation the sheath has charge contributions from both the ionic sheath and the electronic sheath. The behavior of the ionic sheath resembles the DC sheath. The electronic sheath arises from the electronic motion caused by the rapidly varying RF field. During the negative cycle of the applied RF field, electrons are repelled further from the cathode therefore leaving unbalanced ions (since ions can not follow the instantaneous field) and the sheath grows beyond the ionic sheath S and reaches the maximum sheath thickness $S_1$ when the applied RF voltage reaches its maximum negative value (Figure 2.6). Similarly the sheath shrinks during the positive half cycle. Therefore, the sheath width oscillates due to electron motion. In Figure 2.6, $S$ is the ionic sheath, and $S_1$ and $S_2$ are minimum and maximum sheath widths [8, 19]. In the oscillating sheath, the electric field is still predominantly formed by ions but the assumptions of negligible electron density is wrong for $S(t) < S_2$ (Figure 2.6) (collapsing sheath) [20]. The electron density in the ionic sheath does not tail off immediately because during the negative cycle electrons penetrate into the ionic sheath. Therefore the spatial profile of charge density in the sheath ($n_+$-$n_e$) is highly non-linear which causes harmonics. When $\omega_i \sim \omega_{RF} << \omega_{pe}$, ions also can follow the applied oscillating field and

the sheath oscillation is the sum of the electronic sheath oscillation and ionic sheath oscillation. Hence sheath dynamics become even more complicated. Oscillating sheath prohibits the use of time averaged measurements to describe the sheath properties. This is typically the case in low pressure RF discharges [8, 19].

2.3.3 Validity of DC Approximation

The above discussion emphasizes that at low pressure the sheath behavior for an applied oscillating electric field is different than for a DC applied electric field, due to the oscillating electronic sheath. In the atmospheric pressure microplasma the condition $\omega_i << \omega_{RF} << \omega_{pe}$ is not valid, since $\omega_i \sim \omega_{RF}$ (Table 2.1), so that questions of possible ion oscillation in the sheath arise. However, owing to a large number of collisions with neutrals (including charge exchange collisions, the ions can not reach high energies and are not expected to show significant oscillatory behavior[4]. Therefore, the electronic sheath may oscillate. Infact, we will show neither ionic sheath nor electronic sheath has significant contribution to the total sheath thickness, so that sheath oscillation can be neglected in the atmospheric pressure microplasmas. Therefore RMS (Root Mean Square) values of plasma parameters ($I$, $V$, $\Phi$) are sufficient to analyze the slot microdischarge plasmas, considering the non-linearity of the plasma device is small (significant presence of higher harmonic contents may increase contribution from the displacement current considerably [21]).

Following the mathematical expressions from ref. [25] and data provided in Tables 2.1-2.2 we show that electron/ion motion in atmospheric pressure microdischarge plasmas is indeed comparable to that for an effective DC field (i.e. the contribution from the electronic sheath to the total sheath thickness can be discarded, thus reduces the

sheath non-linearity). Measurements and associated discussions of the harmonic contents of microplasmas in the next section validates that the sheath non-linearity is small.

**Table 2.1: Plasma frequencies of electron, $Ar^+$ and $He^+$ at different electron densities.**

| Charge density | $\omega_e$ (GHz) | $\omega_{He+}$ (GHz) | $\omega_{Ar+}$ (GHz) |
|---|---|---|---|
| 1.00E+17 | 14.1 | 0.164 | 0.052 |
| 1.00E+18 | 44.6 | 0.520 | 0.164 |
| 1.00E+19 | 141.0 | 1.640 | 0.520 |
| 1.00E+20 | 446.0 | 5.200 | 1.640 |

**Table 2.2: Collision frequency of $He^+$/ $Ar^+$ ions in their respective neutral gas and electron collision frequency with neutral He and Ar gas at atmospheric pressure.**

| Collision frequency (GHz) | | Collision frequency of electron (GHz) | |
|---|---|---|---|
| $He^+$ in He | $Ar^+$ in Ar | in He | in Ar |
| ~8 [22] | ~6[23] | ~1520[24] | ~4030[24] |

Note: Collisional frequencies are extracted from references [22] and [23] at temperature T=700 K and E/P~10 V/cm-Torr.

We consider the RF electric field given by equation 2.1. The force on a charged particle can be approximated as [25]:

$$m\frac{dv(t)}{dt} = \pm eE(t) + mv(t)\nu_m \qquad 2.3$$

If after a number collisions the change in phase of the charge particle is $\phi$ then the velocity and the position of the charged particles are (for simplicity the subscript RF is dropped from $\omega_{RF}$)

$$v(t) = \pm\frac{eE_0\cos(\omega t+\phi)}{\left(m\omega^2\left(1+\nu_m^2/\omega^2\right)^{1/2}\right)} \qquad 2.4$$

$$r(t) = r_0 \pm\frac{eE_0\cos(\omega t+\phi)}{\left(m\omega^2\left(1+\nu_m^2/\omega^2\right)^{1/2}\right)} \qquad 2.5$$

where, $\phi = \arctan(\nu_m/\omega)$ and $r_0$ is the equilibrium position.

For the APGD microplasma, the collisional frequency is large compared to the applied frequency ($\nu_m >> \omega$) (Table 2.2), so that:

$$v(t) = \pm \frac{eE_0}{m\nu_m} \sin(\omega t + \phi) = \pm \frac{eE(t)}{m\nu_m} \cong \mu E(t) = v_d(t) \qquad 2.6$$

and the plasma constituents move with a drift velocity $v_d$(t), where $\mu = e/(m\nu_m)$ is defined as the mobility of the charged particles.

Table 2.2 shows that the APGD microplasma electron/ion collisional frequencies ($\nu_m$) are large compared to the applied RF frequencies (~$10^7$ to $10^8$ Hz). Under this conditions the motion of the charged particles can be considered due to an effective DC field. This confirms that the electronic sheath oscillation effect is small in APGD microplasma.

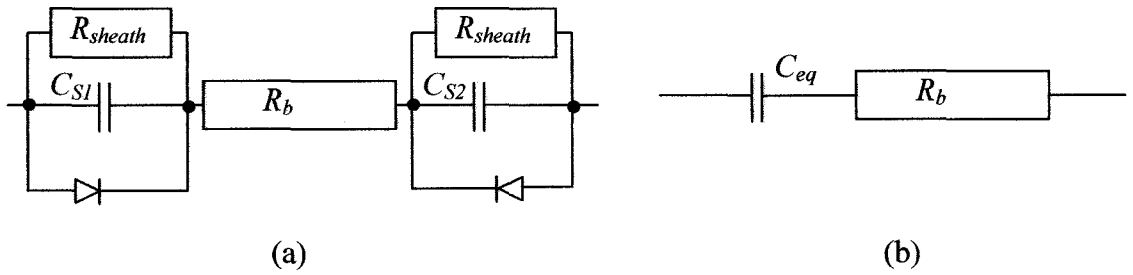


**Figure 2.7: (a) Circuit model of RF (AC) generated plasma and (b) equivalent circuit model of RF generated microplasma.**

2.3.4 Equivalent Circuit Modeling

Sheaths are formed at the electrodes due to space charge accumulation. The current through the sheath will be sum of ion current ($I_{ion}$), displacement current ($I_{disp}$) and electron current ($I_e$). Hence the sheath is modeled as a combination of a diode, a capacitor, and resistances; representing components through which the ion current, displacement current and the electron current are conducted respectively. Since the APGD microplasma satisfies equation 2.2, the bulk can be considered as a conducting media with

high electron velocity. Thus, current through the bulk will be due to electrons ($I_e$) only, and the bulk can be represented by a resistance $R_b$. Therefore the circuit representation of the sheath and plasma take the form shown in figure 2.7a.

As discussed before, the electron density tails off very rapidly in the sheath, so that its contribution to the total sheath current can be disregarded. Hence the electronic sheath resistance, $R_e$ is dropped from the equivalent circuit (Figure 2.7b). The ion conduction current in the sheath can be expressed as, $I_{ion} = n_+ q v_B$ , where $n_+$ is ion density, $q$ is the charge, and $v_B$ is the Bohm velocity. The ion current density in the sheath is much smaller than the displacement current density in a collisionless plasma [26], so one can drop the contribution of the ion current (i.e. remove $R_i$) in the RF collisional plasma[5]. Although each sheath capacitance has time dependence, the total capacitance is time independent [27]. Hence in the (final) equivalent circuit the sheath capacitances are combined to an equivalent capacitance. The equivalent circuit is shown in the Figure 2.7b.

## 2.4 Results and Discussions

This section focuses on interpretations of the experimental observations. We concentrate on harmonic measurements and their significance for validating time averaged sheath behavior, calculation of electrical parameters, *I-V* characteristics, capacitive nature of the microdischarge, asymmetry and its significance on sheath characteristics, and self consistent electron density calculation from sheath capacitance and bulk resistance.

### 2.4.1 Harmonics and Implications on Sheath Behavior

In a low pressure cold plasma, the applied RF current and voltage contain the fundamental frequency and a number of harmonics. Non-linear behavior, i.e. odd and

[5] Ions suffer more elastic collisions and charge exchange collisions, thus the reduced velocity of ions in the sheath conducts negligible ion current compared to the displacement current.

even harmonics, stems primarily from discharge asymmetry and from the non-linearity of the sheath ion distribution [20, 28, 29]. Non-linear response of the electronic sheath to the applied RF voltage (i.e. sheath is not expanding and contracting according to the applied oscillating voltage [30]) can also contribute to higher order harmonics. Other effects such as external circuitry may add non-linearity in the sheath due to self DC bias voltage [20, 31].

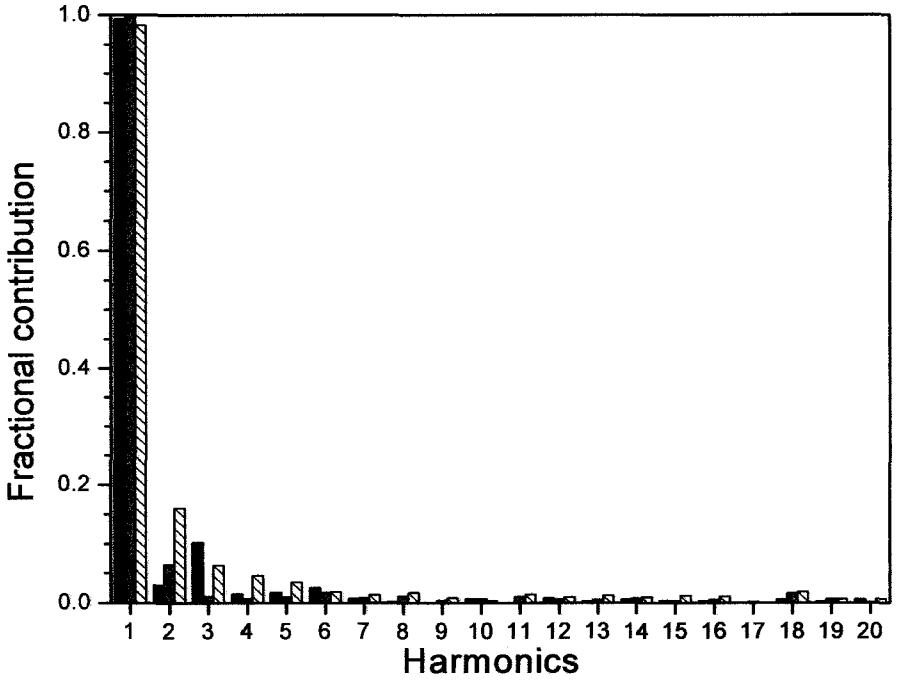


**Figure 2.8a: Voltage harmonic contents of helium microplasmas driven by 13.56 (black), 27.12 (gray) and 60 MHz (hatched) respectively.**

Large non-linearity in the APGD microplasma can result in inaccurate explanations of sheath behavior, because our calculations assume sheath is due to time averaged motion of ions and disregard the sheath oscillation. This section thus focuses on the experimental validation of the approximation that the atmospheric pressure sheath is mainly formed by the time averaged motion of ions and the oscillating electric field do not have any major impact in the sheath behavior as opposed to low pressure RF plasmas [8, 19].

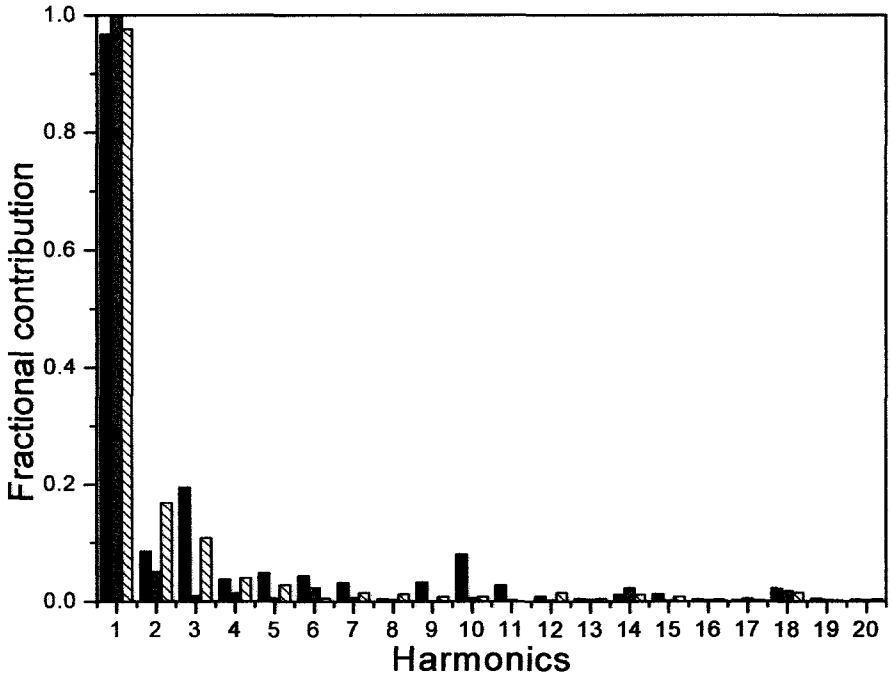


**Figure 2.8b: Current harmonic contents of helium microplasmas driven by 13.56 (black), 27.12 (gray) and 60 MHz (hatched) respectively.**

Figure 2.8a,b show the contributions of different voltage and current harmonic for helium microplasmas at $\nu_{RF}$ = 13.56, 27.12 and 60 MHz. The measured harmonics for all three RF frequencies for argon and helium discharges show that the major contribution is always from the fundamental harmonic and contributions from all higher order harmonics are relatively small (<10%). At higher frequency (60 MHz), contributions from higher harmonics in the voltage are more pronounced. This is due to the contributions from the oscillating sheath rather than the nonlinear distribution of ions in the sheath because:

i. at higher frequencies the sheath width is smaller [30, 32] so any fractional variation in the sheath has a large compared to this smaller time averaged sheath width.

ii. due to smaller sheath width, the time average potential difference across the sheath will have higher potential gradient and therefore higher nonlinear distribution of ions. In the current harmonic, higher order harmonics appear at 13.56 MHz microdischarge

operation. This behavior is not well understood at this time. Figure 2.9a,b show the current-voltage waveform for helium plasma at 27.12 MHz. The distortions (i.e. non-fundamental content) in the voltage and current are clearly small.

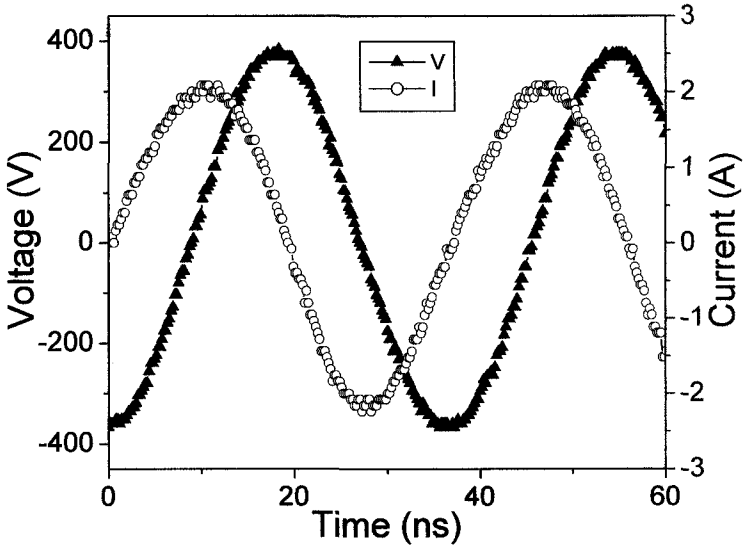


**Figure 2.9a: *I-V* waveform at 27.12 MHz with no load (no ignited plasma and feed gas is argon).**

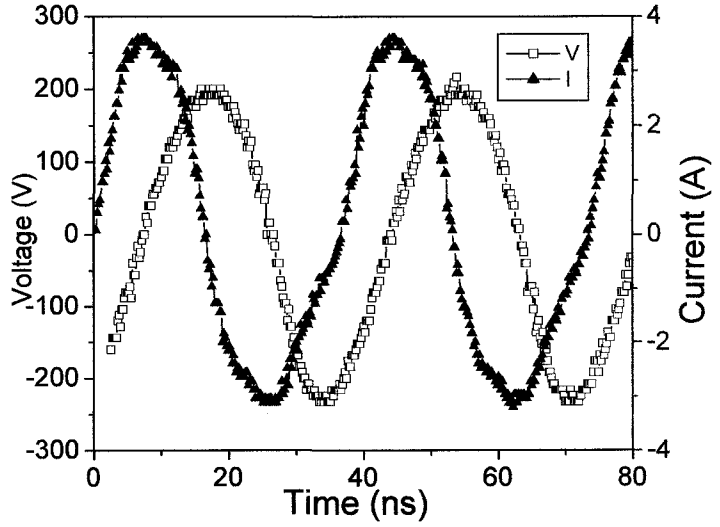


**Figure 2.9b: *I-V* waveform at 27.12 MHz with load (plasma *ON* and feed gas is argon).**

From the experimental observations (small contribution of higher harmonics) it can be concluded that the non-linearity in the sheath (due to time varying electric field

and non-uniform ion distributions in our highly collisional APGD micro plasma) does not prevent us from considering the time averaged sheath (instead of instantaneous sheath dynamics). This is likely due to the fact that in the collisional plasmas, the ion fluxes do not decrease significantly as they traverse toward the electrode (particle conservation): Rather than gaining energy due to the sheath voltage gradient, collisions make the ion energy distribution uniform in the sheath [8, 20]. Non-linearity at lower RF frequencies is observed to be small. To gain more complete knowledge, more data points at different power levels would be useful.

### 2.4.2 Calculation of Electrical Parameters from Measured Values

The experimental setup for data acquisition has been described in section 2.2. Figure 2.4 shows the experimental setup for acquiring time averaged (RMS) electrical parameters using the AE Z-scan probe. The measured time averaged RMS values of current ($I_e$=$I_{RF}$), voltage ($V_{RF}$=$V_g$) and the current-voltage phase ($\Phi$) have been employed to calculate the discharge impedance $Z$, bulk resistance ($R_b$), sheath reactance $X$, capacitance ($C_{eq}$=$C$), sheath voltage $V_s$ and bulk voltage $V_b$ using the equivalent circuit model (Figure 2.7b) and the following set of equations.

$$Z=V_g/I_{RF} \tag{2.7}$$

$$X_{sheath}= Z\ sin(\Phi) \tag{2.8}$$

$$R_b= (Z^2 - X_{sheath}^2)^{1/2} \tag{2.9}$$

$$C=|1/(\omega_{RF}X)| \tag{2.10}$$

$$V_s= I_{RF}*X_{sheath} \tag{2.11}$$

$$V_b= (V_g^2-V_s^2)^{(1/2)} \tag{2.12}$$

Due to the capacitive nature of the discharge there is a phase difference between the current and voltage (and thus real and reactive impedances). Calculations are performed under vector rules. Table 2.3 provides data for glow voltages for 13.56 MHz and 27.12 MHz operation with different interelectrode gaps.

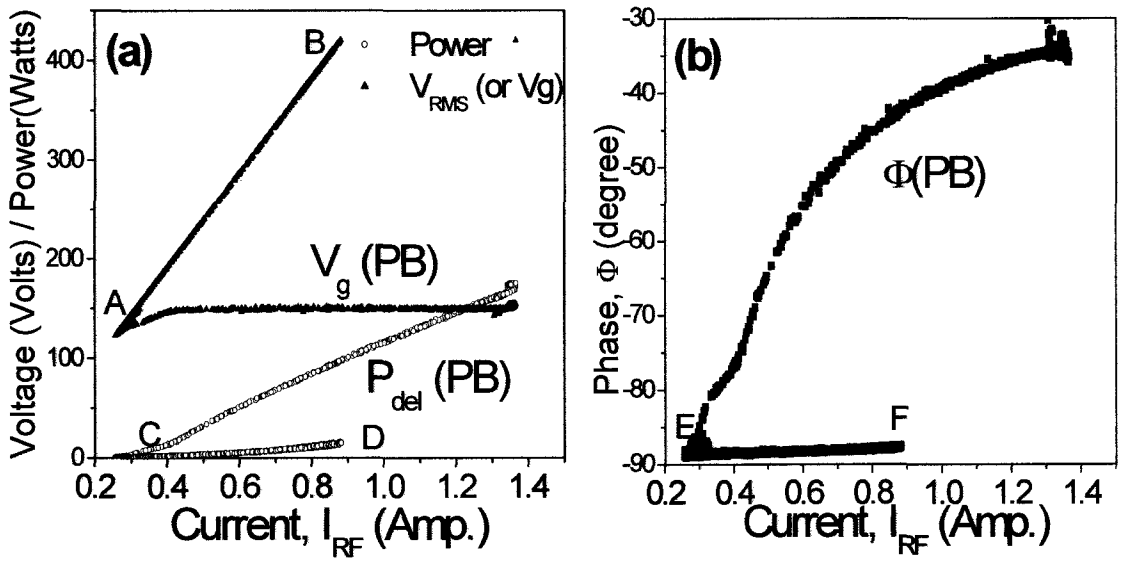


**Figure 2.10 (a) & (b): Power, voltage and phase variations with respect current for 13.56 MHz argon plasmas (electrode separation = 400 μm and argon gas flow rate was =15 slpm).**

**Table 2.3: Hollow slot Ar and He microplasma glow voltages at different frequency and discharge gap [33].**

| Gas | RF frequency (MHz) | Interelectrode spacing (μm) and breakdown voltage (Volts) | | |
|---|---|---|---|---|
| | | 400 (μm) | 500 (μm) | 600 (μm) |
| Argon | 13.56 | 149 V | 154 V | 159 V |
| | 27.12 | 138 V | 140 V | 141 V |
| Helium | 13.56 | 128 V | 135 V | 141 V |
| | 27.12 | 115 V | 116 V | 121 V |

2.4.3 Current, Voltage and Delivered Power Characteristics

A representative *I-V* characteristic for the Ar microplasma driven by a 13.56 MHz RF source for an electrode separation of 400 μm is provided in Figure 2.10a. The figure also shows the delivered power. Figure 2.10b shows the phase variation (w.r.t. current,

$I_{RMS}$) for same condition. In the Figure 2.10a,b A to B regions correspond to the pre-breakdown regions where as the post breakdown regions are denoted by PB in parenthesis. Similar behavior is observed for argon plasma at 27.12 MHz, as well as 13.56 and 27.12 MHz helium plasmas for different electrode separations. Figure 2.10 contains discharge information before and after gas breakdown. Rare gas breakdown voltage is very high (~ 450 V) compared to plasma sustaining glow voltage, $V_g$ (~150 V). The gas breakdown voltage increases with increased discharge gap length as expected. Table 2.3 shows the plasma sustaining voltage for 13.56 MHz and 27.12 MHz Ar and He microplasmas for different electrode separation.

In the pre-breakdown regime (Figure 2.10) $V_g$ increases linearly (section AB) where as the delivered power remain nearly zero and the phase between $I_{RF}$ & $V_g$ is approximately constant at $-\pi/2$ (suggesting a purely capacitive device before gas break down). In the post breakdown region (CD), the glow voltage, $V_g$, remains nearly constant. The voltage characteristic (versus current) in the post breakdown resembles the low pressure DC normal glow (Figure 1.3). Similarly, the *I-V* curve also shows the hysteresis observed for low pressure DC glow discharge, i.e. after gas breakdown the discharge current can be lowered below the point at which the breakdown occurs. In the post breakdown region the power increases linearly with increasing current and the phase angle changes to a lower negative value. Change in the phase angle corresponds to a switch from a purely capacitive behavior to a combination of both capacitive and resistive behavior.

For 60 MHz operation, the post breakdown region shows different *I-V* characteristics for the both helium and argon microplasmas. Instead of constant glow voltage, a

growing $V_g$ (Figure 2.11) is observed with increasing current and approaches a plateau at relatively high discharge current.

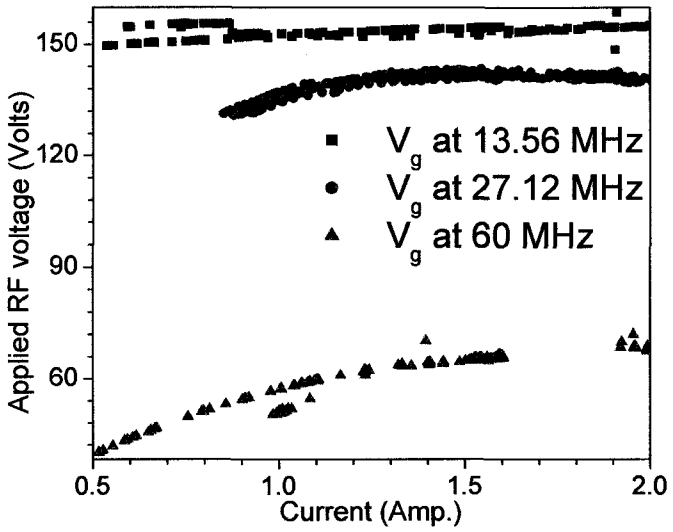


**Figure 2.11: Glow voltage of argon microplasma at different RF frequencies.**

2.4.4 Sheath Characteristics and Electrode Area Asymmetry Effect

In the previous section the capacitive nature of the microdischarge plasma has been described. This section is directed towards the effect of the capacitive nature and its influence on plasma properties. In the RF driven (13.56 and 27.12 MHz) microdischarge plasmas, the observed glow voltage (Figure 2.11) show close resemblance to DC sheaths voltages [11]. Figures 2.12 and 2.13 show the sheath voltage characteristics of argon and helium microplasmas at 13.56, 27.12 and 60 MHz operation for 400 μm electrode separation. Sheath voltage is calculated from the measured RMS current and from calculated reactance values. Voltage drop across the sheath is larger at low current and decreases with increasing current for 13.56 MHz argon/helium microplasmas. It is observed that the sheath voltage drop in the argon microplasmas are larger compared to helium discharge at same RF excitation frequencies. This observation is attributed to (i) Penning ionization[6] and (ii) elastic collision (electron suffers less elastic collisional loss in the

[6] High energy metastables of helium compared to lower energy argon metastables can easily ionize other species that originates from impurity of the gas and from open air operation

helium gas because the loss depends on the ratio electron mass to atomic or molecular mass. Therefore in the (helium) bulk plasma electrons are more effective in generating electron-ion pair by inelastic collisions and thus requires less sheath voltage to sustain the discharge).

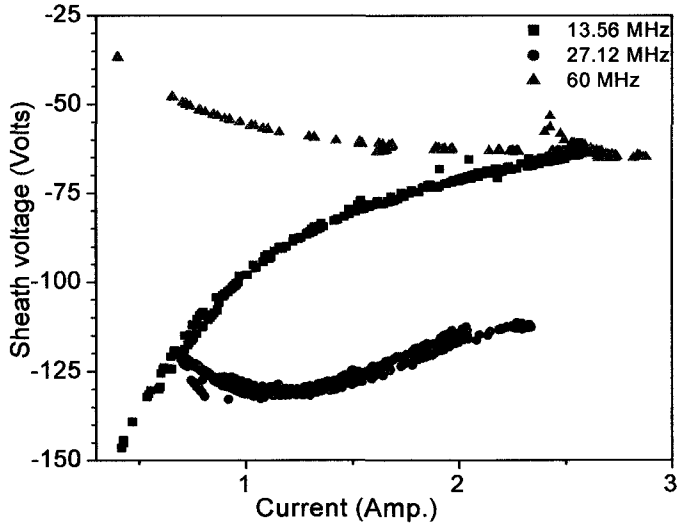


**Figure 2.12: Sheath voltage of argon microplasma at different RF frequencies.**

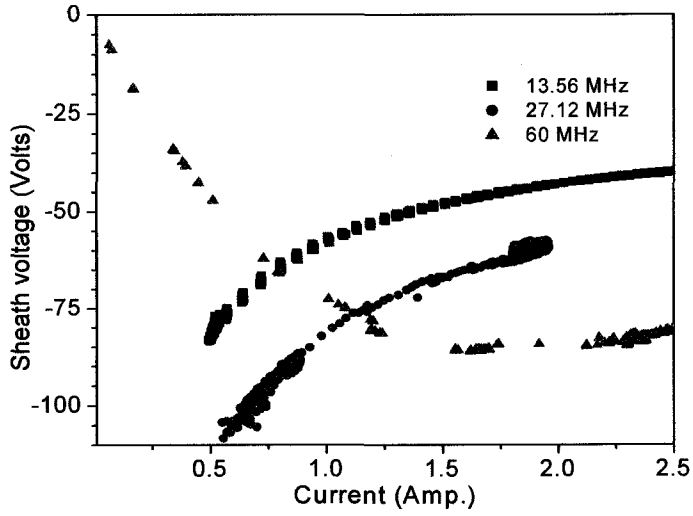


**Figure 2.13: Sheath voltage of helium microplasma at different RF frequencies.**

At 60 MHz operation $V_s$ decreases with increasing discharge current ($I_{RF}$). Sheath voltage ($V_s$) at 13.56 MHz and 27.12 MHz operation follows the same trend (with increasing current, the sheath voltage falls off sharply at lower current region and then falls

off slowly at higher current region). At low current, the sheath voltage is high, therefore the electrons emitted from the cathode have larger contributions in sustaining the plasma. As the current increases, more electrons are generated in the bulk by volume ionization, the discharge therefore self-adjusts its sheath thickness and voltage to maintain the plasma. It is also observed that for all $I_{RF}$ the absolute value of the sheath voltage, $|V_s|$ is greater at 27.12 MHz than that of 13.56 MHz operation. The behavior of the sheath voltage drop is primarily due to the effect of the matching network and discharge geometry (sheath asymmetry at different discharge current) [34, 35]. In a symmetric discharge there is no self bias voltage since both electrodes accumulate the same charge. A brief description of the effects of external circuitry and geometry on the microdischarge is given here based on the work of Kohler et al [34], Raizer and Schneider [36], Chandhok and Grizzle [20] and on detailed discussions of these works by ref. [35].

Figure 2.14 shows asymmetric low pressure plasmas generated by alternating fields. In Figure 2.14a there is no blocking capacitor and averaged potentials across the grounded and powered electrodes are equal [20] thus the DC bias equals zero:

$$V_{dc} = \langle V_{S2} \rangle - \langle V_{S2} \rangle = 0 \qquad 2.13$$

where, $\langle V_{S1} \rangle$ and $\langle V_{S2} \rangle$ are the average DC sheath potentials. Introducing a blocking capacitor (Figure 2.14b) in an asymmetric discharge results in different amount of charge accumulations on the electrodes, i.e. a self bias DC voltage $V_{dc}$ arises [35]. Considering the plasma an ideal conductor (i.e. resistance $R_b \sim 0$), gives:

$$V_{dc} = \frac{C_2 - C_1}{C_2 + C_1} Vg \qquad 2.14$$

and voltage at the powered electrode

$$\bar{V}_2 = \frac{C_1}{C_2 + C_1} Vg \qquad 2.15$$

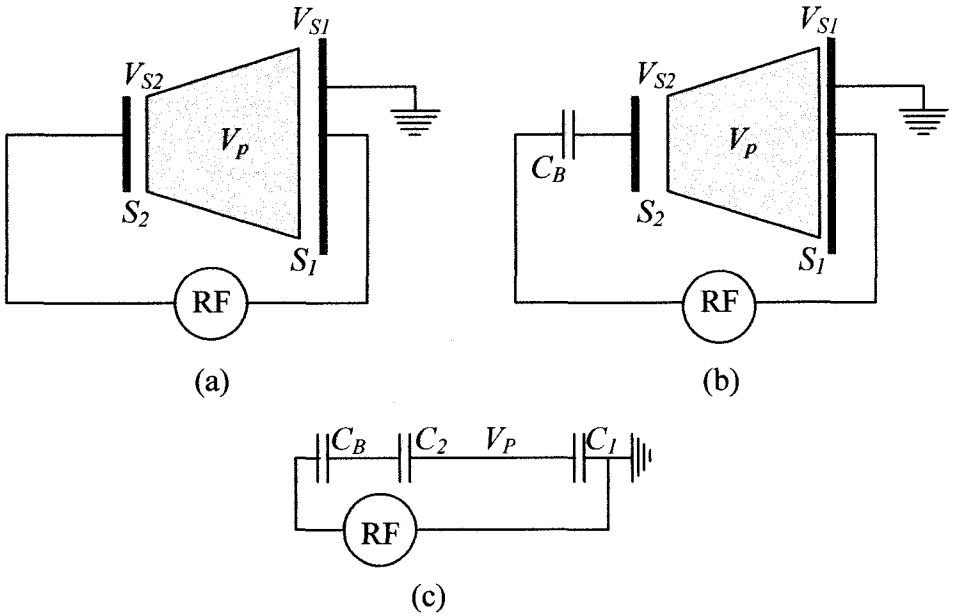


**Figure 2.14: RF driven asymmetric plasma discharge: (a) without and (b) with blocking capacitor $C_B$ [20]; and c) equivalent circuit of figure (b).**

From equation 2.14 it can be seen that the negative DC bias appears when the powered electrode has smaller sheath area and hence smaller capacitance. The microdischarge device has a smaller area powered electrode compared to the grounded electrodes that results in a large negative DC bias voltage when there is a blocking capacitor present (e.g. 13.56 MHz and 27.12 MHz matching network, Figure 2.3a).

Sheath voltage $V_s$ has large negative value at lower RF currents and decreases with increasing current for 13.56 and 27.12 MHz argon and helium microplasmas (Figures 2.12 and 2.13). This observation is most likely the effect of increasing the powered electrode sheath area at a faster rate than the grounded electrode, i.e. $C_2 \cong C_1$ which reduces the self biasing influence. Observation indicates that the 13.56 MHz sheath

voltages are less than those of 27.12 MHz sheath voltages for both argon and helium plasma. This is due to the blocking capacitances (different matching networks have been

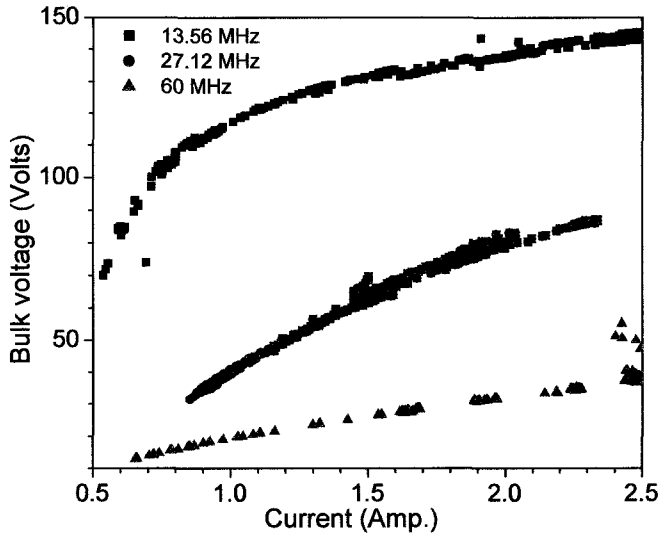


**Figure 2.15: Bulk voltage characteristics of argon microplasmas at 13.56, 27.12 and 60 MHz for electrode separation of 400 μm.**

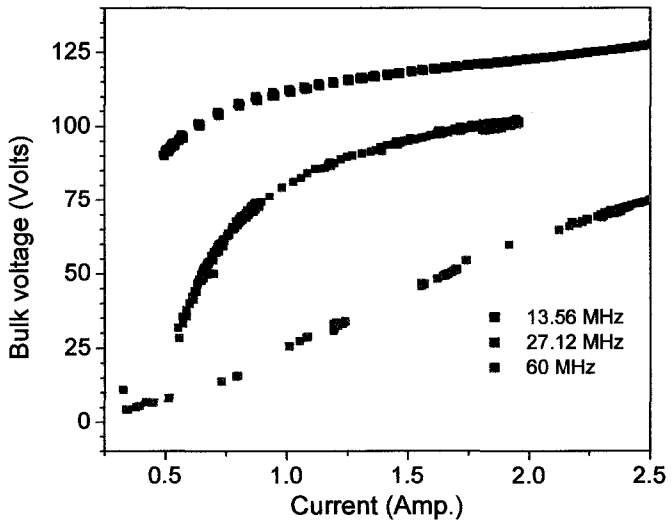


**Figure 2.16: Bulk voltage characteristics of helium microplasmas at 13.56, 27.12 and 60 MHz for electrode separation of 400 μm.**

used and the values of the blocking capacitors were different at 13.56 and 27.12 MHz). In the 60 MHz operation, there is a DC path to ground via an inductor, therefore the behavior of the sheath voltage does not contain a significant amount of self-bias, which

explains the different trend of the sheath voltage drop at 60 MHz operation. At 60 MHz the sheath voltage drop increases with current.

Increase in current decreases the asymmetry hence the sheath width (sheath impedance). Decrease in sheath reactance causes less amount of voltage to drop across the sheath. Since the glow voltage (RF voltage that maintains the plasma) remains the same, the excess voltage will appear in the bulk. This behavior is clearly observed in Figure 2.15 and 2.16. In the 60 MHz operation, the bulk voltage increases with increasing current Sheath voltage is expected to decrease. This contradictory behavior is owing to different *I-V* characteristics (Figure 2.11) of 60 MHz operation where the glow voltage (applied RF voltage) increases with current (as opposed to 13.56 and 27.12 MHz microplasmas where the glow voltage remains nearly constant). This observation does not have any bearing from the sheath asymmetry or larger capacitance value, instead the voltage division between the bulk plasma and the sheath capacitance only.

2.4.5 Bulk Properties

The representative Figures 2.15 and 2.16 show (13.56 MHz and 60 MHz with an electrode separation of 400 μm) the resistance and capacitance with respect to current for the argon and helium microplasmas respectively. Similar behavior is observed for helium and argon microplasmas at all frequencies and electrode separations. The bulk of the plasma can be considered as a conducting medium where the ohmic relation between current and voltage holds. As discussed before (Figure 2.11), the glow voltage $V_g$ ($V_g=V_S+V_b$), remains nearly constant at 13.56 and 27.12 MHz operation, whereas at 60 MHz operation $V_g$ increases with increasing current. The glow voltage is vector sum of the bulk voltage drop and sheath voltage drop. The plasma and sheath behavior show

different characteristics at high currents. The bulk voltage drop increases at relatively low current before reaching a plateau at higher current, especially for low frequency operation. At low current, the resistance has a positive slope, while at the high current resistance decreases (negative *V-I* relationship). Let us consider the simple circuit model of the sheath capacitance as a parallel plate capacitor in series with the bulk resistance (Figure 2.7b) . The Capacitance ($C$) of the sheath and the resistance ($R_b$) of the bulk can be expressed as:

$$C = \frac{\varepsilon_0 A}{S} \tag{2.16}$$

$$R_b = \frac{\rho(L-S)}{A} \tag{2.17}$$

where, $A$ is the sheath area, $L$ is the effective gap between the electrodes (400-600 μm), $S$ is the sheath thickness, $\varepsilon_0$ is the permittivity of free space and $\rho$ is the resistivity of the bulk plasma. In highly collisional (atmospheric pressure) RF plasmas [37]:

$$\rho = \frac{1}{\sigma} = \frac{m_e \nu_e}{e^2 n_e} \tag{2.18}$$

where $\nu_e$ is electron collision frequency with the background gas.

Since both the sheath thickness and sheath area are functions of current and change in the sheath area results in changes in the average bulk plasma length[7], equation 2.17 and 2.18 can be rewritten as:

$$C'(I) = \frac{\varepsilon_0 A'(I)}{S'(I)} \tag{2.19}$$

[7] Due to asymmetric geometry, increase in lateral width of the sheath increases the discharge gap length and thus the bulk plasma length (Figure 2.15).

$$R_b'(I) = \frac{m_e \nu_e}{e^2 n_e} \frac{L'(I) - S'(I)}{A'(I)} \qquad 2.20$$

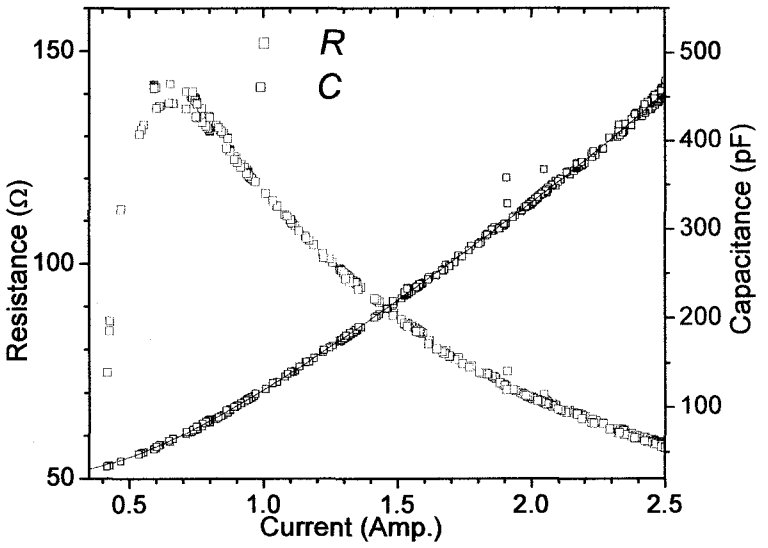


**Figure 2.17: Calculated values of resistance and capacitance of argon microplasma operated at 13.56 MHz.**

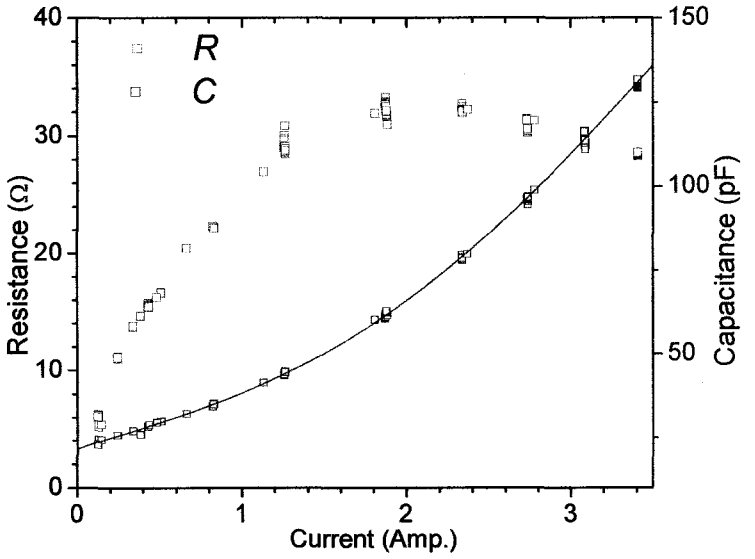


**Figure 2.18: Calculated values of resistance and capacitance of helium microplasma operated at 60 MHz.**

In the low current regime, both $C'$ and $R_b'$ increase with respect to current while at higher current $R_b'$ decreases and $C'$ increases. Increase in the capacitance can be attributed to increase in sheath area and/or decrease in the sheath thickness. Since an increase

in area would result in an increase in the capacitance, but a decrease in the resistance, we conclude that in the low current region decreases in sheath thickness dominates. Therefore, area is only a weak function of current in the low current region, and the term in the numerator of equation 2.20, $L'(I)$-$S'(I)$ increases at a faster rate than the sheath area. This conclusion assumes that both the electron density[8] $n_e$ and electron collision frequency[9,10] in the bulk plasma remain approximately constant [24, 38, 39].

In the high current region, both the sheath thickness and area contribute to the changes in $C'$ and $R_b'$, and therefore the increase in capacitance is non linear. A non-linear curve fit (red lines in figure 2.17 and 2.18) describes the exponential growth of capacitance with respect current.

At higher current, the sheath thickness does not change appreciably so that the resistance decreases with increasing sheath area. The resistance at 13.56 MHz is as high as ~ 7 times compared to the 60 MHz for argon microplasmas (not shown here). This behavior is not consistent with expectations. At high frequencies sheath thickness generally decreases [32, 40], therefore the bulk length and resistance of the plasma should increase. The inverse relationship between RF frequency and resistance has been observed by Beneking [40] as well. Further experiments and investigations are required to explain the bulk plasma properties.

[8] Increase in current is accompanied by the increase in discharge area, therefore electron density remains the same.

[9] Note that electron temperature is almost independent of power density for lowly ionized plasma at constant pressure and electrode separation [38], therefore the mean kinetic energy, hence the time between successive collisions is independent of current (power density). This is not valid if there is a gradient of electron density in the direction of the field, for example, when longitudinal striations are present. In such cases, collision frequency increases with increasing field [39].

[10] At atmospheric pressure plasmas, electron mobility (i.e. collision frequency) can be approximated as a constant [24].

### 2.4.6 Calculation of Electron Density

Electron/ion density and electron/ion energy distribution functions are among the most important parameters for plasma characterization. The Langmuir probe is an effective tool to measure both these parameters for low density plasmas [41]. However, for high pressure plasmas Debye shielding restricts the use of Langmuir probes. APGD microplasmas therefore require other means to characterize these properties. In the absence of probe measurements, sheath voltages (from electrical measurements) have been used to determine the electron densities of APGD microplasmas generated by RF sources.

This section focuses on self consistent electron density calculation. The calculations use the well developed DC model using the Child law sheath [42] and RF collisional sheath model [43]. We employed the collisional sheath model by Liebermann [8, 43, 44] with the modified high pressure Bohm velocity (numerically attained Bohm velocity relation at high pressure by Godyak and Sternberg [8]). With this description, electron densities are calculated self consistently using the calculated values of capacitance and resistances.

High Voltage Sheath (Child Law Sheath)

Formation of sheath and sheath dynamics is discussed in earlier sections. Ions generated in the plasmas move toward the sheath The ions must maintain a velocity greater than the Bohm velocity to enter the sheath. The ion Bohm velocity for collisional plasma can be expressed as [8]:

$$v_B = \left( \frac{e(T_e^{'} + T_i^{'})}{m_i} \right)^{1/2} \left( 1 + \frac{\pi \lambda_d}{2\lambda_i} \right)^{-1/2} \qquad 2.21$$

where, $T'_e$ and $T'_i$ are the electron and ion temperature in electronvolts respectively. The second term in the right hand side of the equation is the correction factor for a collisional plasma while the first term represents the ion Bohm velocity for a collisionless plasma. Note that the Bohm velocity is reduced for collisional plasma. The Debye length, $\lambda_d$, and ion mean free path, $\lambda_i$, are expressed as [45]:

$$\lambda_i = \frac{1}{n_n \sigma} \qquad 2.22$$

$$\lambda_d \approx 7434 \; X \left( \frac{T_e'}{n_e} \right)^{1/2} \; (meter \;) \qquad 2.23$$

where $n_n$ and $\sigma$ are atom density and atom-ion collision cross-section and $n_e$ is electron density in $m^{-3}$.

At very low pressure where $\lambda_d << \lambda_i$ and for $T'_e >> T'_i$ equation 2.21 yields the expression for the ideal (low pressure) Bohm velocity (equation 1.3) [10]. With the reduced Bohm velocity the ion current density at the sheath plasma is:

$$J_0 = nev_B = ne\left( \frac{e(T_e' + T_i)}{m_i} \right)^{1/2} \left( 1 + \frac{\pi \lambda_d}{2\lambda_i} \right)^{-1/2} \qquad 2.24$$

If the electron density in the sheath is negligible, and movements of the ions are mobility limited (i.e. independent of applied field), then according to space charge limited Child sheath theory, the ion current density can be written as [42, 46]:

$$J_0 = \frac{4}{9} \varepsilon_0 \left( \frac{2e}{m_i} \right)^{1/2} \frac{V_S^{3/2}}{S^2} \qquad 2.25$$

where, S is the sheath thickness.

This sheath theory is valid for a time independent sheath. It has already been discussed that although the sheath thickness at each electrode varies with time, the total (sum) sheath thickness remains constant. Instead of using the relative permittivity values for argon or helium, free space permittivity can be considered for atmospheric pressure microplasma because the fractional ionization is very small (~$10^{-6}$ or less) and the permittivity of neutral argon or helium gas have almost identical values compared to that of the free space [47, 48].

For atmospheric pressure microplasmas $\lambda_d / \lambda_i >> 1$ (for example, mean free path of $Ar^+$ in Ar gas for our microplasma is ~ $4\times10^{-8}$ m [23] which is less than Debye length by two order of magnitude even at very high electron density ~$10^{20}$ $cm^{-3}$) and $T'_e >> T'_i$, therefore, equations 2.24 and 2.25 yield:

$$S = 1.77\left(\frac{\varepsilon_0}{en_e}\left(\frac{1}{T_e'}\right)^{1/2} V_s^{3/2}\lambda_d^{1/2}\right)^{2/5} \qquad 2.26$$

Thus, the sheath thickness can be calculated for known values of electron number density, electron temperature, sheath voltage drop and Debye length. Note that Debye length itself is a function of plasma density and electron temperature (equation 2.23).

Sheath voltages are calculated from time averaged electrical measurements (equation 2.15). Electron temperatures for high pressure plasmas are low and are assumed to be in the typical range of 1 to 2 eV. Sheath thickness are calculated from equation 2.26 for different electron densities. Resulting sheath thickness values (<400 μm, limited by the discharge gap length) are used to calculate the sheath area (equation 2.19) using calculated values of capacitances. Once the total area of the sheath is known the sheath lateral

width (Figure 2.19) can be determined by the simple relation,

$$W(I) = \frac{A(I)}{l}(meter); \qquad 2.27$$

where $l$ is the plasma length in the slot microdischarge ($\cong$ 7.5 cm).

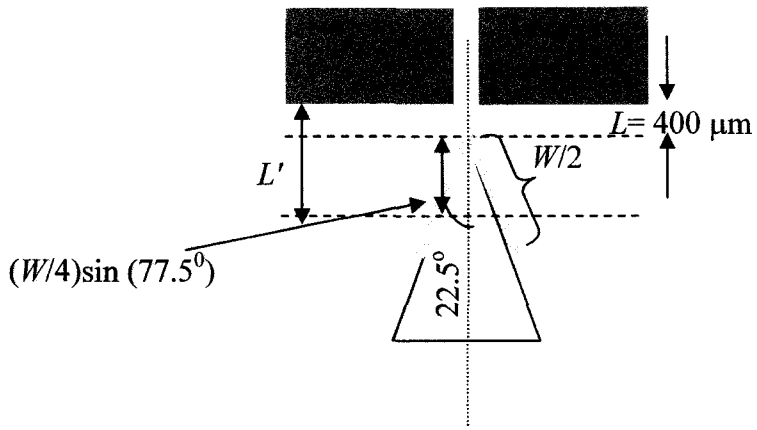


**Figure 2.19: Effect of lateral expansion on the plasma length. Plasma length is by a factor (*W*/4) sin (77.5$^0$) which determines the lateral expansion of sheath w.r.t. current.**

Since sheath lateral width is restricted by the electrode width (~1.6 cm), electron densities are calculated using an iterative process until both the sheath thickness and sheath lateral width criteria are matched. Different sets of sheath thickness and area calculated using the assumed values of electron densities are used in equation 2.20 until the electron density is self-consistently satisfied. During the self-consistent electron density calculation, the discharge gap length $L'(I)$ is varied according to the relation,

$$L'(I) = \left[ d + \frac{W(I)}{4}\sin(77.5^O) - S'(I) \right](meter) \qquad 2.28$$

where the first term in the right hand side denotes the constant discharge gap length, the second term denotes the average increase in the plasma length due to sheath lateral expansion (Figure 2.19) and the third term is the sheath thickness.

Figure 2.20-2.22 show the results for sheath thickness, sheath lateral width and electron density. It is observed that the electron density (Figure 2.22a,b) decreases initially with increasing current. This is due to the positive slope of the resistance values calculated from the measured values (Figure 2.17). Subsequently the electron density increases with current, again owing to decrease in $R_b$ values at higher current (because electron density should stay nearly constant). This observation indicates a more appropriate plasma length approach has to be considered instead of equation 2.28. Since the model works in the high sheath voltage regime, the electron density values at lower current are more appropriate as the sheath voltage is high in this region. No calculations are provided for 60 MHz operation since the sheath voltage is always low, and the discharge characteristics do not obey the normal glow (for which equation 2.26) is valid. Table 2.4 shows the resulting electron densities for different plasma conditions. The calculated electron densities are approximately $5 \times 10^{18}$ $m^{-3}$. The calculated electron densities for collisional sheath and Child law sheath models are comparable (Figure 2.22 and 2.23). In the above mentioned models, the electron temperature deviations do not change electron densities appreciably (Figure 2.22b).

**Table 2.4: Self-consistent electron density calculation for Ar and He RF driven (13.56 and 27.12 MHz) microplasmas.**

| Rare Gas | Electron density, $n_e$ ($m^{-3}$) | |
|---|---|---|
| | 13.56 MHz microplasma | 27.12 MHz microplasma |
| Helium | $5x10^{18}$ | $2.5x10^{19}$ |
| Argon | $5x10^{18}$ | $3x10^{18}$ |

Note: Electron densities at 60 MHz are not calculated because it does not have high sheath voltage therefore the approximation of high sheath voltage collisional model is no longer valid.

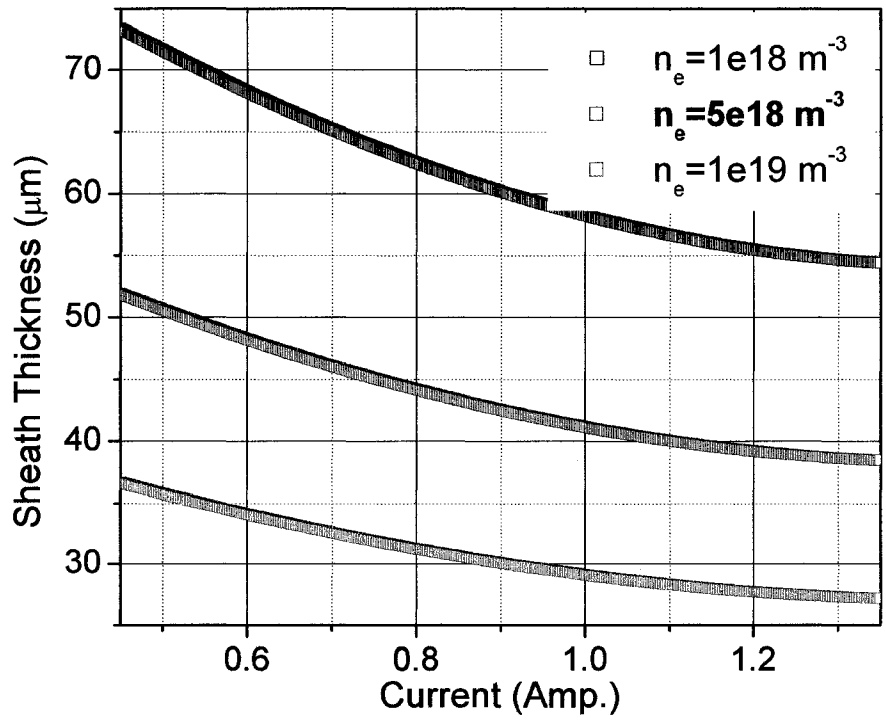


**Figure 2.20a: Sheath thickness calculated from self-consistently determined electron density for argon microplasma driven by 13.56 MHz RF source (electrode separation 400 μm)**

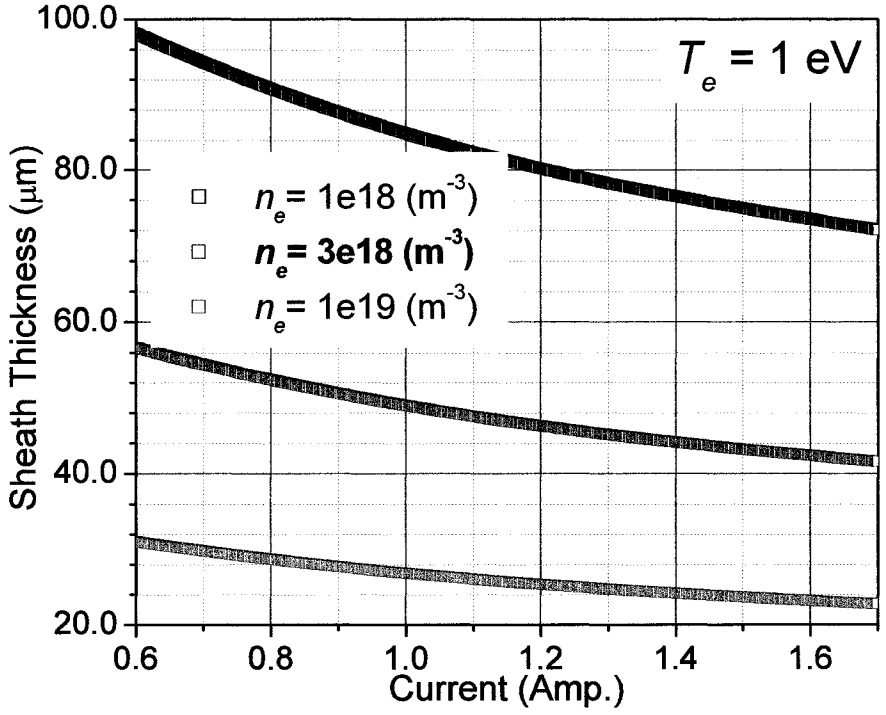


**Figure 2.20b: Sheath thickness calculated from self-consistently determined electron density for helium microplasma driven by 27.12 MHz RF source (electrode separation 400 μm).**

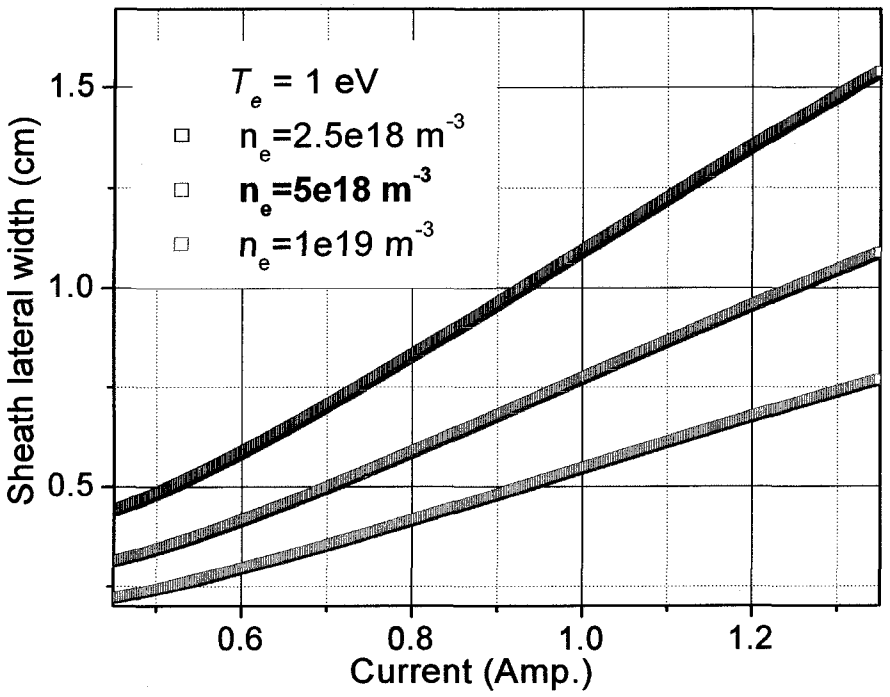


**Figure 2.21a: Sheath lateral width calculated from self-consistently determined electron density for argon microplasma driven by 13.56 MHz RF source (electrode separation 400 μm).**

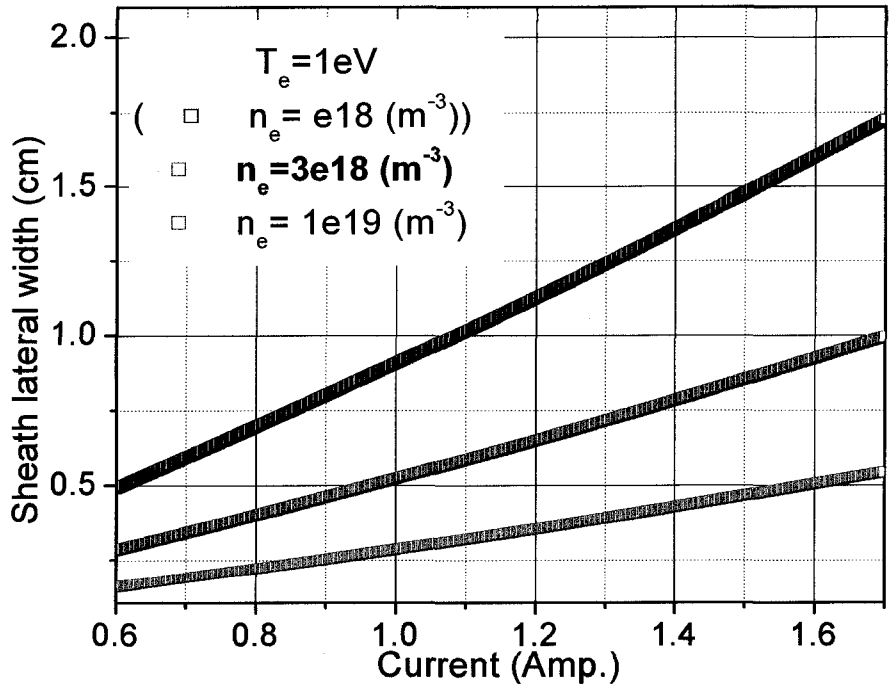


**Figure 2.21b: Sheath lateral width calculated from self-consistently determined electron density for helium microplasma driven by 27.12 MHz RF source (electrode separation 400 μm).**

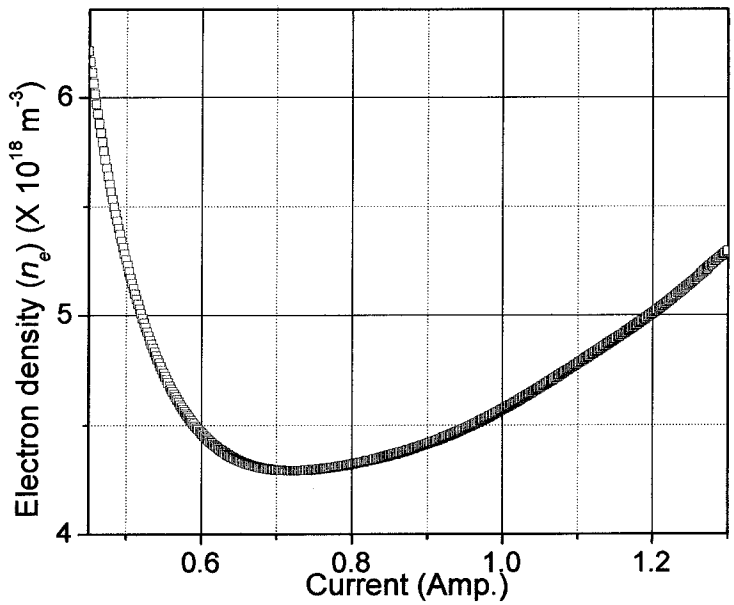


**Figure 2.22a: Self consistent electron density calculation using the calculated values of $R_b'$ and $C'$ and from the collisional model developed by Lieberman. The rare gas medium used is argon and the source is 13.56 MHz. Electrode separation was 400 μm.**

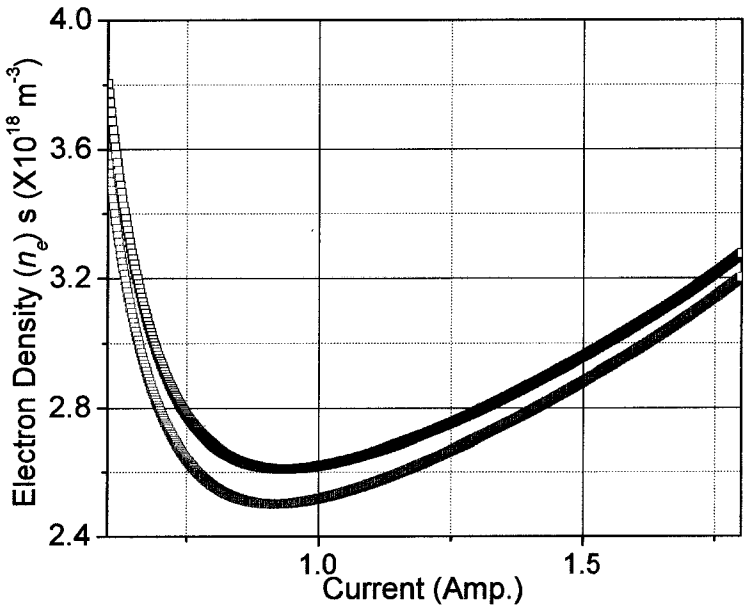


**Figure 2.22b: Self consistent electron density calculation using the calculated values of $R_b'$ and $C'$ and from the calculated values of $V_s$ using collisional model developed by Lieberman and Godyak. The rare gas medium used is argon and the source is 13.56 MHz. Electrode separation was 400 μm. The black and red curves represent the electron density calculations using two different electron temperatures $Te'$= 1 eV and 2 eV respectively. Values obtained for 2 eV is slightly higher.**

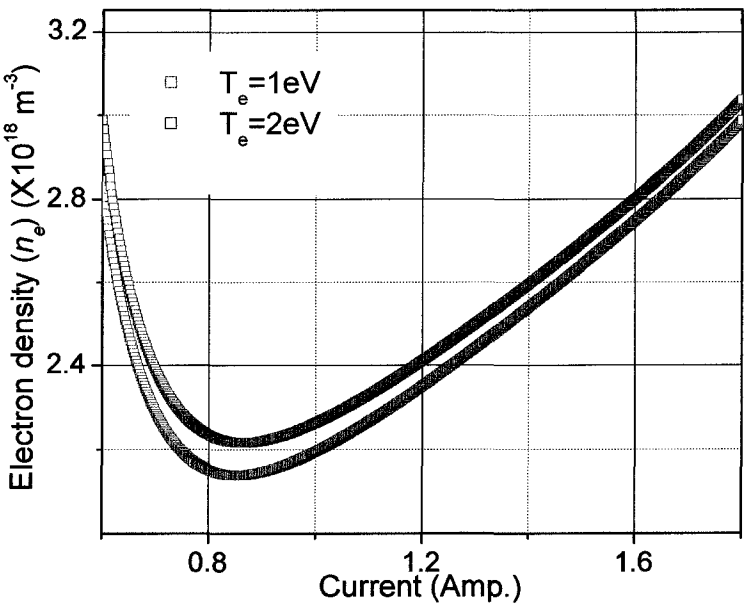


**Figure 2.23: Self-consistently calculated values of electron densities at different electron temperatures using Child-law sheath. The values are close at two different electron temperatures and also similar to the values obtained by the collisional model.**

## 2.5 Conclusion

RF plasma characterization is very complex, asymmetry of the discharge devices adds more complexity to plasma discharge interpretation in terms of simple lumped parameters *R* and *C*. External circuitry can also change the plasma properties. Therefore extreme care is taken to interpret the results. This chapter contains a generalized discussion of the plasma properties. Further research is required to identify the key features ( sheath oscillations, sheath thickness, electron density, ion energy distribution, electron temperature etc.) more accurately.

Here, we summarize the measurements, and results presented in this chapter. Sheath and bulk plasmas are characterized from measured and calculated values. We note that the external circuitry may have contributions to the bulk plasma and sheath characteristics. Identical experiments with and without blocking capacitors are required to identify the effects of the external circuitry. Simultaneous measurements of the DC bias volt-

age can be done in order to find out the capacitances at each electrode, which then can be used to determine the charge densities at each electrode. Harmonic content measurements of the voltage and current are presented. The harmonic content measurements are only done at a fixed power. Since the electrical measurements are carried out at varying power, a detail measurement of harmonic contents is required to identify sheath and bulk non-linear characteristics. The *I-V* characteristics of the microplasmas has been presented. The *I-V* curves of microplasmas at 13.56 and 27.12 MHz operation resemble normal or flat *I-V* curve of low pressure DC plasmas, while at 60 MHz operation a positive *I-V* curve occurs. Phase measurements describes the capacitive nature of the RF discharges. Measurements of resistance and capacitances are coupled to determine electron temperature self consistently using the RF collisional sheath model and high voltage Child sheath law. Electron density measurements assumes the sheath width changes the discharge gap length given by the equation 2.28.

We find that the 60 MHz operation offers more stable operation both spatially and temporally. The bulk characteristics of 60 MHz shows that the resistive component is very low at 60 MHz. Therefore the joule heating at 60 MHz is less compared to the lower frequency operations. It suggests that the observed glow to arc transition at relatively lower current (compared to 60 MHz operation) is due to gas heating. Moreover the discharge could be stably operated at much lower voltage and current at 60 MHz.

**Reference:**


1. Boyd, T.J.M. and J.J. Sanderson, in *The physics of plasmas. (2003)*, Cambridge University Press (1st ed.). p. 456.
2. Eichhorn, H., K.H. Schoenbach, and T. Tessnow, *Paschen's law for a hollow cathode discharge.*, Appl. Phys. Lett., 1993. **63**(18): p. 2481-2483.
3. Schoenbach, K.H., R. Verhappen, T. Tessnow, F.E. Peterkin, and W.W. Byszewski, *Microhollow Cathode Discharges.*, Applied Physics Letters, 1996. **68**(1): p. 13-15.
4. Schoenbach, K.H., A. El-Habachi, M.M. Moselhy, W. Shi, and R.H. Stark, *Microhollow cathode discharge excimer lamps.*, Physics of Plasmas, 2000. **7**(5): p. 2186-2191.
5. Yang, Y., *Alternating-current glow and pseudowglow discharges in atmospheric pressure.*, IEEE Trans. on Plasma Science, 2003. **31**(1): p. 174-176.
6. Yalin, A.P., et al., *Electrical and optical emission characteristics of radio-frequency-driven hollow slot microplasmas operating in open air.*, Applied Physics Letters, 2003. **83**(14): p. 2766-2768.
7. Rahman, A., et al., *Absolute UV and VUV Emission in the 110-400 nm Region from 13.56 MHz Driven Hollow Slot Microplasmas Operating in Open Air.*, Plasma Sources Sci. Tech., 2004. **13**(3): p. 537-547.
8. Godyak, V.A. and N. Sternberg, *Dynamic model of the electrode sheaths in symmetrically driven rf discharges.*, Phys. Rev. A, 1990. **42**(4): p. 2299-2312.

9. Payling, R., D. Jones, and A. Bengtson, eds. *Glow discharge optical emission spectrometry*. 1st ed. 1997, John Wiley and Sons, Inc. pp.114.

10. Chen, F.F., in *Introduction to plasma physics*. 1974, Plenum Press: New York:. p. 244-246.

11. Roth, J.R., *Industrial plasma engineering*. 1st ed. Vol. 1. 2000: Institute of physics publications.

12. Raizer, Y.P., *Gas Discharge Physics*. 1st ed. 1991, New York: Springer.

13. Raizer, Y.P., in *Gas Discharge Physics*. 1991, Springer: New York. p. 24.

14. Chen, F.F., *Introduction to plasma physics*. 1974, New York: Plenum Press.

15. Chen, F.F., in *Introduction to plasma physics (Chapter 1)*. 1974, Plenum Press: New York.

16. Lieberman, M.A. and A.J. Lichtenberg. 1st ed. Principles of Plasma Discharges and Materials Processing. 1994, New York: John Wiley & Sons. p. 351.

17. Lieberman, M.A. and A.J. Lichtenberg, in *Principles of Plasma Discharges and Materials Processing*. 1994, John Wiley & Sons: New York. p. 328.

18. Qiu, H., Y. Wang, and T. Ma, *Collisional effects on the radio-frequency sheath dynamics.*, J. Appl. Phys., 2001. **90**(12): p. 5884-5888.

19. Lieberman, M.A., *Analytical solution of capacitive RF sheath.*, IEEE Trans. on Plasma Science, 1988. **16**(6): p. 638-644.

20. Chandhok, M. and J.W. Grizzle, *Modeling the pressure dependence of DC bias voltage in asymmetric, capacitive RF sheaths.*, IEEE Trans. on Plasma Science, 1998. **26**(2): p. 181-189.

21. Raizer, Y.P., M.N. Schneider, and N.A. Yatsenko, *Radio-frequency capacitive discharges*. 1st ed. 1995, Boca Raton: CRC Press. p.11.

22. Beaty, C.E. and P.L. Patterson, Phys. Rev., 1965. **137**(A): p. 346.

23. McDaniel, E.W. and E.A. Mason, *The mobility and diffusion of ions in gases*. 1972: John Wiley and Sons. p. 267.

24. Raizer, Y.P., in *Gas Discharge Physics*. 1991, Springer: New York. p. 11.

25. Raizer, Y.P., *Gas Discharge Physics*. 1991, Springer: New York. p. 35-37.

26. Lieberman, M.A. and A.J. Lichtenberg, in *Principles of Plasma Discharges and Materials Processing*. 1994, John Wiley & Sons: New York. p. 330.

27. Raizer, Y.P., M.N. Schneider, and N.A. Yatsenko, *Radio-frequency capacitive discharges*. 1st ed. 1995, Boca Raton: CRC Press. p. 28.

28. Sommerer, T.J., W.N.G. Hitchon, R.E.P. Harvey, and J.E. Lawler, *Self-consistent kinetic calculations of helium rf glow discharges.*, Phys. Rev. A, 1991. **43**: p. 4452-4472.

29. Klick, M., *Nonlinearity of the radio-frequency sheath.*, J. Appl. Phys., 1996. **79**(7): p. 34453452.

30. Bletzinger, P. and M.J. Flemming, *Impedance characteristics of an rf parallel plate discharge and the validity of simple circuit model.*, J. Appl. Phys., 1987. **62**(12): p. 4688-4695.

31. Meijer, P.M. and W.J. Goedheer, *Calculation of the auto-bias voltage for RF frequencies well above the ion-plasma frequency.*, IEEE Trans. on Plasma Science, 1991. **19**(2): p. 170-175.

32. Schwarzenbach W., A.A. Howling, M. Fivaz, S. Brunner, and C. Hollenstein, *Sheath impedance effect in very high frequency plasma experiments.*, J. Vac. Sci. Technol. A, 1996. **14**(1): p. 132-138.

33. Rahul, R., *(M.S. Thesis) Electrical characteristics of radio frequency capacitive plasma devices with solid wedge-open electrodes.*, in *Electrical Engineering and Computer Science*. 2004, Colorado State University: Fort Collins.

34. Kohler, K., J.W. Coburn, D.E. Horne, E. Kay, and J.H. Keller, *Plasma potentials of 13.56-MHz rf argon glow discharges in a planar system.*, J. Appl. Phys., 1985. **57**(1): p. 59-66.

35. Raizer, Y.P., M.N. Shneider, and N.A. Yatsenko, *Radio-Frequency Capacitive Discharges*, ed. B.R. CRC Press, pp109-116. 1995.

36. Raizer, Y.P. and M.N. Schneider, *Near-electrode sheath dynamics, current anharmonicity and battery effect in asymmetrical low-pressure radio-frequency discharges.*, Plasma Sources Sci. Technol., 1992. **1**: p. 102-108.

37. Raizer, Y.P., M.N. Shneider, and N.A. Yatsenko. *Radio-Frequency Capacitive Discharges*. in *CRC*. 1995. Boca Raton, FL.

38. Sato, N., S. Lizuka, T. Koizumi, and T. Takada, *Electron-temperature control by movable pins installed in a hollow cathode for discharge plasmas.*, Appl. Phys. Lett., 1993. **62**(6): p. 567-569.

39. Raizer, Y.P., *Gas Discharge Physics*. 1991, New York: Springer. p. 23.

40. Beneking, C., *Power dissipation in capacitively coupled rf discharges.*, J. Appl. Phys., 1990. **68**(9): p. 4461-4473.

41. Boyd, T.J.M. and J.J. Sanderson, in *The physics of plasmas*. (2003), Cambridge University Press (1st ed.). p. 454.

42. Roth, J.R., in *Industrial plasma engineering Vol. 1(1st ed.)*. 2000, Institute of physics publications: Bristol. p. 329.

43. Lieberman, M.A., *Dynamics of a collisional, capacitive RF sheath.*, IEEE Trans. on Plasma Science, 1989. **17**(2): p. 338-341.

44. Lieberman, M.A. and A.J. Lichtenberg, in *Principles of Plasma Discharges and Materials Processing*. 1994, John Wiley & Sons: New York. p. 351.

45. Roth, J.R., *Industrial plasma engineering*. Vol. I. 2000, Bristol: Institute of physics publications. p. 131.

46. Ingold, J.H., *Glow discharges at DC and low frequencies*, in *Gaseous electronics*, M.N. Hirsh and H.J. Oskam, Editors. 1978, Academy press: New York. p. 28.

47. Vejdelek, J. and S. Dado, *Measurement of permittivity of gases.*, http://web.cvut.cz/ctu/research/workshop/prispevky02/ELP043.pdf.

48. http://www.blazelabs.com/e-exp12.asp.

# Chapter 3

# UV/VUV Emission Spectroscopy

### 3.1 Introduction

High pressure high density plasmas are not compatible with internal Langmuir probe measurements of $n_e$ and $T_e$ [1, 2]. Thus external measurements by electrical and optical approaches provide important means to indirectly extract $n_e$ and $T_e$ for such plasmas. In the previous chapter electrical properties of diffuse RF (radio-frequency) driven hollow slot shaped microplasmas have been presented. This chapter and the following chapter focus on microplasma characterization by means of optical spectrum studies, $I(\lambda)$. This chapter focuses on the UV/VUV emission spectroscopy (100 nm to 400 nm) of microplasma, while the next chapter deals with its visible spectroscopy (300 nm to 900 nm). UV/VUV spectroscopy can provide information on the species density, reaction processes and mechanisms as well as understanding the plasma physics and modes of operation. UV/VUV spectroscopy also provides information regarding gas temperature, vibrational temperature and electron energy distribution function (EEDF). Additionally, absolute optical emission measurement also provide a gauge of the potential effectiveness of the plasmas as wide spectrum light source tailored for applications requiring photon fluxes in particular wavelength region.

Herein we report time-averaged spectral emission $I(\lambda)$ in the range 110-400 nm for gas flows of argon and helium with small but varying additive flows all of which exit the grounded open slot electrodes into open-air. Section 3.2 describes the experimental setup. Section 3.3 provides the spectra and a discussion of dominant emission species and their origin. Section 3.4 presents gas (rotational) temperature measurements in the micro-discharges based on the optical emission spectra (2nd positive system of $N_2$), while Section 3.5 presents the vibrational temperature of molecular nitrogen and nitrogen ion. Section 3.6 presents the UV/VUV emission characteristics at different RF excitation frequencies. The total spectral emission as well as the emission efficiency is compared with commercial mercury lamps in the UVC (100-290 nm) and UVB (290-320 nm) regions in Section 3.7. Finally, summary and conclusion are presented in Section 3.8.

## 3.2 Experimental

### 3.2.1 Hollow Slot Microplasma

A schematic of the hollow slot microplasma is shown in Figure 3.1 The difference between the devices used for electrical measurements and optical data acquisition are small. In the device used for optical measurements, both the grounded and powered electrodes are made of copper. (The microplasma device used for electrical measurements has aluminum slotted electrodes). The distance, *d*, between the top of the powered electrode to the slotted electrodes for the optical measurement is 100 μm (as opposed to varying distance *d* (400, 500 and 600 μm) used for electrical measurements). The rare gas used here are UHP (ultra high pure) grade, where as the electrical measurements are done with industrial grade rare gases. UHP grade gas minimizes the effect of impurity from the feed gas, i.e. provides cleaner spectra. These minor changes do not change the electrical

characteristics dramatically but they do help sustain the plasma at a lower power and reduce arc induced instability due to thermionic emission (copper is a better heat conductor than aluminum).

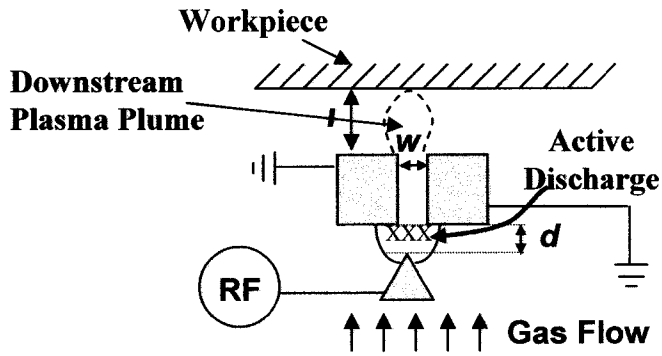


**Figure 3.1: A schematic diagram of RF driven hollow slot micro-discharge configuration is shown with upstream gas flow introduced at the bottom flowing through the electrodes and exiting in open-air. It also shows electrode critical dimensions $w$=200 microns (slot width), $d$=100 microns (wedge to grounded slot interelectrode spacing), and the extent $S$=5mm of the open-slots in the vertical (flow) direction; as well as the active microdischarge and downstream plume regions (current work operates at conditions that do not generate external plume). The wedge and slot electrodes are variable from 1-30 cm in length (dimension into page) creating a "push-broom" source of photons, radicals, and ions, all of which can impinge on a work piece placed in proximity of the grounded slot electrodes.**

The width of the grounded open slot, $w$, is 200 microns. We drive the active discharge with an RF supply at a frequency of 13.56 MHz (also 60 MHz) with current of 0.12 A per cm of slot length. Gas flows in this work are helium and argon, with small additives of hydrogen, oxygen and nitrogen (exact gas flows are given with the spectra). In the inter-electrode region representative operating conditions are $pd$~10 Torr-cm, average rms $E$~10kV/cm, average rms $E/N$~35 Td, current density ~0.7 A/cm$^2$, associated power density ($E\ J\ Cos\ \Theta$) ~14 kW/cm$^3$, and energy per volume delivered to the flowing gas ~50-150 J/L. For these conditions, in the $V$-$I$ curve, glow voltage $V_g$ was approximately constant with current indicating a normal glow type discharge.

As will be discussed, the current absolute $I(\lambda)$ optical detection configuration requires an aperture mask and purge gases, which would interfere with an external plume.

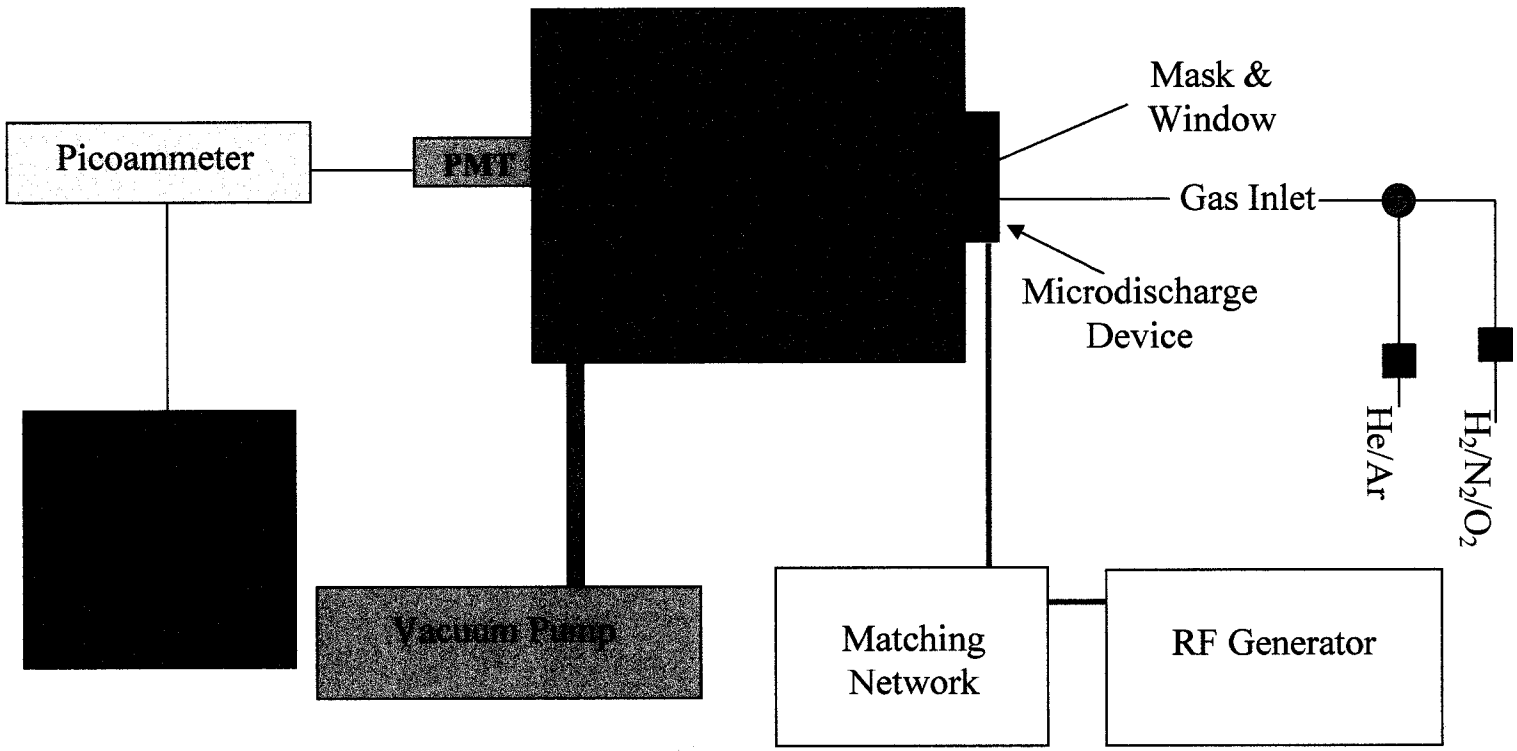


**Figure 3.2: Experimental setup for $I(\lambda)$ data acquisition from hollow slot microplasma device.**

Nevertheless it is informative to briefly consider the nature and extent of the plasma plume as it may be important in certain technological applications. The luminous plume is judged to be due to Penning excitation by energetic metastable species produced in the discharge region and convected through the slot by the upstream gas flow that passes through the active discharge. Owing to open-air operation (without an enclosure), ambient air species mix with the discharge feed gas and clearly is present in the plume region. Depending on operating conditions, the afterglow plume region may be fully contained within the open-slot of Figure 3.1 or may protrude as a distinct plume from the open-slot by as much as ~ 3 mm. Experimentally it is found that the extent of the plume is influenced by choice of RF excitation frequency, gas composition, electrode geometry and gas flow rate.

### 3.2.2 Absolute Optical Emission Measurement System

The $I(\lambda)$ spectra presented in the current work originate from within the slot and may originate from both the active discharge region between the wedge and slot electrodes as well as from the downstream afterglow region. Because of open air operation, the ambient air species ($O_2$, $N_2$, $H_2O$ etc.) mix with the plasma species in the microdischarge as is evidenced from impurity lines in the recorded spectra. The spatial location at which the ambient species mix with the discharge flow varies with flow rate and operating condition. The intent of the current work is to characterize the spatially and temporally averaged optical emissions in order to characterize the device for applications and to make determinations of active plasma mechanisms. Figure 3.2 shows the experimental setup for optical data acquisition from microplasma source. The optical spectra, $I(\lambda)$, are obtained using a 0.2 m McPherson VM 502 scanning monochromator, with a grating

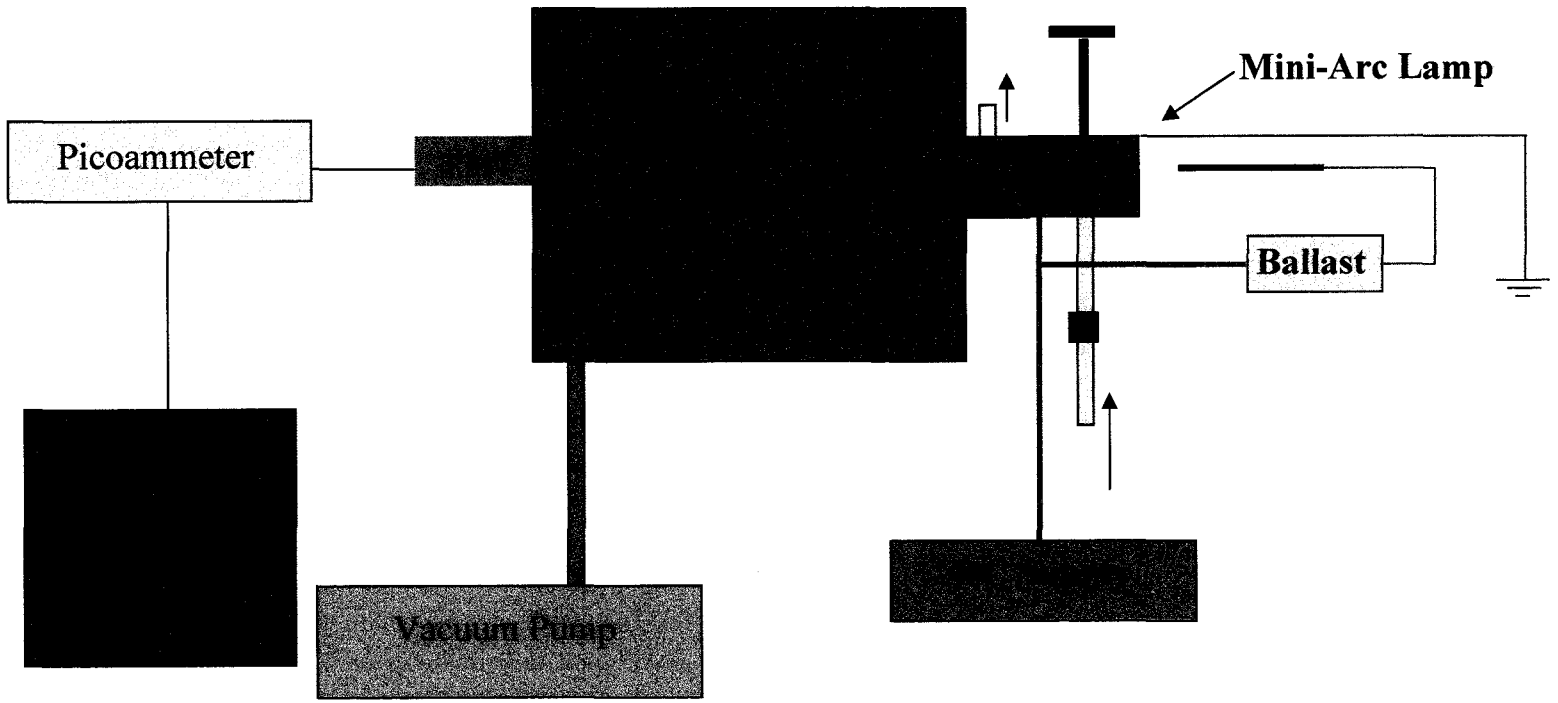


**Figure 3.3: Experimental setup for data acquisition from argon mini-arc lamp for system $I(\lambda)$ calibration.**

of 1200 Grooves/mm blazed at 120 nm. Emission radiation is detected using an Acton 781 photomultiplier tube (PMT). The PMT converts the emission signals into electrical signals that are passed to a picoammeter. The picoammeter measures the current (nA) and sends it to a computer via Labview software.

The optical emission is measured by placing the linear slot plasma in close proximity, and parallel to the entrance slit of the spectrometer. The spectral resolution of the detection system (FWHM of slit function) is experimentally found to be about 0.7 nm. A $MgF_2$ window is introduced at the entrance slit of the monochromator to keep the monochromator chamber under vacuum. Vacuum is required for data acquisition in the highly absorbing Schumann bands [3] due to molecular oxygen (wavelength region ~130-180 nm).

Absolute calibration of the detection system (intensity and wavelength) is obtained using an argon mini-Arc source that is traceable to NIST secondary standards. The experimental setup for obtaining data from the min-arc lamp is shown in Figure 3.3. The mini-Arc lamp is operated with a DC source and with argon as the feed gas. The radiance of the mini-Arc is provided in units of W $cm^{-2}$ $sr^{-1}$ $nm^{-1}$, with 20% uncertainty below 140 nm, 9% uncertainty from 140-250 nm, and 4% uncertainty from 250-400 nm. The low-wavelength cut-off for the calibration is 120 nm due to the $MgF_2$ window. Data is extrapolated from 120 nm to 110 nm, which may not be highly accurate, but the optical emission in this range is minimal. The $MgF_2$ optical window used in the entrance slit of the monochromator for plasma measurement is also used for the calibration. A mask of width 0.75 mm and height 4 mm is employed to define the emitting area of the arc lamp. Optical emission measurements from the slot micro-plasma use the same mask and

collection geometry as the secondary standard mini-Arc scans, so that no geometric corrections are needed (to yield absolute $I(\lambda)$ data). A weak helium purge is flowed between the plasma and monochromator ($MgF_2$) window in order to eliminate absorption of VUV light by ambient air (oxygen) in this region. (Note that the He purge does not fully seal the inside of the hollow slot from the ambient air.) Collected emission radiation is again converted into electrical signals and collected via the picoammeter. The calibration procedure employs the following:

mini-arc optical emission signal, $I_0(\lambda)$ (in nA),

mini-arc radiance (provided with min-arc) (in $W/cm^2/sr/nm$),

mini-arc output function, $I'(\lambda)$ ( in $W\ sr^{-1}\ nm^{-1}$),

microplasma emission collected by the detection system, $I''(\lambda)$ (in nA)

from which we find:

spectral response of the detection system, $R(\lambda)= I_0(\lambda / I'(\lambda)$ (in $nA/W\ sr^{-1}\ nm^{-1}$) and

absolute irradiance from the slot microplasma, $I(\lambda) = I''(\lambda) / R(\lambda)$ (in $W\ sr^{-1}\ nm^{-1}$).

Note that the output spectra (i.e. absolute irradiance from the slot microplasma) correspond to light emitted from a 4 mm length slot (defined by the mask).

### 3.3 Optical Emission Spectra, $I(\lambda)$: 110-400 nm

For clarity of discussion, the microplasma optical emission spectra, $I(\lambda)$, have been divided into three regions. Note that the emission spectra in this section are all for excitation frequency of 13.56 MHz RF source generated microplasmas. Figures 3.4 a-e show the emission from 110-200 nm, Figures 3.5 a-c show the emission from 200-300 nm, Figure 3.6 shows a particular spectrum from 110-400 nm, and Figure 3.7a-c shows the 300-400 nm spectral region. In these plots, intensity selected to allow better

examination of the weaker spectral features at the expense of some stronger features extending beyond the top of the graph. In such cases, the peak values of spectral lines that exceed the top of the scale are labeled at the top of the graph. Tables 3.1-3.3 summarize the atomic and molecular transitions causing the optical emission in the spectral regions 110-200 nm, 200-300 nm, and 300-400 nm respectively. Table 3.4 presents the argon and helium metastables states involved in certain excitation processes. Figures 3.8a-c summarizes the prominent features of the optical emission for the three gas mixtures studied. Figure 3.9 provides simplified Grotrian diagrams for N, $N_2$, and NO, showing key energy levels.

**Table 3.1: Dominant atomic and molecular transitions observed in the 110-200 nm region from the slot microelectrodes of Figure 3.1.**

| Excited Species | Wavelength (nm) | Upper State (eV) | Transition |
|---|---|---|---|
| H | 121.56 | 10.20 | $1s\ ^2S\text{-}2p\ ^2P^O$ |
| O | 130.50 | 9.52 | $2p^4\ 3P\text{-}3s\ ^3S^O$ |
| N | 119.95 | 10.34 | $2p^3\ ^4S^O\text{-}3s\ ^4P$ |
| N | 124.30 | 12.36 | $2p^3\ ^2D^O\text{-}3s\ ^2D$ |
| N | 149.50 | 10.68 | $2p^3\ ^2D^O\text{-}3s\ ^2P$ |
| N | 174.50 | 10.68 | $2p^3\ ^2P^O\text{-}3s\ ^2P$ |
| $H_2$ | ~130 -170 | - | $(B\ ^1\Sigma_u\text{-}X\ ^1\Sigma_g)$ |
| $Ar_2$ | ~125 | 11.06 | $Ar_2(\ ^3\Sigma_u \text{ or } ^1\Sigma_u)\text{-}Ar\ (^1S_0)$ |
| $Ar_2^{++}$ | ~190 | ~12.0 | $Ar_2^{++}(^3\Pi_g) - Ar^+(^3\Pi_u)$ |

### 3.3.1 Optical Emission Spectra in the 110-200 nm region

The spectra given in Figure 3.4a-c corresponding to the 110-200 nm region for the micro-plasma operating with three gas mixtures: helium/hydrogen, argon/hydrogen and argon/nitrogen flows respectively. In each case, the strongest emission lines observed are lines from atomic nitrogen (149 and 174 nm), indicating the active plasma is able to dissociate molecular nitrogen easily. Relatively strong lines originating from atomic oxygen

and hydrogen are also observed. Several of these $I(\lambda)$ features are triplets, but they are unresolved by the detection system. The emitter efficiency of the 149 nm nitrogen is typically 0.0024 [4].

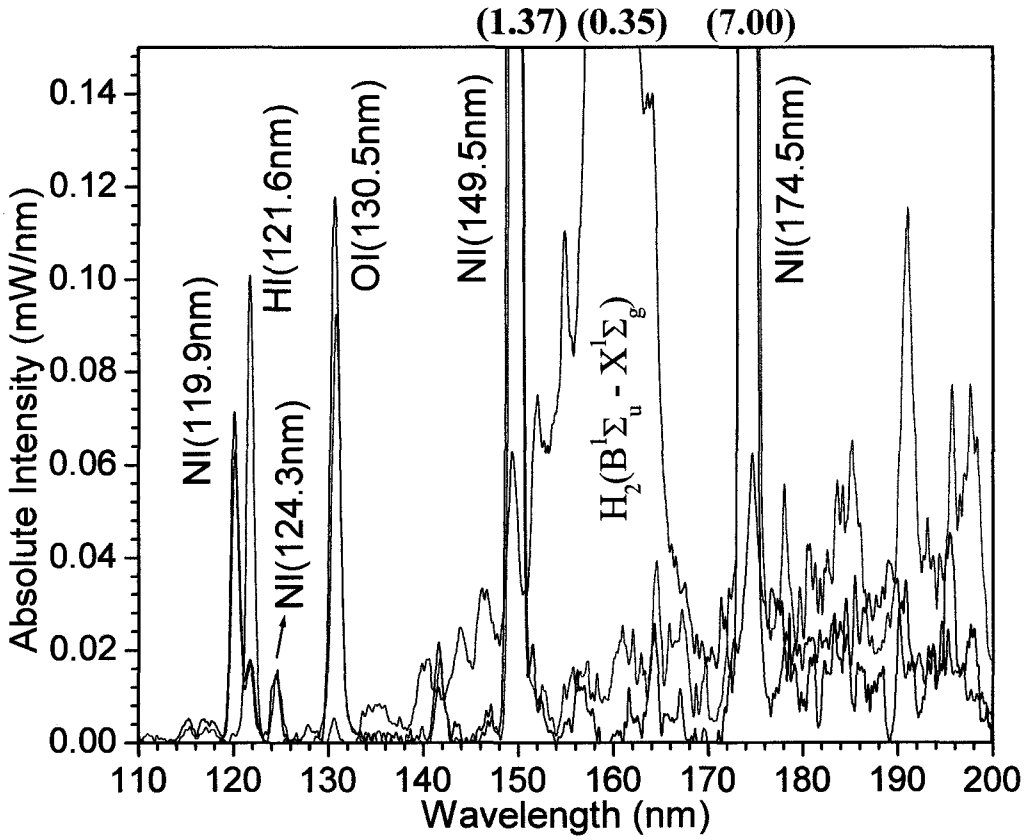


**Figure 3.4a: Absolute optical emission spectra in the 110-200 nm region for He-$H_2$ flow through slot microelectrodes of Figure 3.1 into open air. The upstream He flow rate is 2.0 slpm, while the $H_2$ admixture flow rate is 9.0 sccm (black), 18.0 sccm (red) or 37.0 sccm (blue). The dominant lines for each mixture are from atomic N at 149.5 and 174.5 nm. Other identified transitions are labeled (see Table 3.1) and peak intensities (for the admixtures yielding the largest peaks) are shown in parentheses for cases where the peak exceeds the top of the graph.**

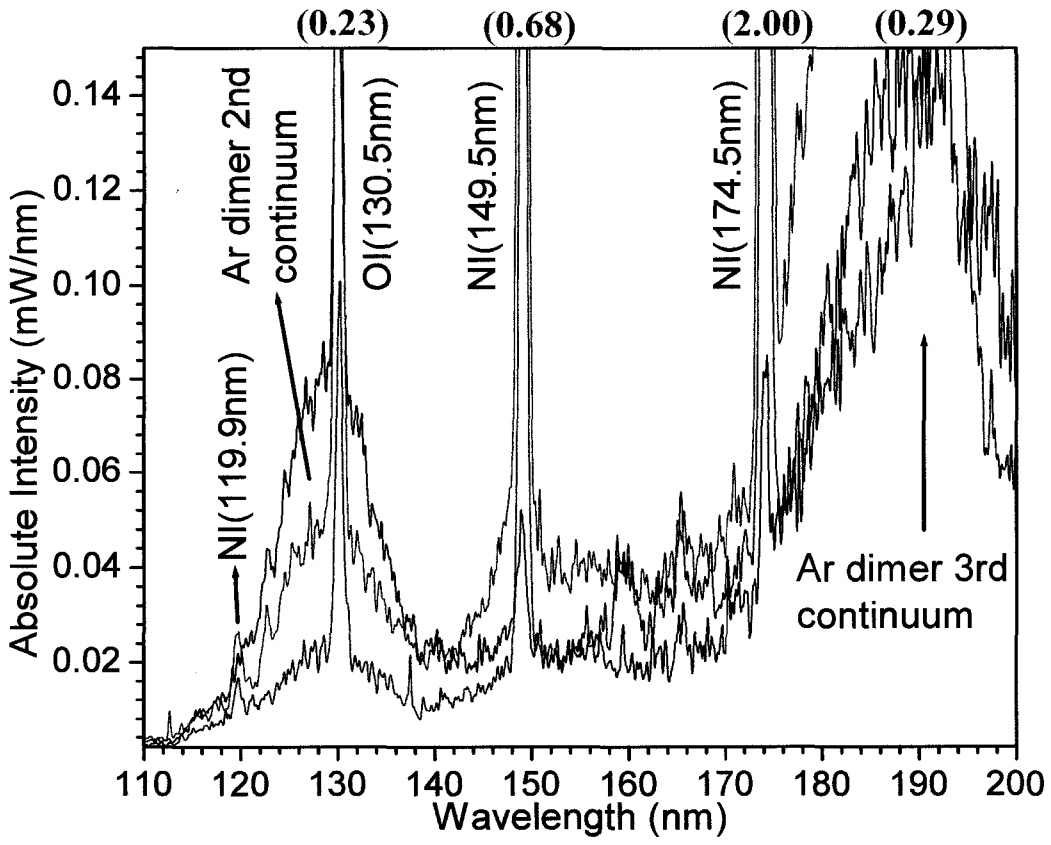


**Figure 3.4b: Absolute optical emission spectra in the 110-200 nm region for Ar-$H_2$ flow through slot microelectrodes of Figure 3.1 into open air. The upstream Ar flow rate is 14.0 slpm, while the $H_2$ admixture flow rate is either 0 sccm (black), 9.0 sccm (red) or 18.0 sccm (blue). Identified transitions are labeled (see Table 3.1) and peak intensities (for the admixtures yielding the largest peaks) are shown in parentheses for cases where the peak exceeds the top of the graph.**

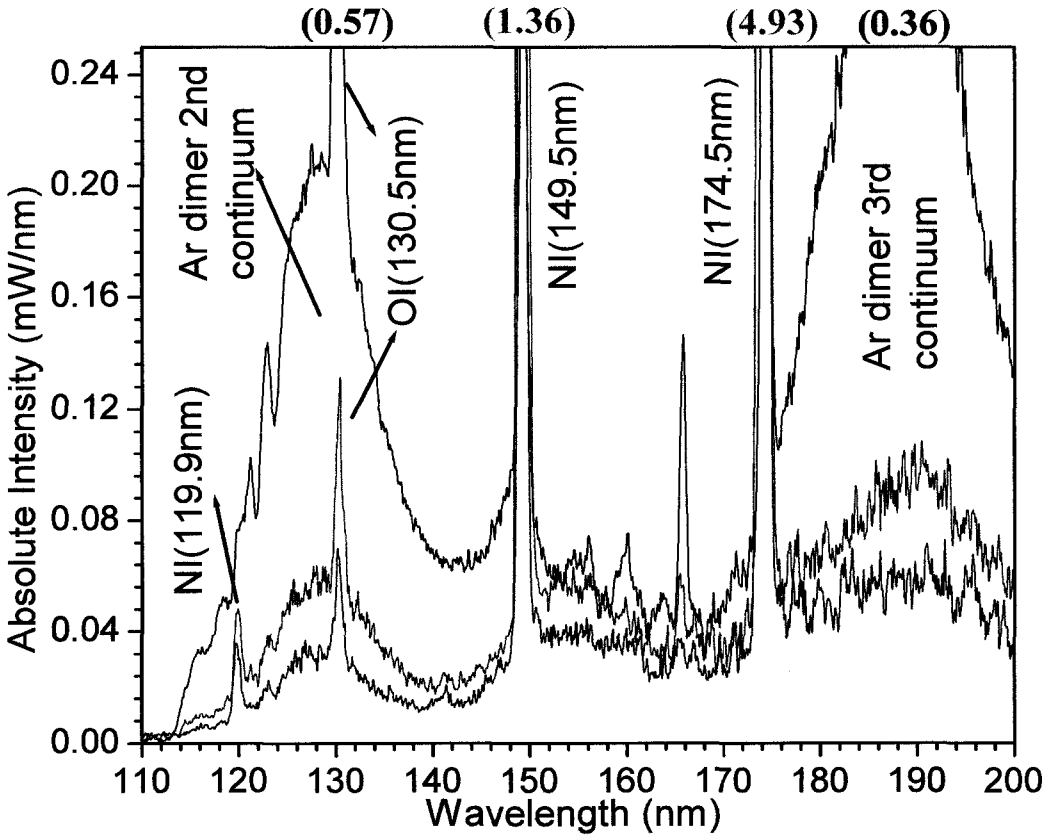


**Figure 3.4c: Absolute optical emission spectra in the 110-200 nm region for Ar-$N_2$ flow through slot microelectrodes of Figure 3.1 into open air. The upstream Ar flow rate is 9 slpm, while the $N_2$ admixture flow rate is 0.0 sccm (black), 5.0 sccm (red) or 10.0 sccm (blue). Identified transitions are labeled (see Table 3.1) and peak intensities (for the admixtures yielding the largest peaks) are shown in parentheses for cases where the peak exceeds the top of the graph.**

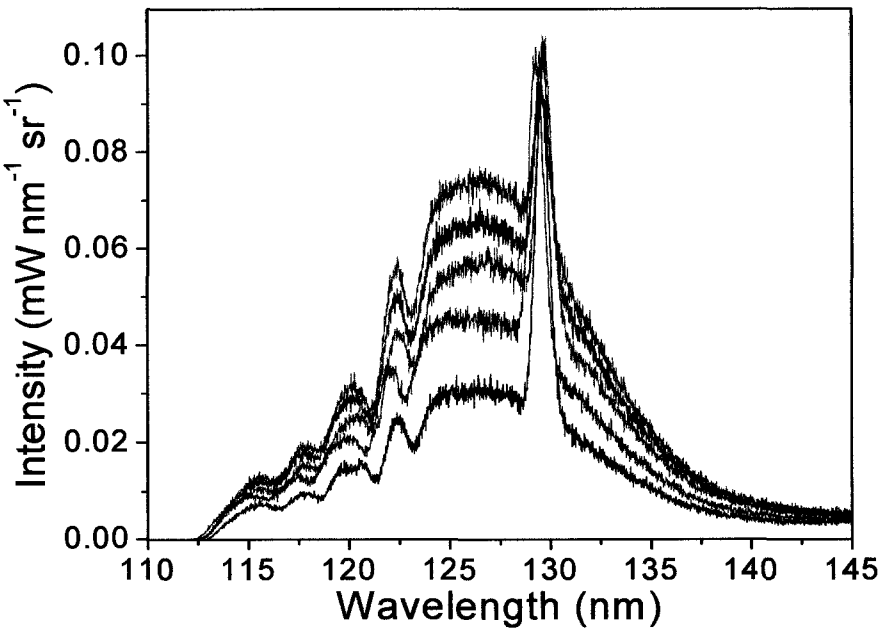


**Figure 3.4d: Absolute optical emission spectra in the 110-145 nm region for Ar flow through slot microelectrodes of Figure 3.1 into open air. The upstream Ar flow rates are 4.5 slpm (black), 9 slpm(red), 13.5 slpm (green), and 29 slpm (magenta) respectively. Emission intensity of the 2nd continuum of the argon dimer increases with increasing argon flow rate (pressure).**

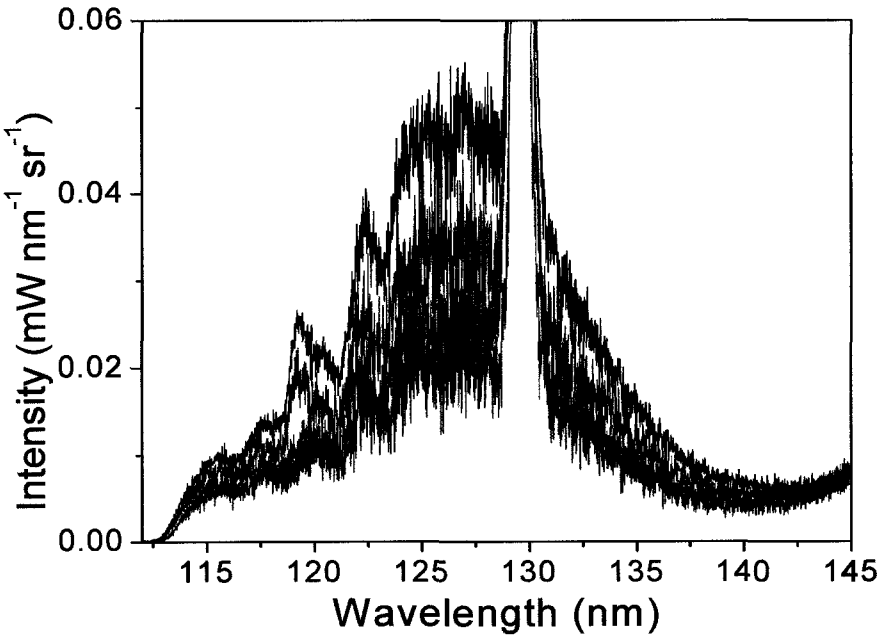


**Figure 3.4e: Absolute optical emission spectra in the 110-145 nm region for Ar-$O_2$ flow through slot microelectrodes of Figure 3.1 into open air. The upstream Ar flow rate is 29 slpm, while the $O_2$ admixture flow rate is 5 sccm (black), 10 sccm (red) or 14 sccm (green) and 18 sccm (blue).**

The atomic nitrogen lines also appear in the spectra for upstream gas flow mixtures that do not contain nitrogen (i.e. helium/hydrogen and argon/hydrogen shown in Figures 3.4a and 3.4b. This indicates the effect of impurity lines due to open air operation. The atomic nitrogen formation is primarily in the plasma plume (where ambient nitrogen clearly mixes), but ambient nitrogen also penetrates into the active discharge region from random walk motion and vortices. Addition of nitrogen greatly enhances molecular nitrogen emissions (Figure 3.4c). The weak atomic nitrogen line at 124 nm emits from the $N(^2D)$ upper state, while the strong lines at 149.5 and 174.5 nm are from the $N(^2P)$ upper state which radiatively decays to the lower metastable states $N(^2D^O)$ and $N(^2P^O)$ respectively, see Table 3.1 Higher energy electrons are required to populate $N(^2D)$ upper state, (than $N(^2P)$) and also $N(^2D)$ state is very efficiently quenched by most gases [5]. Note that dissociation of $N_2$ into atomic N requires 9.8 eV [6]. Atomic emission from nitrogen involves the following three major excitation processes:

i. Metastable (molecular nitrogen)-atom interaction: Reaction R3.1a describes the nature of molecular nitrogen metastable and ground state atomic nitrogen interaction. It is likely that there is strong formation of $N_2(A\ ^3\Sigma_u^+)$ levels via electron impact excitation [7], and that the $N_2(A\ ^3\Sigma_u^+)$ state is mainly responsible for populating the $N(^2P)$ level through the reaction R3.1b followed by electron impact excitation of $N(^2P^O)$ [8, 9].

$$N_2(A\ ^3\Sigma_u^+) + N(^4S) \longrightarrow N_2(X\ ^1\Sigma) + N(^2P^O) \qquad \text{R3.1a}$$

$$N(^2P^O) + e = N(^2P) + e \qquad \text{R3.1b}$$

In principle, one can directly detect the $N_2(A\ ^3\Sigma_u^+)$ state by emission from the Vegard-Kaplan system ($N_2(A\ ^3\Sigma_u^+ - X\ ^1\Sigma_g^+)$). However, in atmospheric pressure plasmas it is more likely that the metastable state $N_2$ $(A\ ^3\Sigma_u^+)$ state is collisionally quenched.

ii Dissociative recombination: This process requires molecular ion of nitrogen (reaction R2) to dissociate upon capturing a slow electron.

$$N_2^+ + e = N^* + N \qquad \text{R3.2}$$

A significant amount of nitrogen molecular ion emission is observed only in the helium plasma where $N_2$ is mixed into the plasma in from the ambient. We conclude that dissociative recombination is not playing an important role in the atomic emission of nitrogen.

iii. Direct electron impact excitation: Electron impact excitation mechanism (reaction R3.3a,b) from the ground state as well as from the metastable states (R3.3c) of atomic nitrogen in the active discharge region play a major role in the argon-nitrogen plasma when nitrogen is added to argon flow. We note that increasing amounts of nitrogen in the active discharge region enhances atomic emission intensities.

$$N\,(^4S) + e = N(^2P) + e \qquad \text{R3.3a}$$

$$N\,(^4S) + e = N\,(^2P^o \text{ or } ^2D^o) + e \qquad \text{R3.3b}$$

$$N\,(^2P^o \text{ or } ^2D^o) + e = N(^2P) + e \qquad \text{R3.3c}$$

$$N(^2P) = N\,(^2P^o) + h\nu \qquad \text{R33.d}$$

We note that the magnitude of the partial hydrogen flow has a significant effect on the strengths of the atomic nitrogen lines, which may be due to a combination of changes in the EEDF (electron energy distribution function) in the active plasma as well as quenching reactions involving hydrogen. (Hydrogen addition can affect the EEDF by decreasing the density of argon metastables and thus the degree of stepwise ionization, as well as introducing the competing direct ionization pathway of atomic hydrogen.) In the helium/hydrogen and argon/hydrogen open-air slot plasmas (Figures 3.4a&b), the

reduction in the magnitudes of the atomic nitrogen lines for large hydrogen flow (>9 sccm in Ar-$H_2$ plasmas and >18 sccm for He-$H_2$ plasmas) is most likely due to quenching reaction (R4) where atomic hydrogen depopulates $N_2(A\ ^3\Sigma_u^+)$ levels [11-13].

$$N_2(A\ ^3\Sigma_u^+) + H = \text{products} \qquad \text{R3.4}$$

When operating the discharge with helium and hydrogen admixtures (Fig. 3.4a), the atomic Hydrogen Lyman α line at 121.6 nm is also present. From the point of view of VUV emission applications, the Lyman α line is of particular interest since it is spectrally located at a sharp minimum in the absorption coefficient of molecular oxygen [14], and is only weakly absorbed in open-air operation. The dissociation of $H_2$ requires 4.48eV [15], while excitation of atomic H ground states to $n=2$ requires an additional 10.2eV [16]. In rare gas-$H_2$ plasmas, the role of metastable-molecule reactions is equally important to direct electron impact. It is likely that the excited $n=2$ atomic hydrogen states are formed by dissociative recombination from molecular hydrogen ion in the He-$H_2$ plasma instead of direct Penning excitation as observed in the Ne-$H_2$ plasma [15, 17]. Note that neon metastable has energy (~15 eV) which is close to the sum of energies of the dissociation of molecular $H_2$ and excitation of an H atom to $n=2$ level where as helium metastables (~19 eV) do not have a close match to form $n=2$ state of atomic hydrogen from molecular hydrogen. Therefore the emission spectra of the Lyman alpha line in the helium microdischarge may have contributions from the following three major excitation pathways:

i. direct electron impact excitation,

$$e + H(^1S_0) = H^*(n=2) + e \qquad \text{R3.5}$$

ii. helium excimers (12.4-21.38 eV) [18] and

$$He_2^* + H_2 = He + H_2^* \quad \text{R3.6a}$$

$$H_2^* = H(^1S_0) + H^*(n=2) \quad \text{R3.6b}$$

iii. dissociative recombination of molecular ions that are generated by Penning mechanism.

$$H_2^+ + e\ (\text{slow}) = H(^1S_0) + H^*(n=2) \quad \text{R3.7}$$

Because of the close match of the energy of the neon metastable to the energy required to form $n=2$ state of atomic hydrogen, the emission intensity of the Lyman-alpha line is in the Ne-$H_2$ plasma observed by Kurunczi and his group [15] is very clean.

For the helium-hydrogen plasmas operating at the highest hydrogen flow rate, a moderate emission feature from molecular hydrogen at ~160 nm [14, 19] is also detected (Figure 3.4a) and is attributed to radiative recombination from the molecular hydrogen ion. This observation indicates that the dissociative recombination may have a major role in the Lyman-alpha line observed in the He-$H_2$ microplasmas. In contrast to the helium plasmas, for the argon plasmas (Fig. 3.4b,c) there is no discernible emission from the Lyman $\alpha$ line consistent with the lower energy of argon metastables (11.55 eV and 11.72 eV) and dimers (9.54 eV), see Table 3.4.

For argon/hydrogen, argon/nitrogen, argon/oxygen mixtures (Fig.3.4b-e), the argon dimer 2nd continuum emission (130 nm region) [20, 21] and argon dimer 3rd continuum emission (190 nm region) [22, 23] are present (see Table 3.1). The importance of the dimers relates to the discharge breakdown mechanism. At higher *E/N* values (~100 Td) resonance photons produce secondary electrons and at *E/N* values lower than 40 Td (in the spectroscopic measurements, the *E/N* values are ~35 Td), the nonresonance VUV

photons (such as the photons from the radiative decay of the dimers) produce secondary electrons [24]. Three body collisions involving Ar atomic metastables ($Ar^M$) favor the formation of excimers $Ar_2^*$ at relatively high gas pressure (reaction R3.8) [15]. Increased gas pressure increases the 2nd continuum emission intensity as observed in Figure 3.4d indicating that the three body collisions are indeed responsible for argon dimer formation. $Ar_2^*$ radiatively decays to ground state Ar atoms and causes the 2nd continuum emission [25], whereas the third continuum emission is the result of radiative decay of $Ar_2^{++}$ into two $Ar^+$ ions [25-27].

$$X^M + X + M = X_2^* + X \qquad \text{R3.8}$$

where, superscript M represents metastable, X stands for Ar (or any other rare gas species) and M denotes a third body (rare gas or any other species)

Owing to open air operation of the plasma, the atomic oxygen line at 130 nm is also visible in Figs. 3.4b,c (dissociation of $O_2$ into atomic O requires 5.1 eV [6]). Increased flow rates of argon increase the intensity of the argon dimer (Figure 3.4d) and addition of either $H_2$ or $N_2$ to a constant argon gas flow passing through the electrodes decreases the observed emission intensity of the argon dimers and atomic oxygen line (Figure 3.4b-c). This behavior is due to efficient quenching of metastable states of argon by impurity species. (order of $Ar^M$ quenching efficiency by impurity is $O_2$>$H_2$>$N_2$ [28]). A similar trend is observed in argon/oxygen mixtures (Figure3.4e), where we also observed an atomic oxygen line at 130 nm superimposed on the argon dimer 2nd continuum emission, and a resonant transfer behavior between this peak and the continuum (similar to that observed in micro-hollow cathode discharges [29]).

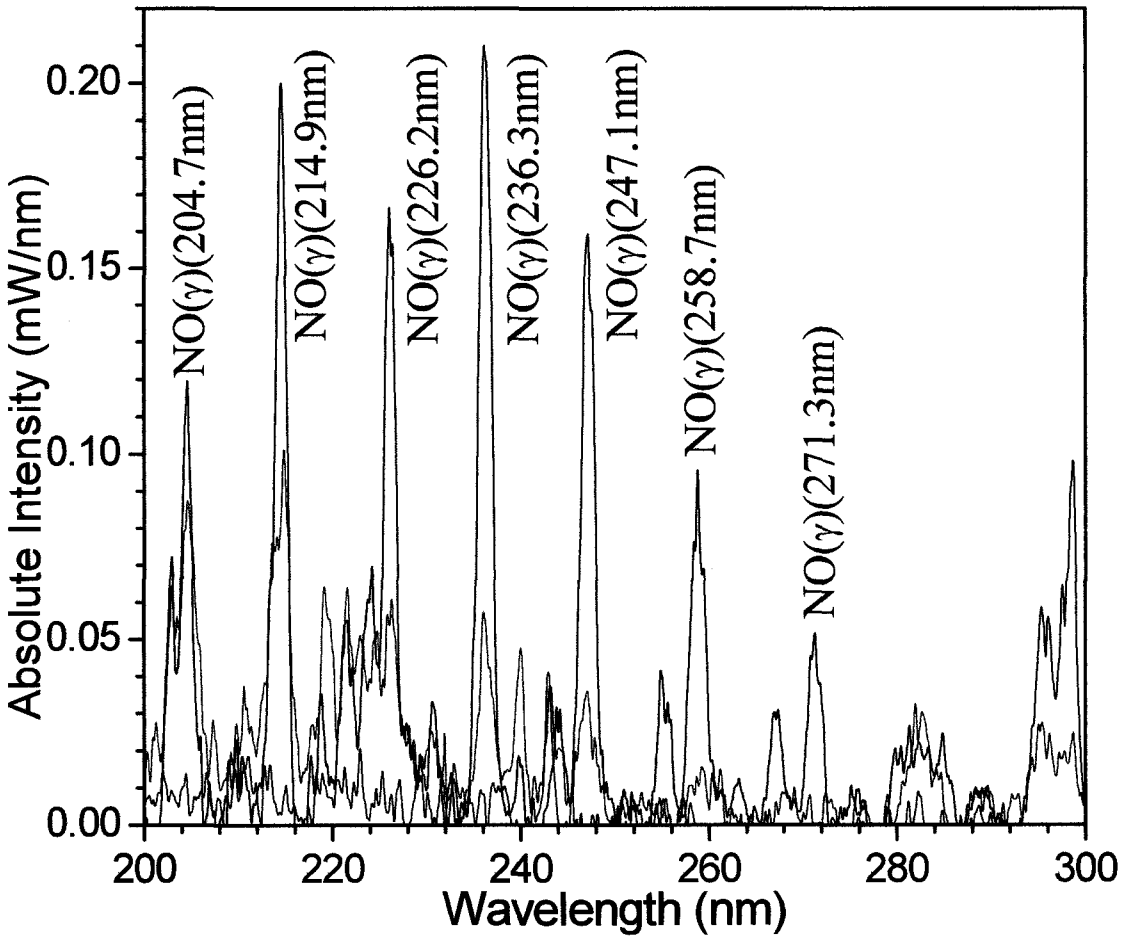


**Figure 3.5a: Absolute optical emission spectra in the 200-300 nm region for He-$H_2$ flow through slot microelectrodes of Figure 3.1 into open air. The upstream He flow rate is 2.0 slpm, while the $H_2$ admixture flow rate is 9.0 sccm (black), 18.0 sccm (red) or 37.0 sccm (blue). Identified molecular transitions are labeled (see Table 3.2). The emission is dominated by NO(γ) bands, while no strong atomic lines are detected in this spectral region.**

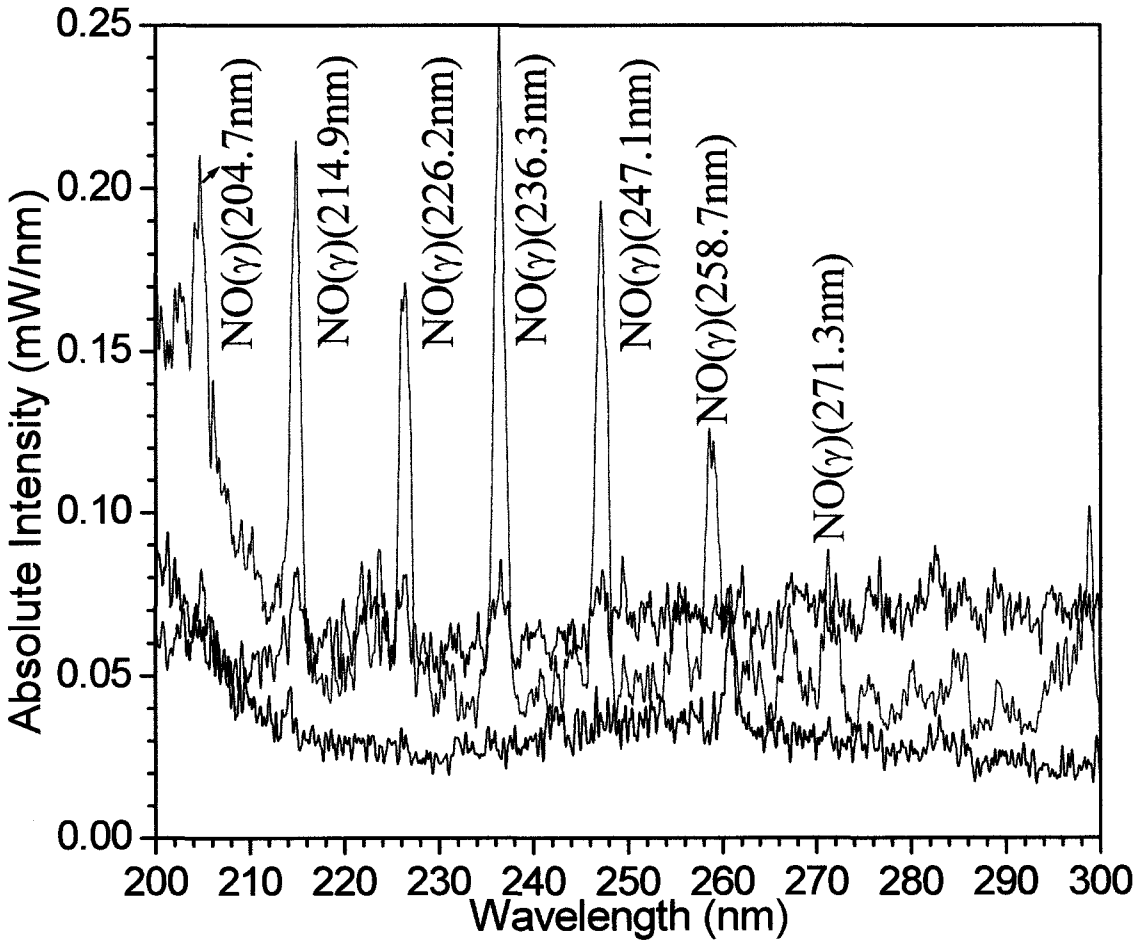


**Figure 3.5b: Absolute optical emission spectra in the 200-300 nm region for Ar-$H_2$ flow through slot microelectrodes of Figure 3.1 into open air. The upstream Ar flow rate is 14.0 slpm, while the $H_2$ admixture flow rate is either 0 sccm (black), 9.0 sccm (red) or 18.0 sccm (blue). Identified molecular transitions are labeled (see Table 3.2). The emission is dominated by NO(γ) bands, while no strong atomic lines are detected in this spectral region.**

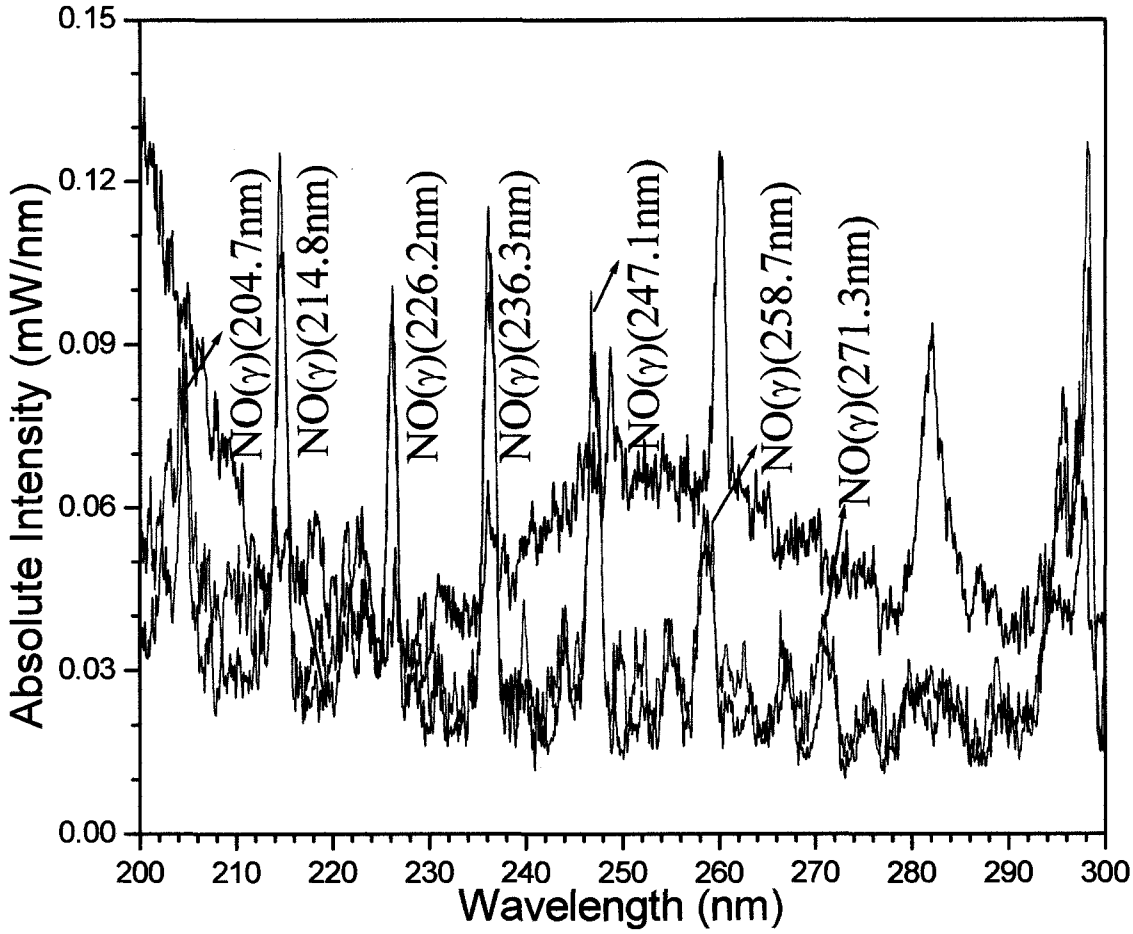


**Figure 3.5c: Absolute optical emission spectra in the 200-300 nm region for Ar-$H_2$ flow through slot microelectrodes of Figure 3.1 into open air. The upstream Ar flow rate is 9 slpm, while the $N_2$ admixture flow rate is 0.0 sccm (black), 5.0 sccm (red) or 10.0 sccm (blue). Identified molecular transitions are labeled (see Table 3.2). The emission is dominated by NO(γ) bands, while no strong atomic lines are detected in this spectral region.**

3.3.2 Optical Emission Spectra, $I(\lambda)$, in the 200-300 nm region

For each of the three gas mixtures, the optical emission intensity in the 200-300 nm region is relatively weak as compared to the 110-200 nm and 300-400 nm regions. Figure 3.5a shows emission spectra in the 200-300 nm region for helium gas flow with varying hydrogen addition. The strongest emission line intensities are significantly less than those observed in the 110-200 nm (by ~30 times) and 300-400 nm (by ~15 times) regions. In the 200-300 nm region the strongest $I(\lambda)$ detected features are the different

vibrational bands of the NO-γ system (A-X), see Table 3.2 and Figures 3.5a-c & 3.8a-c. Strong atomic lines are entirely absent. Metastable $N_2$ ($A\ ^3\Sigma_u^+$) serves as a precursor to NO formation (R9) (both ground and excited states) as has been concluded in several other investigations [10, 30-35].

$$N_2\ (A\ ^3\Sigma_u^+) + O_2 = 2\ NO(X\ ^2\Pi) \qquad \text{R3.9a}$$

$$N_2\ (A\ ^3\Sigma_u^+) + O(^3P) = NO(X\ ^2\Pi) + N(^4S) + 2.9eV \qquad \text{R3.9b}$$

$$N_2\ (A\ ^3\Sigma_u^+) + O(^3P) = NO(X\ ^2\Pi) + N(^2D) + 0.5eV \qquad \text{R3.9c}$$

$$N_2\ (A\ ^3\Sigma_u^+) + NO(X\ ^2\Pi) = NO(A\ ^2\Sigma^+) + N_2(X\ ^1\Sigma) \qquad \text{R3.9d}$$

$$NO(A\ ^2\Sigma) = NO(X\ ^2\Pi) + h\nu \qquad \text{R3.9e}$$

The decrease in intensity of the NO-γ bands for higher $H_2$ flows (18 and 37 sccm) in Fig. 3.5a reaffirms the proposed quenching of $N_2(A\ ^3\Sigma_u^+)$ level by H atoms postulated above.

**Table 3.2: Observed molecular transitions in the 200-300 nm region from the slot microelectrodes of Figure 3.1 into open air. The energy of the upper state NO (A, v=0) is ~5.46eV, while the upper state of the hydrogen continuum is in the range ~2.5-10.3 eV.**

| Excited Species | Wavelength(nm) | Transition | vibrational levels(v'-v") |
|---|---|---|---|
| NO | 204.70 | $NO(A\ ^2\Sigma^+,v'- X,v")$ | 2-0 |
| NO | 214.86 | $NO(A\ ^2\Sigma^+,v'- X,v")$ | 1-0 |
| NO | 226.24 | $NO(A\ ^2\Sigma^+,v'- X,v")$ | 0-0 |
| NO | 236.27 | $NO(A\ ^2\Sigma^+,v'- X,v")$ | 0-1 |
| NO | 247.07 | $NO(A\ ^2\Sigma^+,v'- X,v")$ | 0-2 |
| NO | 258.69 | $NO(A\ ^2\Sigma^+,v'- X,v")$ | 0-3 |
| NO | 271.26 | $NO(A\ ^2\Sigma^+,v'- X,v")$ | 0-4 |
| $H_2$ | ~120-400 | $H_2(a\ ^3\Sigma_g^+ - b\ ^3\Sigma_u^+)$ | - |

Fig.3.6 shows a weak continuum in the Ar-$H_2$ discharge that is observed in the range 200-350 nm for Ar-$H_2$ flows, with three hydrogen admixture concentrations (0, 18 and 37 sccm) of $H_2$. The continuum is not detected with other flow gases. Many

researchers attribute its formation to Penning excitation of molecular hydrogen by argon

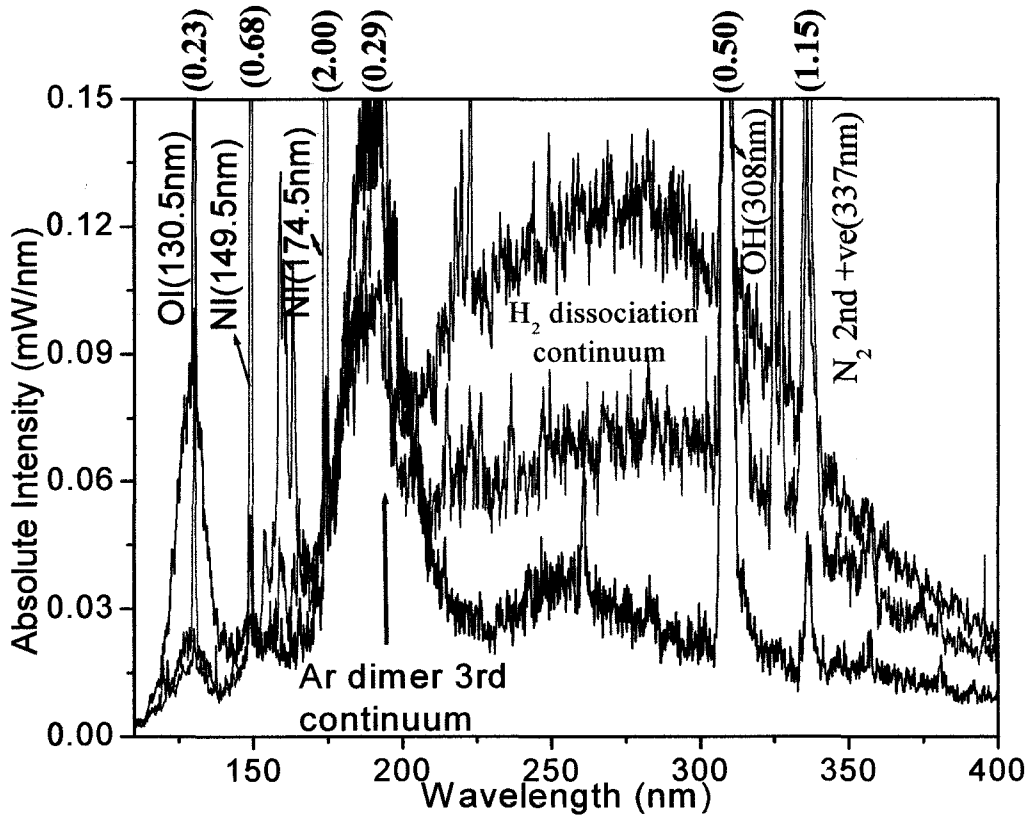


**Figure 3.6: Absolute optical emission spectra in the 100-400 nm regions for Ar-$H_2$ flow through slot microelectrodes of Figure 3.1 into open air. The upstream Ar flow rate is 14.0 slpm, while the $H_2$ admixture flow rate is either 0 sccm (black), 18.0 sccm (red) or 37.0 sccm (blue). A weak continuum originating from $H_2$ dissociation is present. Identified transitions are labeled (see Tables 3.11-3.3) and peak intensities (for the admixtures yielding the largest peaks) are shown in parentheses for cases where the peak exceeds the top of the graph.**

metastables (R3.10a), followed by de-excitation through a repulsive state (R3.10b) [36, 37], see Table 3.2. As the hydrogen concentration increases, the first reaction increases causing the continuum to increase. Note that the energy required to excite to $H_2(a\ ^3\Sigma_g^+)$ is 0.07 eV more than the energy of $Ar(^3P_0)$, the excess energy is supplied by kinetic motion (thermal energy) [36]. Since this process is endothermic, in the collisional microplasma, it is possible that the other high lying states of argon (between 11.79 eV and 14.7 eV) have considerable contribution in the $H_2$ dissociation continuum [38, 39].

$$Ar(^3P_0) \text{ or } Ar^* + H_2(X\ ^1\Sigma_g^+) \longrightarrow Ar + H_2(a\ ^3\Sigma_g^+) \qquad \text{R3.10a}$$

$$H_2(a\ ^3\Sigma_g^+) \longrightarrow H_2(b\ ^3\Sigma_u^+) \longrightarrow H(^2S) + H(^2S) \qquad \text{R3.10b}$$

(Ar* represents excited states of argon that lies above the minimum energy required to form $H_2(a\ ^3\Sigma_g^+)$ and below the minimum energy required to form $Ar_2^+$ i.e. between 11.79 and 14.7 eV ) [39].)

**Table 3.3: Observed atomic and molecular transitions in the 300-400 nm region from the slot micro-electrodes of Figure 3.1 into open air. The upper state energy for the He transition is 23.01eV. For the (0,0) vibrational bands, the energy levels for OH($A\ ^2\Sigma^+$), NH($A\ ^3\Pi$), $N_2(C\ ^3\Pi_u)$ and $N_2^+(B\ ^2\Sigma_u^+)$ are approximately 3.7, 4, 11 and 18.85 eV respectively (relative to their neutral ground states).**

| Excited Species | Wavelength(nm) | Transition | Vibrational Levels |
|---|---|---|---|
| He | 388.86 | $2p\ ^3P^O$-$2s\ ^3S$ | - |
| OH | 308.00 | OH($A\ ^2\Sigma^+$- $X\ ^2\Pi$) | 0-0 |
| NH | 336.00 | NH ($A\ ^3\Pi$ - $X\ ^3\Sigma^-$) | 0-0 |
| $N_2$ (2nd Positive) | 315.80 | $N_2$ ($C\ ^3\Pi_u$ - $B\ ^3\Pi_g$) | 1-0 |
| $N_2$ (2nd Positive) | 337.00 | $N_2$ ($C\ ^3\Pi_u$ - $B\ ^3\Pi_g$) | 0-0 |
| $N_2$ (2nd Positive) | 353.56 | $N_2$ ($C\ ^3\Pi_u$ - $B\ ^3\Pi_g$) | 1-2 |
| $N_2$ (2nd Positive) | 357.58 | $N_2$ ($C\ ^3\Pi_u$ - $B\ ^3\Pi_g$) | 0-1 |
| $N_2$ (2nd Positive) | 375.42 | $N_2$ ($C\ ^3\Pi_u$ - $B\ ^3\Pi_g$) | 1-3 |
| $N_2$ (2nd Positive) | 380.38 | $N_2$ ($C\ ^3\Pi_u$ - $B\ ^3\Pi_g$) | 0-2 |
| $N_2^+$ (1st Negative) | 391.40 | $N_2^+$($B\ ^2\Sigma_u^+$ -$X\ ^2\Sigma_g^+$) | 0-0 |
| $N_2^+$ (1st Negative) | 356.10 | $N_2^+$($B\ ^2\Sigma_u^+$ -$X\ ^2\Sigma_g^+$) | 2-1 |

**Table 3.4: Key energy levels and associated state notations of atomic helium and argon metastables and the molecular $N_2(A)$ metastable.**

| Metastable State | Energy (eV) |
|---|---|
| He ($2s\ ^1S_0$) | 20.61 |
| He ($2s\ ^3S_1$) | 19.82 |
| Ar ($^3P_0$) | 11.55 |
| Ar ($^3P_2$) | 11.72 |
| $N_2(A)$ | ~6.2eV |

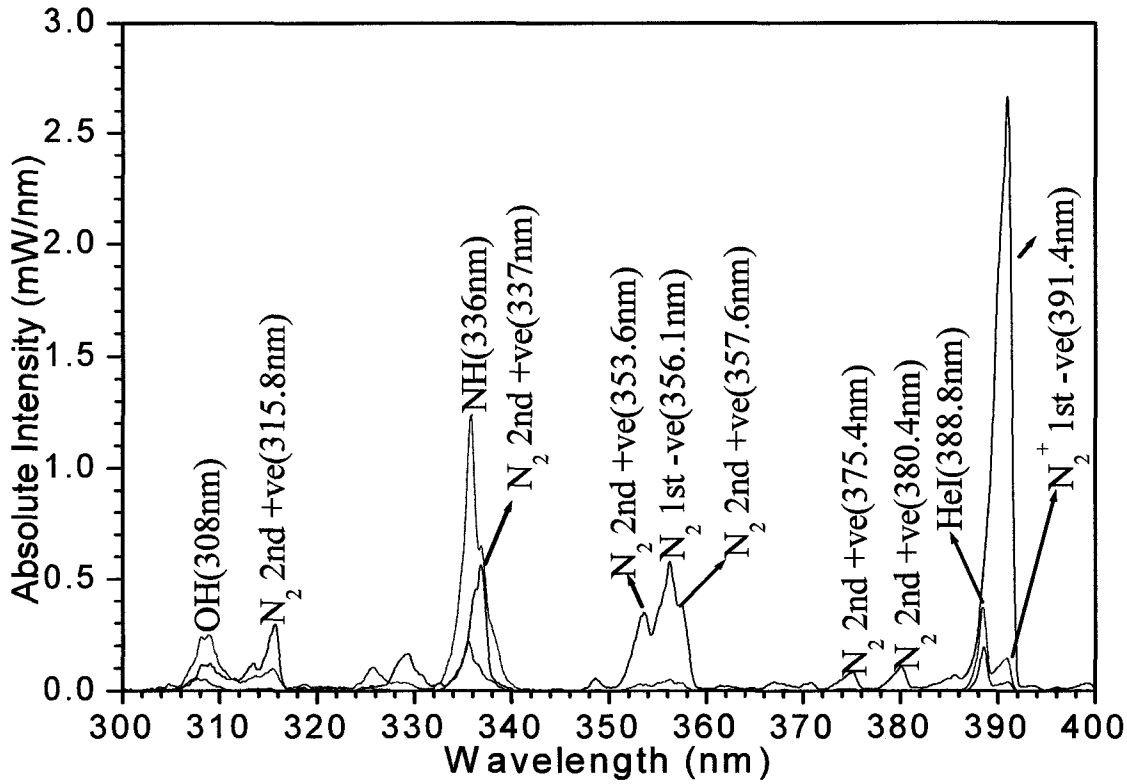


**Figure 3.7a: Absolute optical emission spectra in the 300-400 nm regions for He-$H_2$ flow through slot microelectrodes of Figure 3.1 into open air. The upstream He flow rate is 2.0 slpm, while the $H_2$ admixture flow rate is 9.0 sccm (black), 18.0 sccm (red) or 37.0 sccm (blue). Identified OH, $N_2$, NH and $N_2^+$ transitions are labeled (see Table 3.4).**

3.3.3 Optical Emission Spectra in the 300-400 nm region

Absolute optical emission spectra in the 300-400 nm region for helium with addition of varying hydrogen flows are shown in Figure 3.7a, with transitions listed in Table 3.3. Spectra in this region for argon with addition of hydrogen and nitrogen are similar (Figure 3.7b,c) with salient differences given below. The strongest lines originate from $N_2$, NH molecules, and the OH radical. The feature at 308 nm is from the OH($A\ ^2\Sigma^+$-$X\ ^2\Pi$) transition [40, 41], whose formation is attributed to the presence of water vapor (either from ambient air or as a feed gas impurity). In the vicinity of 336 nm, emission from the NH($A\ ^3\Pi(v'=0)$ -$X\ ^3\Sigma^-(v''=0)$) band [42] is observed for hydrogen admixtures of >18 sccm in He-$H_2$ and Ar-$H_2$ gas flow micro-plasmas respectively.

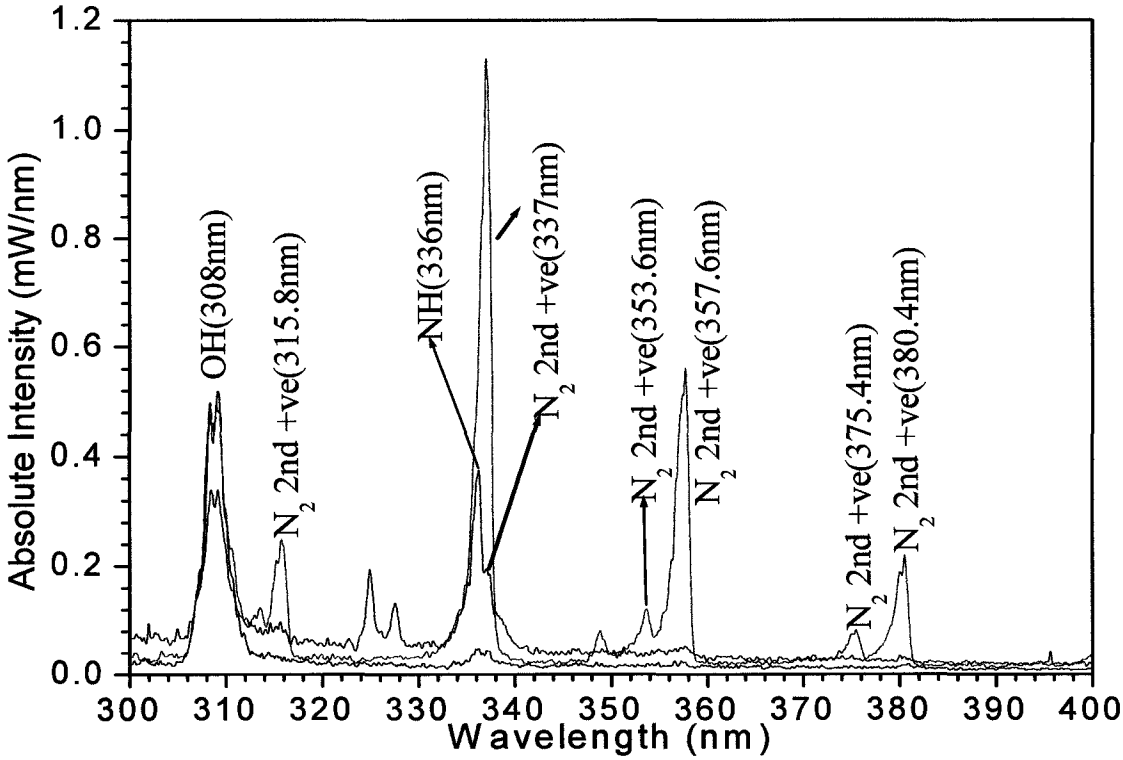


**Figure 3.7b: Absolute optical emission spectra in the 300-400 nm region for Ar-$H_2$ flow through slot microelectrodes of Figure 3.1 into open air. The upstream Ar flow rate is 14.0 slpm, while the $H_2$ admixture flow rate is either 0 sccm (black), 9.0 sccm (red) or 18.0 sccm (blue). Identified OH, NH and $N_2$ transitions are labeled (see Table 3.4).**

Prominent molecular nitrogen lines in the 300-400 nm spectral region include bands from the second positive $I(\lambda)$ systems ($N_2(C\ ^3\Pi_g - B^3\Pi_g)$) at 315.8, 337.0, 353.6, 375.4 and 380.4 nm and from the first negative system of $N_2^+(B\ ^2\Sigma_u^+ - X\ ^2\Sigma_g^+)$ near 391.4 nm. Formation of excited molecular nitrogen states (and 2nd positive emission) arises from electron impact excitation and via energy pooling mechanisms involving the $N_2(A^3\Sigma_u^+)$ [10, 43] metastable state of molecular nitrogen (R 3.11c).

$$N_2(X\ ^1\Sigma_g^+) + e\ (fast) = N_2(C\ ^3\Pi_g) + e \qquad R3.11a$$

$$N_2\ (A\ ^3\Sigma_u^+) + e\ (slow) = N_2(C\ ^3\Pi_g) + e \qquad R3.11b$$

$$N_2(A\ ^3\Sigma_u^+) + N_2(A\ ^3\Sigma_u^+) = N_2(C\ ^3\Pi_g) + N_2(X\ ^1\Sigma_g^+) \qquad R3.11c$$

$$N_2(C\ ^3\Pi_g) = N_2(B\ ^3\Pi_g) + h\nu_{2nd\ pos.} \qquad R3.12$$

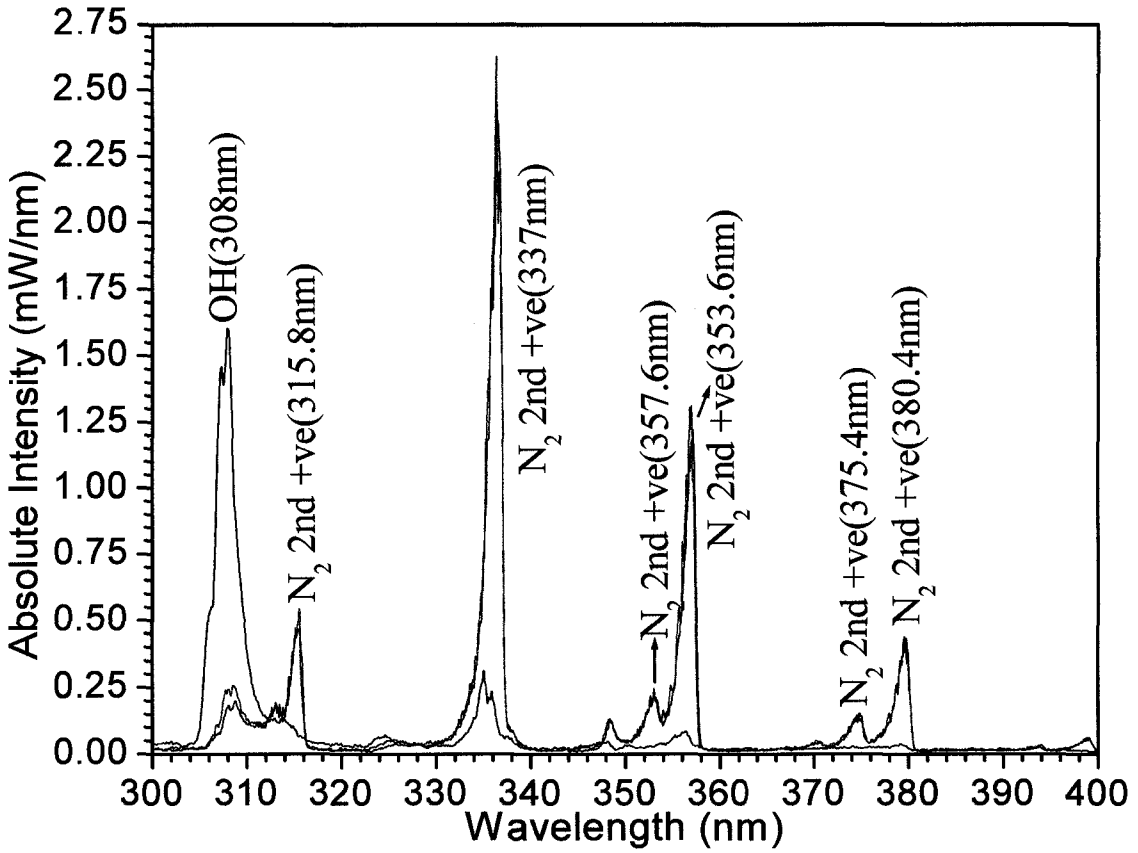


**Figure 3.7c: Absolute optical emission spectra in the 300-400 nm region for Ar-$N_2$ flow through slot microelectrodes of Figure 3.1 into open air. The upstream Ar flow rate is 9 slpm, while the $N_2$ admixture flow rate is 0.0 sccm (black), 5.0 sccm (red) or 10.0 sccm (blue). Identified OH, $N_2$ and NH transitions are labeled (see Table 3.4).**

Also, note that in argon plasmas (on an energetic basis alone) argon metastables can selectively form higher excited states of nitrogen ($N_2(C)$ and $N_2(B)$) via two body collisions that cascade radiatively down to $N_2(A)$ level [44, 45]; however, this is not thought to be the major contributor in pure Ar or in Ar-$H_2$ microplasmas since the 2nd positive band of $N_2$ is relatively weak (Figure 3.7b). We also note that no discernible emission of the 1st positive bands are observed in the UV/VUV emission or in the visible region (Chapter 4). This is probably because in the atmospheric pressure plasma the $N_2(B)$ state (origin of 1st positive emission band) decays non radiatively (i.e. by quenching because, the life time of $N_2(B)$ state is of the order of few microseconds [46] as compared to 36 nanoseconds of the $N_2(C)$ state [47]).

This pooling mechanism conjecture is consistent with the observation of decreased $I(\lambda)$ emissions with increased hydrogen addition (see Fig. 3.7a) since atomic hydrogen quenches the $N_2(A^3\Sigma_u^+)$.

Strong bands of the first negative system of $N_2^+(B\ ^2\Sigma_u^+\text{-}X\ ^2\Sigma_g^+)$ are only observed in helium-hydrogen plasmas and not in the argon-hydrogen or argon-nitrogen plasmas. In the helium plasmas the molecular nitrogen ions are energetically accessible through collisions with helium metastables (He [2s $^3S_1$, 2s $^1S_0$]), while argon metastables (in the argon plasmas) have insufficient energy to create $N_2^+$ levels, see Table 3.4. Electron impact of slow electrons with $N_2^+(X)$ may also contribute to formation of excited nitrogen ions $N_2^+(B)$ [47, 48], though we do not believe this to be the case since we do not see strong emission lines from excited He ($n \geq 4$) in measured visible spectra. (If slow electrons are responsible for forming $N_2^+$ (B), then one would expect to also populate the upper states of He, owing to the similarity in energy spacing and electron impact cross-sections [49, 50] for formation of these states.) For the analogous reasons, we do not believe that slow electrons are responsible for the formation of $N_2(C)$. A full treatment of excitation and de-population of these states using collisional-radiative modeling is required to fully address these questions, but is beyond the scope of the current work.

The observed spectral emission of the He I line (2p $^3P^O$-2s $^3S$) at 388.8 nm in Figure 3.7a is a clear indication of He metastable (2s $^3S_1$) formation. This mechanism would be consistent with the decrease in $N_2^+$ first negative emission as hydrogen is added, since hydrogen can effectively quench the helium metastables [51, 52].

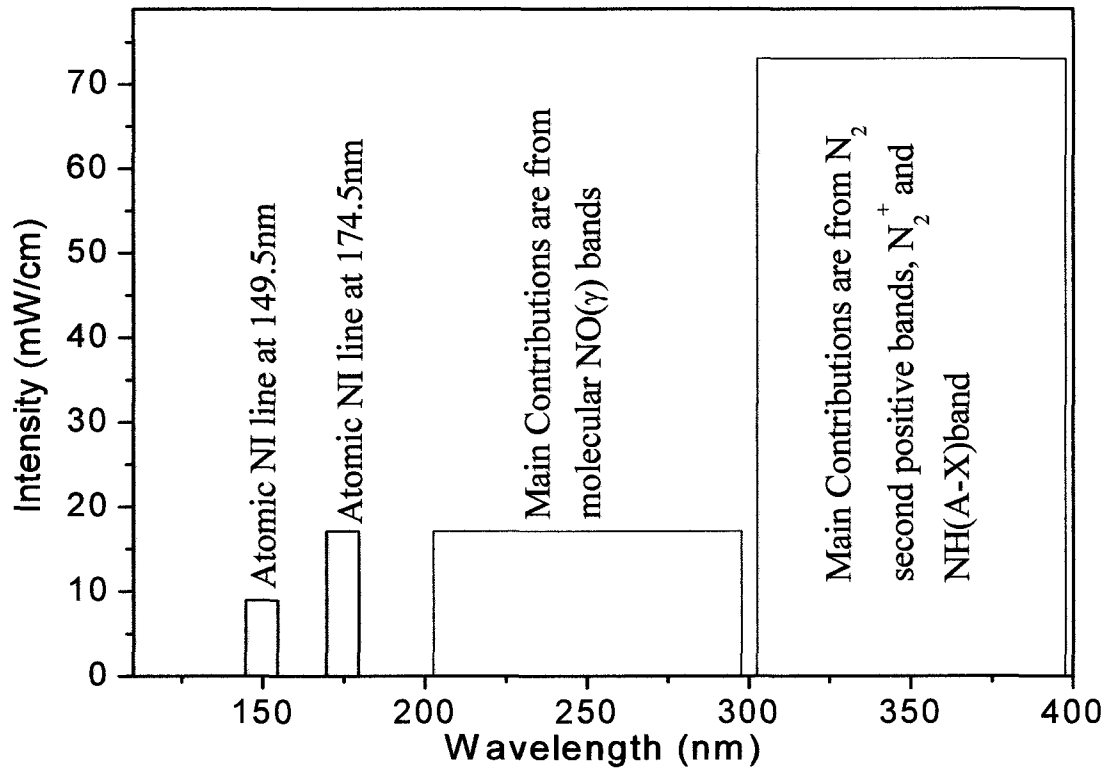


**Figure 3.8a: Summary of key atomic and molecular species generating 150-400 nm optical emission from slot microelectrodes of Figure 3.1 into open air. The plot shows the (spectrally integrated) optical output power per unit slot length for an upstream He flow rate of 2.0 slpm and $H_2$ admixture flow rate of 9.0 sccm.**

3.3.4 Summary of Optical Emission Spectra, $I(\lambda)$, from 110-400 nm

The measured emission spectra are summarized in Figure 3.8a-c for the microplasma operating with He-$H_2$, Ar-$H_2$, and Ar-$N_2$ respectively (flow rates in Figure captions). For Figures 3.8a-c, we have integrated the spectral contributions of the emission features, and we present these plots with units of mW/sr per cm of slot length. We find that in the wavelength region 110-200 nm, atomic lines, particularly nitrogen, dominate the emission. In the 200-300 nm region, the optical power is approximately half that of the 100-200 nm region, and is primarily from NO (γ) bands. The total emitted optical power is highest in the 300-400 nm region and is primarily from molecular nitrogen ($N_2$ (C-B), molecular nitrogen ions ($N_2^+$ (B-X)), and molecular NH (NH (A-X)). The variation in output power over the three wavelength regions are shown in Figure 3.8a-c.

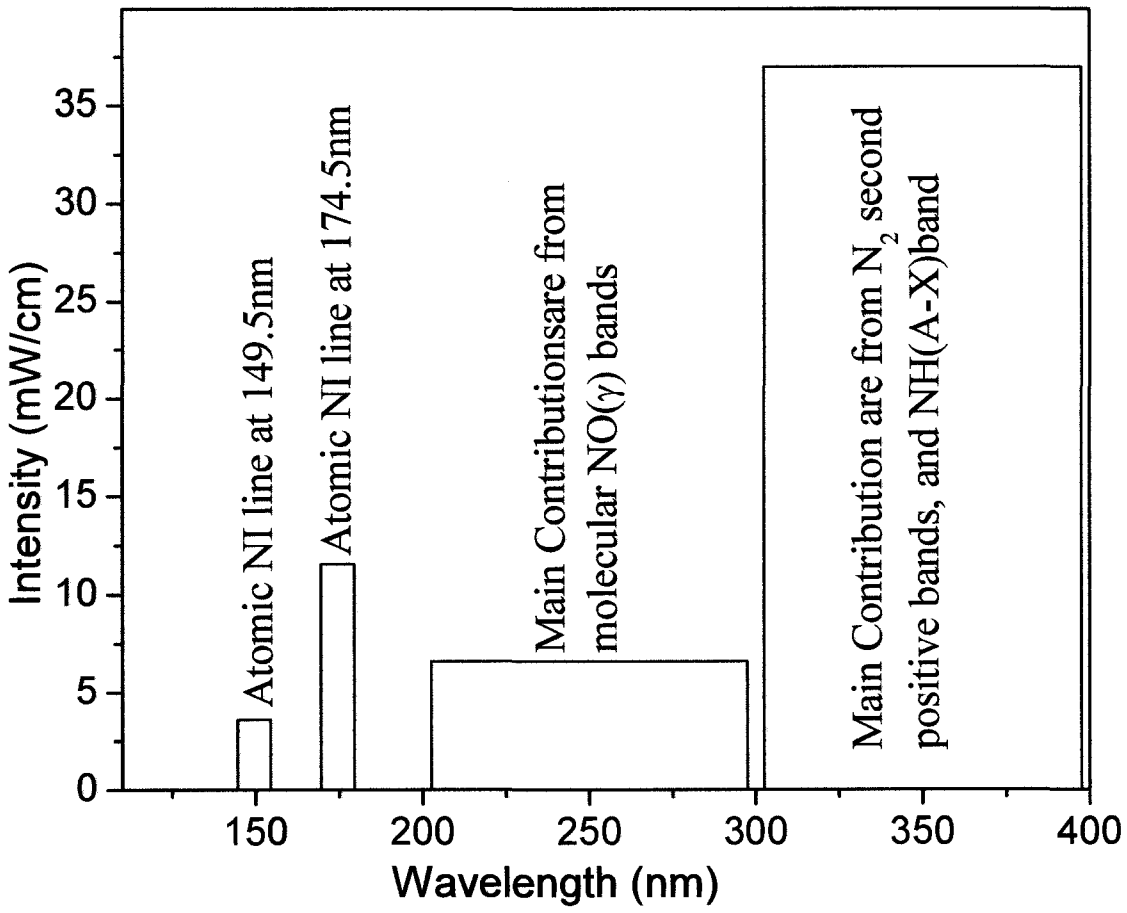


**Figure 3.8b: Summary of key species generating optical emission in the 150-400 nm regions for specified upstream gas flow through slot microelectrodes of Figure 3.1 into open air. The plot shows the (spectrally integrated) optical output power per unit slot length for Ar flow rate of 14.0 slpm and $H_2$ admixture flow rate of 9.0 sccm.**

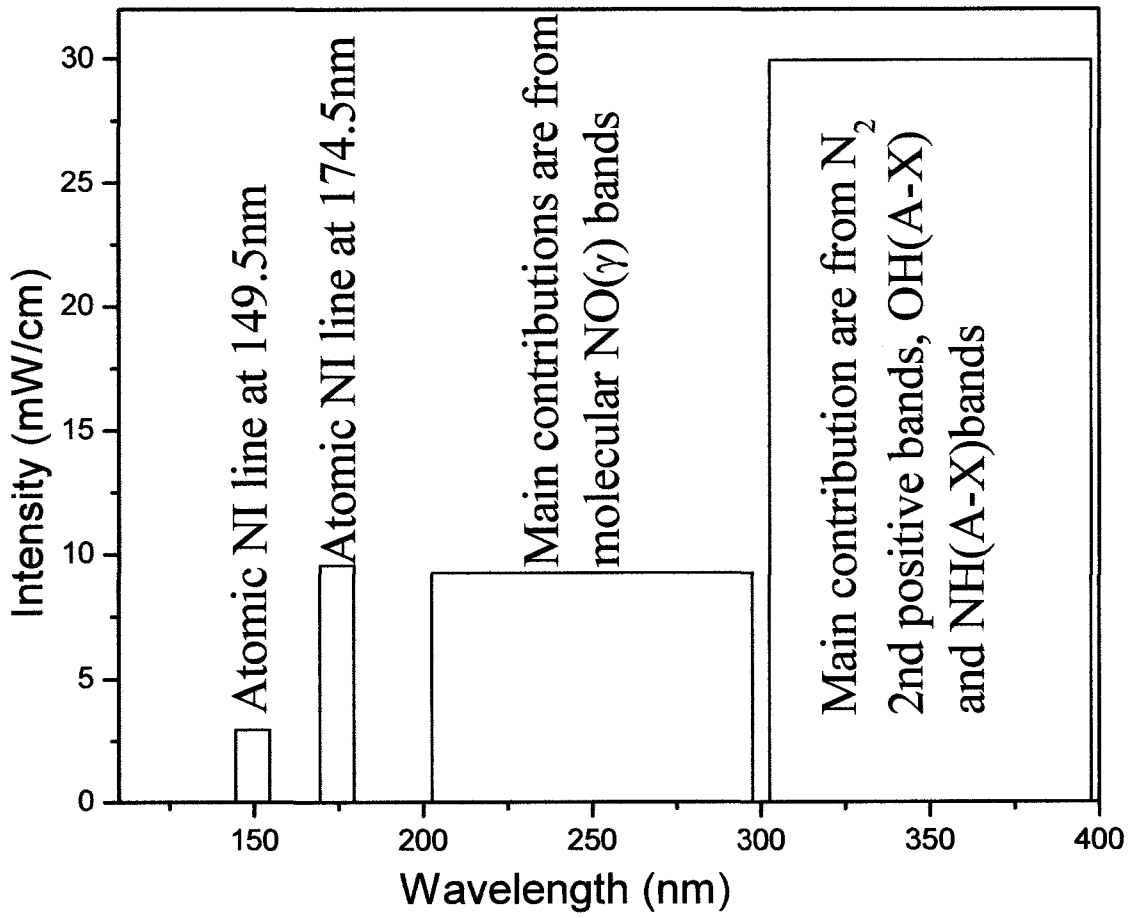


**Figure 3.8c: Summary of key species generating optical emission in the 150-400 nm regions for specified gas flow through slot microelectrodes of Figure 3.1 into open air. The plot shows the (spectrally integrated) optical output power per unit slot length for an upstream Ar flow rate of 9.0 slpm and $N_2$ admixture flow rate of 5.0 sccm.**

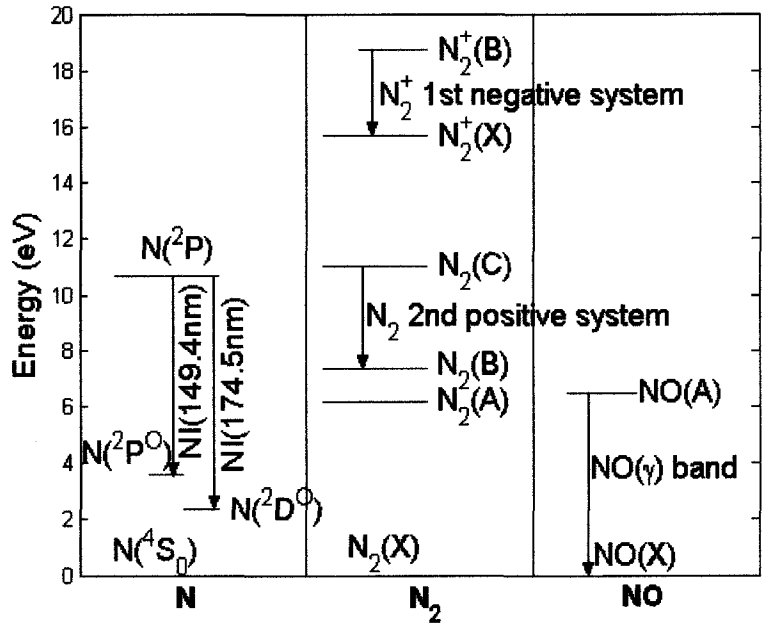


**Figure 3.9. Partial Grotrian diagrams showing key energy levels of $N_2$ and NO molecules and of N atom for micro-discharge in open air. The vertical axis gives energies in eV while the horizontal axis is separated into N, $N_2$ and NO regions. Downward pointing arrows are radiative decays observed from our micro-discharge device.**

### 3.4 Gas Temperature ($T_g$) Measurement

Owing to fast collisional relaxation at atmospheric pressure, the rotational temperature, $T_{rot}$, may be used as an accurate measure of the translational gas temperature, $T_g$

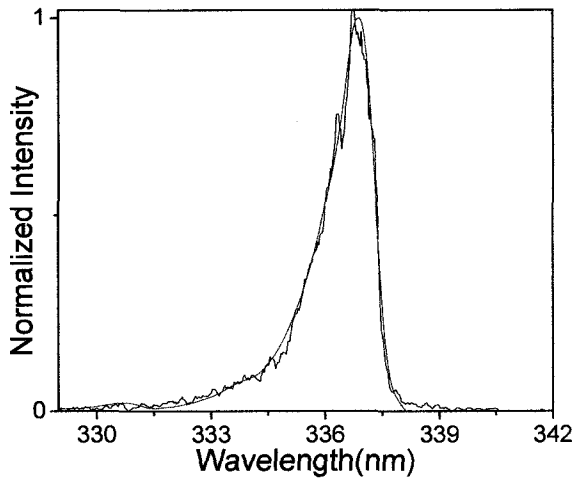


**Figure 3.10: Optical emission spectra from the (0,0) band of the nitrogen 2nd positive system $N_2$ ($C\ ^3\Pi_g$ - $B^3\Pi_g$). Conditions are 14 slpm flow of Ar and 9 sccm flow of $H_2$. Black curve is experimental data, while blue curve is SpecAir simulation for 750 K (the best-fit rotational temperature).**

[53]. Depending on specific plasma conditions a number of molecular bands may be used to measure rotational temperature (e.g. [54]). Here, we have used the (0,0) vibrational band of the second positive system of $N_2(C\ ^3\Pi_g - B^3\Pi_g)$ in the vicinity of 337 nm for determination of gas temperature ($T_g$). In principle, a Boltzmann fitting approach may be used to determine $T_{rot}$ (rotational temperature), but we have opted to use the SpecAir spectral code, which models emission intensities for a host of atomic and molecular transitions and has been extensively verified [55]. By finding the best match between our measured spectrum and that predicted by Specair for different rotational temperatures (using our experimentally measured slit function) we infer a best-fit temperature. For argon plasmas, depending on the magnitude of the hydrogen and nitrogen additive flows, the 337 nm second positive feature suffers from interference with $N_2^+$ emission ($1^{st}$ negative). In cases that are relatively free[11] of interference, we find a rotational temperature of 650 +/- 100 K. Figure 3.10 shows the measured second positive system of $N_2$ ($C\ ^3\Pi_g - B^3\Pi_g$) in the vicinity of 337 nm, as well as that predicted by SpecAir for a rotational temperature of 650 K. Spectral overlap with strong NH emission at 336 nm has prevented us from using this same method with the He plasmas. The current temperature measurement is based on all the light collected from the plasma and its accuracy may suffer from line-of-sight effects which favor the active plasma region. In the future we will perform spatially resolved measurements of the gas temperature using more complex imaging techniques. Clearly, from the point of view of most processing applications, a relatively low gas temperature is desirable.

[11] There is small interference from NH (0-0) emission band at 336 nm, therefore, the estimated temperature, $T_g$, is an upper limit.

### 3.5 Vibrational temperature measurement, $T_v$

Open air operation of the microdischarge allows ambient species to mix into the plasma region. Figures 3.3-3.7 show the presence of numerous atomic emission and molecular bands from nitrogen. The vibrational temperature of molecular nitrogen, $T_v$, may be determined from the relative contributions of vibrational bands of molecular nitrogen and molecular nitrogen ion bands.

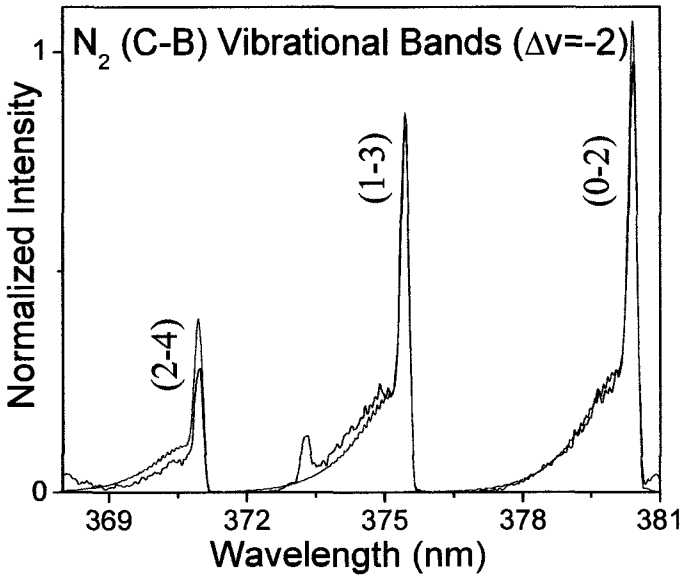


**Figure 3.11a: Optical emission spectra from the Δv=-2 bands of the nitrogen 2nd positive system $N_2(C\ ^3\Pi_g - B^3\Pi_g)$. Conditions are 2 slpm flow of He and 10 sccm flow of $N_2$. Black curve is experimental data, while blue curve is SpecAir simulation for 4800 K (the best-fit vibrational temperature).**

We use the Δv = -2 bands of the second positive $N_2(C\ ^3\Pi_g - B^3\Pi_g)$ in the region 370 nm to 380 nm to determine the vibrational temperature. Similar to the gas temperature measurement (discussed above), the best match between the SpecAir spectral code and the optical measurement is used to determine vibrational temperature of molecular nitrogen. The best match for the vibrational temperature is found to be 4800 K ± 200 K (Figure 3.11), consistent with $T_r<T_v<T_e$ as is typical in nonequilibrium plasma. It can be seen that the vibrational distribution does not follow a pure Maxwellian distribution. The

discrepancy is due to different mechanisms (R3.11a-c) involved in populating the $N_2$ (C $^3\Pi_g$) state. It is known that the pooling mechanism is state specific and a population inversion is expected between the v'=0 and v'=1 state when these levels are populated solely by energy pooling mechanism [47, 56, 57].

It is expected that the vibrational temperature of molecular nitrogen ion be similar to that of the molecular nitrogen. Two methods have been employed to determine the $N_2^+$ vibrational temperature, they are,

i. fitting of SpecAir code with the $\Delta v = -2$ series of the first negative bands, and

ii. peak intensity ratio method using the 0-0 and 2-1 vibrational bands of $N_2^+$(B-X).

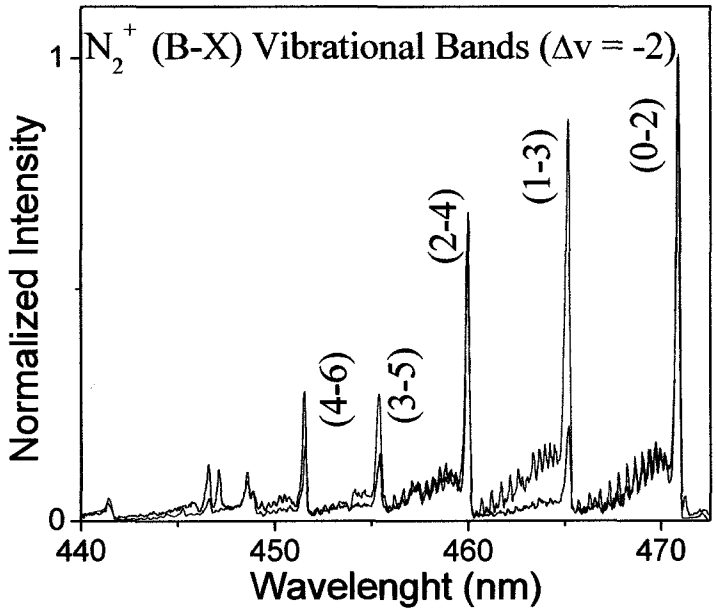


**Figure 3.11b: Optical emission spectra from the $N_2^+$(B-X) $\Delta v = -2$ bands of the 1st negative system . Conditions are 2 slpm flow of He and 10 sccm flow of $N_2$. Black curve is experimental data, while blue curve is SpecAir simulation for 4400 K (the best-fit vibrational temperature).**

The vibrational temperature estimation employing SpecAir fitting to the $N_2^+$(B-X) ($\Delta v = -2$ series) optical emissions is 4800 K which is very close to the vibrational temperature estimated using the vibrational bands of $N_2$(C-B) transition. Note that in determining the vibrational temperature using $N_2^+$(B-X) $\Delta v = -2$ series, we fit only two

vibrational bands, namely the 0-2 and 2-4 bands, because the observed intensities of $N_2^+$(B-X) vibrational transitions in the $\Delta v = -2$ series show highly non-Boltzmann characteristics (Fig. 12). This behavior opposes the earlier observation of Boltzmann like distribution while determining the vibrational temperature from the $\Delta v = -2$ series of $N_2$(C-B) 2nd positive bands. The work of Benedictis et al [48] showed Boltzmann like distribution for the $\Delta v = -2$ series of $N_2^+$(B-X) transitions. Note that in the work of Benedictis et. al. [48], He-$N_2$ plasma was generated at low pressure. Therefore population of the $N_2^+$(B) state is primarily due to electron impact excitation mechanisms and the metastables of $N_2$ or He do not have any major impact on the $N_2^+$(B) state. The Boltzmann like characteristics of the electron energy distribution thus ensures the Boltzmann distribution of the $N_2^+$(B) vibrational levels in their plasmas. Since lifetime of the excited $N_2^+$(B) is very small (59 ns) [48, 50], collisional effect is discarded. We believe this highly non-Boltzmann characteristic is due to rotational perturbation of the $N_2^+$(B) vibrational levels (v' = 0, 1, 3, 5, 9, and 13) by the $N_2^+(A\ ^2\Pi_u)$ state and these perturbed states can suffer a decrease (or increase) in population densities [58]. Here it is assumed that the effect of perturbation by the $N_2^+(A\ ^2\Pi_u)$ state causes the decrease in the intensities of the 1-3 and 3-5 vibrational bands. It is likely that the 0-2 band is not affected because the crossing occur at high rotational levels.

The vibrational temperature of the $N_2^+$(B-X) has also been calculated from the ratio of the peak intensities of the $N_2^+$(B-X) 2-1 band to the 0-0 band [55] in the He-$N_2$ discharge. The vibrational bands at 391 nm (0-0) and at 356 nm (2-1) are chosen because they are free of interferences (from other bands). Note that this calculation is based on the experimental data obtained from visible emission spectra measurements (Chapter 4). The

spectrometer used for visible emission data acquisition has better resolution and helps to detect the first negative 2-1 vibrational band without interference from the neighboring 2nd Positive vibrational bands of $N_2$.

Equation 3.1 shows the dependence of the vibrational temperature on the ratio of the peak intensities (see Appendix A for details).

$$\frac{I_{21}^{P}}{I_{00}^{P}} = \frac{A_{21}}{A_{00}}\left[\exp\left(-\frac{hc}{k}\frac{G(2)-G(0)}{T_v}\right)\right]\frac{\sum_{2-1} SL_{21}\alpha_j^P S_J^P P_{21}(J)\exp\left[\left(-\frac{hc}{k}\right)\frac{F_2(J-1)}{T_r}\right]}{\sum_{0-0} SL_{00}\alpha_j^P S_J^P P_{00}(J)\exp\left[\left(-\frac{hc}{k}\right)\frac{F_0(J-1)}{T_r}\right]} \qquad 3.1$$

The summation is over the slit function for which the total number of rotational contributions are considered for each of the vibrational transitions. The slit function during our experiments had a maximum width at the top and bottom bases (Appendix B) are 0.48 nm and 0.9 nm respectively. The number of the rotational levels considered here are 28 and 32 for the 0-0 band and 2-1 bands respectively. The difference in the number levels for the two bands is due to different spacing of the rotational levels. Note that the ratio of the peak intensities of these vibrational bands depend both on the rotational temperature ($T_r$) and vibrational temperature ($T_v$). The ratio of these bands for different $N_2$ concentrations with 2 slpm He flow rate are given in Table 5. Figure 3.12 shows the simulated value of the ratio of the peak intensities of the two bands at different rotational temperature ( $T_r$ = 400, 500 and 600 K). Figure 3.12 shows that the peak intensity ratio is only a weak function of the rotational temperature. Comparing the optical measurements (black squares) with the simulated values (circles), the obtained vibrational temperature yields a value of ~ 4600+/-200 K and indicates that the rotational temperature, $T_{rot}$, is closed to 400 K, which is consistent with our earlier statement that the estimated rotational

temperature (650 +/- 100 K) is an upper limit. This vibrational temperature is very consistent with the value (4800 K) obtained by fitting the optical data with SpecAir code.

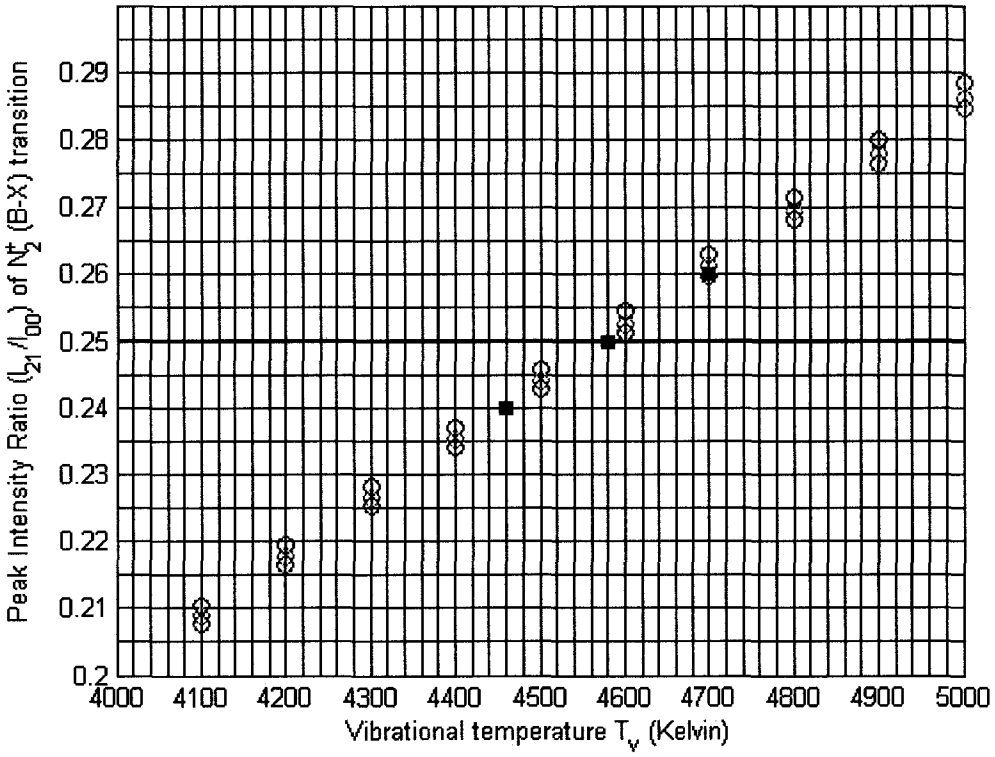


**Figure 3.12: Peak intensity ratio of 2-1 to 0-0 vibrational bands ($N_2^+$(B-X) ) vs. the vibrational temperature. Circles represents the simulated vibrational temperatures for different rotational temperatures (400 K(red), 500 K (green) and 600 K (blue)). The black squares represent experimental value.**

**Table 3.5: Intensity ratio of 2-1 and 0-0 1st positive vibrational bands of $N_2^+$(B-X) transition of He-$N_2$ microplasma. He flow rate is 2 slpm, $N_2$ flow rate varies (5 sccm, 10 sccm and 20 sccm).**

| $N_2$ flow rate (sccm) | $I_{21}/I_{00}$ | $T_v$ (K) |
|---|---|---|
| 5 | 0.23 | 4400 |
| 10 | 0.25 | 4600 |
| 20 | 0.26 | 4700 |

### 3.6 Comparison of Discharge Characteristics at 13.56 and 60 MHz RF Excitation

In this section we focus on studying spectral changes as a function of applied RF frequency. Representative absolute UV/VUV optical emission spectra from the hollow slot microplasma driven by RF frequencies of 13.56 and 60 MHz are shown in Figures

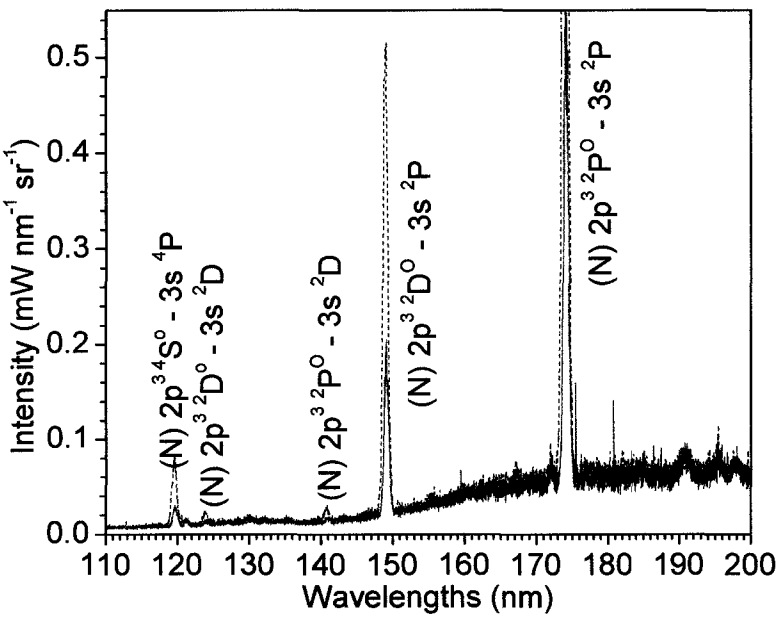


**Figure 3.13a: Absolute optical emission spectra of 13.56 MHz (red) and 60 MHz (blue) driven microplasmas in the 110-200 nm region for He-$N_2$ flow. The upstream He flow rate is 2.0 slpm, while the $N_2$ admixture flow rate is 20 sccm.**

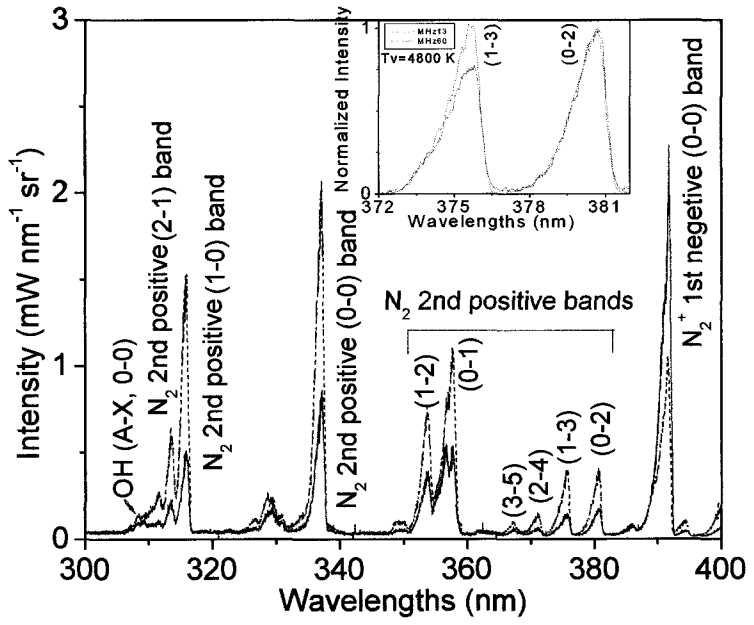


**Figure 3.13a: Absolute optical emission spectra of 13.56 MHz (red) and 60 MHz (blue) driven microplasmas in the 300-400 nm region for He-$N_2$ flow. The upstream He flow rate is 2.0 slpm, while the $N_2$ admixture flow rate is 20 sccm.**

3.13a,b. For both frequencies, the flow rates are 2 slpm He plus 20 sccm of $H_2$, and the delivered powered to the discharge is kept constant at 100 watts. Figure 3.13a shows that

the intensities of the atomic nitrogen transitions in the 110-200 nm region exhibit a distinct increase for RF frequency of 60 MHz as compared to 13.56 MHz. Spectra in the 300-400 nm region (Figure 3.13b) show that the intensity of the 2nd positive band of $N_2$ increases as the RF frequency is increased from 13.56 to 60 MHz, whereas the intensity of the 1st negative band of $N_2^+$ decreases. The increase of the atomic nitrogen emissions with RF frequency suggests an increase in mean electron energy as the upper states of these transitions are excited via electron impact processes [59].

Figure 3.13b shows an increase of nitrogen second positive emission with increased RF frequency. The upper state $N_2(C)$ of the nitrogen second positive emission is judged to be populated through pooling mechanisms involving the metastable $N_2(A)$ (reaction R1a) as well as electron impact excitation of $N_2(A)$ or of the ground state $N_2(X)$ (reactions R11). We also observe that at 60 MHz the ratio of emission from the band from v'=1 to the band from v'=0 increases substantially (see inset of Figure 3.13b). Past research has shown an inversion of these vibrational states associated with energy pooling of long lived metastable $N_2(A)$ states resulting in population of $N_2(C)$ states (reaction R3.11c) [47, 56, 57]. Therefore, the observed increase in second positive intensity and the observed population inversion are likely due to increases in both electron impact excitation reactions (R3.11a,b) and energy pooling reactions (R3.11c), both of which suggest an increase in electron energy (since $N_2(A)$ itself is formed from electron impact reactions).

In contrast to the $N_2(C)$ emission, the $N_2^+(B\text{-}X)$ emission intensities decrease as the RF frequency is increased. For helium gas glows, excitation to the first negative systems of $N_2^+$ is predominantly due to charge transfer mechanisms by helium ions and he-

lium dimer ions [60] and by Penning ionization by helium metastables [47, 60, 61]. (Direct electron impact of $N_2(X)$ is thought to be negligible since the $N_2$ partial pressure is small and the required electron energy is very high.) Increased electron energy quenches the metastables by secondary excitation/ionization processes thus reduces the Penning ionization of $N_2(X)$.

In section 3.4, gas temperature measurements at 13.56 MHz based on the (0,0) vibrational band of the second positive system of $N_2(C\ ^3\Pi_g - B^3\Pi_g)$ in the vicinity of 337 nm were reported [59]. For the 60 MHz operation, we have performed similar temperature measurement by finding the best agreement between measured spectra and simulated spectra (using the spectral simulation tool SPECAIR [62]). At both 13.56 and 60 MHz we find a rotational (gas) temperature of 650+/-100 K. The temperature measurement is path-integrated (so that it can not separate temperature in the plume and interelectrode region) and suffers from some interference from the NH (0-0) band at 336 nm.

**3.7 Comparison with Commercial Mercury Lamps**

We are interested in both the efficiency of generation and the relative magnitude of UV and VUV light production from the hollow slot microdischarges. We compare the microdischarge emission characteristics with well-understood commercial UV/VUV mercury lamps, as the latter provide an industrial/commercial benchmark. We calculate the efficiency and emitted optical power per unit area for the RF driven microdischarges and compare these values to those reported for commercial UV/VUV mercury lamps [63]. Results are presented in Table 3.6a and Table 3.6b, and are for case of the slot microdischarge operating with 2 slpm of helium flow with a hydrogen admixture of 9 sccm. Comparisons are made in both the UVB and UVC regions with the following mercury

lamps: Low Pressure Lamp (LPL), Amalgam Lamp (AL), and Medium Pressure Mercury Arc Lamp (MPMAL) [63]. In Table 3.6a we compare the emitter efficiencies of the slot microdischarge with those of the mercury lamps in the UVB and UVC regions.

**Table 3.6a: Efficiency comparison between UV emission from the open-air microelectrode device and emission levels from various commercial Hg lamps (see text) in the UVB and UVC region.**

| Range(nm) | Emitter Efficiency (η)% | | | |
|---|---|---|---|---|
| | RF micro-slot | LPL | AL | MPMAL |
| 100-290(C) | 0.16 | 35~40* | 30~35* | 8.7** |
| 290-320(B) | 0.03 | - | - | 7.6 |

**Table 3.6b: Comparison of total UV optical power/area emitted between microelectrode device and sealed commercial Hg lamps (see text) in the UVB and UVC region.**

| Range(nm) | Output optical power per unit area ($W/cm^2$) | | | |
|---|---|---|---|---|
| | RF micro-slot | LPL | AL | MPMAL |
| 100-290(C) | 1.07 (22.3) | 0.105~0.167* | 0.263~0.41* | 4.26** |
| 290-320(B) | 0.19 (4.0) | - | - | 3.72 |

* These values correspond to the narrow band of Hg at 254 nm.
** These values are for the wavelength region 200-290 nm.

Emitter efficiency is defined as the ratio of output optical power divided by supplied electrical power. For the microdischarge slot, the optical power is found by integrating our measured spectra (which assume $4\pi$ emission). The electrical power has been measured using RF probes from Advanced Energy. At the given conditions, the current for the microelectrode device is 0.12 A/cm of slot length, while the delivered electrical power to the microelectrode device is approximately 13.4 W per cm of slot length. We find that the emitter efficiencies (Table 3.6a) for the slot microdischarge are significantly (~200 times) lower than those for the benchmark mercury lamps. We anticipate that the emitted intensities (and thus efficiencies) may increase with our future electrode designs, which will focus the active discharge within the open-slot and allow more light from the active discharge region to be emitted through the slot.

Table 3.6b provides a comparison of the output optical power (per unit planform area) emitted from the slot micro-discharge together with benchmark mercury lamp output in UVB and UVC region. To obtain the total optical power per unit area from the slot micro-discharge, we divide the emitted optical power per unit length by the width of the slot (200 microns) and again assume isotropic ($4\pi$) emission. The isotropic assumption corresponds to an ideal (maximum emission) case, though we have yet to characterize the actual solid angle over which our slot microplasmas emit. Again, the values shown in the table correspond to discharge operation for a current of 0.12 A/cm. The values shown in parentheses correspond to a linear scaling of optical output for a current of 2.5 A/cm, which we have shown to be a stable operating condition [4]. For the industrially available Hg lamps, we take the total optical power per unit length and divide it by the lamp diameter. We find that the output powers (Table 3.6b) for the slot micro-discharge compare favorably with those for the mercury lamps, particularly in the UV-C region. For 0.12 A/cm operation, the RF driven micro-discharge UVC intensity exceeds LPL and AL devices, while the micro-discharge UVB intensity is less than the MPMAL device in both the UVB and UVC regions. For operation at extrapolated 2.5 A/cm levels, the optical output of the micro-discharge exceeds each mercury lamp device in both the UCB and UVC regions.

### 3.8 Conclusion

We have presented absolute optical emission spectra in the 110-400 nm region from RF driven (13.56 MHz) hollow slot microplasmas operating with rare gas mixtures flowing through electrodes into open air at atmospheric pressure. The time-averaged optical spectra provide a useful characterization of photon fluxes and light production po-

tentially important for processing applications. UV/VUV spectra from 110-400 nm are presented for gas flows of argon and helium with small admixtures of hydrogen and nitrogen. In the 110-200 nm atomic lines, primarily from atomic nitrogen, dominate the emission. In the 200-300 nm region the emission is dominated by molecular NO emission. In contrast $N_2$ and $N_2^+$ lines dominate the 300-400 nm region.

Optical spectra for 60 MHz operation of the He-$N_2$ microdischarge provide information regarding excitation frequency effects, and also shows that external matching circuitry effects and the electrical measurements at different frequencies (Chapter 2) are consistent with the optical, $I(\lambda)$, observations. The 2$^{nd}$ positive system of molecular nitrogen ($N_2(C\ ^3\Pi_g - B^3\Pi_g)$) is used to measure the rotational (gas) temperature, and yields a (spatially averaged) temperature of 750 +/- 100 K for the case of argon gas flow. The vibrational temperature of the He-$N_2$ microdischarge plasma is determined by fitting optical data with the SpecAir code [62] and from the peak intensity ratio method. The first method used the $\Delta v = -2$ band series of the $N_2$ 2nd positive bands and the second method used the ratio of the 2-1 to 0-0 band of $N_2^+$(B-X) transitions. Both measurements provide close values of the vibrational temperature. Finally, we compare the efficiency and magnitude of light emission from the open air microdischarge with that attainable from commercial sealed mercury lamps. We find that while the micro-discharge has significantly lower emission efficiencies, the attainable output power per area compares favorably for high current operation of the RF micro plasmas.

**Reference:**


1. Moon, S. and W. Choe, *A comparative study of rotational temperatures using diatomic OH, $O_2$ and $N_2^+$ molecular spectra emitted from atmospheric plasmas.*, Spectrochimica Acta Part B, 2003. **58**: p. 249-257.
2. Boyd, T.J.M. and J.J. Sanderson, in *The physics of plasmas. (2003)*, Cambridge University Press (1st ed.). p. 456.
3. Watanabe, K., W.C.Y. Inn, and M. Zelikoff, *Absorption coefficient of oxygen in the vacuum ultraviolet.*, J. Chem. Phys., 1953. **21**(6): p. 1026-1030.
4. Yalin, A.P., et al., *Electrical and optical emission characteristics of radio-frequency-driven hollow slot microplasmas operating in open air.*, Applied Physics Letters, 2003. **83**(14): p. 2766-2768.
5. Lawrence G. Piper, M.E.D., Wilson T. Rawlins, J. Phys. Chem., 1987. **91**: p. 3883.
6. Luo, J., L.S. Steven, Y. Hayashi, and H. Matsumoto, *Emission spectroscopic studies of plasma-induced NO decomposition and water splitting.*, J. Phys. Chem. A, 1999. **103**(31): p. 6151-6161.
7. Garscadden, A. and R. Nagpal, *Non-equilibrium electronic and vibrational kinetics in $H_2$-$N_2$ discharges.*, Plasma Sources Sci. Technol., 1995. **4**: p. 268-280.
8. Young, R.A. and O.J. Dunn, *The excitation and quenching of $N(^2P)$.*, J. Chem. Phys., 1975. **63**(3): p. 1150-1153.

9. Cernogora, G., L. Hochard, M. Touzeau, and C.M. Ferreira, *Population of $N_2(A\ ^3\Sigma_u^+)$ metastable states in a pure nitrogen glow discharge.*, J. Phys. B: At. Mol. Phys., 1981. **14**: p. 2977-2987.

10. Simek, M., *Determination of $N_2(A\ ^3\Sigma_u^+)$ metastable density produced by nitrogen streamers at atmospheric pressure: 1. Design of diagnostic method.*, Plasma Sources Sci. Technol., 2003. **12**(3): p. 421-431.

11. Grace, H.H. and M.F. Golde, *Experimental study of the reactions of $N_2(A\ ^3\Sigma_u^+)$ with H atoms and OH radicals.*, J. Chem. Phys., 1991. **95**(12): p. 8866-8870.

12. Hovis, F.E. and P.D. Whitefield, *Quenching of $N_2(A\ ^3\Sigma_u^+, v=0)$ by H*.*, Chem. Phys. Lett., 1987. **138**(2,3): p. 162-167.

13. Hovis, F.E., P.D. Whitefield, H.V. Lilenfeld, and G.R. Bradburn, *Chemical generation of electronically excited $N_2$ in the H(D)+$NF_2$ flame.*, J. Phys. Chem., 1988. **92**(18): p. 5133-5141.

14. Klose, J.Z., J.M. Bridges, and R.O. William, *Monochromatic source of Lyman-alpha radiation.*, Appl. Optics, 1985. **24**(14): p. 2263-2266.

15. Kurunczi, P., H. Shah, and K. Becker, *Hydrogen Lyman-alpha and Lyman-beta emissions from high-pressure microhollow cathode discharges in Ne-$H_2$ mixtures.*, J. Phys. B: At. Mol. Phys., 1999. **32**(22): p. L651-L658.

16. Striganov, A.R. and N.S. Sventitskii, *Tables of Spectral Lines of Neutral and Ionized Atoms*. 1968, New York-Washington: IFI/Plenum.

17. Wieser, J., et al., *Lyman-alpha emission via resonant energy transfer.*, J. Phys. B. At. Mol. Opt. Phys., 1998. **31**(4589-4597).

18. Kurunczi, P., J. Lopez, H. Shah, and K. Becker, *Excimer formation in high-pressure microhollow cathode discharge plasmas in helium initiated by low-energy electron collisions.*, International Journal of Mass Spectrometry, 2001. **205**(1-3): p. 277-283.

19. Motret, O., J.M. Pouvesle, and J.T. Stevefelt, *Spectroscopic study of the afterglow excited by intense electrical discharges in high-pressure helium hydrogen mixtures.*, J. Chem. Phys., 1985. **83**(3): p. 1095-1100.

20. Wieser, J., et al., *Vacuum ultraviolet rare gas excimer light source.*, Rev. Sci. Instruments, 1997. **68**(3): p. 1360-1364.

21. Becker, K.H., P.F. Kurunczi, and K.H. Schoenbach, *Collisional and radiative processes in high-pressure discharge plasmas.*, Physics of Plasmas, 2002. **9**(5): p. 2399-2404.

22. Schumann, M. and H. Langhoff, *Kinetic-studies of ionic excimers.*, J. Chem. Phys., 1994. **101**(6): p. 4769-4777.

23. Langhoff, H., *The origin of the higher continua emitted by the rare-gases.*, J. Phys. B: At. Mol. Opt. Phys., 1994. **27**(21): p. L709-L714.

24. Phelps, V.A. and Z.L. Petrovic, *Cold-cathode discharges and breakdown in argon: surface and gas phase production of secondary electrons.*, Plasma Sources Sci. Technol., 1999. **8**: p. R21-R44.

25. Griegel, T., W.D. Heinz, J.H. Wolfgang, and K. Petkau, *The 3rd continuum of the rare-gases emitted by heavy-ion beam induced plasmas.*, J. Chem. Phys., 1990. **93**(7): p. 4581-4588.

26. Moller, T., J. Stapelfeldt, M. Beland, and G. Zimmerer, *Oscillatory structures in bound-free fluorescence-spectra of $Xe_2$, $Kr_2$ and $Ar_2$.*, Chem. Phys. Lett., 1985. **117**(3): p. 301-306.

27. Krotz, W., A. Ulrich, B. Busch, G. Ribitzki, and J. Wieser, *3rd excimer continuum of argon excited by a heavy-ion beam.*, Phys. Rev. A, 1991. **43**(11): p. 6089-6094.

28. Velazco, J.E., J.H. Kolts, and D.W. Setser, *Rate constants and quenching mechanisms for the metastable stats of argon, krypton, and xenon.*, J. Chem. Phys., 1978. **69**(10): p. 4357-4373.

29. Moselhy, M., R.H. Stark, K.H. Schoenbach, and U. Kogelschatz, *Resonant energy transfer from argon dimers to atomic oxygen in microhollow cathode discharges.*, Appl. Phys. Lett., 2001. **78**(7): p. 880-882.

30. Young, R.A. and G.A. St. John, *Experiments on $N_2(A\ ^3\Sigma_u^+)$.II. Excitation of NO*.*, J. Chem. Phys., 1968. **48**(2): p. 898-900.

31. Slanger, T.G., B.J. Wood, and G. Black, *Temperature-dependent $N_2(A\ ^3\Sigma_u^+)$ quenching rate coefficients.*, Journal of Photochemistry, 1973/74. **2**: p. 63-66.

32. Piper, L.G., G.E. Caledonia, and J.P. Kennealy, *Rate constants for deactivation of $N_2(A)v'=0,1$ by $O_2$.*, J. Chem. Phys., 1981. **75**(5): p. 2888-2895.

33. Piper, L.G., *The excitation of $N(^2P)$ by $N_2(A^3\Sigma_u^+, v'=0,1)$.*, J. Chem. Phys., 1989. **90**: p. 7087-7095.

34. De Benedictis, S. and G. Dilecce, *Time resolved diagnostics of kinetic studies in $N_2/O_2$ pulsed rf discharges.*, J. Phys. III (France, Paris), 1996. **6**: p. 1189-1204.

35. Babayan, S.E., G. Ding, and R. Hicks, *Determination of the nitrogen atom density in the afterglow of a nitrogen and helium, nonequilibrium, atmospheric pressure plasma.*, Plasma Chem. and Plasma Proc., 2001. **21**(4): p. 505-521.

36. Prince, J.F., C.B. Collins, and W.W. Robertson, *Spectra excited in an argon afterglow.*, The Journal of Chemical Physics, 1964. **40**(9): p. 2619-2626.

37. Vasile-Dan, H., V. Hoffmann, B.M.S. Edward, and W. Klaus, J. Anal. At. Spectrom., 2001. **16**: p. 43-49.

38. McNeely, J.R., G.S. Hurst, W.B. Wagner, and M.G. Payen, *Energy transfer from argon resonance states to nitrogen, hydrogen, and nitric oxide.*, J. Chem. Phys., 1975. **63**(6): p. 2717-2723.

39. Yokoyama, A., T. Ueno, and Y. Hatano, *Pulse radiolysis studies of the deexcitation process of excited argon atoms by $N_2$, $H_2$ and $D_2$.*, Chem. Phys., 1977. **22**: p. 459-466.

40. Hibert, C., I. Gaurand, O. Motret, and J.M. Pouvesle, *[OH(X)] measurements by resonant absorption spectroscopy in a pulsed dielectric barrier discharge.*, J. Appl. Phys., 1999. **85**(10): p. 7070-7075.

41. Hilary, J.C., L.C. Matthew, and G.M. Kenneth, *Effect of collisions on one-color polarization spectroscopy of $OH(A\ ^2\Sigma^+–X\ ^2\Pi)$.*, J. Chem. Phys., 2003. **119**(18): p. 9461-9467.

42. Hofzumahaus, A. and F. Stuhl, *Electronic quenching, rotational relaxation, and radiative lifetime of $NH(A\ ^3\Pi, v'=0, N')$.*, J. Chem. Phys., 1985. **82**(7): p. 3152-3159.

43. Nagpal, R. and P.K. Ghosh, *Role of electronic excitations and atomic quenching on dissociation of nitrogen in dc discharges.*, Chem. Phys. Lett., 1991. **183**(12): p. 129-134.

44. Clark, W.G. and D.W. Setser, *Energy-transfer reactions of $N_2(A\ ^3\Sigma_u^+)$ .5. Quenching by hydrogen halides, methyl halides, and other molecules.*, J. Phys. Chem., 1980. **84**(18): p. 2225-2233.

45. Kolts, J.H., H.C. Brashears, and D.W. Setser, *Redetermination of $N_2(C)$ and $N_2(B)$ branching ratio from $Ar(^3P_{0,2})+N_2$ reaction.*, J. Chem. Phys., 1977. **67**(6): p. 2931-2933.

46. Kalcher, J. and E.A. Reinsch, *Accurate ab initio calculations of radiative transition probabilities between the $A\ ^3\Sigma_u^+$, $B\ ^3\Pi_g$, $W\ ^3\Delta_u$, $B'\ ^3\Sigma_u^-$, and $C\ ^3\Pi_u$ states of $N_2$.*, J. Chem. Phys., 1984. **81**(5): p. 2420-2431.

47. Benedictis, S.D. and G. Dilecce, *Vibration relaxation of N2(C,v) state in N2 pulsed rf discharge; electron impact and pooling reactions.*, Chem. Phys., 1995. **192**: p. 149-162.

48. Benedictis, S.D., G. Dilecce, and M. Simek, *Vibrational excitation of $N_2^+(B,v)$ in He-$N_2$ pulsed rf discharges.*, J. Phys. B: At. Mol. Opt. Phys., 1994. **27**: p. 615-632.

49. Shevelko, V.P. and H. Tawara, *Cross sections for electron-impact induced transitions between excited states in He:n,n'= 2, 3 and 4.* 1995, National Technical Information Service Document No. DE96725192INZ. Copies may be ordered from National Technical Information Service Springfield, VA 22161, NIFS-DATA-28 1995.

50. Crandall, D.H., W.E. Kauppila, R.A. Phaneuf, T. P., and G.H. Dunn, *Absolute cross sections for electron-impact excitation of $N_2^+$.*, Phys. Rev. A, 1974. **9**(6): p. 2545-2551.

51. Lindinger, W., A.L. Schmeltekopf, and F.C. Fehsenfeld, *Temperature dependence of de-excitation rate constants of He(2 $^3S$) by Ne, Xe, $H_2$, $N_2$, $O_2$, $NH_3$ and $CO_2$.*, J. of Chem. Phys., 1974. **61**(7): p. 2890-2895.

52. Fort, J., T. Bolzinger, D. Corno, T. Ebding, and A. Pesnelle, *Velocity dependence of cross-sections for penning, rearrangement, and total ionization of $H_2$ and $D_2$ molecules by He ($2^3S$) and He ($2^1S$) metastable atoms.*, Phys. Rev. A, 1978. **18**(5): p. 2075-2080.

53. Hubert, J., M. Mosian, and A. Ricard, *A new microwave plasma at atmospheric pressure.*, Spectrochimica Acta, 1979. **33B**: p. 1-10.

54. Laux, C.O., T.G. Spence, C.H. Kruger, and R.N. Zare, *Optical Diagnostics of Atmospheric Pressure Air Plasmas.*, Plasma Sources Science and Technology, 2003. **12**: p. 125-138.

55. Laux, C.O., *Optical Diagnostics and radiative emission of air plasmas; PhD Thesis*, in *Mechanical Engineering*. 1993, Stanford University: Stanford.

56. Piper, L.G., *State-to-state $N_2(A\ ^3\Sigma_u^+)$ energy-pooling reactions. I. The formation of $N_2(C\ ^3\Pi_u)$ and the Herman infrared system.*, J. of Chem. Phys., 1988. **88**(1): p. 231-239.

57. Hays, G.N. and H.J. Oskam, *Reaction rate constant for 2 $N_2(A\ ^3\Sigma_u)$-$N_2(C\ ^3\Pi_u)$+$N_2(X\ ^1\Sigma_g^+, v'>0)$*.*, J. of Chem. Phys., 1973. **59**(11): p. 6088-6091.

58. Herzberg, G., *Molecular spectra and molecular structure (2nd ed.)*. Vol. I. 1989, Florida/New York: Krieger Publishing Company (Florida). p.289.

59. Rahman, A., et al., *Absolute UV and VUV Emission in the 110-400 nm Region from 13.56 MHz Driven Hollow Slot Microplasmas Operating in Open Air.*, Plasma Sources Sci. Tech., 2004. **13**(3): p. 537-547.

60. Pouvesle, J.M., A. Bouchoule, and J. Stevefelt, *Modeling of the charge transfer afterglow excited by intense electrical discharges in high pressure helium nitrogen mixtures.*, J. Chem. Phys., 1982. **77**(2): p. 817-825.

61. Pouvesle, J.M., J. Stevefelt, and C.B. Collins, *Study of two-body and three-body channels of the reaction of metastable helium atoms with nitrogen.*, J. Chem. Phys., 1985. **82**(5): p. 2274-2279.

62. Laux, C.O., *Optical Diagnostics and Radiative Emission of Air Plasmas*, in *Mechanical Engineering*. 1993, Stanford University: Stanford, CA. p. 232.

63. http://www.uv-light.co.uk/applications/disinfection/uv_disinfection.htm.

# Chapter 4

# Visible Emission Spectroscopy

## 4.1 Introduction

This chapter focuses on measurements and interpretation of visible emission spectra, $I(\lambda)$ for $400<\lambda<850$ nm, from the RF (13.56 MHz) excited microplasmas. Visible spectroscopy is complementary to UV/VUV emission spectroscopy of Chapter 3 and can also provide significant new information about plasma kinetics and plasma chemistry, such as electron temperature and electron energy distribution function (EEDF), electron number density, secondary processes, and cathode sputtering.

We employ the same slot microplasma device (Figure 3.1a) to obtain the visible emission spectra. Rare gas (Ar or He) is flowed through the hollow slot microplasma device with varying admixtures of $N_2/H_2/O_2$. Operating conditions of the hollow slot microplasmas are kept similar to those used to measure the UV/VUV spectra (i.e., $\langle E/N \rangle \sim$ 35 Td, $\langle E \rangle \sim 10$ kV/cm, and current density $j \sim 0.7$ A/cm$^2$). Unlike absolute UV/VUV emission spectra, we only have recorded relative calibration of the visible detection system.

Section 4.2 discusses the experimental setup and relative calibration, Section 4.3 describes general trends of the observed optical emission under varying conditions,

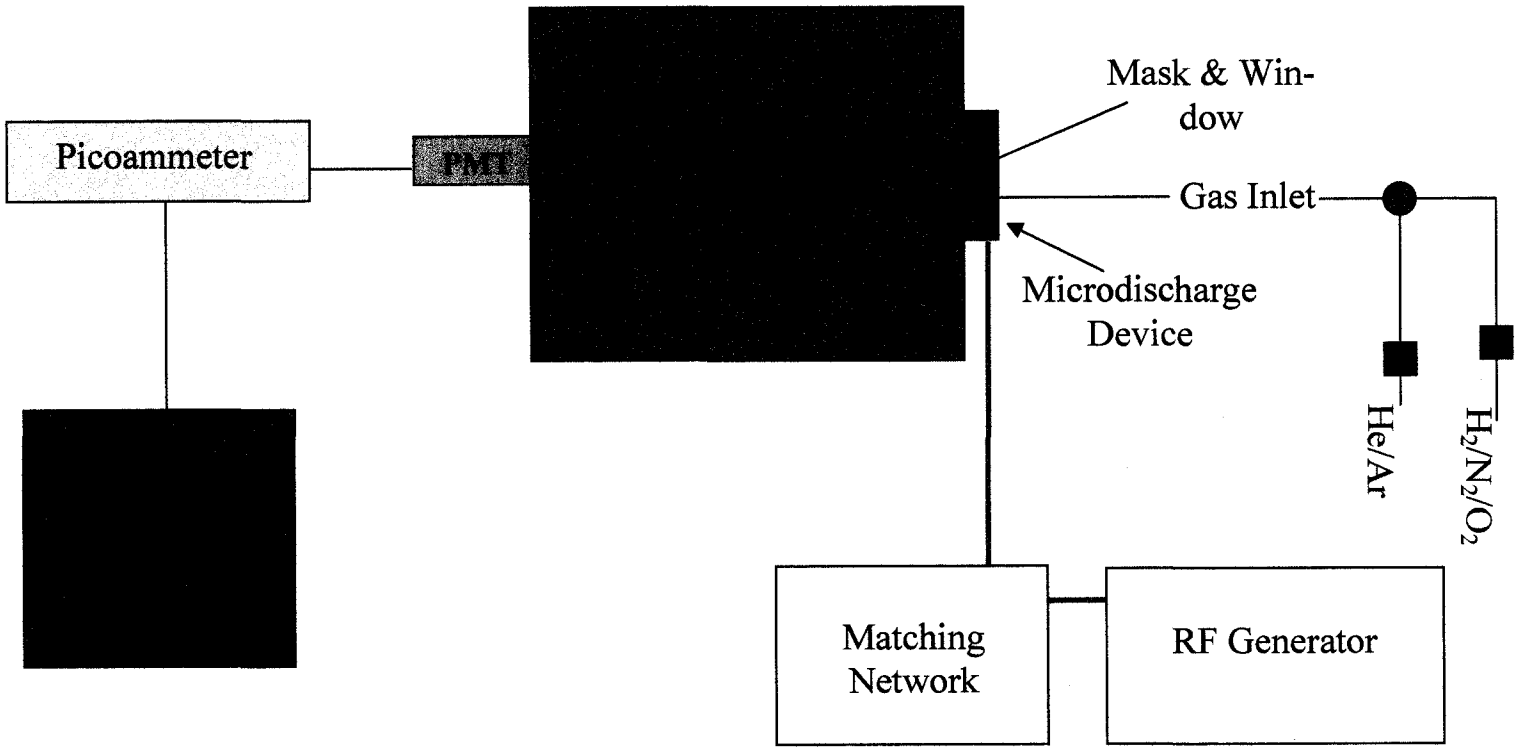


**Figure 4.1 Experimental setup for recording the visible emission spectra from hollow slot microplasma device**

Sections 4.4 through 4.7 present plasma characterization and calculated plasma properties. Visible spectroscopy results are summarized in Section 4.8.

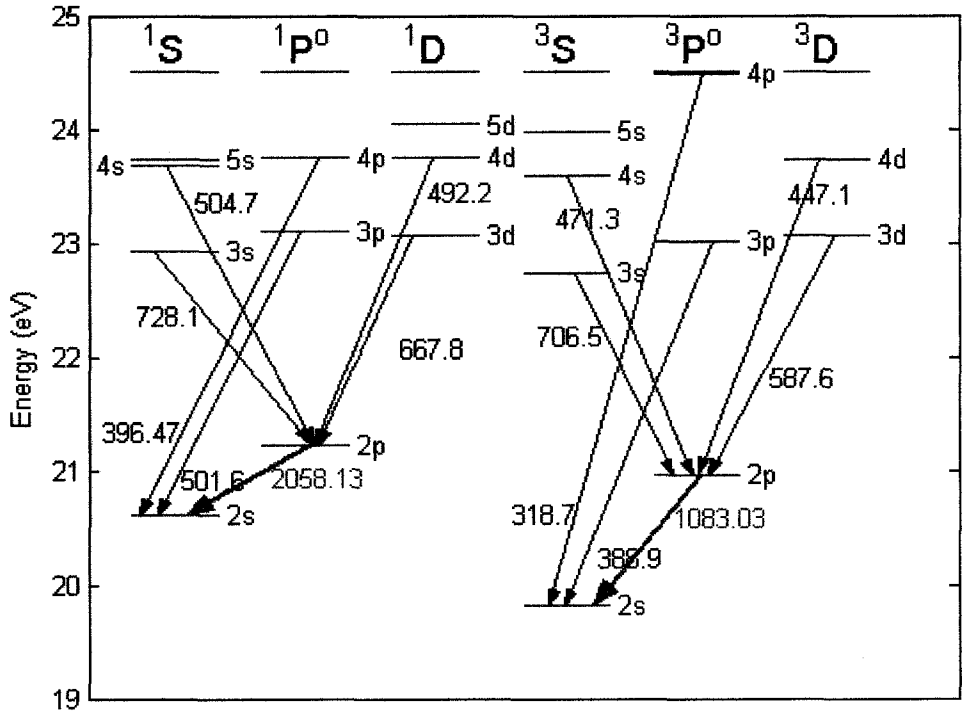


**Figure 4.2: Partial energy level diagram of atomic helium transitions. Emission transitions labeled by the red arrow are beyond the covered spectral region in this work.**

## 4.2 Experimental

### 4.2.1 Experimental Setup

Typical flow conditions for which optical emission spectra are obtained from the hollow slot microplasmas for Ar and He plasmas include: flow rates of Ar and He of 9 slpm and 2 slpm respectively with varying addition of $H_2$ or $N_2$ or $O_2$. Again, the microdischarge operates in open air which mixes into the active plasma; while this adds complexity it represents actual desired operating conditions.

The spectral measurement region encompasses the entire visible region (400-700 nm) and includes parts of the UV (300-400 nm) thus overlapping the experimental

observations of Chapter 3[12]. This overlap allows measurement validation in the two limited wavelength regions. The spectral scans also cover parts of the IR region in the range 700-850 nm where numerous atomic transitions of Ar and He are present.

Figure 4.1 shows the experimental setup for recording the visible emission spectra. Microplasmas use the same AE RF source (13.56 MHz) and matching network as described in Chapter 3 (Figure 2.3a). The slot plasma device is placed parallel and in close proximity to the entrance slit of a Jarrel Ash 0.6 m scanning monochromator. The monochromator has a grating of 1200 grooves/mm blazed at ~ 550 nm. Vacuum is not necessary for light propagation in this wavelength region; therefore, the $MgF_2$ window and the vacuum pump are not employed. A photomultiplier tube is employed in the exit slit of the spectrometer to obtain the diffracted optical signal. The optical data acquisition range (wavelength) is primarily limited by the PMT response to 300-900 nm. The current signal from the PMT is passed to a computer via a Kithley 486 picoammeter.

4.2.2 Relative Calibration

Relative calibration of the detection system is performed using an Acton Research Corporation white light source. The white light lamp source is an Oriel Corporation quartz tungsten halogen lamp (Model QTH 6334). This lamp has known emission spectrum from 200 nm to 900 nm. The lamp is focused into the input slit of the monochromator and spectral data are acquired from 300 nm to 900 nm.

The calibration process employs the following:

$I'(\lambda)$ = QTH emission spectra (nA).

[12] Note that the vibrational temperature presented in Chapter 3 (Section 3.5), calculated from the peak intensity ratio of the 0-0 to 2-1 vibrational emission bands of $N_2^+$(B-X), is determined from the UV portion of the visible experimental setup.

$I''(\lambda)$ = QTH irradiance curve (arbitrary unit).

The spectral response of the system $R(\lambda) = I'(\lambda)/I''(\lambda)$ (nA/arbitrary unit).

After determining the spectral response of the system, each spectral scan from the microdischarge plasma device is divided by the spectral response data to obtain the corrected (relative) spectrum. Specification from the Oriel Corporation notes that the output efficiency may have a deviation of ± 15% from lamp to lamp. In addition, output efficiency on day to day operation may vary up to ± 50% for the same lamp; therefore, absolute optical intensity calibration is not reliable. However, we find that the output efficiency does not vary by more than ± 20% over day to day operation and does not vary more than ±1% on the same day. Therefore, relative calibration of the microplasma emission spectra allows reliable comparison of intensities of different transitions within an individual scan. Of course comparison of the intensities of the same transition for different gas mixture does not depend on the system calibration (since the detection system response at a given wavelength is fixed).

As an additional calibration a He-Ne laser is employed to determine the (instrumental function) spectral resolution (FWHM), $\Delta\lambda$, of the system. Spectral resolution at ~632.8 nm is found to be, $\Delta\lambda = 0.10 \pm 0.01$ nm and $0.18 \pm 0.01$ nm for slit openings of 100 μm and 150 μm respectively (Appendix C).

**4.3 General Discussions on Discharge Behavior Inferred from Visible Spectra**

In this section we present observed trends of the optical emission spectra from the microplasmas for different gas admixtures. Spectra in the visible range (400-700 nm) are dominated mainly by atomic emissions with contributions from molecular emissions,

while the UV (300-400 nm) region is dominated by molecular nitrogen emissions and the IR region (700-850 nm) primarily contains atomic emissions.

$$(X^+)^* + M = X^+ + M + K.E. \text{ (non radiative collisional de-excitation)} \quad R4.1$$

$$X^+ + e \text{ (slow)} \longrightarrow X \text{ (non-radiative recombination)} \quad R4.2$$

where, M is rare gas or any other species.

It is noteworthy that emissions from atomic ions are weak. Very weak emission from excited $Ar^+$ is observed and no detectable emission from excited $He^+$ is ever observed. This observation indicates that the atomic ion concentration is small and/or the ions are lost through processes that do not involve radiative emissions (R4.1 and R4.2). In addition to collisional de-excitation (followed by non-radiative recombination) it is possible that two processes, formation of dimer ions[13], and symmetrical charge transfer (SCT)[14], may account for loss of atomic ions. At atmospheric pressure, formation of dimer and dimer ions is very likely [1-3]. Excited atoms or ions of rare gases can combine with neutral atoms in a three body reaction (R 4.3 & R 4.4) to form dimer or dimer ions [1, 3]. It is also possible that the discharge is forming dimer ions to sustain the plasmas. Note that the formation of dimer ions (R 4.3 and R 4.4) requires less energy [4, 5] than ionizing the respective atoms and thus are increasingly likely in rare gas atmospheric (collisional) plasma:

$$X + X^* + M = X_2^+ + M \quad R\ 4.3$$

$$X^+ \text{ or } (X^+)^* + X + M = X_2^+ + M + K.E. \quad R\ 4.4$$

[13] Dimer ions decay non radiatively upon capturing a slow electron.

[14] Symmetrical charge transfer refers to charge transfer between atoms (or molecules) of the same species (R4.5).

where X stands for a rare gas atom, M stands for rare gas or any third body present in the plasma, and the asterisk (*) represents the excited state.

The reaction (R 4.3) requires that the excited state of an atomic helium possess an energy of ~23.1 eV or more to form helium dimer ion [5]. Therefore atomic excited states with principal quantum number $n \geq 4$ and some $n=3$ states may form dimer ions[15] and provide substantial amount of the electron-ion pairs required to sustain the plasmas. (In the case of Ar, the dimer ion formation requires 14.7 eV [5], which is slightly lower than the argon ionization energy (15.5 eV) [6].) Ions or excited ions may also form dimer ions via reaction R 4.2. The APGD microplasmas are highly collisional, thus three body reactions R4.1 and R4.2 are likely to be present.

A second possible channel for non-radiative decay of the excited atomic ions is via a charge transfer process. Charge transfer among same species (symmetric charge transfer (SCT)) is highly probable [7] and at atmospheric pressure the collision frequency is very high (Table 2.2). Hence excited ions may transfer their charge through reaction R 4.5:

$$X + (X^+)^* \longrightarrow X^+ + X + K.E. \qquad \text{R 4.5}$$

and the newly generated ground state ions can recombine non-radiatively (R4.2) with slow electrons.

For clarity, the spectra of the microplasmas for different rare gas-impurity admixtures are presented separately. Subsections 4.3.1 and 4.3.2 describe the trend of helium and argon microplasmas respectively. Note that like UV/VUV emission spectra, the optical spectra collected by the detection system are both time averaged and path integrated.

[15] Even though metastable-metastable interaction can form dimer ions, we disregard this contribution, because, at high pressure forming dimers via R3.8 is more probable.

### 4.3.1 Helium Plasma

The flow rate of helium in the helium open-air microplasmas is 2 slpm and flow rates of added impurities are varied. Figure 4.2 shows the partial energy level diagram of atomic helium and Table 4.1 presents the most intense atomic helium transitions observed in the helium plasmas. The sample spectra are shown in Figure 4.3a-d. Figure 4.3a,b show the most intense transitions originating from the second positive bands of $N_2$ and first negative bands of $N_2^+$, and Figure 4.3c,d shows different atomic transitions of He I in the visible region (500-775 nm). The $N_2$ and $N_2^+$ bands are strong for plasmas with nitrogen addition but weak in the pure He, He-$H_2$ and He-$O_2$ plasmas, therefore, these transitions are judged to predominantly originate in the active discharge region, i.e. they are not due to mixing of the ambient nitrogen.

**Table 4.1: Observed atomic transitions from He microplasma with added impurity of $H_2$, $N_2$ or $O_2$. In the term representation, terms in the left represent the lower energy state and the term in the right represent the higher energy state. All the transitions are taken from ref. [6]. Spectral resolution of the system is not sufficient to resolve the fine-structure.**

| Transitions (nm) | Energy States | Energy (eV) |
|---|---|---|
| 318.77 | $2s\ ^3S\text{-}4p\ ^3P^o$ | 19.82-23.71 |
| 388.86 | $2s\ ^3S\text{-}3p\ ^3P^o$ | 19.82-23.01 |
| 396.47 | $2s\ ^1S\text{-}4p\ ^1P^o$ | 20.61-23.74 |
| 447.15 | $2p\ ^3P^o\text{-}4d\ ^3D$ | 20.96-23.73 |
| 492.19 | $2p\ ^1P^o\text{-}4d\ ^1D$ | 21.22-23.74 |
| 501.57 | $2s\ ^1S\text{-}3p\ ^1P^o$ | 20.61-23.09 |
| 587.60 | $2p\ ^3P^o\text{-}3d\ ^3D$ | 20.96-23.07 |
| 667.82 | $2p\ ^1P^o\text{-}3d\ ^1D$ | 21.22-23.07 |
| 706.52 | $2p\ ^3P^o\text{-}3s\ ^3S$ | 20.96-22.72 |
| 728.13 | $2p\ ^1P^o\text{-}3s\ ^1S$ | 21.22-22.92 |

Numerous atomic transitions from $n=3,4$ states to $n= 2,3$ states are observed (Figures 4.3c,d). No He II transition is identified in the visible range (nor in the UV/VUV

region [8]). Transitions from other atomic species (H, O, Ne etc.) are observed (Figure 4.5, 4.9, and 4.10) and are due to source gas impurities and/or ambient mixing from open air operation.

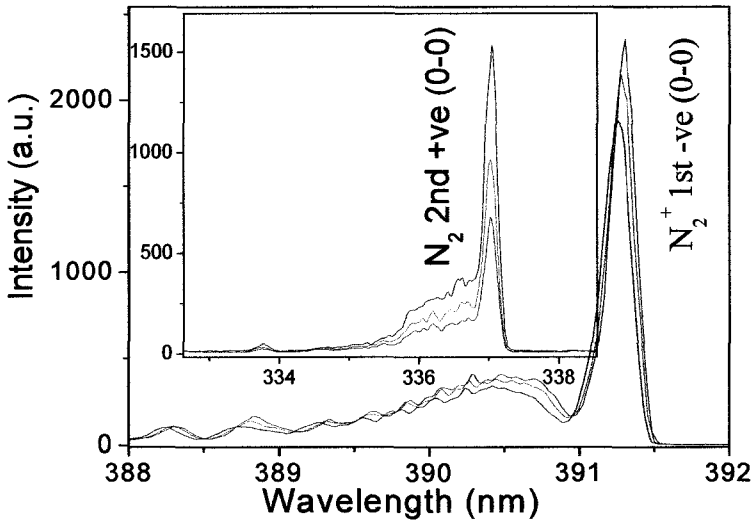


**Figure 4.3.a: Spectra of the first negative 0-0 vibrational band of molecular nitrogen ion $N_2^+$(B-X) and the second positive 0-0 vibrational band of molecular nitrogen (inset) excited in a He-$N_2$ open-air microplasmas. Flow rate of He is 2 slpm and flow rate of $N_2$ are 5.0 sccm (red), 10 sccm (green), 20 sccm (blue).**

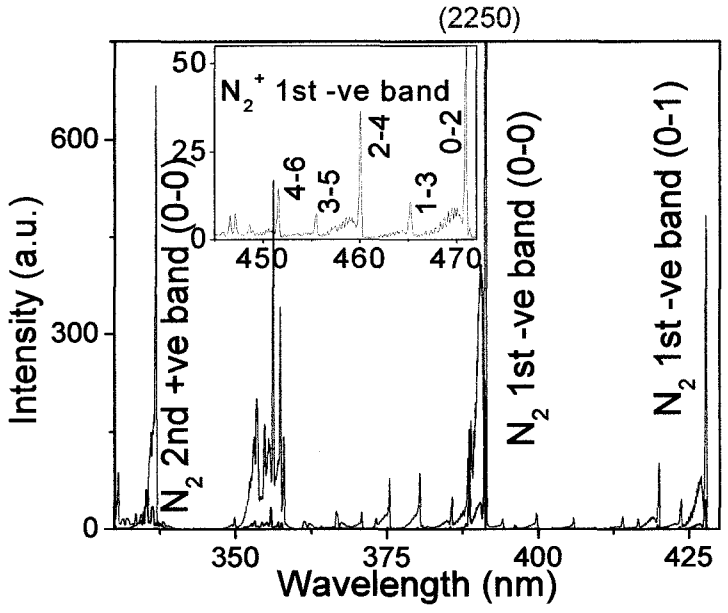


**Figure 4.3.b: Spectra of an open-air He-$N_2$ microplasma in the spectral range from 300 nm to 500 nm. Flow rate of He is 2 slpm and flow rate of $N_2$ are 0.0 sccm (black) and 5.0 sccm (red)). Strong emissions are observed from $N_2$ (2nd positive) and $N_2^+$ (1st negative) bands. Inset shows $N_2^+$ $\Delta v = -2$ series of 1st negative bands.**

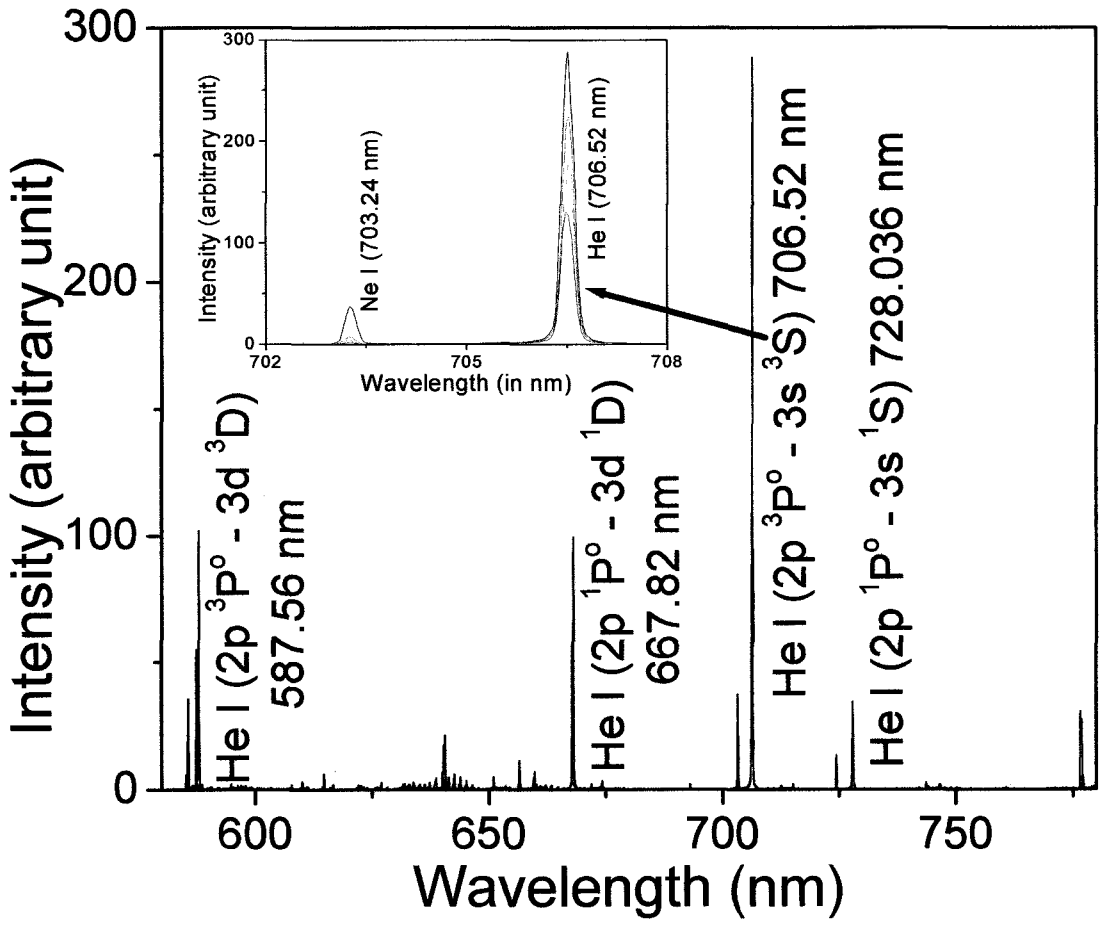


**Figure 4.3.c: Strong atomic emission in the visible region from excited He I atoms are labeled. Plasmas are sustained for He flow rates of 2 slpm with different admixtures of $N_2$ (0.0 sccm (black) and 5.0 sccm (red), 10.0 sccm (green) and 20 sccm (blue)). Inset shows the intensity changes of a He I (706.52 nm) transition.**

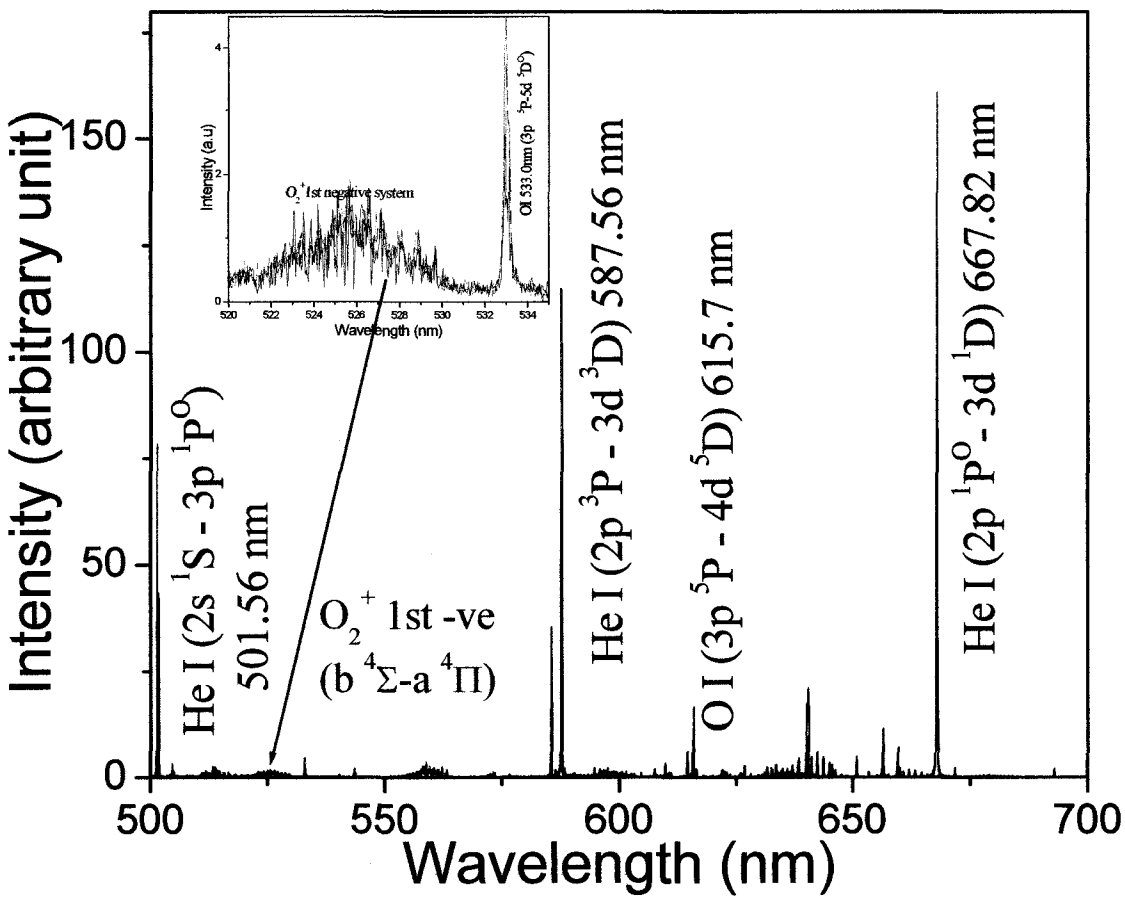


**Figure 4.3d: Spectra of He-$O_2$ microplasmas in the spectral range from 500 nm to 700 nm. Flow rate of He is 2 slpm and flow rate of $O_2$ are 0.0 sccm (black) and 5.0 sccm (red), 10.0 sccm (green) and 20 sccm (blue). Strongest emissions are from excited atomic helium.**

4.3.1a Helium-Nitrogen Plasma

This sub-section and the following two sub-sections discuss the observations and the interpretations of He microplasmas emission spectra, $I(\lambda)$, with varying addition of $N_2$, $H_2$ and $O_2$. Strong He I atomic emissions are observed for He-$N_2$ microplasmas. The primary reaction mechanisms judged to be involved in excitation and emission of He are listed below:

$$He(1s\ ^1S) + e\ (fast) = He^* \text{ or } He^{**} + e \qquad \text{R 4.6}$$

$$He^* + e\ (slow) = He^{**} + e \qquad \text{R 4.7}$$

$$He^M + e\ (slow) = He^*/He^{**} + e \qquad \text{R 4.8}$$

$$He^* \longrightarrow He(1s\ ^1S) + h\nu \quad \text{R4.9}$$

$$He^{**} \longrightarrow He^*/He^M + h\nu \quad \text{R4.10}$$

$$He^*/He^{**} + He/e \longrightarrow He(1s\ ^1S) + He(1s\ ^1S)/e \quad \text{R4.11}$$

$$He^M + N_2/H_2/O_2 \longrightarrow He + (N_2^+)^*/(H_2^+)^*/(O_2^+)^* + e \quad \text{R 4.12}$$

where * and ** signs denote lower and upper excited states (singlet or triplet) respectively and superscript M stands for metastables.

**Table 4.2: Observed He atomic transitions from He-$N_2$ microplasmas with constant helium flow rate of 2 slpm and varying nitrogen flow rate as indicated in the table. The transitions with asterisk (*) sign are either poor in intensity of suffered interference from other transitions. The transition intensities are normalized to respective transitions at zero nitrogen partial pressure. $E_u$, $E_l$ and $\Delta E$ represents the energy of the upper state, lower state and the difference in energy between the respective levels. All the transitions are taken from ref. [6]. Spectral resolution of the system is not sufficient to resolve the fine-structure.**

| Wavelength (nm) | Type | Nitrogen flow rate (sccm) (First Row) Normalized Intensity (a.u.) | | | | Energy (eV) | | |
|---|---|---|---|---|---|---|---|---|
| | | 0 | 5 | 10 | 20 | $E_u$ | $E_l$ | $\Delta E=E_u-E_l$ |
| *318.77 | Triplet-Triplet | 1 | 0.79 | 0.68 | 0.52 | 23.71 | 19.82 | 3.89 |
| *388.86 | Triplet-Triplet | 1 | 0.92 | 0.77 | 0.59 | 23.01 | 19.82 | 3.19 |
| *396.47 | Singlet-Singlet | 1 | 0.61 | 0.44 | 0.58 | 23.74 | 20.61 | 3.13 |
| 447.15 | Triplet-Triplet | 1 | 0.79 | 0.53 | 0.46 | 23.73 | 20.96 | 2.77 |
| 492.19 | Singlet-Singlet | 1 | 0.731 | 0.56 | 0.48 | 23.74 | 21.22 | 2.52 |
| *501.57 | Singlet-Singlet | 1 | - | - | - | 23.09 | 20.61 | 2.48 |
| *504.77 | Singlet-Singlet | 1 | - | - | - | 23.67 | 21.22 | 2.45 |
| 587.56 | Triplet-Triplet | 1 | 0.51 | 0.37 | 0.27 | 23.07 | 20.96 | 2.11 |
| 667.82 | Singlet-Singlet | 1 | 0.75 | 0.56 | 0.45 | 23.07 | 21.22 | 1.85 |
| 706.52 | Triplet-Triplet | 1 | 0.76 | 0.59 | 0.47 | 22.72 | 20.96 | 1.76 |
| 728.13 | Singlet-Singlet | 1 | 0.75 | 0.61 | 0.48 | 22.92 | 21.22 | 1.7 |

Table 4.2 shows the integrated intensities of different He I intensities, with varying concentrations of $N_2$. All transitions are normalized with respect to the corresponding transition intensities for a pure helium microplasma. Transitions suffering interference from other transitions are labeled with an asterisk in the wavelength column (Table 4.2). The intensities of the helium atomic transitions decrease (Table 4.2) with increase in

nitrogen flow rates (5, 10 and 20 sccm). As will be explained below, this is due to a combination of: decrease in the high energy tail of the EEDF (R4.6) [9], increased quenching of He metastables by $N_2$ (R4.12) [10, 11], and cascading effect[16] from upper and lower states (R4.7, R4.8, and R4.10). No optical transitions from levels $n \geq 5$ are observed, indicating these energy levels are either lowly populated or quickly collisionally combine to form dimer ions ($He_2^+$) (R 4.3).

The addition of $N_2$ in the He discharge decreases the high energy tail of the electron energy distribution function (EEDF) and causes a shift in the mean EEDF toward lower energy [9]. This decrease in the high energy tail of EEDF affects the population of excited states directly (R4.6) and/or indirectly (R4.7 and R4.8). Since the metastable states (singlet (2s $^1$S) and triplet (2s $^3$S)) and the 2p $^3$P$^o$ state have large electron impact excitation cross-sections from the ground state He (1s $^1$S) (R4.6) [12], the population of these levels decreases most.

Quenching of helium metastable states specifically the 2s $^3$S state is very sensitive to any impurity addition (even ppm) at pressures higher than 100 Torr due to their long lifetime and large cross-section [10]. Nitrogen impurities in the high pressure He plasma can deplete the He metastable states by Penning ionization of $N_2$ to $N_2^+$ (reaction R4.12) [10, 11]. Quenching of metastables affects the secondary excitation processes (reaction R4.8). Note that the decrease in the metastable concentration does not depend only on the Penning mechanism (R4.12) but also on other processes, such as reduction in the reduced electric field, *E/N*, due to the lower ionization potential of atomic and molecular nitrogen.

[16] The lifetime of the excited states are very short compared to the metastable states, therefore the cascading effects are disregarded in our consideration (except for upward cascading from 2p $^3$P$^o$ state since it has very large excitation cross-sections for electron impact excitation to the upper states, and also have large population density).

Singlet states can have dipole allowed transitions to the ground state (He (1s $^1$S)) while the triplet metastable state acts as the virtual ground state for the excited triplet states. In addition the metastable state He(2s $^1$S) is at higher energy compared to the triplet metastable state He(2s $^3$S), so that the population density of the triplet metastable state is expected to be greater than the singlet metastable state population density. Table 4.2 shows that the intensities of the triplet transitions decrease at a faster rate as nitrogen is added compared to the singlet transitions; hence, slow electrons are judged to contribute to the excited state population (R4.7 and R4.8). If the effect of the slow electrons is small and only reaction R4.6 contributes primarily to populate the excited states, then the singlet and triplet transition intensities should decrease roughly by the ratio of their excitation cross-sections from the ground state. The intensity trends of the 587 nm triplet emission is the best example (Figure 4.4) of slow electron-metastable interaction (see Appendix D for detail).

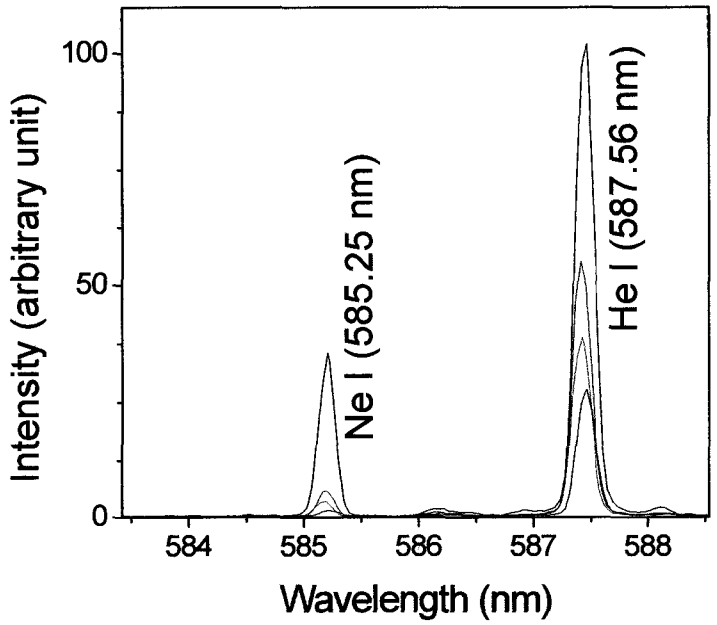


**Figure 4.4: Strong atomic emission from the 587.5 nm He I transition. Plasmas are sustained for He flow rates of 2 slpm with different admixtures of $N_2$ (0.0 sccm (black) and 5.0 sccm (red), 10.0 sccm (green) and 20 sccm (blue)).**

Adding small amounts of $N_2$ (5 sccm) flow to the upstream primary He (2 slpm) flow sharply increases the $N_2^+$(B-X) emission (Figure 4.3.a), the upper state of which is formed due to both electron impact (direct and secondary) excitation and Penning ionization of $N_2$ [10, 11]. However, any further increase in $N_2$ (10 and 20 sccm) decreases the $N_2^+$(B-X) emission because of quenching of the metastables. This behavior suggests the $N_2^+$(B) state is predominantly formed via Penning mechanism in the active discharge region.

There are a few emissions (584, 702 and 724 nm) in the helium plasma (Figure 4.3c and Figure 4.4) which coincide very well with the Ne I lines. Most likely the origin of these lines are from the impurity of the feed gas. Intensities of these lines decrease very sharply with the addition of $N_2$. The upper levels of these transitions (~18.38 and 18.8 eV above the ground level of the Ne I) are very close to the energy of the He (2s $^3$S) metastable state, so that the reduction in transition intensities are consistent with quenching of metastables by added impurity.

4.3.1b Helium-Hydrogen Plasma

The addition of upstream hydrogen to the helium plasmas yields similar behavior to the helium-nitrogen plasmas as regards the atomic He I transitions. That is, atomic transitions of helium are observed to decrease with upstream $H_2$ addition (5 sccm and 10 sccm). The amount of gas flow matters as twenty sccm of $H_2$ in helium plasma shows an increase in intensity of He I transitions as compared to the 10 sccm of $H_2$ flow in the He plasma. This non-linear behavior was explained in Chapter 3.

Table 4.3 provides relative intensities of different helium atomic lines for different hydrogen flow rates. The addition of $H_2$ decreases He I atomic emission intensities.

Similar to He-$N_2$ discharge, the 587 nm transition intensity decreases sharply in the He-$H_2$ microplasma. Again, the triplet-triplet transitions are affected more as compared to the singlet-singlet transitions and this trend shows the importance of the secondary process involving slow electrons and triplet metastables (He 2s $^3$S). It can also be inferred that $H_2$ quenches the He metastables efficiently [11]. No detectable emission transition from excited $H_2^+$ is observed in the visible region. Further 486 nm and 656 nm emissions are indicators of the existence of $H_2^+$ (Section 4.5), and thus supports the $H_2$ (B-X) radiative recombination emission near ~ 165 nm (Chapter 3).

**Table 4.3 Observed atomic transitions from He-$H_2$ microplasmas with constant helium flow rate of 2 slpm and varying hydrogen flow rate as indicated in the table. Triplet and singlet transitions are indicated by red and black color letters respectively. The transition intensities are normalized to respective transitions at zero hydrogen partial pressure. $E_u$, $E_l$ and $\Delta E$ represents the energy of the upper state, lower state and the difference in energy between the respective levels. All the transitions are taken from ref. [6]. Spectral resolution of the system is not sufficient to resolve the fine-structure.**

| Wavelength (nm) | Type | Hydrogen flow rate (sccm) (First Row) / Normalized Intensity (a.u.) | | | | Energy (eV) | | |
|---|---|---|---|---|---|---|---|---|
| | | 0 | 9 | 18 | 37 | $E_u$ | $E_l$ | $\Delta E=E_u-E_l$ |
| 318.77 | Triplet-Triplet | 1 | 0.68 | 0.77 | 0.84 | 23.71 | 19.82 | 3.89 |
| 388.86 | Triplet-Triplet | 1 | 0.74 | 0.23 | 0.25 | 23.01 | 19.82 | 3.19 |
| 396.47 | Singlet-Singlet | 1 | 0.93 | 0.32 | 0.33 | 23.74 | 20.61 | 3.13 |
| 447.15 | Triplet-Triplet | 1 | 0.65 | 0.24 | 0.32 | 23.73 | 20.96 | 2.77 |
| 492.19 | Singlet-Singlet | 1 | 0.83 | 0.45 | 0.52 | 23.74 | 21.22 | 2.52 |
| 501.57 | Singlet-Singlet | 1 | 0.84 | 0.47 | 0.55 | 23.09 | 20.61 | 2.48 |
| 587.56 | Triplet-Triplet | 1 | 0.60 | 0.45 | 0.49 | 23.07 | 20.96 | 2.11 |
| 667.82 | Singlet-Singlet | 1 | 0.78 | 0.68 | 0.89 | 23.07 | 21.22 | 1.85 |
| 706.52 | Triplet-Triplet | 1 | 0.79 | 0.65 | 0.64 | 22.72 | 20.96 | 1.76 |
| 728.13 | Singlet-Singlet | 1 | 0.87 | 0.70 | 0.82 | 22.72 | 22.92 | 1.7 |

Both triplet and singlet transitions show smaller decrease in intensities for longer wavelength (smaller $\Delta E$) transitions, which provide a further indication of reduction in

mean electron energy towards the lower energy (the slow electron effects (R4.7 and R4.8) are more pronounced in the He-$H_2$ microplasmas).

4.3.1c Helium-Oxygen Plasma

Helium-oxygen discharges tend to suffer little plasma instability due to the higher electron affinity of oxygen (which converts free electrons into negative ions). Small addition of oxygen (up to 5 sccm) into helium plasmas increases the helium atomic emission intensities (Fig. 4.3d), due to a decrease in the population of low energy electrons because of electron attachment. The discharge therefore requires higher electric fields in order to sustain the plasmas[17], so that intensities of the atomic helium lines increase (R4.6-R4.8). Also, the negative ions of atomic oxygen generate local electric fields that may contribute to increased localized changes in atomic transition intensities and striations. In this situation the discharge automatically adjusts the $\boldsymbol{E}$ field to sustain the plasma, and hence the intensities of the He I transitions vary. Along with the adjustment of the $\boldsymbol{E}$ field, the quenching of He metastables (by $O_2$) decrease the secondary processes, and the intensities of both He I and O I transitions to decrease.

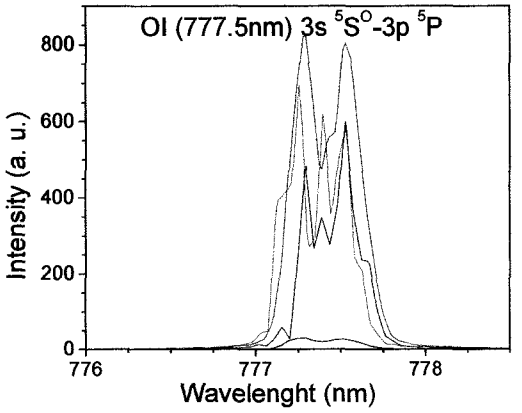


**Figure 4.5: Spectra of atomic oxygen emitted from a He-$O_2$ microplasmas. Flow rate of He is 2 slpm and flow rate of $O_2$ are 0.0 sccm (black) and 5.0 sccm (red), 10.0 sccm (green) and 20 sccm (blue).**

[17] Inverse ionization effect, discussed in Chapter 1.

Strong emissions from atomic oxygen at 777 nm (Figure 4.5) and 844 nm indicate the open air discharge is very effective in producing energetic atomic oxygen which is favorable for etching organic films [13], surface treatment of organic materials [14, 15], and ashing processes in the semiconductor and other industries. Also, molecular ion $O_2^+$ may have some contribution in producing the strong atomic oxygen emission due to dissociation at the discharge wall. We also observe weak $O_2^+(b\ ^4\Sigma - a\ ^4\Pi)$ first negative band at around 525 nm (Figure 4.3d).

4.3.2 Argon Plasma

Quantitative understanding the optical plasma emission trends for the atmospheric pressure Ar microplasmas[18] is very difficult as it requires information on: electron impact excitation cross-sections from the ground state and metastable states, termolecular reaction rates, cascading effects, radiative recombination rates, optically allowed transition probabilities, etc. Thus, computer simulation and modeling is needed to fully analyze the Ar microplasmas, which is beyond the scope of the current work. (It is the object of future collaboration with Professor M. G. Kong of Loughborough, University. (UK)). Nonetheless, in this subsection we explore these processes by estimating the electron impact excitation cross-sections, metastable quenching effects, and the dipole allowed Einstein A co-efficient of the observed argon atomic transitions.

Argon requires less ionizing energy as compared to helium (15.6eV vs. 24.6 eV) and is therefore more prone to plasma instabilities at atmospheric pressure. Further, argon has a higher secondary emission coefficient of electrons ($\gamma(Ar^+) \cong 2\gamma(He^+)$ [16]) from the cathode surface. Secondary electrons can cause electron avalanche in the bulk of the

[18] Because Ar is heavier atom, its has more energy levels (and energy gap between these levels are small) compared to He.

plasma leading to arc instability. Therefore, the argon microplasmas require higher gas flow rates (higher pressure inside the slot) compared to the helium microplasmas for stable operation. The higher flow rate helps also reduces the gas heating effect, and thus maintains a lower *E/N* value.

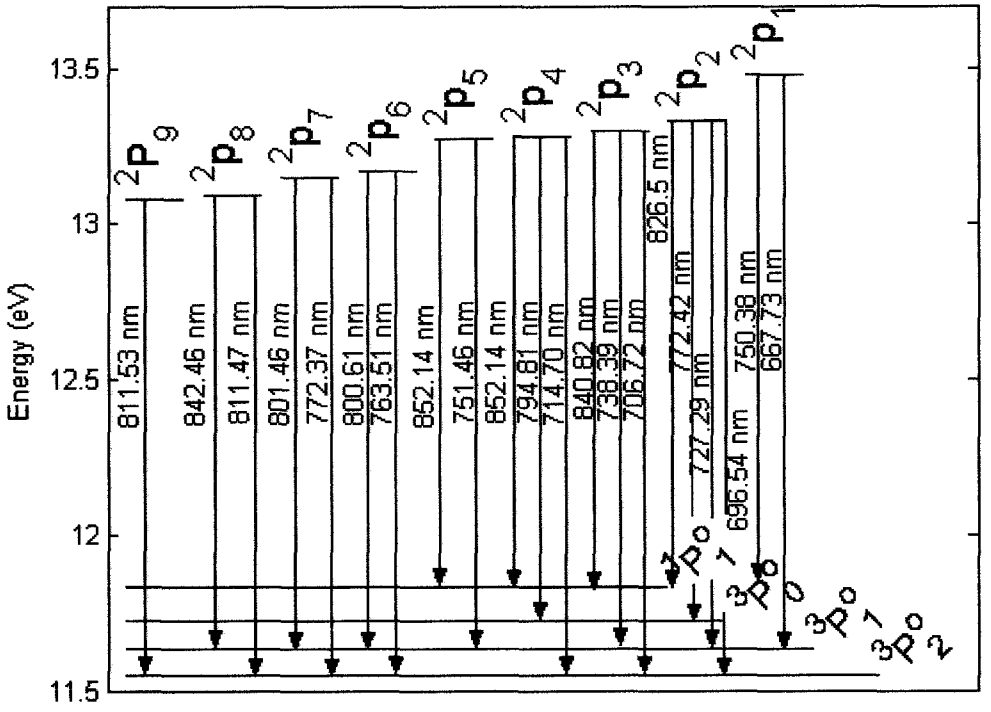


**Figure 4.6: Partial energy level diagram of Ar I and associated emission recorded from the Ar microplasma. Observed strong Ar I emissions are shown by downward arrows.**

In the argon microplasmas, Ar flow rates are 9 slpm with varying concentrations of $N_2$ and $H_2$. Like helium microplasmas, dimers [8, 17-20] and dimer ions [17, 19, 21-24] may be formed in atmospheric pressure argon microplasmas. UV/VUV spectra have already validated the formation of argon dimer and dimer ions and the importance of VUV photons from 2nd continuum for the microplasma breakdown has been discussed (Chapter 3). Figure 4.6 shows a partial energy level diagram of atomic Ar. Figures 4.7a,b show numerous strong atomic emission of in the visible and near IR regions. Several

weak emissions from excited $Ar^+$ are also observed in 400-600 nm region. (In contrast, note that the emissions from ionic helium are completely absent in the He microplasmas.)

A partial energy level diagram of argon is shown in Fig 4.6, where only the most intense transitions of the Ar microplasmas are labeled. The spin quantum number is not a good quantum number [25], so that L-S coupling does not apply and Paschen notation is used. Exceptions are the *1s* (Paschen notation) states which are described by the LS scheme. The *1s* state has four energy levels (*J=0, 1, 1* and *2*). For these levels and the ground state it is more convenient to use the Russell-Saunders (LS) scheme: the first four excited levels, namely, $^3P^o_2$, $^3P_1$, $^3P^o_0$, and $^1P_1$ and the ground state is $^1S_0$. The $^3P^o_0$ and $^3P^o_2$ are metastable states of argon while the other two excited states are coupled to the ground state via resonance transition and are linear combination of the *J=1* states ($^3P^o_1$ and $^1P^o_1$). Intense transitions are observed from the *2p* (*2p1* to *2p10* in Paschen notation) states to $^1P$ state and $^3P$ states (Table 4.4). All these states along with high lying states are thought to play an important role in sustaining RF (13.56 MHz) driven atmospheric pressure hollow slot Ar microplasmas.

**Table 4.4: Wavelengths (nm) of Ar *2p-1s* allowed transitions observed from Ar microplasmas. Wavelength table is taken from the ref. [26].**

| | *2p1* | *2p2* | *2p3* | *2p4* | *2p5* | *2p6* | *2p7* | *2p8* | *2p9* | *2p10* |
|---|---|---|---|---|---|---|---|---|---|---|
| *1s2* | 750.4 | 826.5 | 840.8 | 852.1 | *858.1 | 922.4 | 935.4 | 978.5 | | 1148.8 |
| *1s3* | | 772.4 | | 794.8 | | | 866.8 | | | 1047.0 |
| *1s4* | *667.7 | 727.3 | 738.4 | 747.1 | 751.5 | 800.6 | 810.4 | 842.5 | | 965.5 |
| *1s5* | | 696.5 | 706.5 | 714.7 | | 763.5 | 772.4 | 801.5 | 811.5 | 912.3 |

* Intensity is very weak.

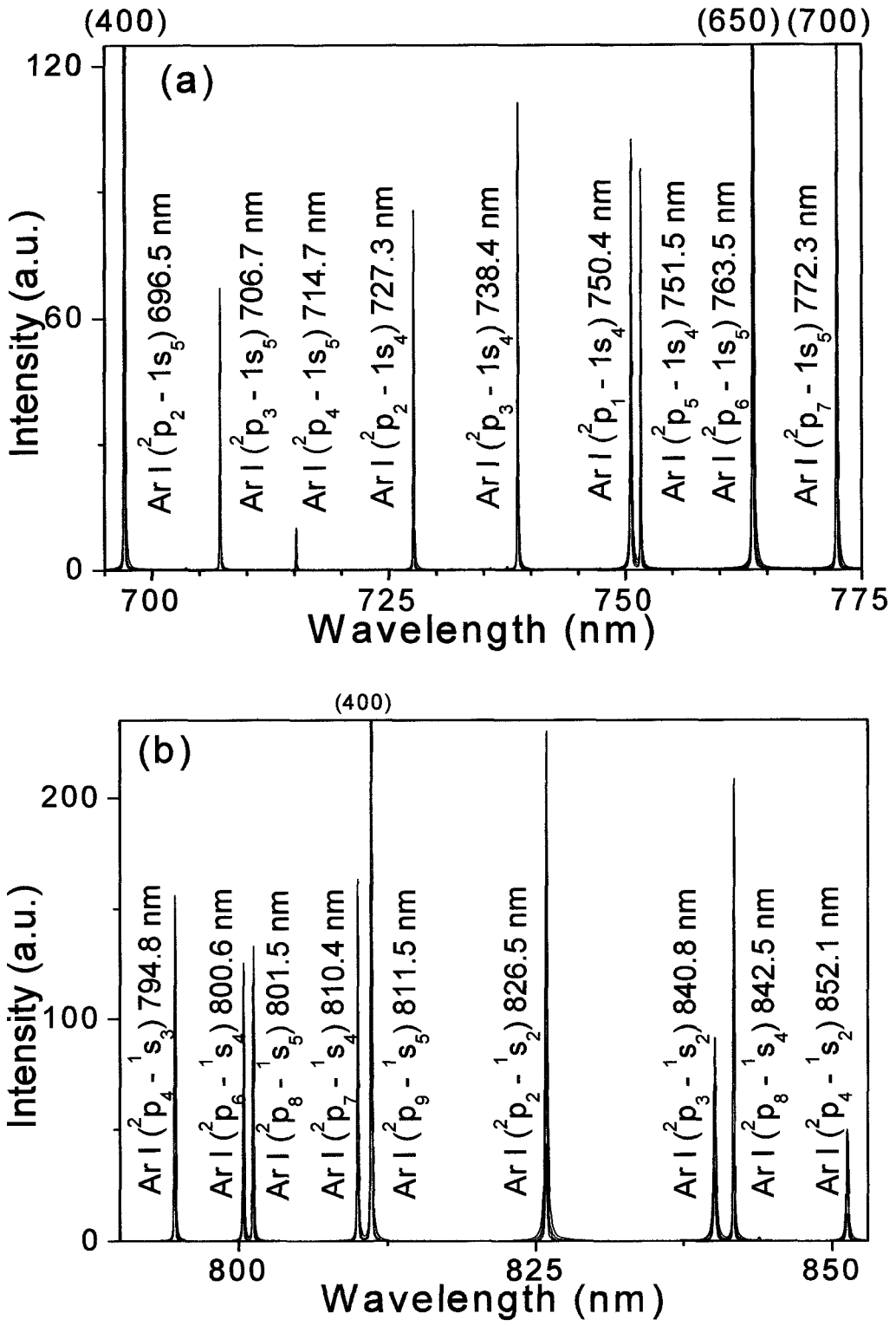


**Figure 4.7: Strong Ar I emissions emitted from the hollow slot microplasmas are labeled. For clarity, the emission transitions are divided into two regions: (a) 690 to 775 nm region and (b) 775 to 875 nm region. Relatively weak emissions from Ar I and Ar II are observed in the 400-690 nm region. The plasma conditions are: Ar flow rates are 9 slpm with varying $H_2$ flow rates (0.0 sccm (black), 9 sccm (red), 18 sccm (green) and 37 sccm (blue)).**

**Table 4.5: Einstein A coefficients for different atomic transitions of atomic Ar [27].**

| $\lambda$ (nm) | $A_{ki}$ ($10^6$ $s^{-1}$) | Lower State | Upper State | $E_l$-$E_u$ |
|---|---|---|---|---|
| 667.73 | 0.24 | $1s_4$ ($^3P^o_1$) | $2p_1$ | 11.62-13.48 |
| 696.54 | 7.2 | $1s_5$ ($^3P^o_2$) | $2p_2$ | 11.55-13.33 |
| 706.72 | 4.4 | $1s_5$ ($^3P^o_2$) | $2p_3$ | 11.55-13.30 |
| 714.70 | 0.7 | $1s_5$ ($^3P^o_2$) | $2p_4$ | 11.55-13.28 |
| 727.29 | 1.9 | $1s_4$ ($^3P^o_1$) | $2p_2$ | 11.62-13.33 |
| 738.39 | 8.9 | $1s_4$ ($^3P^o_1$) | $2p_3$ | 11.62-13.30 |
| 750.38 | 45 | $1s_2$ ($^1P^o_1$) | 2p1 | 11.83-13.48 |
| 751.46 | 44 | $1s_4$ ($^3P^o_1$) | $2p_5$ | 11.62-13.27 |
| 763.51 | 27.4 | $1s_5$ ($^3P^o_2$) | $2p_6$ | 11.55-13.17 |
| 772.37 | 5.4 | $1s_5$ ($^3P^o_2$) | $2p_7$ | 11.55-13.15 |
| 772.42 | 12.5 | $1s_3$ ($^3P^o_0$ | $2p_2$ | 11.72-13.33 |
| 794.81 | 19 | $1s_3$ ($^3P^o_0$) | $2p_4$ | 11.72-13.28 |
| 800.61 | 4.6 | $1s_4$ ($^3P^o_1$) | $2p_6$ | 11.62-13.17 |
| 801.47 | 9.5 | $1s_5$ ($^3P^o_2$) | $2p_8$ | 11.55-13.09 |
| 810.36 | 26 | $1s_4$ ($^3P^o_1$) | $2p_6$ | 11.62-13.15 |
| 811.53 | 35 | $1s_5$ ($^3P^o_2$) | $2p_6$ | 11.55-13.08 |
| 826.45 | 17 | $1s_2$ ($^1P^o_1$) | $2p_2$ | 11.83-13.33 |
| 840.82 | 23 | $1s_2$ ($^1P^o_1$) | $2p_3$ | 11.83-13.30 |
| 842.46 | 21 | $1s_4$ ($^3P^o_1$) | $2p_8$ | 11.62-13.09 |
| 852.14 | 13 | $1s_2$ ($^1P^o_1$) | $2p_4$ | 11.83-13.28 |
| 866.79 | 2.6 | $1s_2$ ($^1P^o_1$) | $2p_7$ | 11.72-13.15 |

Decrease in the intensities of the argon atomic lines is observed for upstream hydrogen addition, while upstream nitrogen addition show oscillatory changes in line intensities. Numerous weak transitions of atomic argon from higher energy levels are observed. Among the ten excited states described ($2p_1$ through $2p_{10}$), transitions originating from the $2p_{10}$ level are beyond the spectral region of our detection system.

4.3.2a Argon-Hydrogen Plasma

Addition of upstream hydrogen to the argon microplasmas decreases the intensities of the Ar I transitions, which we believe is due to a decrease in the average electron on energy [28] and quenching of Ar metastables[19]. The quenching rate constant

[19] Molecular hydrogen is very effective in destroying the Ar metastables [29].

**Table 4.6: Integrated intensities of atomic Ar I emissions from Ar-$H_2$ microplasmas with constant Ar flow rate of 9 slpm and varying hydrogen flow rate as indicated in the table.**

| $\lambda$ (nm) | $H_2$ flow rate (First Row) Integrated Intensity (a.u.) | | | | Energy (eV) | | |
|---|---|---|---|---|---|---|---|
| | 0 sccm | 9 sccm | 18 sccm | 37 sccm | $E_u$ | $E_l$ | $\Delta E$ |
| 667.73 | 1 | 0.84 | 0.71 | 0.46 | 13.48 | 11.62 | 1.86 |
| 696.54 | 1 | 0.51 | 0.36 | 0.20 | 13.33 | 11.55 | 1.78 |
| 706.72 | 1 | 0.77 | 0.56 | 0.33 | 13.3 | 11.55 | 1.75 |
| 714.70 | 1 | 0.6 | 0.56 | 0.27 | 13.28 | 11.55 | 1.73 |
| 727.29 | 1 | 0.46 | 0.34 | 0.18 | 13.33 | 11.62 | 1.71 |
| 738.39 | 1 | 0.76 | 0.55 | 0.30 | 13.30 | 11.62 | 1.68 |
| 750.38 | 1 | 0.82 | 0.61 | 0.37 | 13.48 | 11.83 | 1.65 |
| 751.46 | 1 | 0.49 | 0.38 | 0.25 | 13.27 | 11.62 | 1.65 |
| 763.51 | 1 | 0.696 | 0.45 | 0.25 | 13.17 | 11.55 | 1.62 |
| *772 | 1 | 0.57 | 0.36 | 0.19 | 13.33 | 11.72 | 1.61 |
| 794.81 | 1 | 0.81 | 0.45 | 0.25 | 13.28 | 11.72 | 1.56 |
| 800.61 | 1 | 0.79 | 0.38 | 0.21 | 13.17 | 11.62 | 1.55 |
| 801.47 | 1 | 0.93 | 0.47 | 0.28 | 13.09 | 11.55 | 1.54 |
| 810.36 | 1 | 0.79 | 0.54 | 0.27 | 13.15 | 11.62 | 1.53 |
| 811.53 | 1 | 1.12 | 0.58 | 0.35 | 13.08 | 11.55 | 1.53 |
| 826.45 | 1 | 0.60 | 0.47 | 0.16 | 13.33 | 11.83 | 1.50 |
| 840.82 | 1 | 0.97 | 0.51 | 0.29 | 13.30 | 11.83 | 1.47 |
| 842.46 | 1 | 0.81 | 0.54 | 0.25 | 13.09 | 11.62 | 1.47 |
| 852.14 | 1 | 0.65 | 0.42 | 0.23 | 13.28 | 11.83 | 1.45 |

* Overlap of two transitions.

for the $2p_6$ state of Ar I by $H_2$ ($6.8 \times 10^{-10}$ $cm^{-3}$ $sec^{-1}$) is larger than the quenching rate for $2p_1$ ($0.27 \times 10^{-10}$ $cm^{-3}$ $sec^{-1}$), and $2p_8$ ($5.8 \times 10^{-10}$ $cm^{-3}$ $sec^{-1}$) [30] (collisional quenching of Ar* by H or $H_2$ should be insignificant since the partial pressure of $H_2$ is very small and lifetimes of Ar* are small). The emission spectra of Ar-$H_2$ show that the emission intensities of the transitions originating from the $2p_6$ state (763 nm and 800 nm) decrease at a faster rate compared to the transitions originating from the $2p_1$ and $2p_8$ states (750, 667, 800, 763 and 811 nm) but at smaller rate compared to the $2p_5$ state (752 nm) (although this state has smaller quenching rate constant by $H_2$ ($4.10 \times 10^{-10}$ $cm^{-3}$ $sec^{-1}$)). This observation indicates that the collisional quenching of $Ar^*$ may have contributions from other species. It is likely that excited Ar atoms are collisionally quenched by the same species

(Ar) owing to argon partial pressure being ~ 200 times larger than $H_2$ partial pressure (even though self quenching rates of these states ($2p_1$, $2p_5$ and $2p_8$ ) are order of magnitude smaller as compared to quenching by $H_2$). The observation also indicates that the transitions with larger self quenching rate for the excited Ar state suffers the largest decrease in intensity with addition of $H_2$. This behavior is not well understood. At present it is believed that gas heating may increase considerably with the addition of $H_2$ due to filamentary channels, thus increases self-quenching.

**Table 4.7: Measured full width at half maximum (FWHM) and width at 10% (of normalized intensity) for 2p-1s transitions for pure Ar microplasmas are tabulated below.**

| Wavelength (nm) | FWHM $\Delta\lambda$(nm) | At 10% intensity, $\Delta\lambda$ |
|---|---|---|
| *667.73 | - | - |
| 696.54 | 0.124 | 0.250 |
| 706.72 | 0.127 | 0.250 |
| 714.70 | 0.131 | 0.260 |
| 727.29 | 0.127 | 0.225 |
| 738.39 | 0.138 | 0.257 |
| 750.38 | **0.174** | **0.450** |
| 751.46 | 0.120 | 0.250 |
| 763.51 | 0.127 | 0.250 |
| 772.4 | 0.125 | 0.242 |
| 794.81 | 0.130 | 0.252 |
| 800.61 | 0.131 | 0.260 |
| 801.47 | 0.141 | 0.254 |
| 810.36 | 0.138 | 0.285 |
| 811.53 | 0.124 | 0.276 |
| 826.45 | **0.193** | **0.506** |
| 840.82 | **0.218** | **0.585** |
| 842.46 | 0.121 | 0.251 |
| 852.14 | **0.222** | **0.557** |
| *858.1 | - | - |
| 866.79 | 0.128 | 0.252 |

* Intensity is very weak.

Transitions from the $2p_2$ states (826.5 nm, 772.4 nm, 727.3 nm and 696.5 nm) have Einstein A coefficients (in $10^6$ $sec^{-1}$) of ~17, 12.5, 1.9 and 6.2 respectively (Table 4.5) [27]. Table 4.6 shows that for addition of 9 sccm of $H_2$, the intensity drop is a maxi-

mum for transitions with the minimum Einstein A coefficient, and this trend is generally followed for higher $H_2$ flow rates for transitions originating from $2p_3$ and $2p_4$, $2p_5$, $2p_7$ states ($2p_6$ and $2p_8$ do not follow the trend)[20]. This observation indicates the plasma is optically thin at these wavelengths. Since Einstein's A coefficient is inversely proportional to the spontaneous radiative life time [32], non-radiative collisional deactivation may account for the intensity reduction. This behavior is consistent with the previous hypothesis of self quenching.

The transitions (750.4 nm, 826.5 nm, 840.8 nm and 852.1 nm) that involve the $1s_2$ ($^1P_1$-4s'[1/2]$^0_1$) state as the terminating state, show considerable line broadening in relation to other *2p-1s* transitions (these transitions are shown in bold in Table 4.7). This observation can not account for with collisional broadening or radiative recombination broadening. If the broadening were the effect of collisional broadening, transitions from the same upper level would exhibit similar broadening (and this is not observed). Radiative recombination of $Ar_2^+$ can also not account for this behavior either because $Ar_2^+$ ( ~14.5eV) has a strong probability of dissociative recombination to the *3d* and *3d'* states (of energy 13.86 and 14.30 eV) [33] as opposed to *2p* states. These broadened transitions have the same lower energy level ($^1P_1$) state, so the broadening is most likely associated with the lower level. The broadening may be a consequence of the splitting of the Stark levels of the lower energy state, but more theoretical work and simulation are required to understand this behavior.

[20] Exception for $2p_6$ and $2p_8$ levels could be due to their larger integral cross sections [31]. Also the lower lying levels, such as $2p_8$ levels is expected to show different behavior due to collisional coupling between $2p_8$ and $2p_9$ pair [30] and collisional effect with slow electron from metastable states.

4.3.2b Argon-Nitrogen Plasma

In the Ar-$N_2$ plasmas, intensities of transitions from the $N_2(C)$ to $N_2(B)$ state increase with increased upstream $N_2$ flow rate as expected. Most of the molecular transitions lie in the range 300-500 nm (2nd order diffraction transitions are observed at higher wavelengths). No $N_2^+$(B-X) transitions are observed in the Ar-$N_2$ plasma. The energy required to form $N_2^+$(X) is 15.6eV, which is greater than the ionization energy of the Ar atom and much higher than the metastable energies of argon atom, thus precluding Penning ionization. Since $N_2$ curtails the high energy electron tail [34] of the argon discharge, direct electron impact excitation to $N_2^+$ (B) is also highly improbable.

The addition of a small amount of $N_2$ (5sccm) into the Ar flow decreases the intensity of argon atomic transitions. However, addition of 10 sccm $N_2$ increases the intensities of the atomic transitions in comparison to the 5sccm case, but yields intensities less than those of the pure argon microplasma. Further increase in $N_2$ addition (20sccm) to the main stream decreases the atomic transition intensities. This nonlinear behavior is not well understood but suggests multiple processes are in competition. It is known that addition of $N_2$ decreases the high energy tail of the EEDF [34], which in turn decreases the excitation and ionization of the argon atoms. It is likely that the addition of $N_2$ not only quenches the metastables of Ar but also prevents formation of argon metastables [35]. Moreover elastic energy loss of electrons to $N_2$ is large compared to $H_2$. These factors may contribute to the reduction of stepwise ionization and $Ar_2^+$ formation. Therefore, in contrast to the He plasmas, it is likely that the Ar plasmas are sustained predominantly by atomic ions as opposed to dimer ions.

## 4.4 Cathode Sputtering

Cathode sputtering by Ar and combinations of Ar with other molecular gases ($H_2$, $N_2$, $O_2$ etc.) is discussed in the literature (e.g. ref. [28, 36] and the references there in). In ref. [36], sputtering of a Cu cathode by Ar, $Ar^+$, $H_2^+$, $H^+$, $ArH^+$ etc. has been described in detail on the basis of emission spectra (but under very high excitation voltage (1000 V)).

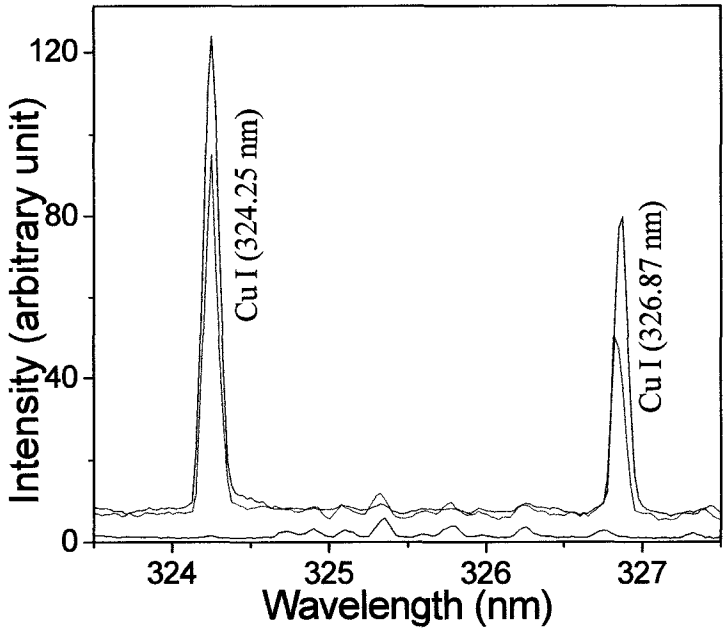


**Figure 4.8: Cu I resonance lines emitted from the Ar-$H_2$ microplasma. The flow rate of Ar is 9 slpm and the varying hydrogen flow rates are 0.0 sccm (black), 9 sccm (red), and 37 sccm (blue).**

In this work electrode sputtering is also observed in optical emission. Figure 4.8 shows strong Cu I resonance transitions in argon microplasmas with admixtures of $H_2$. Ion impact is responsible for dislodging Cu atoms from the cathode. We believe the ion responsible is $ArH^+$. It is interesting to note that the Cu I atomic transitions do not appear in detectable levels in pure Ar, pure He, He-$H_2$ or He-$N_2$ plasmas. Therefore it can be concluded that energetic Ar, $Ar^+$, $N_2^+$, $H_2^+$ or $H^+$ do not have significant contributions to cathode sputtering. And, since there is no cathode sputtering from argon ions in the pure argon plasma it can be concluded that argon ions undergo efficient symmetrical charge

transfer (SCT) [7, 28] reaction (R4.13) and the ions do not gain sufficient kinetic energy from the electric field to dislodge the Cu atoms from the cathode.

$$Ar^+(fast) + Ar(slow) = Ar^+(slow) + Ar(fast) \qquad R\ 4.13$$

$ArH^+$ is believed to be responsible or the copper sputtering. In contrast to $Ar^+$, $ArH^+$ does not have a neutral counterpart [37] and can not undergo symmetrical charge exchange, thus it can accelerate through the plasma and sheath electric field towards the cathode. Hence, the $ArH^+$ can impinge on the cathode with far higher energies than $Ar^+$ for the microplasmas of our consideration. Increases in the Cu I (323 nm) resonance transition with increasing $H_2$ partial pressure in Ar plasmas have been observed by other researchers [38], possibly because of increased $ArH^+$ concentration. The possible paths for $ArH^+$ formation in Ar-$H_2$ microplasma are listed below (R4.14-R4.17) [35]:

$$Ar^{**} + H = ArH^+ + e \qquad R\ 4.14$$

$$Ar_2^+ + H_2 = ArH^+ + H + Ar \qquad R\ 4.15$$

$$Ar^{**} + H_2 = ArH^+ + H^- \qquad R\ 4.16$$

$$Ar^+ + H_2 = ArH^+ + H \qquad R\ 4.17$$

$$He_2^+ + H_2 \longrightarrow He + He + (H_2^+)^* \qquad R4.18$$

$$He^* + H_2 \longrightarrow He + (H_2^+)^* \qquad R4.19$$

$$(H_2^+)^* + e \longrightarrow H^* + H + K.E. \qquad R4.20$$

**4.5 Wing Broadening of Atomic H Transitions**

Addition of upstream $H_2$ to the helium and argon microplasmas results in H atomic emissions. Figure 4.9 and 4.10 show two transitions of hydrogen lines at 486 nm and 656 nm respectively. A very weak line at 434 nm is also detected. In the He-$H_2$ plasma, considerable wing broadening for these transitions is observed, but no such wing

broadening is present in the Ar-$H_2$ plasmas. Since Ar metastables are unable to excite $H_2$ to $(H_2^+)^*$ or $H_2^+$ due to energy mismatch[21], the observed H I emissions in the Ar-$H_2$

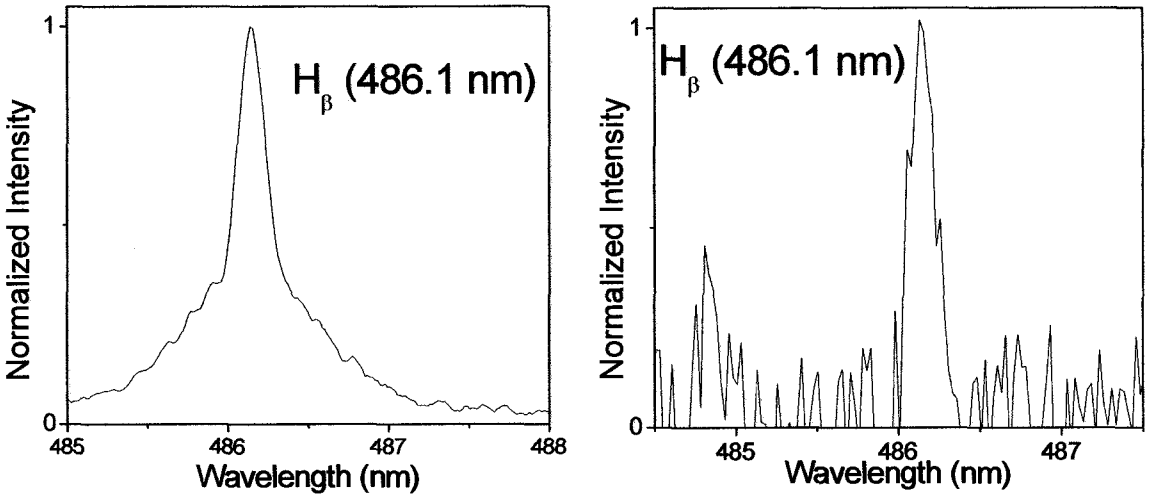


**Figure 4.9: $H_\beta$ line at 486 nm from He-$H_2$ microplasma (left) and from Ar-$H_2$ (right) microplasma. He and Ar flow rates are 2 slpm and 9 slpm respectively, and. $H_2$ flow rates are 37 sccm.**

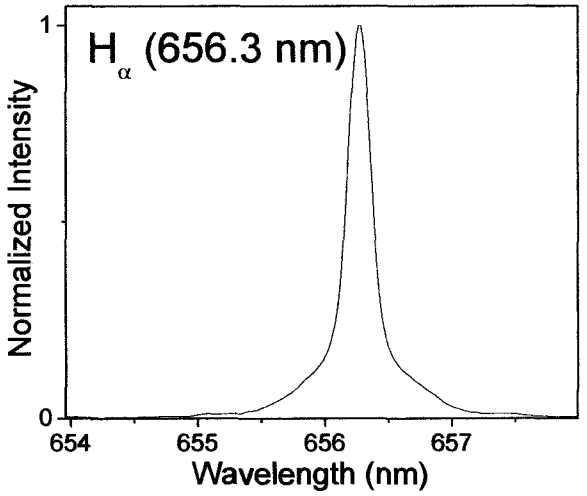


**Figure 4.10: $H_\alpha$ line at 656 nm from He-$H_2$ microplasma. The plasma condition is: He flow rate is 2 slpm and $H_2$ flow rate is 37 sccm.**

plasma are judged to be a consequence of direct electron impact excitation of atomic H from the ground state. In the Ar-$H_2$ plasma a dissociation continuum is observed (Chapter 3). On the contrary, in the He-$H_2$ microplasma no $H_2$ dissociation continuum is present;

[21] $He_2^+$ or He* can form $(H_2^+)^*$ via reactions R4.18 and R4.19.

instead there is emission from molecular $H_2$ (Figure 3.4a), which we attribute to radiative recombination(Chapter3). From the above, it is concluded that production of excited atomic H* (and its emission) in the He-$H_2$ plasma is due to the recombination effect of the $H_2^+$ via reactions R 4.20 and that the recoil energy of the atoms leads to the observed wing broadening.

**4.6 Electron Number Density ($n_e$) Calculation**

Optical transitions are affected by different line broadening mechanisms depending on their environment. Perturbation due to ambient charge particle density (electric field) gives rise to Stark broadening. In the microplasmas, it is assumed that the perturbation of the atomic levels is predominantly due to the motion of the charged particles (electrons). Therefore, Stark broadening can (in principle) provide number density measurements. The theory of Stark broadening of atomic H is very well developed and it has been extensively used to determine electron number density [39-44]. In these $n_e$ measurements small amounts of atomic H are typically seeded into the plasma flow without significantly altering the plasma properties.

The optical data acquisition for our Stark measurements is done using a high resolution 1 m SPEX 1401 spectrometer to minimize the effect of instrumental broadening. The experimental setup remains the same as shown in Figure 4.1, with the Jarrel-Ash monochromator replaced by the 1 m SPEX 1401 monochromator. The best possible resolution of this monochromator, $\Delta\lambda$, is ~ of 0.01 nm. Due to the low emission intensity of the $H_\beta$ line at 486.1 nm, wider slit opening (20 μm) is employed, and the resolution reduces to, $\Delta\lambda$ ~0.02 nm for He-$H_2$ microplasma.

In the He-$H_2$ the atomic H lines at 486.1 nm and 656.1 nm can be used to determine plasma density from the Stark lineshape profile. The Stark broadening of the 486.1 nm $H_\beta$ line has a very weak dependence on the electron temperature but strong dependence on the electron density [44]. The following equation relates the number density to the Stark half-width at half-maximum (HWHM) [44]:

$$\Delta\lambda_{Stark}[A^o] = 1.740X10^{-10}(n_e[cm^3])^{2/3} \quad 4.1$$

In addition to Stark broadening, Doppler broadening, natural broadening, resonance broadening, van der Walls broadening, and instrumental broadening are also present in the measured atomic lines. The effects of all broadening must be accounted for in the Stark profile analysis. Natural line broadening of atomic transitions in the visible range is negligible. Resonance broadening of any atomic transition requires the perturbing atom to be the same kind [40], and in the He-$H_2$ microplasma, the $H_2$ flow rates are small enough for the resonance broadening to be negligible [45]. Therefore, in addition to the Stark broadening the major contributors to the line broadening are Doppler broadening, van der Walls broadening and instrumental broadening. Mathematical expressions employed to obtain the Doppler broadening [44] and the van der Walls broadening [45] at half width at half maximum are:

$$\Delta\lambda_{Doppler}[A^o] = 1.74X10^{-3}T_g^{1/2} \quad 4.2$$

$$\Delta\lambda_{vanderWalls}[A^o] = 4.09\times10^{-13}\lambda^2\left(\bar{\alpha}\bar{R}^2\right)^{2/5}\left(\frac{T_g}{\mu}\right)^{3/10} n_{He} \quad 4.3$$

where, $T_g$ is gas temperature, $\lambda$ (4861.1 A ) is the transition wavelength, $a_0$ is Bohr radius in cm, $\bar{\alpha}$ ($1.38\text{x}\,a_0^3\,\text{cm}^3$) is polarizability of He, $\bar{R}^2$ ($635\text{x}\ a_0^2$) (is a parameter determined

from H ionization energy level and the levels associated with the 4861.1 A transition), $\mu$ is the reduced mass of the perturber (He), and $n_{He}$ is the number density of He atom.

The Stark and the van der Walls line profile are both Lorentzian while the instrumental broadening is Gaussian [43, 45]. The resulting line shape profile is Voigt profile (convolution). Due to complexity of the deconvolution process, a simple mathematical expression [46] has been applied to calculate the FWHM of the total Lorentzian line shape:

$$\Delta\nu_{Voigt}[s^{-1}] = \sqrt{c^2\Delta\nu_L^2 + \Delta\nu_G^2} + (1-c)\Delta\nu_L \qquad 4.4$$

where, c~0.34, $\Delta\nu_L$ is Lorentzian FWHM, and $\Delta\nu_G$ is the Gaussian FWHM.

Lorentzian line widths add in a simple additive way [32], so that, equations 4.1-4.4 can be used to find the electron number density.

**Table 4.8: Half Widths at Half Maximum in [$A^0$] for $H_\beta$ line at 4861 $A^0$ and calculated electron number densities.**

| Plasma | Stark | van der Walls at 1atm. (1.25 atm.) | Instrumental | Doppler | $n_e$ (in $m^{-3}$) |
|---|---|---|---|---|---|
| He-$H_2$ | 0.15 | 0.68 (0.88) | 0.1 | 0.04 | $[2.5\pm0.5]\times10^{19}$ ($[6.3\pm0.5]\times10^{18}$) |

The contributions of the van der Walls broadening, instrumental broadening, Stark broadening and resulting $n_e$ are presented in the Table 4.8. Instrumental broadening is taken from the provided data by Jobin-Yvon Inc. for the spectrometer employed.

The number density for He microplasma (at 1atm.) obtained from the Stark HWHM is found to be $2.5\times10^{19}$ $m^{-3}$ (Table 4.8). This value is ~5 times compared to the calculated value ($5*10^{18}$ $m^{-3}$) in the earlier chapter (Table 2.4). We judge that the discrepancy arises primarily from the pressure broadening (van der Walls) calculation (the high flow rate of gas through the slot of the microplasma device cause the pressure inside the

slot to be higher than the 1 atm. used in the van der Walls broadening). Our calculation (Table 4.8) also provides electron density calculation at higher pressure (1.25 atm.), the calculated electron density[22] (~$6*10^{18}$ $m^{-3}$) is very close to the calculated value in the earlier chapter ($5*10^{18}$ $m^{-3}$) (Table 2.4). In addition, the instrumental broadening may have some contribution to the $n_e$ calculation. Neglecting the effect of the ions in the broadening may add second order effects to the line broadening [47]. Along with spatial measurement, a more careful analysis is therefore required with the inclusion of precise instrumental broadening and more appropriate calculation of van der Walls broadening.

### 4.7 Electron Temperature ($T_e$) Calculation

Cunninghum [48] first proposed that the electron temperature ($T_e$) be measured from helium singlet and triplet line intensity ratios, utilizing the fact that the cross-section for excitation to the excited singlet states and triplet states are very different and are functions of electron energy. This method is valid for a tenuous plasma where direct process (DP) is dominant, i.e. all the emitting levels are considered to be excited from the ground level via electron impact. Then transition intensity from an upper level $f$ to a lower energy level $i$ can be expressed as [49]:

$$I_{fi} = N_0 n_e < Q_{fi}(v_e) v_e > h\nu_{fi} \qquad 4.5$$

where, $Q_{fi}(v_e)$ = excitation cross section to level $f$ from level $i$, $v_e$ = electron velocity, $h\nu_{fi}$ = energy of the emitted photon, $N_0$ = population in the level $i$, and, $n_e$ = electron density.

[22] Typically, Stark broadening in the quasi-static (used in this section) approximation is not a good choice for electron density calculation for $n_e$<$10^{19}$ $cm^{-3}$.

Similarly for another transition from level $k$ to level $i$ the transition intensity is:

$$I_{ki} = N_0 n_e < Q_{ki}(v_e) v_e > h\nu_{ki} \qquad 4.6$$

Thus, the ratio of the transition intensities yield:

$$\frac{I_{fi}}{I_{ki}} = \frac{< Q_{fi}(v_e) v_e > h\nu_{fi}}{< Q_{ki}(v_e) v_e > h\nu_{ki}} \qquad 4.7$$

The average values in the numerator and the denominator are function of the electron velocity (electron temperature). Therefore, the electron temperature can be calculated from the line intensity ratio for the helium plasma provided that the EEDF is Maxwellian and transition upper levels are populated by means of direct electron impact excitation from same lower levels (in this case from the ground state He ($1s\ ^1S$)).

In the high density plasma other excitation processes (such as metastable-slow electron impact excitation, cascading from upper levels to the emitting levels, self-absorption, radiative recombination, and collision induced emission) may be comparable to direct electron impact excitation from the ground state. In such circumstances the electron temperature measurement becomes very complicated. It is believed the contributions from the metastable-slow electron impact excitation (R4.8) is the most prominent secondary process (SP) in the microplasmas of interest. Therefore, to determine the Cunninghum method be applied, it is of utmost importance to determine the effect of the metastable-slow electron impact excitation processes in the atmospheric pressure microplasmas.

The ratio of the intensity of the triplet (388 nm) to the singlet (706 nm) transition is employed as a probe to determine the effect of the SP versus direct electron impact excitation from the ground state [50]. Table 4.9 shows that the observed He-$H_2$ plasma with

higher $H_2$ concentration can be used to estimate the relative electron temperature as well as metastable effects. Clearly He-$O_2$ plasma is not a good choice due to higher values of the $I_{388}/I_{706}$ ratio (Table 4.10) that indicate other processes contribute considerably in populating the upper states of the He atomic transitions. Interference of the 388 nm line with the first negative bands of $N_2^+$ prevent us from applying this method for He-$N_2$ microplasmas.

There are several options in choosing the triplet-singlet transition pairs. Transition pairs that originate from high-lying states have relatively lower cross sections for the secondary processes, and thus usually provide better determination of electron temperature. In the He microplasmas, transitions from n≥5 level are absent and transitions originating from *n=4* levels are very weak in the microplasma. However, *n=4* level is considered as the only choice for the $T_e$ calculation because of the smaller secondary effect compared to *n=3* levels. Therefore, the ratio of the intensities of the transitions originating from 4p $^3$P (471 nm) and 4p $^1$P (504 nm) levels are considered for $T_e$ calculation. Note that there is slight interference from the 1st negative band of $N_2^+$ at 471 nm.

The excitation cross section can be written as [49]:

$$Q_{if}(e) = Q_{if}(\varepsilon_m)\frac{\varepsilon_e - \varepsilon_\alpha}{\varepsilon_m - \varepsilon_\alpha}\exp\left[1 - \frac{\varepsilon_e - \varepsilon_\alpha}{\varepsilon_m - \varepsilon_\alpha}\right] \qquad 4.8$$

where, $Q_{if}(\varepsilon_m)$ = maximum of cross-section function, $\varepsilon_e$ = electron energy, $\varepsilon_m$ = energy at maximum cross-section, and $\varepsilon_\alpha$ = threshold energy.

Averaging the cross section function over a Maxwellian distribution and using equation 4.7, yields [49]:

$$\frac{I_{fi}}{I_{ki}} = \frac{I_{\alpha}}{I_{\beta}} = \frac{\lambda_{\beta}}{\lambda_{\alpha}} \frac{Q_{\alpha}(\varepsilon_m)}{Q_{\beta}(\varepsilon_m)} \left[ \frac{3\varepsilon_{m\beta} - 3\varepsilon_{\alpha\beta} + 2T}{3\varepsilon_{m\alpha} - 3\varepsilon_{\alpha\beta} + 2T} \right]^2 \left[ \frac{\varepsilon_{m\alpha} - \varepsilon_{\alpha\alpha}}{\varepsilon_{m\beta} - \varepsilon_{a\beta}} \right]$$

$$X \left[ \frac{2T(2\varepsilon_{m\alpha} - \varepsilon_{a\alpha}) + 3\varepsilon_{a\alpha}(\varepsilon_{m\alpha} - \varepsilon_{a\alpha})}{2T(2\varepsilon_{m\beta} - \varepsilon_{a\beta}) + 3\varepsilon_{a\beta}(\varepsilon_{m\beta} - \varepsilon_{a\beta})} \right] \quad 4.9$$

where $\alpha$ and $\beta$ correspond to 471 nm and 504 nm transitions respectively (in this particular case).

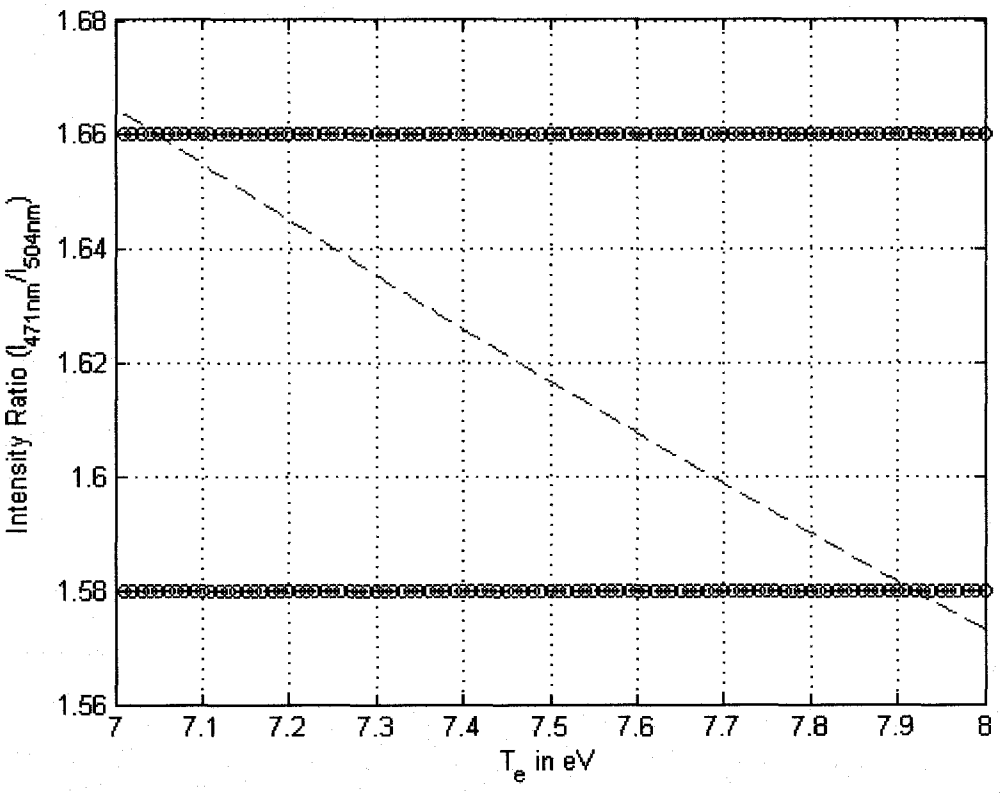


**Figure 4.11: Simulated intensity ratio (red) and observed intensity ratio for He I lines emitted from He-$H_2$ microplasmas. The lower and upper blue lines represent 20 and 10 sccm flow rate of $H_2$ in with 2 slpm of He. The crossing of the red line and blue line give the respective electron temperature.**

The values of the maximum cross-sections and corresponding energies are taken from [12]. Threshold energies are for the respective transitions are taken from [6]. Simulated line intensity ratio for different $T_e$ (in eV) and the measured ratio of the transitions from the optical data are plotted in Figure 4.11. The crossing of the simulated ratio (in

red) and the measured ratio are the electron temperature (~ 7±3 eV) of the respective microplasmas. There are large errors associated with the measured intensity ratios (Table 4.11) due to background errors from weak line intensities and from the interference of 1st negative band of $N_2^+$.

The value of the electron temperature is large as compared to the typical values (1~2 eV ) for similar atmospheric pressure plasmas. We judge that this discrepancy primarily arise from the path integrated optical signal. The *n=4* to *n=2* transitions mostly occurs in the negative glow region as it is known that electrons with large $T_e$ value exist in the negative glow region (in a low pressure hollow cathode He plasma, Gill and Webb [51] found electrons in three energy groups (0.5, 5 and 25 eV) in the negative glow region). Besides, the SP and the collisional deactivation of the excited states in addition to poor intensities of the transitions may contribute to this discrepancy. Therefore a more rigorous study with the inclusion of the SP, and a spatial measurement is required in determining the $T_e$ value more accurately.

**Table 4.9: Triplet-singlet line intensity ratios of He-$H_2$ microplasmas (from *n=3* to *n=2* levels). He flow rate is 2 slpm. Intensities are in arbitrary unit.**

| $H_2$ (sccm) | 706 nm (triplet) | 728 nm (singlet) | 388nm (triplet) | Ratio ($I_{706}/I_{728}$) | Ratio ($I_{388}/I_{728}$) |
|---|---|---|---|---|---|
| 0 | 84.61 | 11.66 | 36.09 | 7.26 | 3.10 |
| 9 | 66.79 | 9.54 | 26.30 | 7.01 | 2.76 |
| 18 | 54.5 | 7.36 | 8.30 | 7.41 | 1.13 |
| 37 | 52.53 | 9.13 | 9.03 | 5.76 | 0.99 |

**Table 4.10: Triplet- singlet line intensity ratios of He-$O_2$ microplasmas (from *n=3* to *n=2* levels). He flow rate is 2 slpm. Intensities are in arbitrary unit.**

| $O_2$ (sccm) | 706 nm (triplet) | 728 nm (singlet) | 388nm (triplet) | Ratio ($I_{706}/I_{728}$) | Ratio ($I_{388}/I_{728}$) |
|---|---|---|---|---|---|
| 0 | 68.14 | 9.06 | 31.4 | 3.47 | 7.52 |
| 5 | 62.66 | 13.02 | 43.57 | 3.35 | 4.81 |
| 10 | 52.11 | 9.56 | 34.26 | 3.58 | 5.45 |
| 20 | 37.75 | 5.06 | 25.6 | 5.60 | 7.46 |

**Table 4.11: Triplet-single intensity ratio of He-$H_2$ plasma, excited state orbital quantum number, $n=4$. He flow rate is 2 slpm. Intensities are in arbitrary unit.**

| $H_2$ | 471 nm (triplet) | 504 nm (singlet) | Ratio ($I_{471}/I_{504}$) |
|---|---|---|---|
| 0 | 0.79 | 0.38 | 2.08 |
| 9 | 0.63 | 0.32 | 1.97 |
| 18 | 0.35 | 0.21 | 1.66 |
| 37 | 0.34 | 0.22 | 1.58 |

## 4.8 Conclusion

Optical spectra, $I(\lambda)$, for $300<\lambda<850$ nm, emitted from the hollow slot microplasma driven by RF (13.56 MHz) and operated in open air are presented in this chapter. The time-averaged optical spectra in the visible region provide a useful tool for atmospheric microplasma characterization. In the visible and IR region, most of the intense transitions originate from excited atoms. The molecular bands of $N_2$ are also dominate part of the visible region.

Both He and Ar microplasmas show changes in atomic emission intensity with upstream impurity addition ($H_2$, $N_2$ or $O_2$). Impurity addition causes changes to both the EEDF and metastable populations. These two factors are considered to be the major contributors to the decrease in the atomic emission intensities of the excited rare gas atoms observed in our work. In the atmospheric pressure rare gas microplasmas excited ion (atomic) emission is either not detectable or very weak which we attribute to charge exchange transfer and dimer ion formation. The cathode sputtering in the Ar-$H_2$ microplasma and the strong wing broadening of the atomic H emission in the He-$H_2$ microplasma supports the hypothesis that charge transfer mechanism is very effective in the atmospheric pressure microplasma.

Stark measurements are employed to estimate the electron number density ($n_e$) calculation. The $n_e$ value calculated from Stark broadening is higher (~5 times) compared to the calculated values using the modified Child-sheath law. This discrepancy stems primarily from the van der Walls broadening calculation. The calculated $n_e$ values from the optical measurement corresponds to the upper limit while the $n_e$ values calculated from the electrical measurements corresponds to the lower limit (since in the electrical measurement diffusions are not considered).

The electron temperature is calculated for He-$H_2$ microplasmas. The $T_e$ value obtained via He line intensity ratio method corresponds to very high value ~7±3 eV. This value is uncharacteristic for atmospheric pressure plasmas. The source of these high values may arise from the change of the discharge operation from diffuse glow to filamentary plasma or a combination of both. Another source of the discrepancy is the line of sight measurement that includes the negative glow region. A more precise model that includes the effect of slow electrons as well as collision induced emission along with the spatial observation will be helpful to determine the electron temperature more accurately.

Plasma characterization by means of optical observation in the visible range is complementary to UV/VUV measurements. Visible range emission spectroscopy provides information regarding microplasma sustaining mechanisms, trend of the EEDF, electron temperature, and electron number density.

**References:**


1. Kurunczi, P., J. Lopez, H. Shah, and K. Becker, *Excimer formation in high-pressure microhollow cathode discharge plasmas in helium initiated by low-energy electron collisions.*, International Journal of Mass Spectrometry, 2001. **205**(1-3): p. 277-283.
2. Becker, K.H., P.F. Kurunczi, and K.H. Schoenbach, *Collisional and radiative processes in high-pressure discharge plasmas.*, Physics of Plasmas, 2002. **9**(5): p. 2399-2404.
3. Motret, O., J.M. Pouvesle, and J.T. Stevefelt, *Spectroscopic study of the afterglow excited by intense electrical discharges in high-pressure helium hydrogen mixtures.*, J. Chem. Phys., 1985. **83**(3): p. 1095-1100.
4. Yokoyama, A., T. Ueno, and Y. Hatano, *Pulse radiolysis studies of the de-excitation process of excited argon atoms by $N_2$, $H_2$ and $D_2$.*, Chem. Phys., 1977. **22**: p. 459-466.
5. Wellenstein, H.F. and W.W. Robertson, *Collisional relaxation processes for the n=3 states of helium. II. Associative ionization.*, J. Chem. Phys., 1972. **56**(3): p. 1077-1082.
6. Striganov, A.R. and N.S. Sventitskii, *Tables of Spectral Lines of Neutral and Ionized Atoms*. 1968, New York-Washington: IFI/Plenum.
7. Raizer, Y.P., *Gas Discharge Physics*. 1991, New York: Springer. p.24.

8. Rahman, A., et al., *Absolute UV and VUV Emission in the 110-400 nm Region from 13.56 MHz Driven Hollow Slot Microplasmas Operating in Open Air.*, Plasma Sources Sci. Tech., 2004. **13**(3): p. 537-547.

9. Benedictis, S.D., G. Dilecce, and M. Simek, *Vibrational excitation of $N_2^+(B,v)$ in He-$N_2$ pulsed rf discharges.*, J. Phys. B: At. Mol. Opt. Phys., 1994. **27**: p. 615-632.

10. Payne, M.G., C.E. Kolts, and G.S. Hurst, *Kinetic processes determining the time dependence of VUV emission in He*.*, J. Chem. Phys., 1975. **63**(4): p. 1422-1428.

11. Lindinger, W., A.L. Schmeltekopf, and F.C. Fehsenfeld, *Temperature dependence of de-excitation rate constants of He($2\,^3S$) by Ne, Xe, $H_2$, $N_2$, $O_2$, $NH_3$ and $CO_2$.*, J. of Chem. Phys., 1974. **61**(7): p. 2890-2895.

12. Kato, T. and R.K. Janev, *Parametric representation of electron impact excitation and ionization cross-section for helium atoms.*, Suppl. Journ. Nuclear Fusion, 1992. **3**: p. 33-39.

13. Jeong, J.Y., et al., *Etching materials with an atmospheric-pressure plasma jet.*, Plasma Sources Sci. Technol., 1998. **7**(3): p. 282-285.

14. Massines, F. and G. Gouda, *A comparison of polypropylene-surface treatment by filamentary, homogeneous and glow discharges in helium atmospheric pressure.*, J. Phys. D: Appl. Phys., 1998. **31**: p. 3411-3420.

15. Lee, Y.H., C.H. Yi, M.J. Chung, and G.Y. Yeom, *Chararcteristics of He/$O_2$ atmospheric pressure glow discharge and its dry etching properties of organic materials.*, Surface and Coatings Technology, 2001. **146-147**: p. 474-479.

16. Raizer, Y.P., *Gas Discharge Physics*. 1st ed. (corrected reprint 1997). 1991, New York: Springer. p. 71.

17. Neeser, S., T. Kunz, and H. Langhoff, *A kinetic model for the formation of $Ar_2$ excimers.*, J. Phys. D: Appl. Phys., 1997. **30**: p. 1489-1498.

18. Kurunczi, P., H. Shah, and K. Becker, *Hydrogen Lyman-alpha and Lyman-beta emissions from high-pressure microhollow cathode discharges in Ne-$H_2$ mixtures.*, J. Phys. B: At. Mol. Phys., 1999. **32**(22): p. L651-L658.

19. Griegel, T., W.D. Heinz, J.H. Wolfgang, and K. Petkau, *The 3rd continuum of the rare-gases emitted by heavy-ion beam induced plasmas.*, J. Chem. Phys., 1990. **93**(7): p. 4581-4588.

20. Yalin, A.P., et al., *Electrical and optical emission characteristics of radio-frequency-driven hollow slot microplasmas operating in open air.*, Applied Physics Letters, 2003. **83**(14): p. 2766-2768.

21. Moller, T., J. Stapelfeldt, M. Beland, and G. Zimmerer, *Oscillatory structures in bound-free fluorescence-spectra of $Xe_2$, $Kr_2$ and $Ar_2$.*, Chem. Phys. Lett., 1985. **117**(3): p. 301-306.

22. Krotz, W., A. Ulrich, B. Busch, G. Ribitzki, and J. Wieser, *3rd excimer continuum of argon excited by a heavy-ion beam.*, Phys. Rev. A, 1991. **43**(11): p. 6089-6094.

23. Langhoff, H., *The origin of the higher continua emitted by the rare-gases.*, J. Phys. B: At. Mol. Opt. Phys., 1994. **27**(21): p. L709-L714.

24. Langhoff, H., *The origin of the third continua emitted by excited rare gases.*, Opt. Comm., 1988. **68**(1): p. 31-34.

25. Velazco, J.E., J.H. Kolts, and D.W. Setser, *Rate constants and quenching mechanisms for the metastable stats of argon, krypton, and xenon.*, J. Chem. Phys., 1978. **69**(10): p. 4357-4373.

26. Chilton, J.E., J.B. Boffard, R.S. Schappe, and C.C. Lin, *Measurement of electron-impact excitation into the 3p^54p levels of argon using fourier-transform spectroscopy.*, Phys. Rev. A, 1998. **57**(1): p. 267-277.

27. Radzig, A. and B. Smirnov, *Reference Data on Atoms, Molecules, and Ions*. 1985, New York: Springer-Verlag.

28. Bogaerts, A., *Hydrogen addition to an argon glow discharge: a numerical simulation.*, J. Anal. At. Spectrom., 2002. **17**(8): p. 768-779.

29. McNeely, J.R., G.S. Hurst, W.B. Wagner, and M.G. Payen, *Energy transfer from argon resonance states to nitrogen, hydrogen, and nitric oxide.*, J. Chem. Phys., 1975. **63**(6): p. 2717-2723.

30. Sadeghi, N. and D.W. Setser, *Quenching rate constants for reactions of Ar(4p'[1/2]0, 4p[1/2]0, 4p[3/2]2,4p[5/2]2) atoms with 22 reagent gases.*, J. Chem. Phys., 2001. **115**(7): p. 3144-3154.

31. Madison, D.H., C.M. Maloney, and J.B. Wang, *Integral and differential cross section for electron-impact excitation of 12 of the lowest states of argon.*, J. Phys. B. At. Mol. Opt. Phys., 1998. **31**: p. 873.

32. Svelto, O. and D. Hanna, *Principles of lasers (4th ed.)*. 1998, New York: Plenum Press.

33. Shon, J.W. and M.J. Kushner, *Excitation mechanisms and gain modeling of the high-pressures atomic Ar laser in He/Ar mixtures.*, J. Appl. Phys., 1994. **75**(4): p. 1883-890.

34. Sa, P.A. and J. Loureiro, *A time-dependent analysis of the nitrogen afterglow in $N_2$ and $N_2$-Ar microwave discharges.*, J. Phys.D: Appl. Phys., 1997. **30**: p. 2320-2330.

35. Jackson, G.P. and F.L. King, *Probing excitation/ionizatin processes in millisecond-pulsed glow discharges in argon through the addition of nitrogen.*, Spectrochimica Acta Part B, 2003. **58**: p. 185-209.

36. Bings, N.H., A. Bogaerts, and J.A.C. Broekaert, *Atomic Spectroscopy.*, Anal. Chem., 2004. **76**: p. 3313-3336.

37. Budtz-Jorgensen, C.V., P. Kringhoj, and J. Bottiger, *The critical role of hydrogen for physical sputtering with Ar-H2 glow discharges.*, Surface and Coatings Technology, 1999. **116-119**: p. 938-943.

38. Vasile-Dan, H., V. Hoffmann, B.M.S. Edward, and W. Klaus, J. Anal. At. Spectrom., 2001. **16**: p. 43-49.

39. Griem, H.R., *Spectral line broadening by plasmas*. 1st ed. 1974, New York and London: Academic Press.

40. Griem, H.R., *Plasma spectroscopy*. 1st ed. 1964, New York: McGraw-Hill Book Company.

41. Smith, E.W., J. Cooper, and C.R. Vidal, *Unified classical-path treatment of stark broadening.*, Phys. Rev., 1969. **185**(1): p. 140-151.

42. Vidal, C.R., J. Cooper, and E.W. Smith, *Hydrogen stark broadening calculations with the unified classical path theory.*, J. Qaunt. Spectrosc. Radiat. Transfer., 1970. **10**: p. 1011-1063.

43. Luque, J.M., M.D. Calzada, and M. Saez, *Experimental research into the influence of ion dynamics when measuring the electron density from the stark broadening of the H-alpha and H-beta lines.*, J. Phys. B. At. Mol. Opt. Phys., 2003. **36**: p. 1573-1584.

44. Laux, C.O., *Optical Diagnostics and radiative emission of air plasmas; PhD Thesis*, in *Mechanical Engineering*. 1993, Stanford University: Stanford.

45. Wang, Q., I. Koleva, V.M. Donnelly, and D.J. Economou, *Spatially resolved diagnostics of an atmospheric pressure direct current helium microplasma.*, J. Phys. D: Appl. Phys., 2005. **38**: p. 1-8.

46. Hagelstein, P.L., *Development of the MIT tabletop soft x-ray laser.*, SPIE (Ultrashort-Wavelength Lasers), 1992. **1551**: p. 254-274.

47. Olchawa, W., R. Olchawa, and B. Grabowski, *Stark broadening of hydrogen spectral lines with fine structure effects.*, Eur. Phys. J., 2004. **D 28**: p. 119-124.

48. Mewe, R., *Note on the singlet and triplet population in helium.*, Brit. J. Appl. Phys., 1966. **17**: p. 1239-1240.

49. Schieber, D., S. Gavril, and M.S. Erlicki, *Electron temperature determination in a low density helium plasma.*, Plasma Physics, 1970. **12**: p. 897-899.

50. Sovie, R.J., *The effects of cascadin and metastable atoms on the determination of electron temperature from relative line intensities in a tenuous helium plasma.*, J. Qaunt. Spectrosc. Radiat. Transfer., 1968. **8**: p. 833-838.

51. Gill, P. and C.E. Webb, *Electron energy distributions in the negative glow and their relevance to hollow cathode lasers.*, J. Phys. D: Appl. Phys., 1977. **10**: p. 299-311.

# Chapter 5

# Volume Plasma Generation

## 5.1 Introduction

Generation of large volume non-thermal APGD plasmas may enable new applications in thinfilm processing and treatment of industrial material surfaces. These industries either employ low pressure non-thermal plasmas which require vacuum technology and costly maintenance or they do not employ plasmas due to cost issues. Large volume APGD plasmas would not only remove costly equipment barrier, but may also provide faster processing rates due to higher electron/ion densities, photon fluxes and radical densities. Production of large volume APGD plasma in the normal glow mode suffers numerous challenges associated with the spatial uniformity and the temporal stability. Until now, few successful large volume non-thermal APGD plasma devices have been reported. This chapter focuses on generation of large volume plasmas using the microplasma device as the source of energetic species.

Generation of atmospheric pressure glow plasma generally is limited by the *pd* product (Chapter 1). High pressure, $p$, therefore requires smaller electrode separation, $d$, to reach $(pd)_{opt}$ values. One is to use arrays of microdischarges [1, 2], where each microdischarge employs micron size $d$, and the array allows large area coverage. As

discussed in Chapter 1 these plasma arrays essentially are two dimensional sources. Stark and Schoenbach [3] employed a third electrode along with the microhollow cathode discharge to successfully generate volume plasmas but with an upper limit of several cubic millimeters in volume. They also employed parallel microhollow discharge arrays along with third electrodes. However, since these are arrays of individual microplasma sources separated by regions of no plasmas, questions of spatial uniformity arise.

Generation of volume plasmas at atmospheric pressure may become possible with suitable choice of device design, power source and gas species. Most of the plasma instabilities originate in the sheath region due to high cathode fall voltage in the sheath. Electrons exit the sheath with high kinetic energy, and hence can cause an avalanche of electrons in the bulk plasma, which may lead to arc instability, the most prominent instability associated with glow discharges. Creating multiple sheaths (primary and secondary) and separating the primary sheath from the operating region can help stabilize the plasma operation. It is more probable to attain stable operation using RF or pulsed sources (or combination of these two) in comparison to the DC operation. This is because, for pulsed or RF excitation the loss balance is more stable since electrons gain their maximum energy for a short period of time (and in the remaining times electrons are unable to ionize atoms or molecules). Judicious choice of gas composition may also help to sustain stable non equilibrium APGD volume plasmas. All these factors are considered while generating the large area atmospheric pressure volume plasma described below.

**5.2 Experimental**

Figure 5.1 shows the cross section of the CSU designed device employed for volume plasma generation at atmospheric pressure. The plasma length is perpendicular to

the plane of the paper and may extend for ten's of centimeters. The hollow slot microplasma device located below in the bottom of the Figure 5.1 is used as the primary

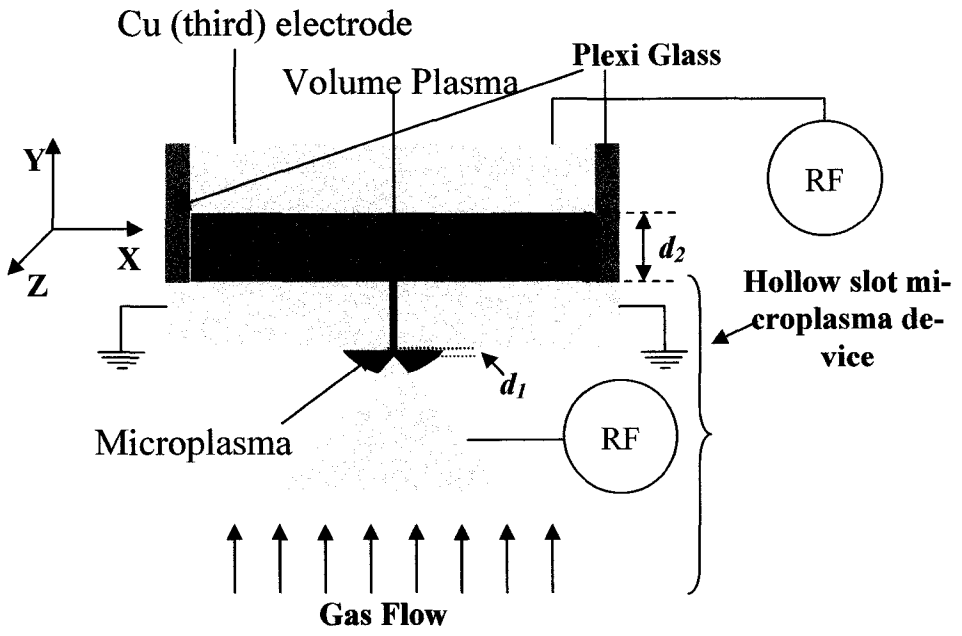


**Figure 5.1: Schematic of volume plasma device. A Cu electrode is added on top of the microplasma device of Figure 3.1a. The upper electrode is powered with RF. All the electrodes are water cooled. The rare gas enters the volume plasma region through the slot of the microplasma device.**

source in the upper region of Figure 5.1. The same hollow slot microplasma device (Fig. 3.1) [4, 5] with an electrode separation, $d_1$ (~100 μm), is used as the primary source of the energetic species. The upper (third) electrode is separated from the top surface of the grounded (slotted) electrodes by a distance, $d_2$. The upper electrode can be moved vertically up and down and thus the volume of the plasma can be minimized to facilitate gas breakdown (shorter gap requires lower breakdown voltage) and then enlarged for volumetric operation. Depending on the rare gas and rare gas-impurity combination, the separation, $d_2$, can be varied up to 1 cm in the vertical direction whereas the plasma length ($l$ ~ 6 cm, into page) and width ($w$ ~ 2 cm,) remain fixed. There is an enclosure (plexiglass) around the top electrode and plasma volume. The purpose of this enclosure is to minimize mixing of ambient gases with the rare gas that enters the volume plasma

region through the slotted electrodes. The enclosure has two square holes on either side of the plasma (for optical diagnostics) thus allowing some ambient air to mix into the plasma. The maximum volume plasma maximum volume of plasma generated in this configurations is ~ 12 $cm^3$ (2cm × 1cm × 6cm).

The rare gas in the volume plasma region enters through the exit port of the slot microplasma device, i.e., through the slot of the grounded electrodes. Depending on the separation, $d_2$, and the gas mixture, the volume plasma can be generated with or without the assistance of the lower hollow slot microplasmas. The hollow slot microplasma device is driven by 13.56 MHz RF generator, and is used as the primary source of excited species. Note that the existence of the plume plasma (Chapter 3) beyond the top surface of the slot shaped grounded electrode which confirms the presence of energetic species in the volume plasma region from the primary source (hollow slot microplasma device). After igniting the plasma in the hollow slot microplasma device, the upper electrode is driven by either 13.56 MHz or 60 MHz RF excitation and sustains the volume plasma. After stabilizing the volume plasma, the volume of the plasma covers the whole electrode region.

The optical and electrical data provided in this chapter is for a proof of principle slot-third electrode separation of $d \sim 4$ mm. The electrical data are collected by an AE Z-scan probe, whereas the optical data are collected by the scanning monochromator used for visible emission spectra. In this case, the optical emission from the volume plasmas is collected along the plasma length (whereas the emission spectra of the slot discharge were collected in the direction perpendicular to the plasma length). The optical data recorded for volume plasmas do not include absolute calibration either. The optical data covered the spectral range of 300 nm to 900 nm.

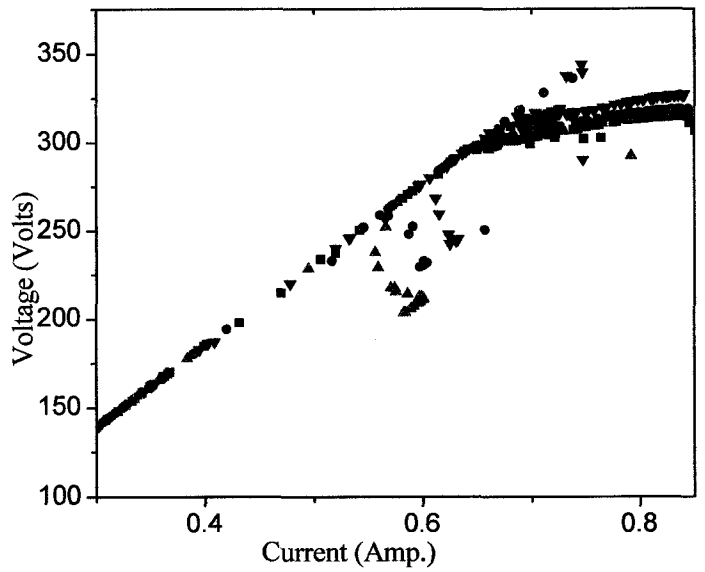


**Figure 5.2: *I-V* curves of He-$N_2$ volume plasmas before (linear voltage) and after gas breakdown (no. The gas breakdown occurs approximately at 350 Volts. The glow operations is observed for a current regime of ~ 0.6 to 0.85 Ampere. The flow rate of He is 5 slpm and the flow rate of $N_2$ are 0 sccm (black), 5 sccm (green), 10 sccm (red) and 20 sccm (blue).**

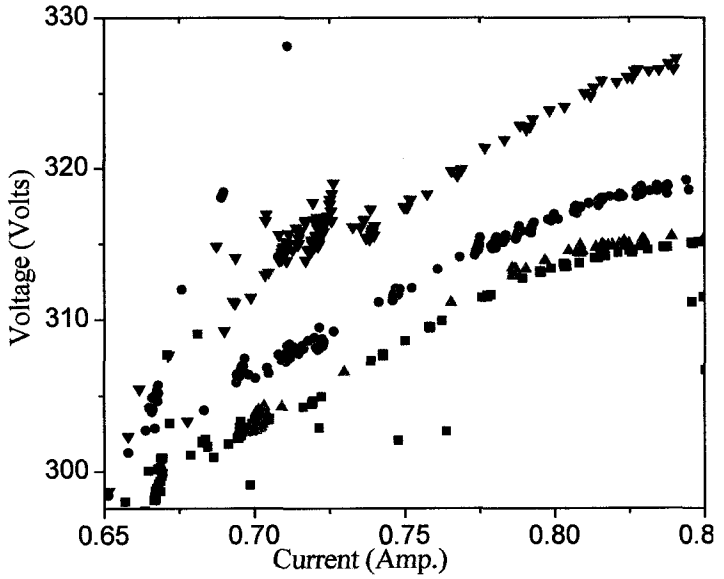


**Figure 5.3: *I-V* curves of He-$N_2$ volume plasmas after gas breakdown. The flow rate of He is 5 slpm and the flow rate of $N_2$ are 0 sccm (black), 5 sccm (green), 10 sccm (red) and 20 sccm (blue).**

## 5.3 Results and Discussion

### 5.3.1 Electrical

It is observed that ignition of the Ar volume plasma is difficult for 13.56 MHz excitation without the assistance of the lower secondary source of preionization (i.e. without

the microplasma source). In the similar condition the 60 MHz RF generator is easily able to generate Ar volume plasma, although it requires high power (~800 W) and the plasma immediately transforms into arc mode. Addition of small amount of $N_2$ suppresses the arc and the normal glow operation can be achieved.

Ignition of the argon volume plasma becomes easier (requires much less power) with an RF source sustaining the lower hollow slot microplasma which provides preionization. The 13.56 MHz RF source is employed to sustain the microplasma and hence acts as a source of energetic species. In Chapter 3, evidence of energetic species beyond the top surface of the slotted electrodes is depicted. These energetic species help the gas breakdown and help sustaining the Ar volume plasma while the upper electrode is driven by either the 13.56 MHz or 60 MHz RF source.

The helium volume plasma can be ignited and sustained with only 13.56 MHz RF source as the only excitation of the upper electrode (i.e. without introducing the slot plasma). In contrast the 60 MHz cannot ignite the He volume plasma without first turning on the lower microplasma source. This preliminary behavior is opposite to the Ar volume plasma, and may arise from the matching networks employed, since the matching networks used for upper electrode are the matching networks designed for the microplasmas and not optimized for the volume plasmas driven by 13.56 MHz and 60 MHz respectively.

Plasma ignition becomes easier with the aid of the lower microplasma source preionization for both Ar and He volume plasma. Once the volume plasma is ignited, the microplasma device does not contribute significantly and can be turned off without interrupting the volume plasma. We believe the effect of the microplasma is not pronounced

in this case because the channel through which energetic species come into the volume plasma is very small compared to the width, *w*, of the volume plasma.

Typical breakdown voltage for He plasma is about 350 Volts for 13.56 MHz operation where as the Ar volume plasma requires as much as 550 Volts. It is observed that the addition of $N_2$ into the He flow requires higher voltage to sustain the plasma. The stable operating regime requires ~300 Volts for the He volume plasma. The operating regime for He plasma lies between 0.6 to 0.85 A, i.e. the current density ranges from 50 $mA/cm^2$ to 70 $mA/cm^2$. For current density higher than 70 $mA/cm^2$ the discharge tends to an arc discharge.

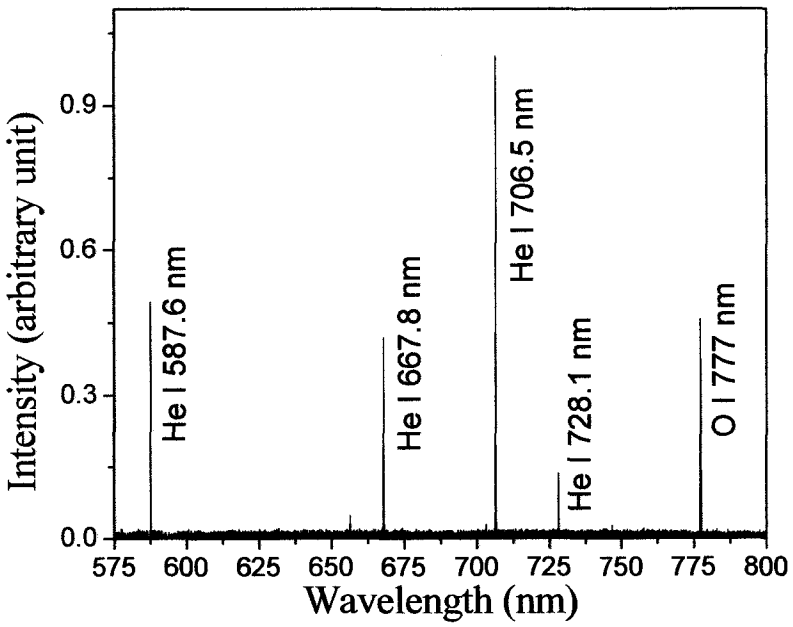


**Figure 5.4: Emission spectra (575-800 nm) from He column plasma using 13.56 MHz RF. The flow rate of He is 2 slpm. Atomic He I and O I transitions are clearly visible.**

5.3.2 Optical

At low gas pressure or high discharge current the volume plasma changes to a constricted plasma. At high discharge current, constricted plasma is narrow and luminous with a less bright plasma around the sharp and intense region. The diameter of the bright

channel is less than a millimeter. The spatial position of this luminous plasma continuously shifts and does not allow reliable recording of the optical emission. Further the moving constricted plasma results in electrode surface damage. This behavior is very consistent with arc mode.

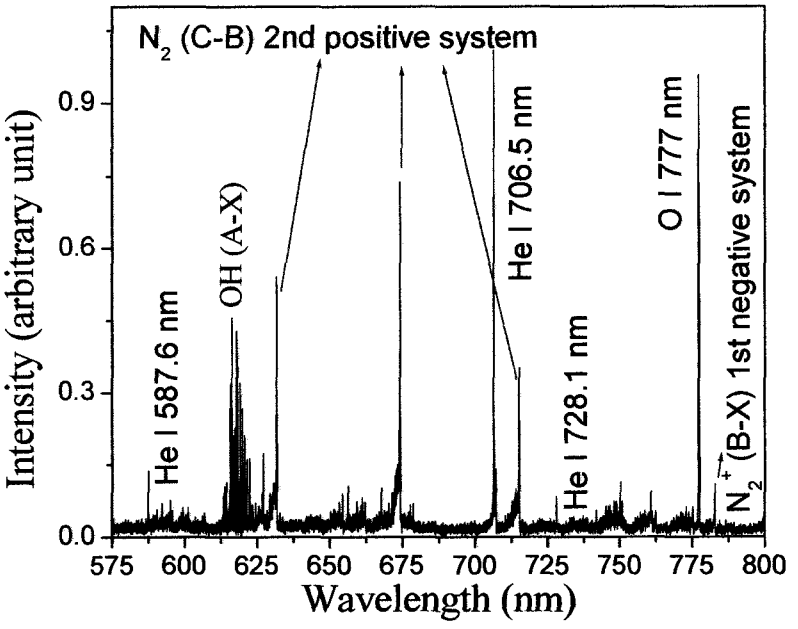


**Figure 5.5: Emission spectra from He volume plasma using 13.56 MHz RF source in the 575-800 nm spectral range. The flow rate of He is 2 slpm and the flow rate. Observed $N_2$ second positive bands, $N_2^+$ 1st negative band and OH(A-X) emission band are due to second order diffraction from the monochromator grating. Strong and clean OH rotational transitions are observed.**

At low pressure, the plasma also constricts into a luminous column. The luminous column in this particular case is larger in diameter (several millimeters) and does not change position with time thus allowing the acquisition of emission spectra. Figure 5.4 shows the optical emission spectra of the helium column plasma in the spectral range 575 - 800 nm.

The volume of the plasma can be increased by moving the electrodes apart. Generation of larger volumes is easier in the He plasma than Ar plasma. The Ar plasma is more prone to switch to arc mode. With the increase in the separation, $d_2$, the optical

intensity of the volume plasma decreases considerably. In the He plasma the excited atomic He I emission transitions are weak compared to the column plasma (except for the triplet 3s-2p transition at 706.5 nm). Compared to the column plasma, in the volume plasma the 587.8 nm and 667.8 nm transition are much weaker, whereas the difference in intensity for the 728.1 nm transition is less (Figure 5.4 and 5.5). We believe this behavior is due to self absorption. The Einstein A coefficients for the 667.8, 587.8 nm, 728.1 nm and 706.5 nm transitions are 0.638, 0.529, 0.181 and 0.154 (in $10^8$ $sec^{-1}$) respectively [6]. Due to long plasma length, transitions with high Einstein A coefficients (587.8 nm and 728.1 nm) suffer most in intensities due to self absorption. The atomic emissions from excited He I is suppressed when small amount of $N_2$ is added into the He volume plasma, which may be due to either self absorption or reduction of slow electron-metastable impact excitation reaction mechanism. The latter may arise due to metastable quenching or the loss of slow electrons (<3 eV) via inelastic loss with $N_2$.

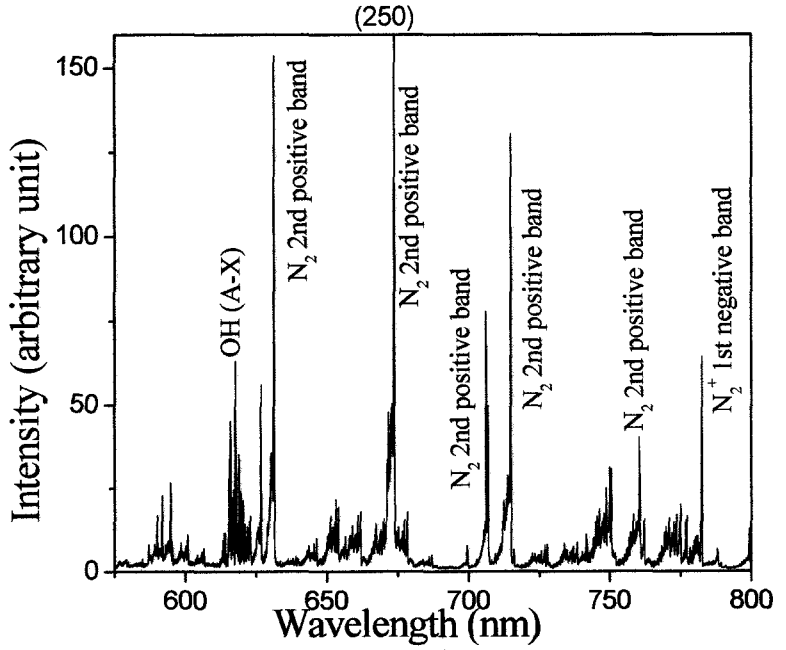


**Figure 5.6: Emission spectra from He-$N_2$ volume plasma using 60 MHz RF source in the spectral range 575-800 nm. The flow rate of He is 5 slpm and the flow rate of $N_2$ is 20 sccm. Observed OH (A-X) emission and few 2nd positive bands of N2 (C-B) transitions are labeled (these transitions are the second order effect). No strong atomic emissions are observed.**

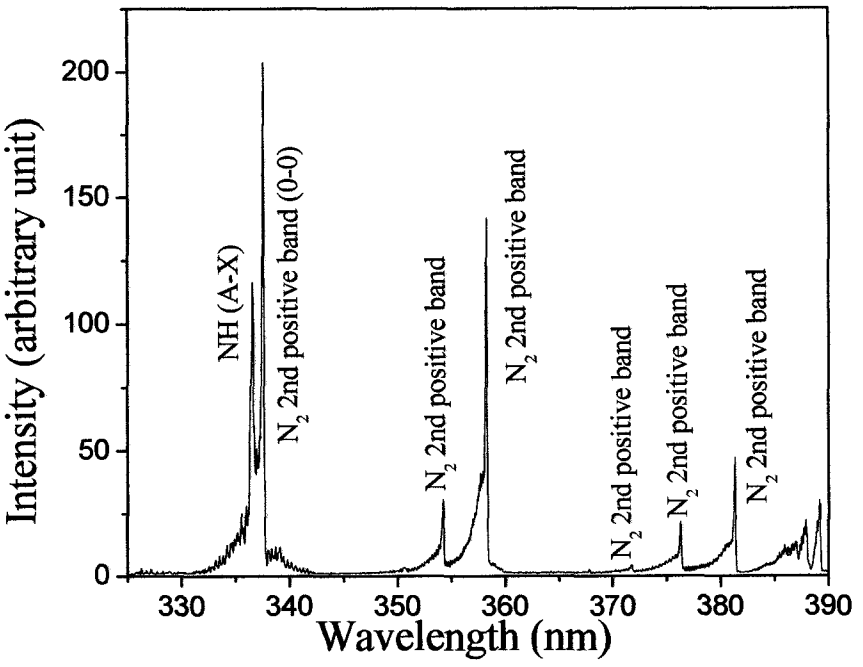


**Figure 5.7: Argon volume plasma in the wavelength range 325-390 nm. A 13.56 MHz RF source is used in the upper electrode.**

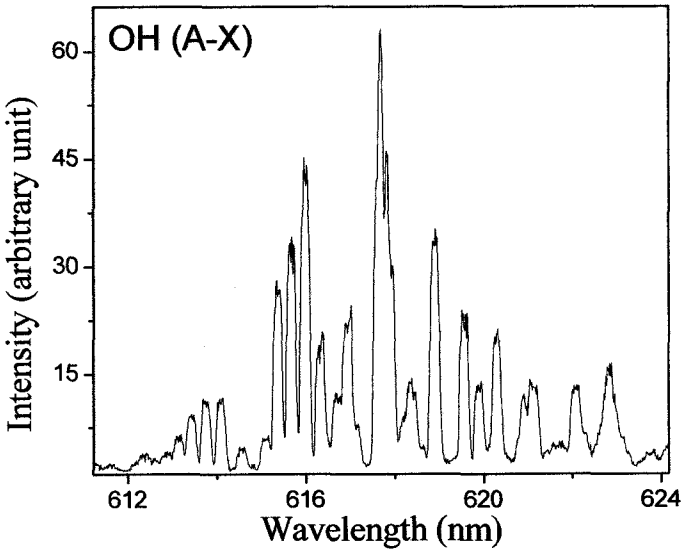


**Figure 5.8: Emission spectra from He-$N_2$ volume plasma in the 612-624 nm spectral range. The flow rate of He is 5 slpm and the flow rate of $N_2$ is 20 sccm. Observed OH(A-X) emission band is due to second order diffraction from the monochromator grating. Strong and clean OH rotational transitions are observed.**

In the Ar-$N_2$ volume plasma, all atomic Ar I transitions which are observed in the microplasmas are also detected in the visible and in the infra-red region. Strong emission

from the NH (A-X) at 336 nm can be observed while the emission from this band is weaker for the He-$N_2$ volume plasma. In the He volume plasma the OH emission band (Figure 5.5 and 5.8) is much stronger compared to the hollow slot microplasma emission spectra. The existence of these radicals can be of major importance for certain plasma processing applications.

**5.4 Conclusion**

Volume plasma generation at atmospheric pressure using two tandem sources has been attempted, studied and explained. Brief descriptions of electrical and optical characteristics are provided. It is observed that the volume plasma is stable only over a small RF current range. In the Ar volume plasma, addition of small amount of $N_2$ is observed to stabilize the glow plasma. In the future, other impurities can be examined to sustain larger volume plasmas without causing arc transitions. Strong emissions from $N_2$, $N_2^+$, OH and NH are observed in the volume plasmas. The radicals OH and NH are important for certain plasma processing applications. Future work on the volume plasmas will address several issues. Better matching networks which can be varied over wide ranges are required to improve the generation and sustainment of the volume plasma. Since the spectroscopy along the length of the plasma suffers from self absorption future spectra can be obtained perpendicular to the plasma length, *l*, that is in the YZ plane (Figure 5.1). Also spatially resolved spectroscopy can be performed. Finally, important plasma parameters, such as electron density, electron temperature, gas temperature, may be found using external probes (electrical and optical measurements).

**Reference:**


1. Schoenbach, K.H., A. El-Habachi, M. Moselhy, W. Shi, and R.H. Stark, *Micro-hollow cathode discharge excimer lamps.*, Physics of Plasmas, 2000. **7**(5): p. 2186-2191.
2. Chen, J., S. Park, Z. Fan, J.G. Eden, and C. Liu, *Development and characterization of micromachined hollow cathode plasma display devices.*, J. of Microelectromechanical Systems, 2002. **11**(5): p. 536-543.
3. Stark, R.H. and K.H. Schoenbach, *Direct current glow discharges in atmospheric pressure air.*, Appl. Phys. Lett., 1999. **74**(25): p. 3770-3772.
4. Yalin, A.P., et al., *Electrical and optical emission characteristics of radio-frequency-driven hollow slot microplasmas operating in open air.*, Applied Physics Letters, 2003. **83**(14): p. 2766-2768.
5. Rahman, A., et al., *Absolute UV and VUV Emission in the 110-400 nm Region from 13.56 MHz Driven Hollow Slot Microplasmas Operating in Open Air.*, Plasma Sources Sci. Tech., 2004. **13**(3): p. 537-547.
6. NIST, *NIST Chemical Kinetics Database, version 2.0*, in *National Institute of Standards and Technology, Standard Reference Data Program.* 1990, U.S. Department of Commerce: Gaithersburg, MD.

# Chapter 6

# Conclusion and Future Work

## 6.1 Conclusion and Future Work

This thesis presents electrical and optical measurements of RF driven microplasmas to characterize their electrical, optical and chemical properties. This device requires RF excitation field and employs flowing inert gas (Ar or He) as the active plasma medium. The microhollow discharge device operates in the in the open air and in the normal glow mode at relatively high current density ($j \sim 0.7$ A/cm$^2$) and generates energetic species (N, NO, OH, NH etc.) that can be used in a variety applications. The linear dimension of the microplasma is extended up to ~35 cm and therefore can treat large surface area in the push broom geometry. In addition, this device can be used as an external source for volume plasma breakdown at atmospheric pressure.

Electrical measurements provide information of both the plasma sheath impedance and bulk plasma properties of the glow region. It is experimentally verified that the non-linear effects in the plasma sheath are not prominent. Harmonic measurements (at constant power) show that the current and voltage waveform distortions are small. Since other electrical measurements are collected at varying delivered power, more detailed harmonic measurements at different powers are needed to provide more detailed

information on nonlinear plasma sheath behavior. The characteristic *V-I* curves of the RF driven (13.56 and 27.12 MHz) microplasmas resemble those of low pressure DC plasmas. At 60 MHz, the behavior of both the sheath and bulk plasma is different as compared to the 13.56 and 27.12 MHz excitation. This behavior originates from the lack of a DC sheath due to a different choice for a matching network. In future work, matching networks with the same configurations will be employed to better investigate the difference in the discharge behavior at different frequencies. In addition, a DC probe and stark splitting spectroscopy will be employed to determine contributions from the DC sheath. Using the modified high sheath voltage Child law (Liebermann-Godyak) and the resistance and capacitance values electron density of the plasmas are calculated. The calculated electron densities are in the order of $5x10^{18}$ $m^{-3}$.

Absolute optical emission spectra in the 110-400 nm region from RF driven (13.56 MHz and 60 MHZ) hollow slot microplasmas are presented. Optical emission spectra are divided into two classes, UV/VUV emission spectra and visible emission spectra. Measurements are time averaged and path integrated. In the UV/VUV region, atomic emissions from H I, O I and N I are observed mainly in the 110-200 nm region. This region also contains 2nd and 3rd continuum emission from Ar dimers in Ar microplasmas and $H_2$(B-X) emission in the He-$H_2$ microplasmas. At higher power, sputtering from the Cu electrode is observed . Emission from NO(γ) bands is dominant in the 200-300 nm region. Molecular emissions dominate the 300-400 nm region. Strong 2nd positive bands of $N_2$ along with relatively weak OH(A-X) and NH(A-X) bands are observed from Ar and He microplasma with different admixtures of $N_2$ and $H_2$. It is argued that the $N_2$(A) metastable state is a precursor to many atomic and molecular transitions.

Evidence of sputtering and strong resonance transition from Cu I cathode is observed in the Ar-$H_2$ microplasma. We attribute the sputtering to the formation of $ArH^+$ in the plasma. In the He microplasmas strong emission from the 1st negative band ($N_2^+$(B-X)) is observed. Excited $N_2^+$ ions are due to Penning ionization of $N_2$(X) by He (2s $^3$S) metastable state.

The 2nd positive band of $N_2$ (0-0) at 337 nm is employed to determine the rotational and gas temperature. The Boltzmann fitting estimation of the gas temperature is 650 +/- 100 K. This value corresponds to the upper limit of the gas temperature due to the NH(A-X) contribution (NH(0-0) band increases the width of the $N_2$ (0-0) band). Comparison of a theoretical simulation to the observed $N_2^+$ vibrational emission (by peak intensity ratio method) shows that the gas temperature is ~500 +/- 100 K.

We also have presented vibrational temperature measurements (from $N_2$ and $N_2^+$) based on Boltzmann fitting (SpecAir simulation code) and a peak intensity ratio method. All these measurements provide approximately the same vibrational temperature: 4600 ± 200K. The large difference between the gas temperature and the vibrational temperature indicates that the microplasmas are indeed non-equilibrium. The vibrational temperature estimation of $N_2^+$ employing the Boltzmann analysis (SpecAir simulation) shows that the vibrational bands of $N_2^+$(B) state are very strongly perturbed by other states (possibly by $N_2^+$(A)).

The emission spectra of 60 MHz driven hollow slot microplasma show different, $I(\lambda)$, spectra as compared to 13.56 MHz excitation. Most notably, stronger atomic emissions are observed in the VUV range and intensities of the 2nd positive bands of molecular nitrogen are increased. Both suggest an increase in the mean electron energy, $T_e$. On

the other hand emission from the $N_2^+$(B-X) transitions are observed to decrease. Since the upper state of this transition is primarily populated by Penning ionization, we conclude that the He (2s $^3$S) metastables are quenched (stepwise excitation/ionization) by the energetic electrons more effectively at high frequency (60 MHz) operation due to an increase in mean electron energy.

Visible emission spectra, $I(\lambda)$, provide information on the electron energy distribution function (EEDF). The spectra show that the effect of slow electrons is more pronounced in the He-$H_2$ microplasma compared to the He-$N_2$ microplasma. Stark measurements are performed to attain additional information in the electron number density. The calculated electron density from the optical spectra is ($2.5x10^{19}$ $m^{-3}$) (±20%), greater than the calculated density using the electrical measurements ($5x10^{18}$ $m^{-3}$). This discrepancy is likely due to gas pressure inside the slot is higher than the atmospheric pressure thus the measured collisional broadening contributions may be higher than anticipated. In future we will perform spatial measurement as well as polarization dependent Stark measurement. The latter one will provide the information of the electric field in the sheath region as well as in the bulk plasma region.

The electron temperature of He microplasma is determined using the line intensity ratio method suggested by Cunninghum. The method provides only a rough estimation since it does not include secondary effects (e.g. slow electron-metastable effects). The calculated value (7±3 eV) is very high compared to the typical values (1~2 eV) of APGD microplasmas. This large error bar stems primarily from the non-inclusion of the collisional quenching of the excited states and due to poor intensity and interference from background of the transitions considered. In addition, the discrepancy may be the result

of the line of sight measurement that includes the negative glow region where the electrons are very highly energetic. The transitions considered originates from $n=4$ level, and it is possible that these high lying states are excited only in the negative glow region so that the experimental result and simulated value of the electron temperature provides the negative glow electron temperature. In future work spatial measurements will be performed to determine the electron temperature more precisely. Since the $N_2(C)$ state has a very short radiative life time, the spatial emission spectra of $N_2(C\text{-}B)$ can provide important information about both spatial and temporal variation of the EEDF. A possible method of determining the electron temperature for Ar microplasmas is to probe the (weak) Ar II transitions.

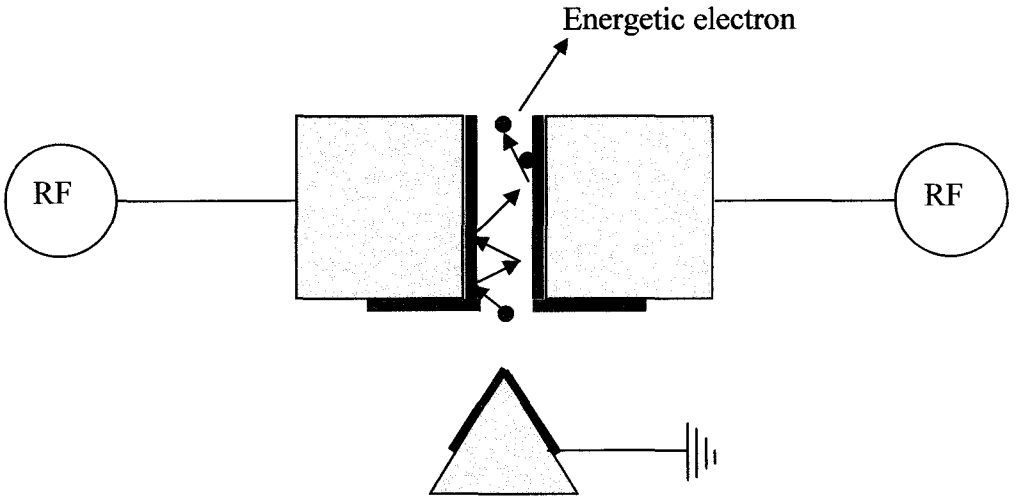


**Figure 6.1: RF source and ground connections are reversed (compared to Figure 2.1 b). Electrons generated in the active region will exit through the slot. Red dot exhibits the nature of the electron when traversing the slot region. Due to sheath at each wall, electrons will show considerable pendulum effect, i.e. electrons will gain energy from the sheath. Increased electron energy will generate more bulk electrons in the slotted region and thus the plasma should require less sustaining. Another potential advantage is that more energetic species will be available in the plume plasma.**

Volume plasma generation using the microplasma device as the source (cathode) for energetic species is also presented. It is found that for large separation of the volume electrode (third electrode), the microplasma device helps gas breakdown but does not

have any significant effect in sustaining the volume plasmas. Arc suppression of Ar volume plasma can be achieved by adding small amount of $N_2$ in the feed gas. Thus judicious choice of gas may help in better sustaining large volume plasmas. In the future, we will investigate introducing low ionization potential molecular gases into the He volume plasma to sustain larger volume plasmas.

Finally we suggest an alternative plasma source design for possible future investigation (Figure 6.1). The new design will be closer to conventional hollow cathode discharge. Energetic electrons will swing between the slotted electrodes since the self-bias DC sheath will be formed inside the slot as well as on the surface. Due to the Pendel effect, the device will be more efficient. In addition, its range of operation may be extended from low to high temperature operation. Hollow cathode discharges are already used in many (low pressure) applications such as spectral lamps [1, 2], plasma switches [1], lasers [2, 3], plasma conatctors in space crafts [1], plasma jets etc [1]. Because the proposed hollow electrode microdischarge operation resembles effective of hollow cathode/anode mode operation, this device may function well in similar applications.

**Reference:**


1. Kirkici, H. and D. Bruno, *Operating characteristics of a segmented hollow cathode over a wide pressure range.*, IEEE Trans. Plasma Sci., 1995. **23**(3): p. 229-234.
2. Arslanbekov, R.R., A.A. Kudryavtsev, and R.C. Tobin, *On the hollow-cathode effect: conventional and modified geometry.*, Plasma Sources Sci. Tech., 1998. **7**: p. 310-322.
3. Peard, K.A., Z. Donko, K. Rozsa, L. Szalai, and R.C. Tobin, *Comparison of CU-II 781 nm lasers using high-voltage hollow-cathode and hollow-anode discharges.*, IEEE J. Quantum Elect., 1994. **30**(9): p. 2157-2165.

# APPENDIX

## Appendix A

Rotational transition between two electronic states can be expressed as [1]:

$$\nu = \nu_0 + F'(J') - F''(J'') \quad \text{A1}$$

where, $\nu_0$ is called as the zero line or the position of the band head, $J$ is rotational angular momentum quantum number (single prime and double prime correspond to upper electronic state and lower electronic state respectively), and $F(J)$ is known as rotational term value and expressed as:

$$F(J) = B_v(J)(J+1) + \Lambda^2(A - B_v) - D_v(J)(J+1)^2 + .... \quad \text{A2}$$

Since the second term in the right side does not depend on the rotational levels, assimilating its effect in $\nu_0$, the position of a rotational transition can be written as:

$$\nu = \nu_0 + B_v'J'(J'+1) - D_v'J'(J'+1)^2 - B_v''J''(J''+1) + D_v''J''(J''+1)^2 \quad \text{A3}$$

where,

$$B_v = \sum_{i=0...} Y_{i1}(v+1/2)^i \quad \text{A4}$$

$Y_{ij}$ are known as Dunham expansion coefficients and $v$ is the vibrational level.

Depending on the rotational levels, rotational transitions are divided into three categories, P , Q and R branch

$\Delta J$=-1; P branch

$\Delta J$=0; Q branch

$\Delta J$=1; R branch

Therefore, for a P branch transition, position of a rotational transition is given by:

$$\nu = \nu_0 + F'(J-1) - F''(J) \qquad \text{A5}$$

$$\nu = \nu_0 + B'_v J(J-1) - D'_v J(J-1)^2 - B''_v J(J+1) + D''_v J(J+1)^2 \qquad \text{A6}$$

The 0-0 and 2-1 vibrational bands of $N_2^+$(B-X) transitions predominantly are formed by the P branches, the spacing of the rotational transitions can be determined using equation A4 along with the tabulated values of the constants (Table A1 and A2). The slit function (Appendix B) determines the number of rotational levels contributing to the vibrational band. Due to different values for the constants, the number of rotational levels contributing to the 2-1 vibrational band is more compared to the 0-0 vibrational band.

Intensity of any $J^{th}$ rotational line (P branch) is given by:

$$I^P_{v'v''} = K\left[A_{v'v''}\exp\left(-\frac{hc}{k}\frac{G(v')}{T_v}\right)\right]\left[\alpha^P_J S^P_J \exp\left[\left(-\frac{hc}{k}\right)\frac{Fv'(J-1)}{T_r}\right]\right]P(J) \qquad \text{A7}$$

where, $h$, $c$ and $k$ have their usual meaning. $T_r$ and $T_v$ are rotational temperature and vibrational temperature respectively. K is a constant and independent of the transitions considered here. $A_{v'v''}$ is band Einstein A coefficient. $G(n')$ can be expressed as

$$G_v = \sum_{i=1\ldots} Y_{i0}(v+1/2)^i \qquad \text{A8}$$

The even and odd rotational transition intensities of the P branches of the homonuclear molecule, $N_2^+$, with nuclear spin $I=1$, alternate in intensity with even and odd $J$ values such that

$$\alpha^P_J\,|_{even} = 2;$$

$$\alpha^P_J\,|_{odd} = 1;$$

and the line strength is given by:

$$S_J^P = \frac{J^2 - 1/4}{J}$$

Ratio of the intensities of the two $N_2^+$ (B-X) vibrational bands (2-1) and (0-0) is used to determine the vibrational temperature. Values of the constants are given in Table.

$$\frac{I_{21}^P}{I_{00}^P} = \frac{A_{21}}{A_{00}}\left[\exp\left(-\frac{hc}{k}\frac{G(2)-G(0)}{T_v}\right)\right]\frac{\sum_{2-1} SL_{21}\alpha_j^P S_J^P P_{21}(J)\exp\left[\left(-\frac{hc}{k}\right)\frac{F_2(J-1)}{T_r}\right]}{\sum_{0-0} SL_{00}\alpha_j^P S_J^P P_{00}(J)\exp\left[\left(-\frac{hc}{k}\right)\frac{F_0(J-1)}{T_r}\right]}$$

**Table A1: Spectroscopic constants for $N_2^+$(B-X) 0-0 and 2-1 vibrational transitions [2, 3].**

| Band (v'-v") | $T_{v'v''}$ ($cm^{-1}$) | $B_{v'}$ ($cm^{-1}$) | $B_{v''}$ ($cm^{-1}$) | $10^6 D_{v'}$ ($cm^{-1}$) | $10^6 D_{v''}$ ($cm^{-1}$) | $A_{v'v''}$ ($x10^7 s^{-1}$) |
|---|---|---|---|---|---|---|
| 0-0 | 25566.07 | 2.0746 | 1.9233 | 6.330 | 5.940 | 1.214 |
| 2-1 | 28081.92 | 2.0275 | 1.9033 | 6.890 | 5.979 | 0.861 |

**Table A2: Spectroscopic constants for $N_2^+$(B-X) 0-0 and 2-1 vibrational transitions [2, 3].**

| | $N_2^+$(X) | $N_2^+$(B) |
|---|---|---|
| $Y_{10}$ | 2207.22 | 2421.14 |
| $Y_{20}$ | -16.226 | -24.07 |
| $Y_{30}$ | $4*10^{-3}$ | -0.3 |
| $Y_{40}$ | $-6.1*10^{-3}$ | -0.0667 |
| $Y_{50}$ | $3.9*10^{-4}$ | |
| $Y_{60}$ | $-1.4*10^{-5}$ | |
| $Y_{70}$ | $2.0*10^{-7}$ | |
| | | |
| $Y_{01}$ | 1.93171 | 2.08507 |
| $Y_{11}$ | -0.018816 | -0.0212 |
| $Y_{21}$ | $-6.77*10^{-5}$ | $-5*10^{-4}$ |
| $Y_{31}$ | $-2.32*10^{-6}$ | $-8.8*10^{-5}$ |

## Appendix B

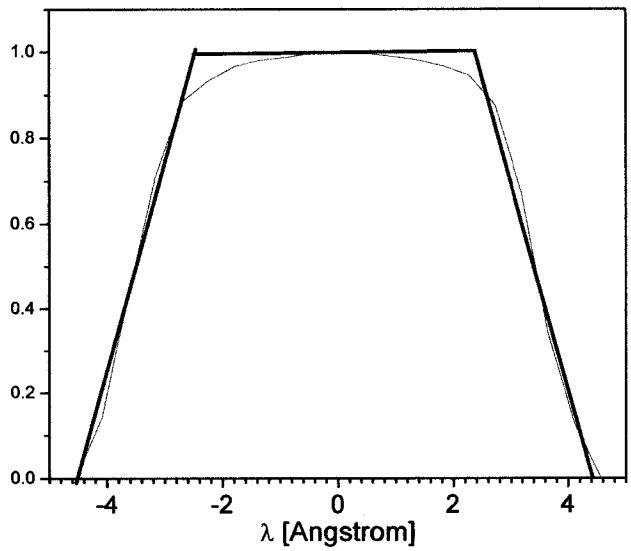


**Figure B1: Experimental slit function used for vibrational temperature measurement (Chapter 3). The fitted trapezoid has a base width of 8.9 A and top width of 4.9 A.**

## Appendix C

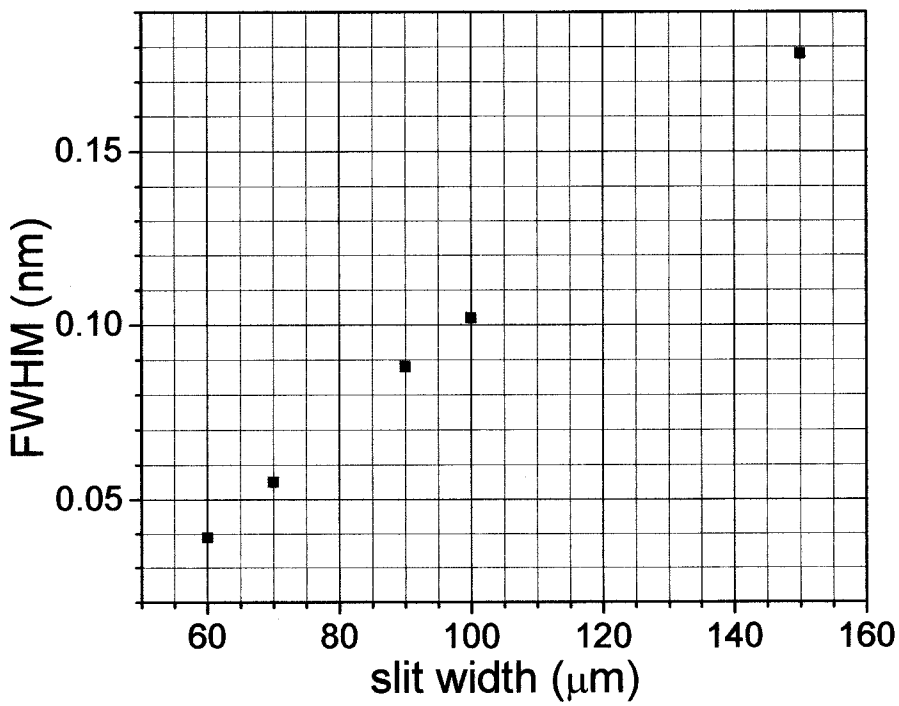


**Figure C1: Measured FWHM of a He-Ne laser line at 632.8 nm for different slit openings (both entrance and exit slit have the same slit openings).**

## Appendix D

The intensity trends of the 587 nm triplet emission is the best example (Figure 4.4) of slow electron-metastable interaction. This particular transition has several processes acting on populating its upper state as well as the lower state. Intensities of the 587 nm optical transition dropped sharply with a small amount of $N_2$ (5sccm) addition and continued to decrease with increased nitrogen addition (10 sccm and 20 sccm). The 2p $^3P^o$-3d $^3D$ (587 nm) transition experiences the largest decrease in intensity in comparison to the other helium atomic transitions. The maximum of the electron impact excitation cross-section from the triplet metastable state to the upper energy level of the 587 nm transition is an order of magnitude higher compared to the cross-sections of other transitions that are excited via same process [4]. The lower level (2p $^3P^o$) of the 587 nm transition is the most populated excited (He) atomic state[23] (besides the metastable states) and can contribute significantly in populating the upper state of the 587 nm transition via reaction R4.5. In addition to the metastable slow electron effect (R4.6), slow electron impact from the lower energy level (2p $^3P^o$ ) of the 587 nm transition is affected from the decrease in the high energy tail of the EEDF. The intensity of the 587 nm transition does not decrease by an order of magnitude as compared to the other He I transitions. The observed reduction in the intensity is judged due to both reduction of the high energy tail of the EEDF and the quenching of metastables, where the latter is less dominant because of efficient metastable (He (2s $^3S$)) quenching by impurity $N_2$.

Apart from the slow electron impact, non-radiative recombination of $He_2^+$ can also populate the 3d $^3D$ state (upper state of the 587 nm emission transition). Formation

[23] The 2p $^3P^o$ level has large electron impact excitation cross-sections (from ground stated and from triplet metastable state).

of $He_2^+$ requires an energy of ~23.1 eV [5]. Even though $He_2^+$ has well separated vibrational levels, it may undergo dissociative recombination upon capturing a slow electron which favors formation of 3d $^3$D state of atomic helium [6]. Quenching of metastables and decrease in the high energy tail of the EEDF hinders formation of $He_2^+$ and hence the 3d $^3$D population. Since a large portion of the ionization required to sustain the discharge is supplied by the added impurities (impurities with lower ionization energy), this causes a decrease in the helium metastable densities and ion densities and hence the dimer ions. Reduction of dimer ions consequently reduces the 3d $^3$D population and hence intensity of the 587 nm transition. If the upper state is populated via dimer ions, the 587 nm transition should show some wing broadening from recoil motion. The recoil energy, if shared by both the atoms equally, is approximately 1 eV for each (binding energy of the $He_2^+$ minus the energy of the excited atom, which is approximately 2 eV [7, 8]). No such broadening is clearly observed. This mechanism may be an added effect to the slow electron-metastable induced secondary process.

**Appendix E**

The ratio of the intensity of the triplet (388 nm) to the singlet (706 nm) transition is employed as a probe to determine the effect of the SP versus direct electron impact excitation from the ground state [9]. Interference of the 388 nm line with the first negative bands of $N_2^+$ prevent us from applying this method for He-$N_2$ microplasmas. If the intensity ratio $I_{388}/I_{706}$ the ratio lies between 1 and 2 when direct electron impact excitation from the ground state dominates. On the other hand, if the triplet metastable contribution (SP) is large in populating 3p $^3$P state, the ratio lies between 13 and 20 [9]. Table 4.9 &

4.10 shows the intensity ratio $I_{388}/I_{706}$ for different $H_2$ and $O_2$ concentration in He-$H_2$ and He-$O_2$ microplasmas.

This is possible because the 388 nm transition is a very strong function of the SP. In this section the effect of the SP to that of the higher excited levels of He in He-$H_2$ and He-$O_2$ from the metastables are discussed in terms of the line intensity ratio method mentioned above. The 388 nm triplet transition has the strongest dependence on the metastable states in the spectral region of our interest. We show (next paragraph) that the He-$O_2$ is not compatible for determining electron temperature ($T_e$) and only He microplasmas with higher $H_2$ concentration (10 and 20 sccm) are therefore considered for $T_e$ calculation.

The ratio of 706 nm to 388 nm line intensities is a measure of the effect of the metastables in populating upper excited levels via slow electron impact excitation (SP process). Metastables have the largest effect via SP to the $n=3$ levels, in particular, the 3 $^3$P state. The ground state is a singlet state, and triplet-singlet transitions are forbidden by the spin parity selection rule. No resonance transition to the ground state is allowed from the triplet states. The triplet $n=2$ level (He (2 $^3$S)) acts as the virtual ground to the triplet transitions. In addition, direct electron impact excitation to this level (2 $^3$S) has a larger cross-section compared to the singlet metastable state (reproduced cross-sections are shown in Figure E1 and Figure E2 [10]), thus He 2 $^3$S has much higher population density in the plasma. It can be inferred that the triplet emission transition from the 3 $^3$P to 2 $^3$S (388 nm) intensity will be very large compared to the singlet emission transition 3s $^1$S to 2p $^1$P if the SP process dominates. On the contrary, if the effect of SP is small, the ratio of the intensity of these lines ($I_{388}/I_{706}$) should be roughly equal to the ratio of their

respective electron impact excitation cross-sections from the ground state. The maximum of the direct electron impact excitation cross-sections for 3s $^1S$ and 3p $^3P$ from the ground state are approximately $4X10^{18}$ $cm^2$ and $8X10^{18}$ $cm^2$ respectively (reproduced cross-sections from ref. [10] are provided in Appendix D), i.e. the ratio is ~2. Table 4.9: Triplet- singlet line intensity ratios of He-$H_2$ microplasmas (from $n$=3 to $n$=2 levels). He flow rate is 2 slpm.

The decrease in the ratio of the intensities clearly indicates that the secondary effect of triplet metastables in populating the 3p $^3P$ level decreases with increasing $H_2$ concentration. This observation agrees with earlier statement that the metastables are quenched with increasing $H_2$ concentration (4.3.1). In the He-$O_2$ plasma, the ratio decreases as $O_2$ is added (5 sccm) and then increases with higher $O_2$ concentration (10 and 20 sccm). This behavior can not be attributed to the destruction of metastable states by $O_2$, but suggests a competing process due to attachment process owing to high electron affinity of oxygen. Oxygen is highly electronegative gas, and addition of $O_2$ in the discharge generates atomic O by dissociation which requires 5.08 eV [11]. Oxygen atoms capture slow electrons, thereby reducing the secondary effect that in turn causes the ratio of the intensities ($I_{388}/I_{706}$) to decrease (reduced slow electron density reduces secondary effect). Consequently the discharge requires to increase the electron temperature (i.e. electric field) in order to sustain the microplasma. This effect increases the intensities of all helium atomic transitions due to increased direct impact excitation from the ground state (and thus increases intensity ration $I_{388}/I_{706}$). Therefore, this is a competing process where secondary process dominates marginally over direct electron impact excitation from the ground state at low $O_2$ partial pressure (Table 4.10). Increased $O_2$ concentration

(10 sccm and 20 sccm) shows that the ratio $I_{388}/I_{706}$ increases, thus indicating the SP dominates over the direct electron impact excitation from the ground state (Table 4.10).

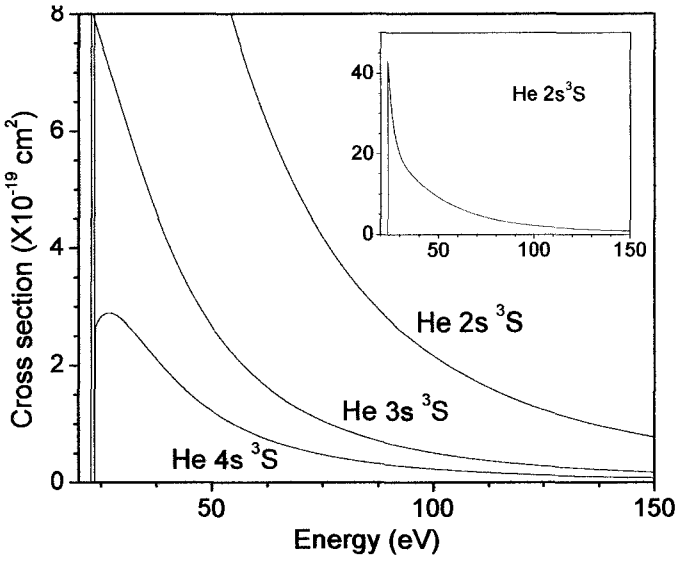


**Figure E1: Electron impact excitation cross section from the ground state helium to the triplet excited states for *n=2 ,3* and *4* (subset shows the cross-section for *n=2* level) [10].**

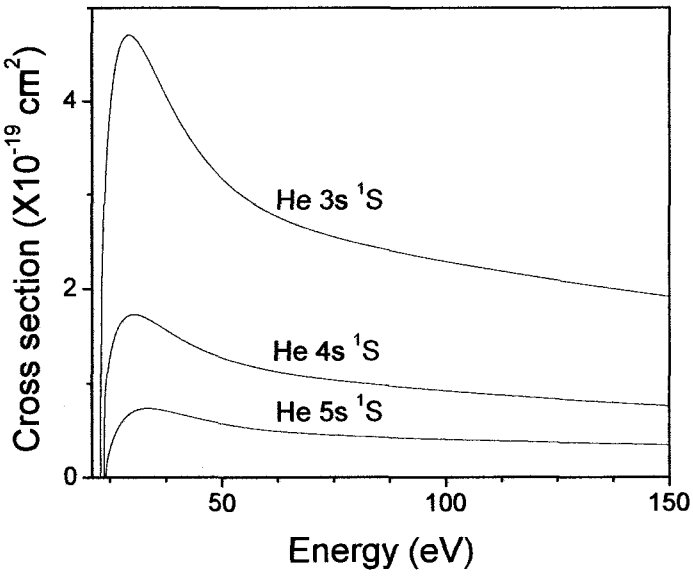


**Figure E2: Electron impact excitation cross section from the ground state helium to the singlet excited states for *n=3, 4* and *5* [10].**

**Reference:**


1. Herzberg, G., *Molecular Spectra and Molecular Structure I. Spectra of Diatomic Molecules*. Second ed. Vol. I. 1950, New York, NY: Van Nostrand Reinhold.
2. Klynning, L. and P. Pages, *The band spectrum of $N_2^+$.*, Phys. Scripta, 1982. **25**: p. 543-560.
3. Laux, C.O., *Optical Diagnostics and radiative emission of air plasmas; PhD Thesis*, in *Mechanical Engineering*. 1993, Stanford University: Stanford.
4. Shevelko, V.P. and H. Tawara, *Cross sections for electron-impact induced transitions between excited states in He:n,n'= 2, 3 and 4*. 1995, National Technical Information Service Document No. DE96725192INZ. Copies may be ordered from National Technical Information Service Springfield, VA 22161, NIFS-DATA-28 1995.
5. Wellenstein, H.F. and W.W. Robertson, *Collisional relaxation processes for the n=3 states of helium. II. Associative ionization.*, J. Chem. Phys., 1972. **56**(3): p. 1077-1082.
6. Biondi, M.A., *Studies of the mechanism of electron-ion recombination. I.*, Phys. Rev., 1963. **129**(3): p. 1181.
7. Biondi, M.A. and T. Holstein, *Concerning the mechanism of electron-ion recombination.*, Phys. Rev., 1951. **82**: p. 962-963.
8. Rogers, W.A. and M.A. Biondi, *Studies of the mechanism of electron-ion recombination. II.*, Phys. Rev., 1964. **134**(A5): p. A1215-A1225.

9. Sovie, R.J., *The effects of cascading and metastable atoms on the determination of electron temperature from relative line intensities in a tenuous helium plasma.*, J. Qaunt. Spectrosc. Radiat. Transfer., 1968. **8**: p. 833-838.

10. Kato, T. and R.K. Janev, *Parametric representation of electron impact excitation and ionization cross-section for helium atoms.*, Suppl. Journ. Nuclear Fusion, 1992. **3**: p. 33-39.

11. Herzberg, G., *Molecular spectra and molecular structure*. 2nd ed. Vol. I. 1989, Florida: Krieger Publishing Company. p. 558.